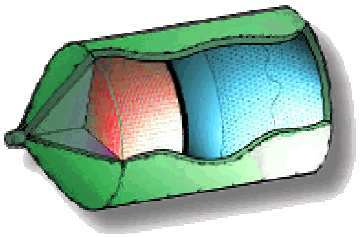

CENTER FOR SIMULATION OF DYNAMIC RESPONSE OF MATERIALS

A DOE ASCI / ASAP CENTER OF EXCELLENCE

TECHNICAL REPORT 032

The 1998 Center for Simulation of Dynamic Response in Materials
Annual Technical Report

Center for Simulation of Dynamic Response in Materials

Annual Technical Report

Sept. 3, 1997 - Sept. 30, 1998

W. A. Goddard, D. I Meiron, M. Ortiz,
J. E. Shepherd, J. Pool

California Institute of Technology
Pasadena, CA 91125

Prepared for
DOE ASCI Alliances Program
Lawrence Livermore National Laboratory

December 28, 1998

Contents

Chapter 1

Introduction

This annual report describes research accomplishments for FY 98 of the Center for Simulation of Dynamic Response of Materials. The Center is constructing a virtual shock physics facility in which the full three dimensional response of a variety of target materials can be computed for a wide range of compressive, tensional, and shear loadings, including those produced by detonation of energetic materials. The goals are to facilitate computation of a variety of experiments in which strong shock and detonation waves are made to impinge on targets consisting of various combinations of materials, compute the subsequent dynamic response of the target materials, and validate these computations against experimental data.

The research is centered on the three primary stages required to conduct a virtual experiment in this facility: detonation of high explosives, interaction of shock waves with materials, and shock-induced compressible turbulence and mixing. The modeling requirements are addressed through five integrated research initiatives which form the basis of the simulation development road map to guide the key disciplinary activities:

1. Modeling and simulation of fundamental processes in detonation,
2. Modeling dynamic response of solids,
3. First principles computation of materials properties,
4. Compressible turbulence and mixing, and
5. Computational and computer science infrastructure.

The project team consists primarily of a diverse group of Caltech faculty comprised of applied mathematicians, chemists, computer scientists, engineering faculty in fluid and solid mechanics, materials scientists, and physicists. In addition, to further strengthen the team in the selected areas of computational science and materials science, a few key researchers from Brown University, University of Tennessee, Indiana University, University of Illinois, the Carnegie Institute of Washington, and the Information Sciences Institute at USC have joined in this collaboration.

Work achieved in FY 98 is described in Chapters 2-6. On Chapter 7 we outline our implementation plans for FY99 and provide an overview of our integration plan as well as the proposed budget.

Chapter 2

High Explosives

2.1 Introduction

One of the three major stages of the overarching simulation is the detonation of high explosives (HE). One goal of the Caltech ASCI Alliance center is to make significant improvements in the state of the art in simulations of the detonation process in high explosives. As part of the proposal process and during the first year of the project, we have identified a number of issues that we need to address in order to do that.

An interdisciplinary team of faculty, postdoctoral scholars and students has been organized to work on these issues. This research team, dubbed the HE (high explosives) group, is one of the five major organizational components of the Caltech ASCI Alliance. The HE group is led by Joe Shepherd and has about 15 members drawn from the different disciplines involved in the Caltech ASCI Alliance. The purpose of this group is to coordinate research activities, educate the members about different approaches to HE modeling, and to develop the simulation methodology and tools for the high explosive component of the virtual test facility. The group meets regularly on a weekly basis. In the beginning of the year, the meetings were tutorial and and we emphasized learning about the vocabulary and capabilities of the different participants. Later, as collaborations developed, the group meeting was used to review technical progress in the specific focus areas.

There are two tracks to the research program in high explosives. Work is proceeding on both tracks simultaneously. Within each track, the work has concentrated on a few specific materials. A goal of achieving a simple version of the integrated simulation has served to focus the efforts of the whole group. In addition there is a third component which addresses the integration of these activities with other research activities of the project:

1. **First Principles** - Selected problems are being studied using detailed and realistic chemical and physical description of explosives. One problem that is being studied in this fashion is the equation of state of of explosives, binders and reactions. Another problem is reactive flow hydrodynamics in gases using detailed chemistry networks and reaction rates.

2. **Evolutionary** - Existing engineering models of high explosives are being extended and incorporated into high resolution computations using adaptive mesh refinement.

Developing an engineering modeling capability is essential for the two-dimensional prototype of the virtual test facility, and also enables us to assess the issues with the state of the art in detonation simulation.

3. **Integrated Simulation Goal** - The focus issue within the HE group has been to integrate the results from each discipline into a framework that can feed into the simulation of a model high explosives problem. This model problem is the so-called "corner-turning problem" that involves the diffraction of a detonation around a convex corner, and interaction of the detonation with a contact surface. This contains two of the three elements of the overarching application being studied by the alliance.

The activities in the the first year (FY 98: October 1, 1997 to September 30, 1998) of the program are briefly described below and more detail is given in subsequent sections.

- **Material Properties** - This work is being primarily carried out in the Material Properties group led by W. Goddard. The work in the first year has been targeted toward three specific materials: the explosives HMX and TATB, the binder Kel-F. The principle participants from that organization are S. Dasgupta, L. Sun, G. Caldwell, R. Muller, and T. Cagin. The focus of the Material Properties work in FY98 was to develop force fields and carry out classical molecular dynamics simulations to obtain the $PVET$ surfaces of hot, high-pressure HMX, TATB and Kel-F. Once these surfaces were obtained, further thermodynamic analyses were carried out by other members (Arienti and Hung) of the HE group. The principle results of these analyses were Grüneisen coefficient, heat capacity, shock adiabats or Hugoniots, and isothermal compression curves. In turn, these results were used to improve and extend empirical equations of state, such as the Mie-Grüneisen model, that are used in the numerical simulation of HE propagation by still other members (Morano, Shepherd) of the HE group. There was substantial interaction between all of participants in this activity. Validation of molecular dynamics results against data (primarily generated in the DP laboratories) was an important activity by the HE group and resulted in refinement of the force fields and choice of MD techniques.

- **Reaction Zone Modeling in Gases with Detailed Kinetics** - This work was carried out within the HE group by C. Eckett. The goals of this effort are to develop simplified reaction mechanisms and implementation into the numerical simulations of gaseous detonation. The work is initially focused on existing gas-phase reaction schemes and transition over to encompass high-pressure states as the project progresses. The activities this year included:

  - Development of simplified reaction models for H2-O2-diluent systems. An existing reaction mechanism was used to develop a reduced mechanism for H2-O2. The reduced mechanism was implemented in the steady 1D ZND detonation model and validated against with the results of the full mechanism.
  - Full chemical kinetics subroutines The CHEMKIN subroutines and a stiff ordinary differential equation solver were incorporated into Amrita and the `amr_sol` flow solver module.

  - 1D unsteady simulations. A set of one-dimensional unsteady computations were carried out with full kinetics and validated against test case involving shock tube and steady propagating wave solutions.

- **Engineering Model of High Explosives** - This activity was carried out by E. Morano and J. Shepherd of the HE group. A simplified engineering model of a high explosive with a resolved reaction zone was implemented within the Amrita and `amr_sol` flow solver framework. A Mie-Grüneisen model of the equation of state was used together with a one-step irreversible depletion law with a pressure-dependent reaction rate (p^n). Simulation results were validated against steady traveling wave solutions and non-reactive shock tube solutions. A 2D simulation of corner-turning and wave interaction with an inert interface was carried out using adaptive mesh refinement.

- **Micromechanics of PBX** - This activity was carried out by W. Knauss and S. Sundaram of the HE group. Stress wave propagation in an elastomer binder was simulated for simple one-dimensional situations. The binder was treated as a nonlinear viscoelastic material with pressure stiffening.

2.2 Materials Properties

Classical force fields were developed for the explosive molecules HMX and TATB and the binder Kel-F. Molecular dynamics simulations were carried out with these forces to determine trajectories which were averaged using statistical mechanics to find thermodynamic properties. The goal of the Molecular Mechanics/Dynamics work was to provide the Equation Of State (EOS) quadruples (E,P,V,T) to the HE group for use in their simulation of detonation.

One important facet of this work was determining which MD ensemble is best suited to these types of calculations. While early work was done with NPT ensembles, it was found volume, the free variable, was slow to converge. Currently we are using NVE dynamics since the free variable, pressure, converges quite rapidly to a steady value. We have also focussed on calculating what range and grid spacing needs to be used for the calculations.

2.2.1 HMX

HMX is widely used (PBX9404, PBX9501) in DOE formulations. HMX ($C_4H_8N_8O_8$) exists in 4 crystallographic forms - the stable room temperature β, and the higher temperature δ, γ and α forms. We obtained the crystal structures, (Fig. 2.1) from the Cambridge Crystallographic Database. HMX occurs in 2 molecular conformations, chair (β) and boat (α, δ and γ). We have used Density Functional Theory (B3LYP/6-31G**) to calculate the differences in energy of the 2 forms - 2.2 kcal/mole with the chair form being lower in energy. The computed geometric parameters are in reasonable agreement with the experimental crystallographic values. Starting with a very simple force field, Dreiding II, we have modified the van der Waals interactions from the standard and fast Lennard-Jones (LJ or 12-6) form to the slower Exponential-6 form. There is computational evidence that the inner wall for LJ

is too steep and for systems under compression, is not adequate to describe the inter-atomic potential accurately. Exponential-6 models have also found wide application in other areas of detonation modeling such as product statistical mechanics.

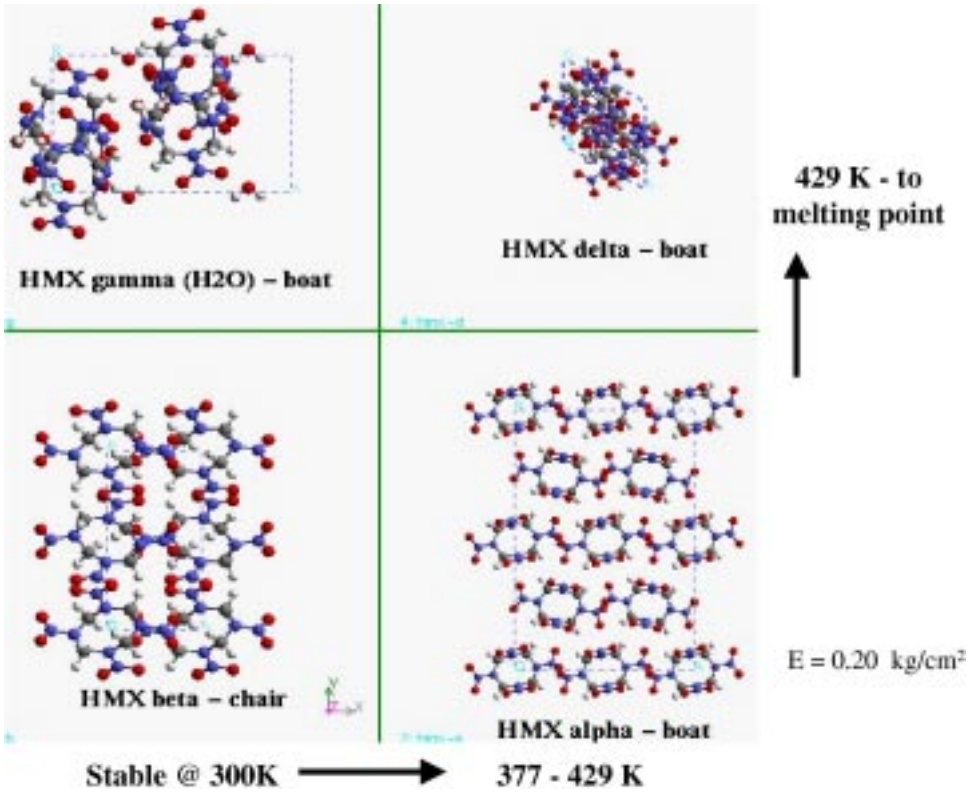

Figure 2.1: Crystallographic forms for HMX, their stable temperature range, and shock sensitivity.

Our calculated zero-pressure structures are in close agreement with the experimental cell parameters for all 4 forms. There is cold compression data from Cady and Ollinger on the stable β form, and our calculated compression curve is in very good agreement with this data, (Fig. 2.2). We have done the cold compression on all the 4 isomorphs of HMX and Fig. 2.3 shows their relative compressibility. Although most of the initial studies were done with the NPT ensemble, the NVE ensemble is now being used. Some preliminary results are shown in Fig. 2.4.

Specific heat is an important variable that is used in the engineering equations of compressible fluid flow. Current practice is to use a single specific heat value that is independent of temperature and pressure. However, since the main contribution to specific heat - the vibrational degrees of freedom - are strongly temperature dependent, we have used both ab initio frequencies for the single molecule, and the force-field-based calculation of the Einstein oscillator frequencies of the solid material with Brillouin zone averaging. Fig. 2.5 shows that the simple Dreiding force field is qualitatively accurate in modeling the single-molecule vibrational frequencies of HMX, even though specific modes are not within experimental accuracy. Fig. 2.6 shows the specific heats as a function of temperature. With the vibrationally accurate force field, scheduled for year 2 of the program, these calculations will be

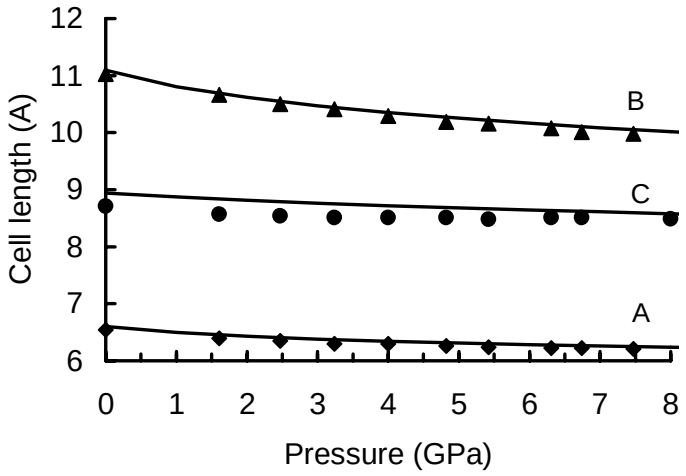

Figure 2.2: Comparison of cell parameters for β-HMX under hydrostatic compression with experimental data from Cady and Ollinger

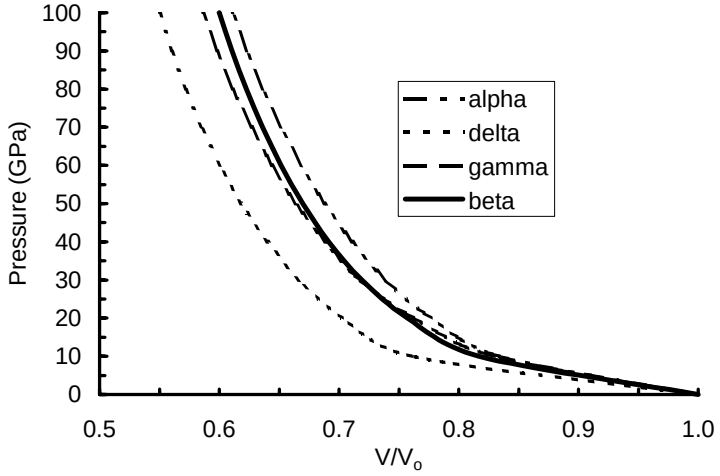

Figure 2.3: Relative compressibility of various HMX isomorphs.

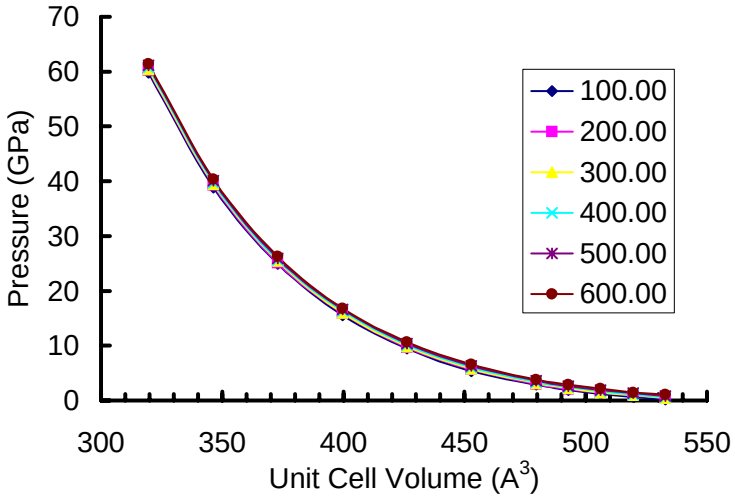

(a)

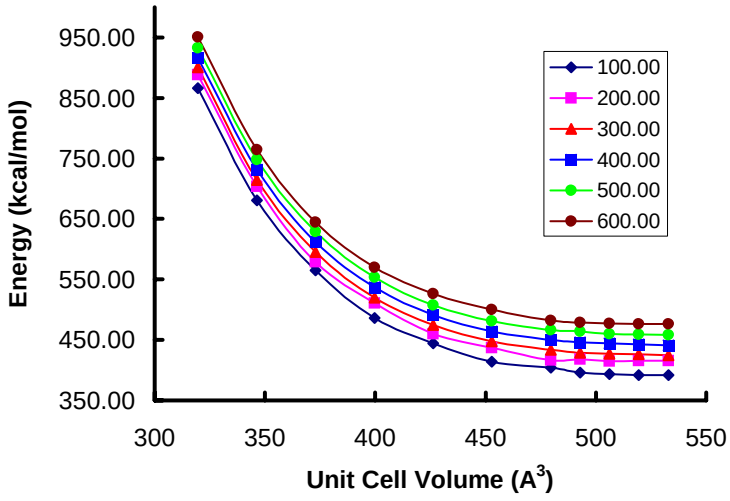

(b)

Figure 2.4: EOS for β-HMX from NVE dynamics.

further improved.

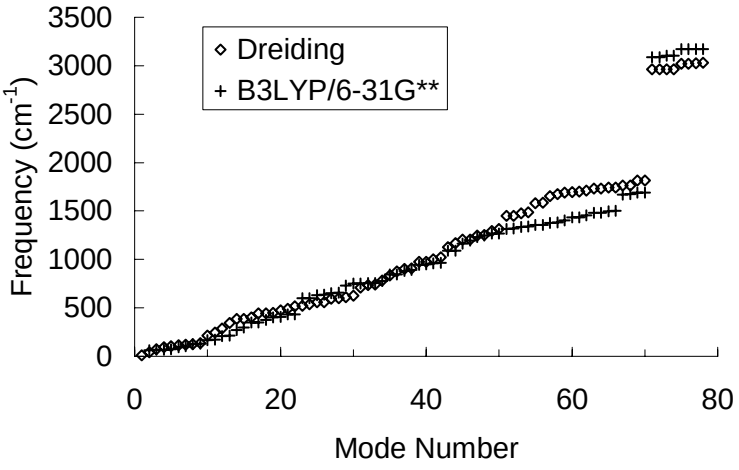

Figure 2.5: Comparison of Dreiding force field frequencies with DFT frequencies.

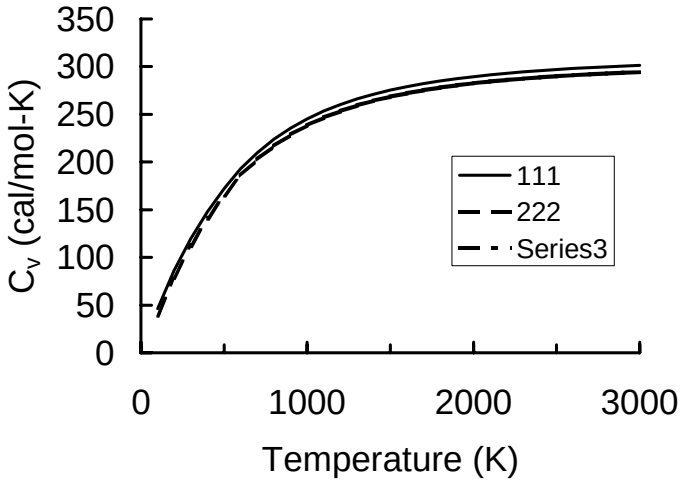

Figure 2.6: β-HMX specific heat as a function of temperature.

2.2.2 Equation of State of TATB

TATB, 1,3,5-triamino-2,4,6-trinitrobenzene (Fig. 2.7) is an insensitive high explosive used in some DOE formulations (PBX9502, LX17). At standard temperature and pressure, the density of TATB is 1.9374 g/cc. The unit cell parameters of experimental structure are a=9.01 Å, B=9.028 Åand C=6.812 Å, with space group P-1.

Molecular dynamics simulations on TATB crystals were done with three different force fields. Cold compression and isothermal curves at temperatures between 0 and 1500 K were obtained and compared with experimental data (Fig. 2.8 and 2.9). Among the three force

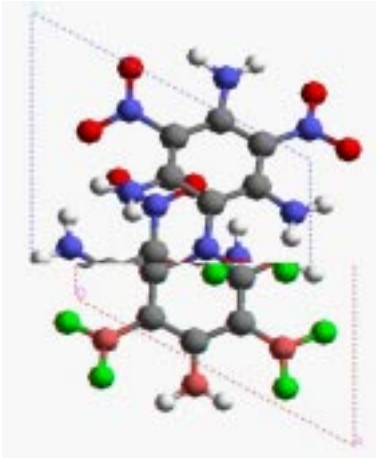

Figure 2.7: TATB unit cell at STP calculated from Exponential-6 Dreiding Force Field.

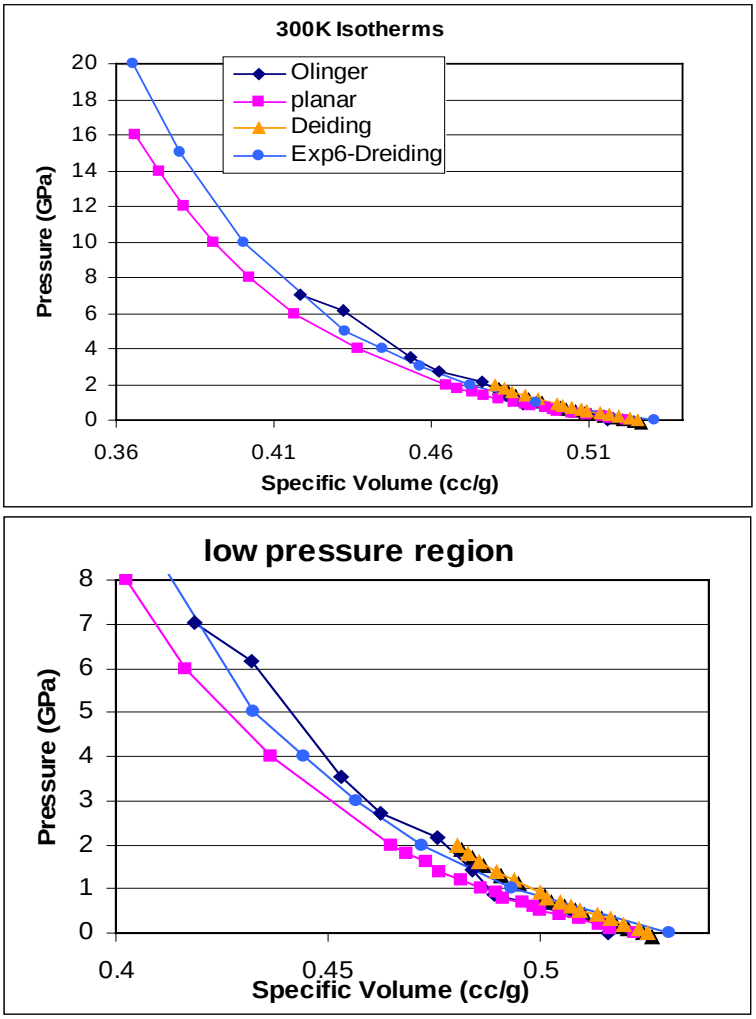

Figure 2.8: Isothermal compression at 300 K from the three different force fields and from experiment.

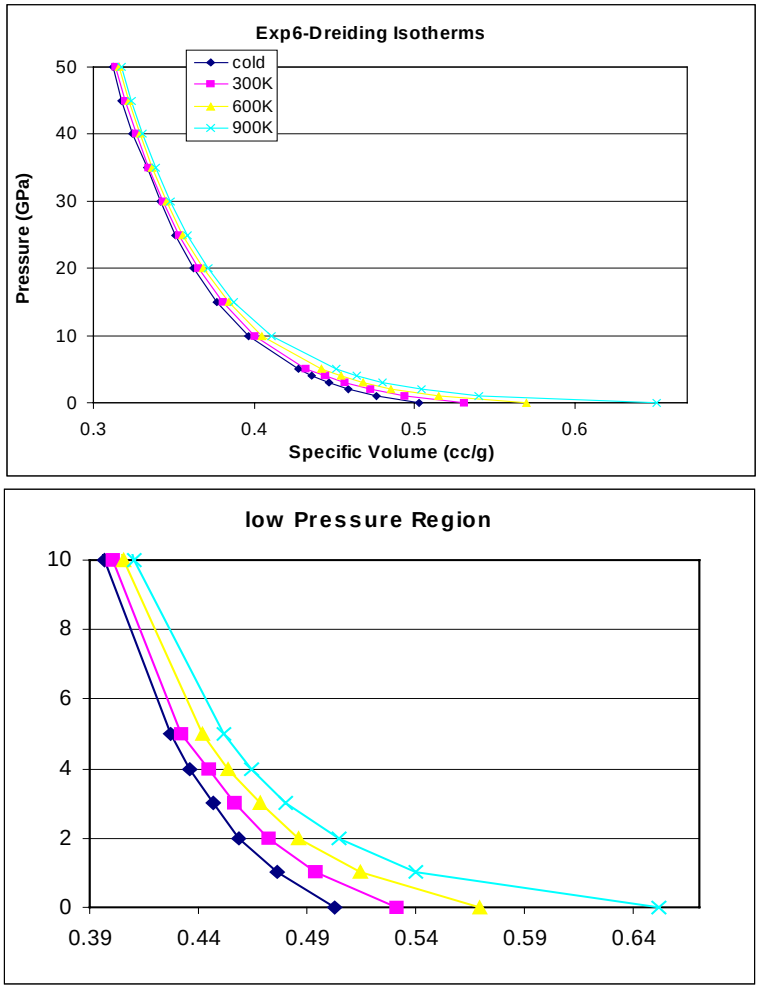

Figure 2.9: Isotherms (including cold compression) using Exponential-6-Dreiding force field.

fields we tried, Dreiding, Exponential-6-Dreiding and Planar, Exponential-6-Dreiding was found to give the best fit with the experimental data.

The Exponential-6-Dreiding force field uses a Morse bond-stretch potential and Exponential-6 potential for Van der Waals interactions. The Exponential-6 Van der Waals interaction has a more gradual inner wall than that of Lennard Jones 12-6 potential and leads to a more accurate density. The computed density is 1.8852 g/cc at standard temperature and pressure, which is within 2.69% of the experimental value. Cell parameters calculated with the Exponential-6-Dreiding force field are: A=8.986 Å(0.27%), B=8.976 Å(0.58%), C=6.883 Å(1.04%). The Planar force field also uses Morse potentials for bond stretch and Exponential-6 for Van der Waals interactions, but it has different parameter settings for Exponential-6 Van der Waals interactions. But in comparison, Exponential-6-Dreiding force field fits the experiment better than planar force field.

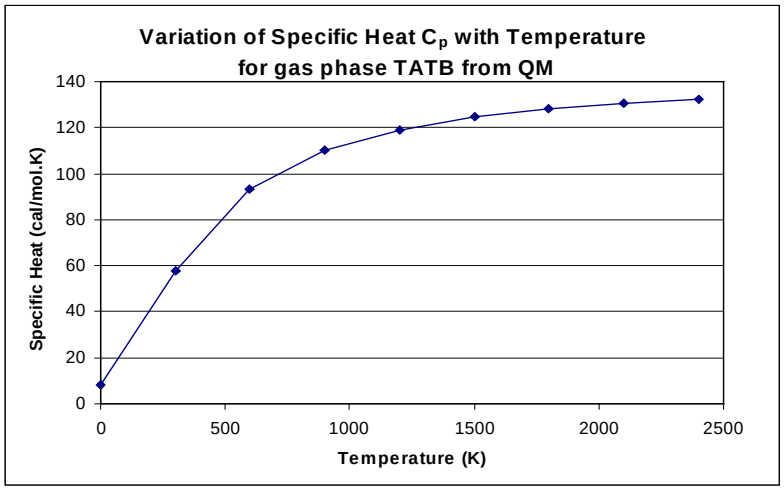

Figure 2.10: Variation of specific heat C_p with temperature for gas phase TATB.

Specific heats at constant pressure for gas phase TATB have been calculated at different temperatures using the computed vibrational frequencies. At present, there are significant differences between computed and measured volumes under static compression. Torsion of the NO_2 and NH_2 groups and hydrogen bonding appear to be significant factors in this discrepancy. Ab initio computations of the molecular structure (using Jaguar) are being carried out to develop improved force fields and address these two specific issues. Torsional energy variation with angle is shown for the NO_2 group in Fig. 2.11. The binding energy of two TATB molecules (a dimer) as a function of the H2N-NO2 separation distance in Fig. 2.12.

2.3 Thermodynamic analysis of molecular dynamics results

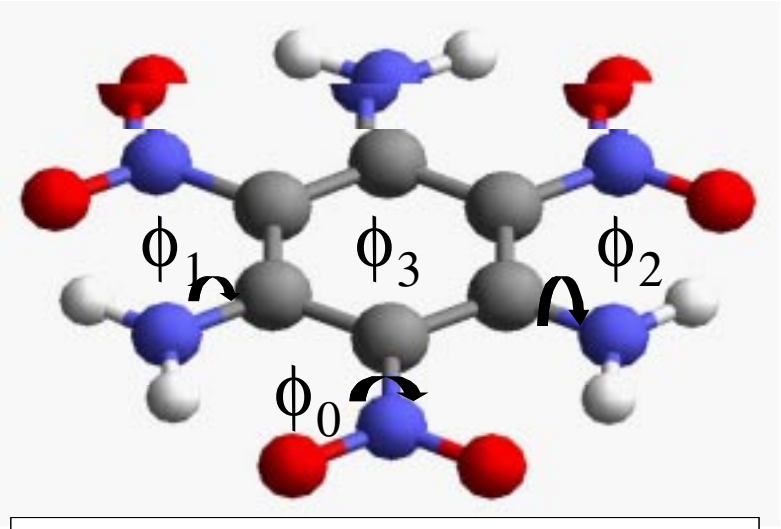

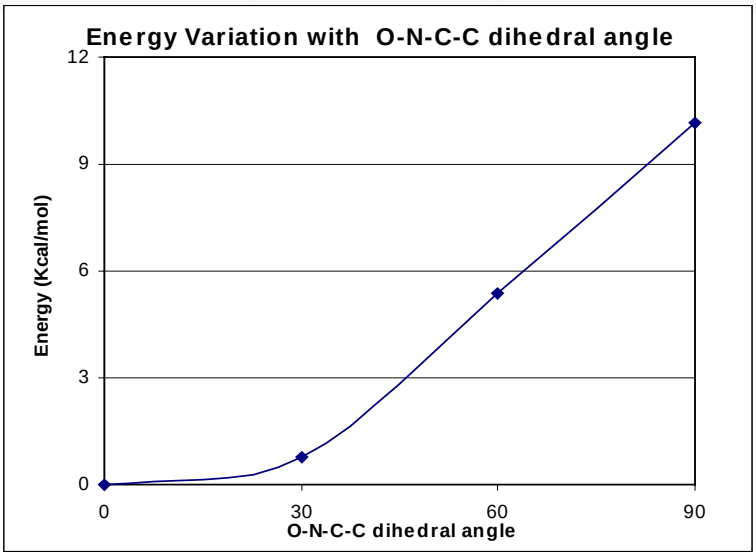

Figure 2.11: Torsion energy variation with O-N-C-C dihedral angle.

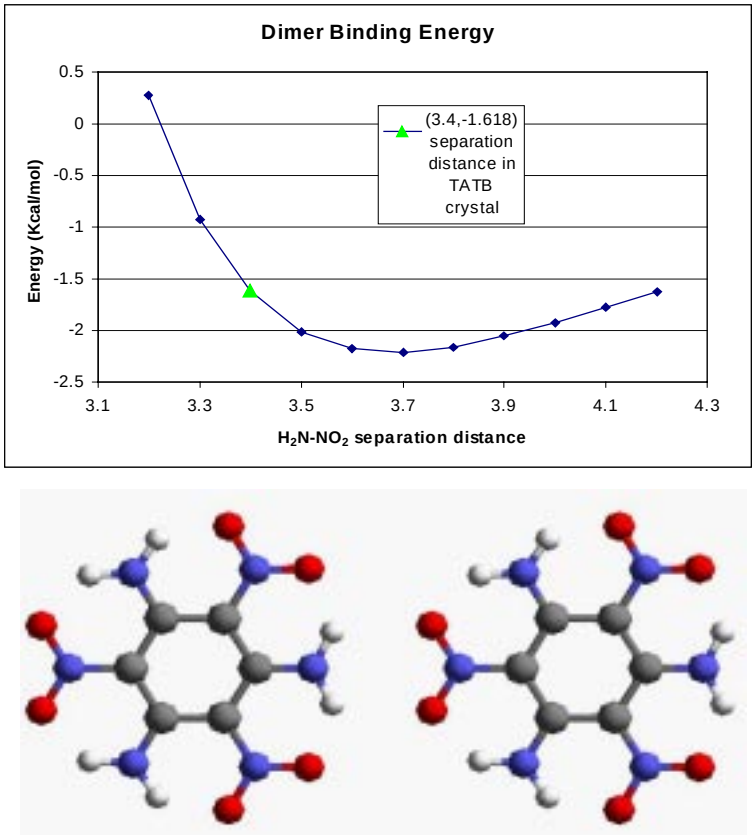

Figure 2.12: Dimer binding Energy of two TATB molecules as a function of the H2N-NO2 separation distance. (At STP, the H2N-NO2 separation distance in TATB crystal is 3.400 Å in a direction, 3.421 Å in b direction)

An accurate description of the behavior of materials in the form of a detailed Equation of State (EoS) is needed in Computational Fluid Dynamics applications. For materials such as high explosives where experimental data are lacking, an accurate EoS can be formulated from Molecular Dynamics (MD) simulations. Unfortunately, MD simulations tax even the fastest of computers to the extent that an accurate evaluation of a parameter like the Grüneisen coefficient is difficult.

In this report, we present the conclusions of a thermodynamic analysis performed on a set of MD data for $\beta-$HMX. One major result was the determination of the Grüneisen coefficient (a key parameter in the Mie-Grüneisen EoS) for pressures of up to 60 GPa. Also, a detailed description of the dependence of the specific heat at constant volume $c_v(T)$ made possible a realistic evaluation of the temperature along the HMX shock adiabat. More results include the derivation of physical properties of $\beta-$HMX, such as the thermal expansion coefficient. Comparison of these values with experimental data enabled us to verify the consistency (and to a more limited extent, the accuracy) of the MD simulations.

2.3.1 β-HMX isotherms

Molecular Dynamics data from the NPT (Number-Pressure-Temperature) ensemble are shown in Fig. 2.13. For a detailed description of MD results, refer to section 2.2.

2.3.2 The warm compression curve of β-HMX

Results from MD can be grouped in a set of P, v (pressure-specific volume) and e, v (internal energy-specific volume) isotherms. In this regard, experimental compression curves (warm, i.e. $T > 0$ K) provide the most obvious and accurate basis for data validation, as MD isotherms are free from interpolation artifacts (see later). Experimental data for β-HMX compression are available at standard temperature from [3] and [5]. Thus, a direct comparison can be performed by using NPT ensemble data at $T = 300$ K. In [3] a 3^{rd}-order Birch Murnaghan (BM) fitting is proposed, in the form

$$P = \frac{3}{2}B_0\left[x^{-7/3} - x^{-5/3}\right]\left[1 - 3\left(1 - B'/4\right)\left(x^{-5/3} - 1\right)\right] \tag{2.1}$$

where $x = v/v_0$, and $v_0 = 1/\rho_0$ is the specific volume at $P = 0$, $T = 300$ K. From MD analysis, $\rho_0 = 1.782$ g/cc at standard conditions. This value is 6% lower than the measurements reported by LASL [6] ($\rho_0 = 1.900$ g/cc, pure crystal). The parameter B_0 is the bulk modulus [GPa], and $B' = dB_0/dP$.

A comparison of our results is presented in Fig. 2.15. At this stage, estimation of density at low compressions using NPT ensemble appears to be questionable. The bottom curve in the plots (Fig. 2.15), is obtained by using the same coefficients B_0 and B', but with $\rho_0 = 1.900$ g/cc as the normalizing parameter. Recent analyses using data from the NVE ensemble (to be described in a upcoming report) have shown promise in mitigating this problem.

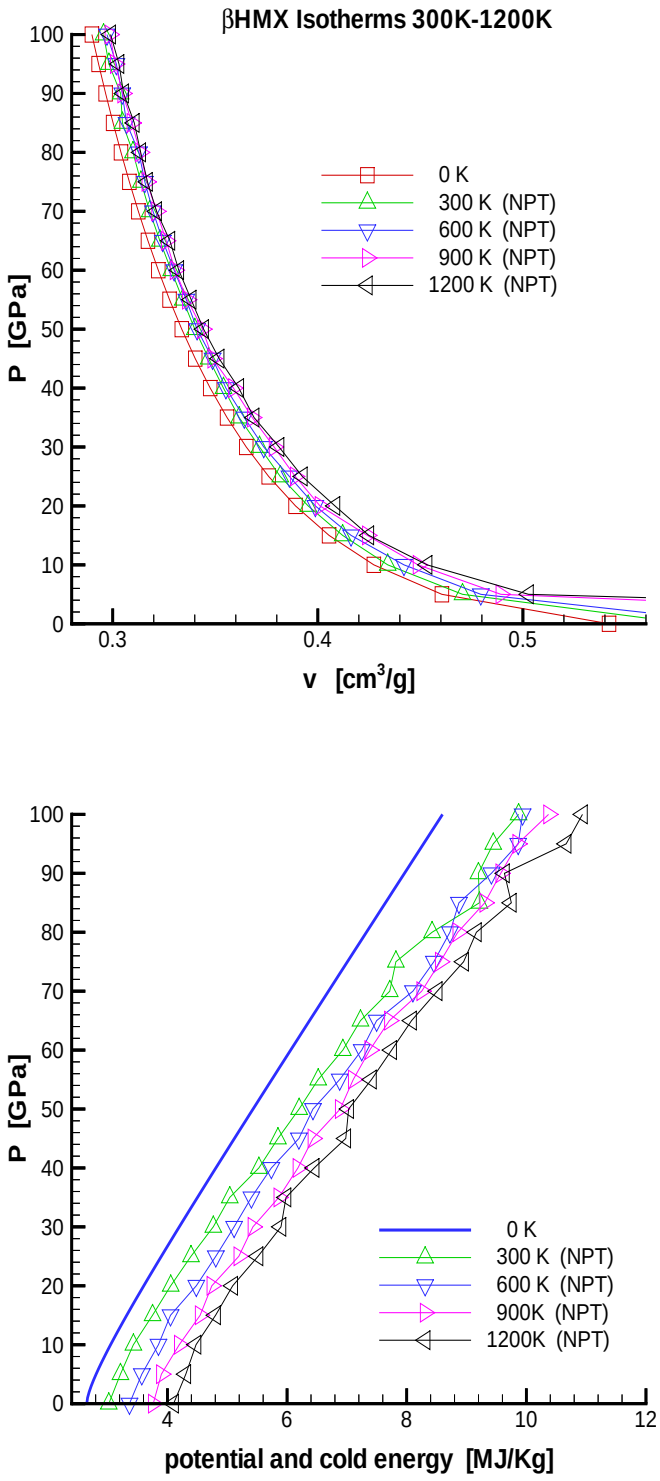

Figure 2.13: NPT ensemble data for HMX: potential energy and cold (0 K) energy.

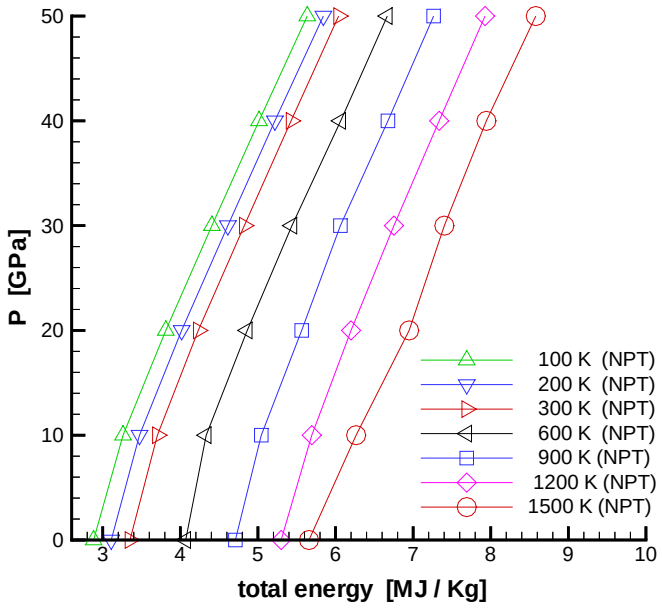

Figure 2.14: NPT ensemble data for HMX: total energy.

2.3.3 The Grüneisen coefficient

The Grüneisen coefficient G for β-HMX is obtained from MD simulations performed with Exponential-6 force field (cf. section 2.2). The result is plotted in Fig. 2.16. Notice that if the Mie-Grüneisen EoS holds, then $G(v,\ T) = G(v)$ (only a function of the specific volume):

$$e - e_c = \frac{v}{G(v)}(P - P_c) \tag{2.2}$$

The cold compression curves $P_c(v)$ and $e_c(v)$, and the warm compression curves form pairs of isotherms that can be used in a finite difference approach to estimate partial derivatives at constant v. Each pair of curves yields an independent estimate of $G(v)$ using Eqn. 2.2. Ideally, if the Grüneisen coefficient is truly a function of only one variable v, then the result from each pair will converge to a unique function.

In fact, this is not so. NPT isotherms are given at the same values of pressures, and not of specific volume, so numerical artifacts due to interpolation performed over a very limited range of data are likely to appear. This problem vanishes of course if we can access NVE data.

Interpolation was carried out only on the set of warm compression curves. Points at zero pressure are excluded from the computation, because they clearly appear not to be reliable. Also, it is reasonable to think that the HMX melts above 600 K, at least for moderate pressures. Thus, results from the isotherms at 1200 K and 1500 K are of no practically use.

We are therefore left with 5 data points for 2 sets of 5 isotherms, in the $e,\ v$ and $P,\ v$ planes. Interpolation was carried out using Mathematica 3.0 by fitting polynomial curves of

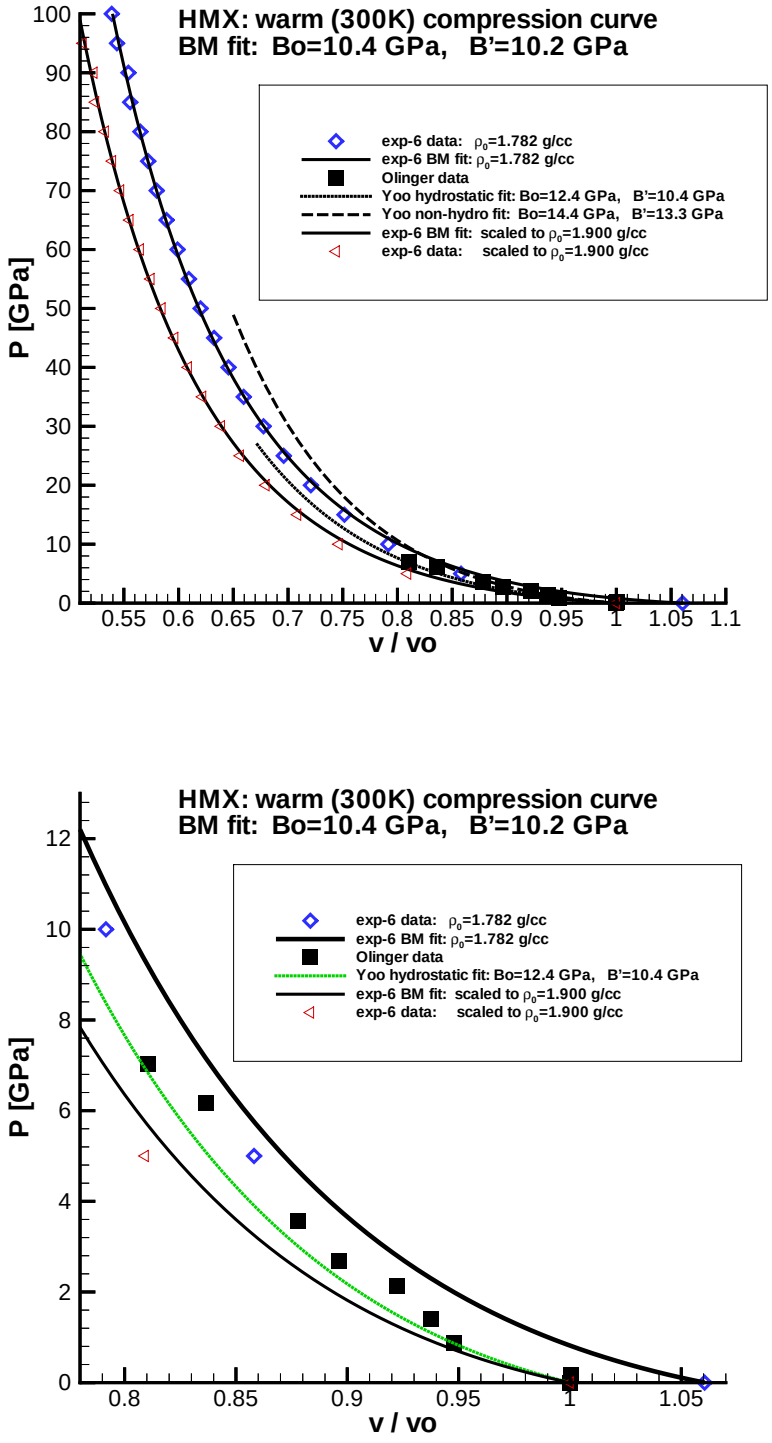

Figure 2.15: Warm (300 K) compression curve for HMX using the NPT ensemble, for the complete range of compressions (upper); closeup (lower).

order 3 through the data points. $G(v)$ was then obtained from the following expression:

$$G_i(v) = v\frac{P_{Ti+1}(v) - P_{Ti}(v)}{e_{Ti+1}(v) - e_{Ti}(v)} \tag{2.3}$$

evaluated over an interval of v. Eqn. 2.3 can be interpreted as a central finite difference scheme, for a temperature $\overline{T_i} = (T_{i+1} + T_i)/2$. Results are shown in Fig. 2.16 as a function of the relative specific volume, v/v_0 where $v_0 = 5.28821$ cc/g. Notice that we do not have any reliable information on G at $v/v_0 > 0.92$.

The arithmetic average of $G_i(v)$ from the first 4 isotherms is used to estimate a least squares linear fit in the form:

$$G(v) = 0.5607 + 0.09330\frac{v}{v_0}$$

This result is plotted as a solid line in Fig 2.16. From this approximate evaluation of the Grüneisen coefficient it is possible to extrapolate G to standard conditions: $G(v_0) = 0.6540$.

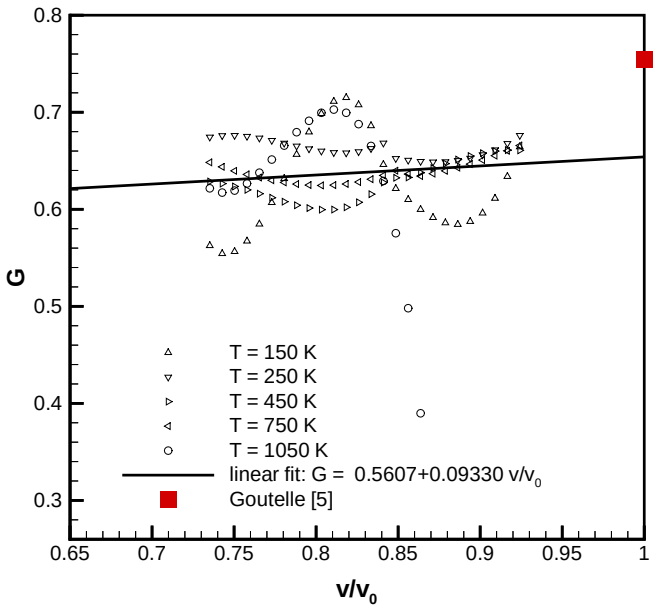

Figure 2.16: Grüneisen coefficient for HMX from NPT ensemble.

Availability of experimental values of G is extremely limited for HMX. In [7], a value of $G = 0.754$ for solvent-pressed β-HMX is given at standard temperature and pressure conditions (STP). This point is plotted in Fig 2.16. However, in [8], G/v is quoted to be 2.09 g/cc, which amounts to $G = 1.1$ at STP.

2.3.4 Coefficient of thermal expansion

The coefficient of thermal expansion α is defined as

$$\alpha = \frac{1}{v}\left(\frac{\partial v}{\partial T}\right)_P, \tag{2.4}$$

That is, α represents the change of volume per unit volume under isobaric heating (or cooling). The MD $P(v)$ isotherms can be treated with an appropriate finite-difference technique [1] to get an estimate of $\alpha(v,T)$. The result, as well as one experimental value $5 \cdot 10^{-5}$ K^{-1} at STP, is shown in Fig. 2.17. Since a set of only 5 isotherms is used for this calculation, the evaluation of the partial derivative (2.4) is obviously of limited accuracy.

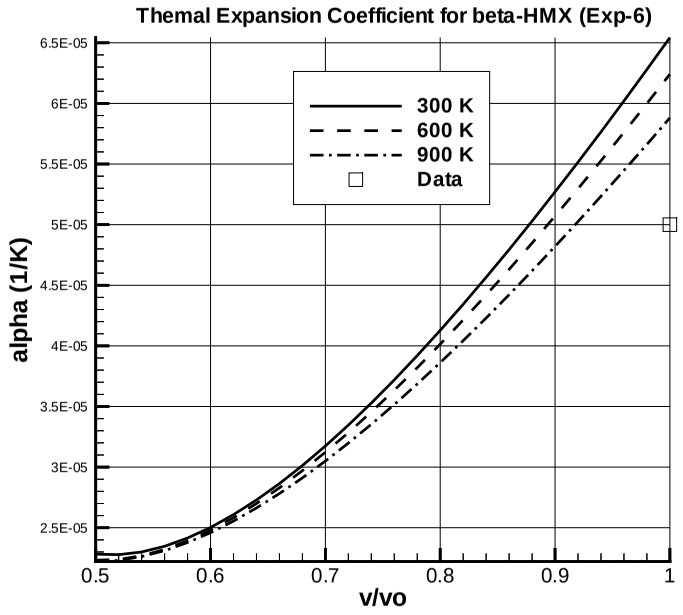

Figure 2.17: Coefficient of thermal expansion for beta HMX.

2.3.5 The Isothermal Bulk Modulus

The isothermal bulk modulus K_T is defined by

$$K_T = -\frac{1}{v}\left(\frac{\partial v}{\partial P}\right)_T. \tag{2.5}$$

K_T gives the change of volume per unit volume under isothermal compression. The minus sign makes the value of K_T positive. Note that the bulk modulus used in the BM EoS (Eq 2.1) defines the bulk modulus as the reciprocal of K_T.

[1] Central differences using $P(v)$ data at $T = 0, 300, 600, 900, 1200\,K$ are performed according to the definition of α in Eqn. 2.4.

Armed with the $P(v)$ isotherms from MD, K_T is readily calculated by using Eqn. (2.5) [2]. The resulting value (in GPa^{-1}) is plotted in Fig. 2.18. In [8], a value of (the reciprocal) bulk modulus for β-HMX is given at 0.129 MBar, which corresponds to $K_T = 0.078$ GPa^{-1}.

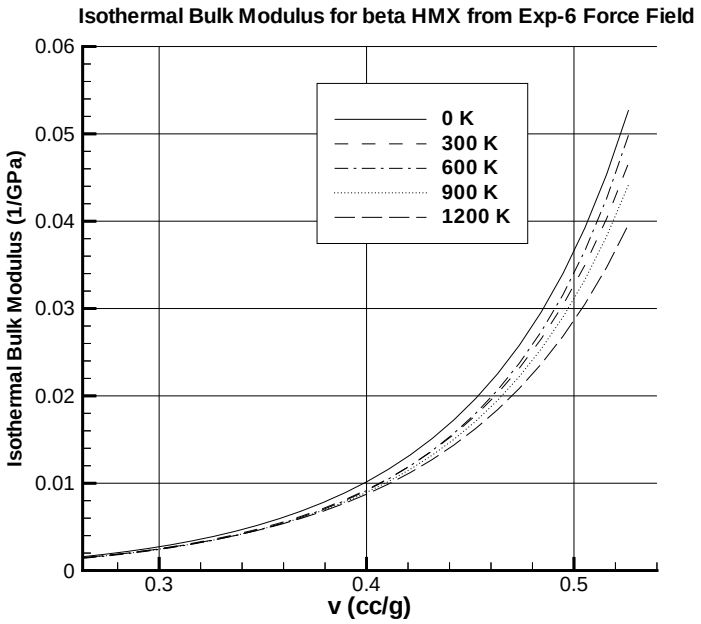

Figure 2.18: Isothermal bulk modulus for $\beta-$HMX.

2.3.6 Hugoniot curve

For typical high-explosives (such as HMX), experimental hydrostatic compression data are of limited help in the formulation of an EoS because of the limited range of compression. In this sense, shock experiments represent a source of information more relevant to our needs. A summary of all available shock data for β-HMX is shown below.

- pure crystal ($\rho_0 = 1.900$ g/cc) Hugoniot: LASL, in P, v and U_p, U_s planes[6].
- solvent-pressed ($\rho_0 = 1.891$ g/cc) Hugoniot: LASL in P, v and U_p, U_s planes[6].
- pressed samples and mixtures of HMX ($\rho_0 = 1.903$ g/cc): Bernecker [4].

In order to compute the shock curve, we need the Mie-Grüneisen Eqn. 2.2 (repeated and rearranged here for convenience):

$$e = e_c + \frac{v}{G}\left(P - P_c\right),$$

where $P_c(v)$ (cold pressure), $e_c(v)$ (cold energy) and $G(v)$ (Grüneisen coefficient) are obtained from fitting of MD data. We will use the following results:

[2]The partial derivatives are found from differentiating the BM fits of the $P(v)$ isotherms.

- P_c from least squares fit in the form of Eqn. 2.6

$$P_c = a\left(\frac{1}{x^{7/3}} - \frac{1}{x^{5/3}}\right)\left(4 - 3\frac{1}{x^{2/3}}\right) + b\left(\frac{1}{x^{7/3}} - \frac{1}{x^{5/3}}\right)\left(\frac{1}{x^{2/3}} - 1\right) \tag{2.6}$$

  $a = 28.45$ GPa, $b = 162.6$ GPa,
  $x = v/v_{00}$, $1/v_{00} = 1.845$ g/cc at $T = 0$ K, $P = 0$ Pa

- e_c from least squares fit (in 10^8J/kg):

$$e_c = a\frac{1}{x^{4/3}} + b\frac{1}{x^2} + c\frac{1}{x^{2/3}} + d \tag{2.7}$$

  $a = 0.5071$, $b = 0.2096$, $c = 0.3809$, $d = -0.05692$

- G, the fitted Grüneisen coefficient Eqn. 2.8:

$$G = a + bx \tag{2.8}$$

  $a = 0.5607$, $b = 0.09330$.

The intersection of $e(P, v)$ with the Rankine-Hugoniot equation Eqn.2.9:

$$e = e_0 + \frac{1}{2}(P + P_0)(v_0 - v) \tag{2.9}$$

defines the shock Hugoniot, $P_H(v)$. This line is compared with available shock data in Fig. 2.19.

This result is highly sensitive to the predicted specific volumes at low compressions. Further analyses using the NVE ensemble suggest that the predicted specific volume at low compression is unrealistically high. To amend the problem, we believe that more unit cells are needed in MD simulations (cf. 2.2 for details). A set of points P_{Hi} is obtained from solving Eqns. 2.9 and 2.2. Then, an analytical expression of the Hugoniot can be derived by fitting a modified BM curve:

$$P_H = a_H\left(\frac{1}{x^{7/3}} - \frac{1}{x^{5/3}}\right)\left(4 - 3\frac{1}{x^{2/3}}\right) + b_H\left(\frac{1}{x^{7/3}} - \frac{1}{x^{5/3}}\right)\left(\frac{1}{x^{2/3}} - 1\right) + c_H \tag{2.10}$$

Here $a_H = 20.91$ GPa , $b_H = 175.9$ GPa, $c_H = 0.4325$ GPa, $x = v \cdot \rho_0$, $\rho_0 = 1.891$ g/cc.

A numerical derivative dP/dv_{Hi} is evaluated directly from P_{Hi} by finite differencing. A least squares fit leads to:

$$\frac{1}{\rho_0}\left(\frac{dP}{dv}\right)_H = \frac{d_H x^{2/3} + e_H + f_H x^{4/3}}{x^4} \tag{2.11}$$

where $d_H = 957.8$ GPa , $e_H = -532.2$ GPa, $f_H = -448.4$ GPa, $x = v \cdot \rho_0$. Notice that Eqn. 2.11 is simply the derivative of Eqn. 2.10, with fitted coefficients from $dPdv_{Hi}$.

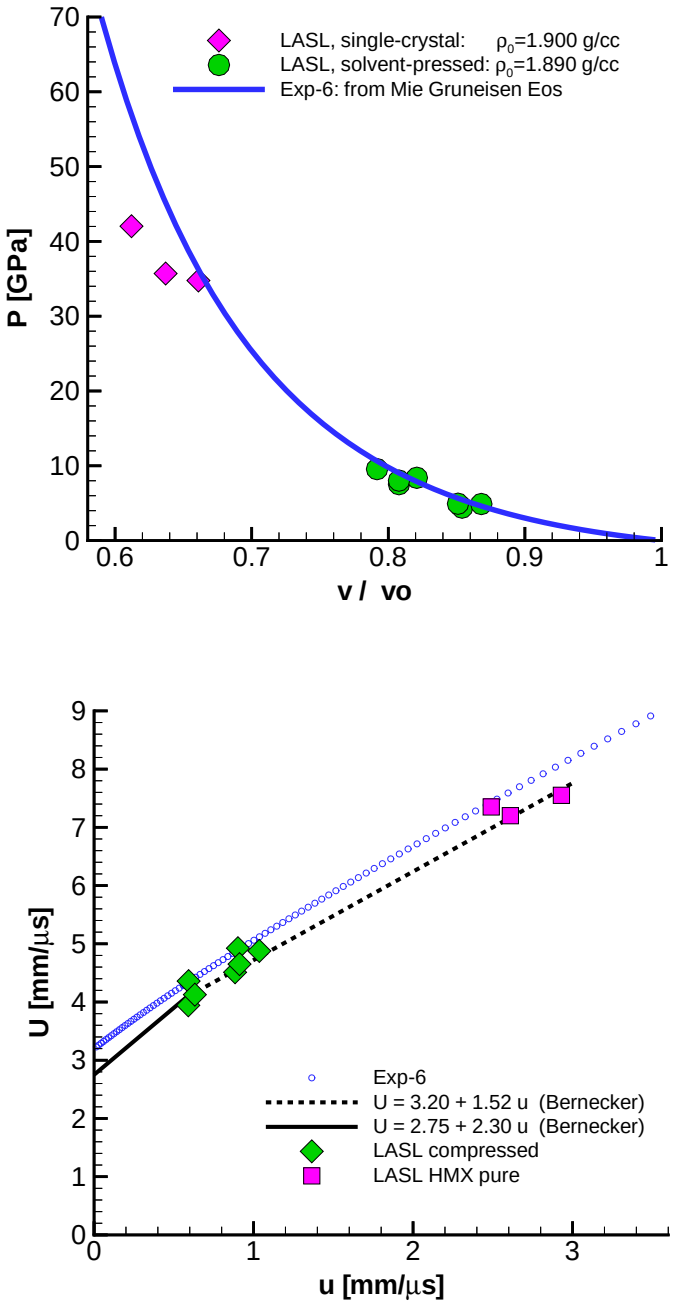

Figure 2.19: HMX Hugoniot.

2.3.7 Temperature along the Hugoniot curve

In addition to the isotherms, MD also provides the specific heat at constant volume as a function of temperature, $c_v(T)$. An accurate knowledge of $c_v(T)$ is necessary for a realistic computation of the temperature along the shock Hugoniot. The fundamental relation of thermodynamics can be written as

$$ds = c_v \frac{dT}{T} + c_v T \frac{G}{v} dv. \tag{2.12}$$

Manipulation of Eqn. 2.12 leads to the ODE:

$$\begin{gathered} \frac{\partial T}{\partial v} + T\frac{G}{v} = \frac{1}{2c_v}\left[(v_0 - v)\left(\frac{\partial P}{\partial v}\right)_H + P_H - P_0\right] \\ T(v_0) = T_0 \end{gathered} \tag{2.13}$$

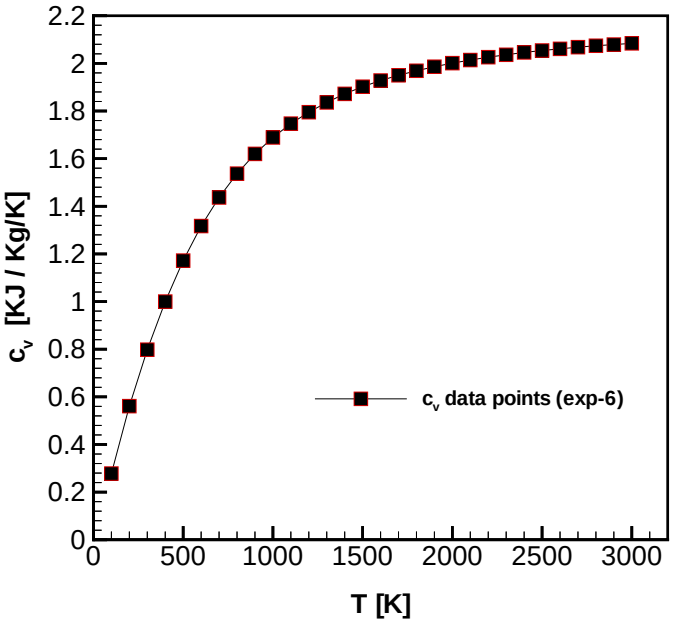

Figure 2.20: The specific heat at constant volume, $c_v(T)$ for βHMX: notice the sharp increase below 1000 K

Eqn. 2.13 can be integrated by using $G(v)$, $P_H\,(v)$ and $(dP/dv)_H$ derived in the previous section. Numerical integration was performed by using the software package Mathematica. As a representative result of this integration, we estimate the intersection of the Rayleigh line with the unreacted Hugoniot, i.e. the Von Neumann (VN) point. The Chapman-Jouguet (CJ) point is experimentally given by:

$$D_{CJ} = 9100.\ \mathrm{m/s}^2$$

This value directly gives the slope of the Rayleigh line in the $P,\ v$ plane:

$$\frac{P - P_0}{v - v_0} = -J^2 = -\rho_0 D_{CJ}^2, \tag{2.14}$$

where J indicates the mass flow rate. For any point along the Rayleigh line, conservation of momentum and mass holds. Once reference conditions $\rho_0,\ P_0$ are given, the Von Neumann point is uniquely determined by solving the equation

$$-\rho_0 D_{CJ}^2 = \frac{P_H\left(v_{VN}\right) - P_0}{v_{VN} - v_0} \tag{2.15}$$

We find

$$v_{VN} = 0.3188 \text{ cc/g} \qquad P_{VN} = 61.78 \text{ GPa}$$

Currently, typical estimates of temperature along a shock adiabat are based upon the assumption that c_v is constant. In the present study, this assumption is removed and $c_v = c_v(T)$. Fig. 2.20 is the motivation for this, since c_v increases dramatically at low temperature as more and more vibrational modes are excited. Indeed, we note that the assumption of a constant specific heat may lead to a large difference in T_{VN}. For the following results, we used the analytical expression ($[c_v] = \text{kJ/kg}$)

$$c_v = -49450.7 - 3.5404T + 7152.3 \cdot \lg\left(T + 1000\right) + 0.3167 \cdot 10^{-3} T^2 \tag{2.16}$$

The expression 2.16 provides a good fit of c_v over the range of temperatures of interest.

In Table 2.1, the VN temperature is seen to be very sensitive to the value assumed by c_v over the range $[T_o,\ T_{VN}]$. This same result is presented in Fig. 2.21. Integration of the ODE in Eqn. 2.13 using the constant value of c_v evaluated at STP produces a difference of more than 100% in the final result (compare rows 2 and 4 in Table 2.1, with row 1, where the ODE is integrated by using the fit of $c_v\left(T\right)$ and $G\left(v\right)$). Notice that if we still want to assume a constant specific heat, then a higher reference value is required (see row 5, where $c_{v_{av}}$ is an average value of $c_v\left(T\right)$ for high temperatures). On the other hand, the condition on $G\left(v\right)$ may be relaxed. In row 4 we see that taking a constant Grüneisen coefficient only mildly affects the result.

In addition, we also considered a linear $U_s - U_P$ relation

$$U_s = c_0 + sU_p. \tag{2.17}$$

It is easy to show that the pressure along the Hugoniot is given by:

$$P_H = \rho_0 U_s U_P = \rho_0 c_0^2 \frac{\varphi}{\left(1 - s\varphi\right)^2}; \tag{2.18}$$

where $\varphi = 1 - \frac{v}{v_0}$(see for instance section 2.5). Here, c_0 and s are derived from experimental data [6]:

$$c_0 = 3.07 \text{ km/} \quad \text{s} \ = 1.79$$

In this case, values of $\rho_0 = 1.891$ g/cc, and $G = 0.7$ are used to integrate Eqn. 2.13. Thus, the only feature in common with the previous cases is the $c_v\left(T\right)$ dependence which is given

c_v Form	G form	T_{VN}
$c_v(T)$	$G(v)$	2364 K
$c_{v_0} = 798$ J Kg^{-1}K^{-1}	$G(v)$	4605 K
$c_v(T)$	0.7	2390 K
$c_{v_0} = 800$ J Kg^{-1} K^{-1}	0.7	4653 K
$c_{v_{av}} = 1600$ J Kg^{-1}K^{-1}	0.7	2539 K
$c_v(T)$: linear $U_p - U_s$	0.7	2323 K

Table 2.1: Sensitivity study for VN point.

in 2.16. The shock curve described in Eqn. 2.18 is obtained from extrapolation of data at low pressure, and it appears to be stiffer if compared to the curve described by Eqn. 2.10. If we keep the same Rayleigh line, then the new Von Neumann point is:

$$v_{VN_{lin}} = 0.3329 \text{ cc/g} \qquad P_{VN_{lin}} = 58.13 \text{ GPa}$$

The result is displayed in Fig. 2.21 as a dotted line. We notice that this second curve is slightly stiffer. Indeed, extending the solution of Eqn. 2.13 for pressures greater than P_{VN} shows that the difference rapidly grows. Now the estimate for the temperature is $T_{VN_{lin}} = 2323$ K, a value which is around 2% smaller.

To conclude, it is worth observing that the results are deeply affected by the value of specific volume we take for v_{VN}. For instance, integration of Eqn.2.13 to a specific volume 3% lower than v_{VN} gives $T = 2859$ K, whereas an increase in 3% of v_{VN} corresponds to $T = 1968$ K. This is due to the high stiffness of the temperature function along the Hugoniot.

2.4 Reaction rate modeling and hydrodynamic simulations of gas–phase detonations

Despite the emphasis on solid–phase detonations in the ASCI program, the more fundamental field of gas–phase detonations is still of considerable interest. First and foremost, the scientific study of gaseous detonations provides a useful prelude to understanding the more complex problem of detonations in high explosives. Secondly, there is an advantage from a computer programming perspective, in that the modular design of flow solvers and driver scripts for gaseous detonation problems allows easy portability to other equations of state and reaction models, such as those utilized in high explosives. Finally, there is a direct benefit in the development of reaction kinetics models, as the study of reactions in gaseous nitramines (nitromethane, HMX, TATB) provides reaction pathways for the kinetics in high explosives.

2.4.1 Reduced Reaction Models

In the past computational investigations of gas–phase detonations, the reaction model used by us and most other investigators in the field was a simple one–step model $\text{A} \rightarrow \text{B}$ between

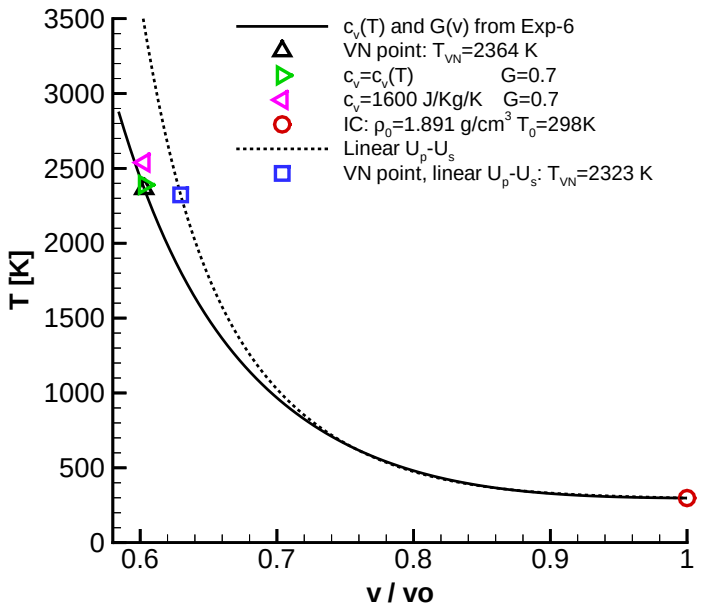

Figure 2.21: Temperature vs. relative specific volume across the Hugoniot.

perfect gases with constant specific heats. The reaction rate was a simple expression involving the fraction of reactant present and an Arrhenius–type exponential factor. This simple model suffers from a number of deficiencies. It produces no significant induction zone (as is seen in real systems), it has poor stability characteristics at high activation energy or close to Chapman–Jouget (CJ) velocity, and it provides no mechanism for quenching of the detonation wave.

Clearly, a more advanced reaction model was necessary. Following the paradigms of ASCI, the ideal solution would be to implement the best, most detailed reaction model available. For gaseous systems, this involves the use of detailed chemical kinetics, where a chemical system is described by an extensive mechanism of elementary reactions between stable and radical molecules. In the temperature and pressure ranges of interest, the molecules can be approximated as thermally perfect gases although they should have variable specific heats. These large reaction mechanisms are quite well understood for hydrogen and simple hydrocarbon systems, having been developed for several decades in the combustion community. In the case of small hydrocarbons, the mechanisms may include up to 50 molecules and 300 reactions. Unfortunately, even on today's parallel ASCI platforms, it is too computationally expensive to fully resolve all the processes occurring inside the detonation reaction zones with these large reaction mechanisms.

Hence, it became clear that something in between was necessary: a reaction model that could capture the basic chemistry of the detailed reaction mechanism but was computationally inexpensive. After an investigation into several alternatives, we decided to utilize reduced reaction models. These models are developed via a systematic analytic reduction from detailed reaction mechanisms, using educated assumptions of several species being in

an approximate steady–state, and several reactions being in partial equilibrium.

The example system we chose for development purposes was the hydrogen oxygen system, as it is the smallest, simplest detonable gas system. We started with a detailed reaction mechanism from Maas and Warnatz [11] involving 8 species (H_2, H, O_2, O, OH, HO_2, H_2O_2, H_2O) and 19 reversible reactions. After careful examination of reaction rates in steady one–dimensional detonation calculations, it was decided that the species O, OH and H_2O_2 could be approximated as being in steady–state. Upon their removal from the thermodynamic system via algebraic steady–state relations, the system was reduced to a 3–step mechanism:

$$\begin{aligned} 3H_2 + O_2 &\rightleftharpoons 2H + 2H_2O, \\ 2H &\rightleftharpoons H_2, \\ HO_2 + H &\rightleftharpoons H_2 + O_2. \end{aligned}$$

The rates of these reduced reactions are expressed as sums of several rates in the original mechanism. Some of these rates involve the concentrations of the eliminated steady–state species which are computed from the algebraic steady–state relations (simplified by truncation). So the H_2–O_2 system was reduced from 8 species and 19 reactions in the detailed mechanism to 5 species and 3 pseudo-reactions in the reduced model. The reduction savings would be much greater for larger systems such as hydrocarbons or nitramines, although the reduction technique would be too tedious by hand. In FY99 we plan to transition over to an automated reduction strategy such as the method of Computational Singular Perturbations (CSP) [12].

The reduced reaction models were validated against the detailed reaction mechanisms from which they were derived, using 1D steady detonation structure computations (ZND or Zel'dovich–von Neumann–Doering model of a detonation). The computations were performed over a wide range of mixtures, and the results are presented in Fig. 2.22. Detonation

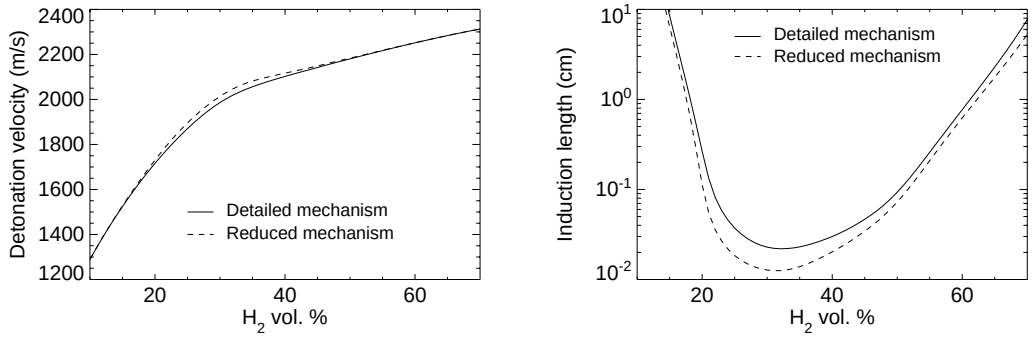

Figure 2.22: Chapman–Jouget detonations in H_2–air, initially at 1 atm and 300 K.

velocity and induction length are two measurable quantities which have a strong impact on all behavior of the detonation. The detonation velocity depends only on the thermodynamics of the system, while the induction length is a dynamic parameter that depends on the kinetics as well. The agreement between computed detonation velocities in Fig. 2.22 is excellent, while the induction lengths differ by up to a factor of two. This is not too unreasonable given the large uncertainty in the original detailed mechanism. A search for

closer agreement between detailed and reduced mechanisms would be somewhat unjustified. Hence this reduced reaction model is considered satisfactory, and the reduction technique validated.

2.4.2 Implementation of Detailed Chemistry in Unsteady Flow Solver

Although it is not feasible to use detailed reaction mechanisms in 2D and 3D detonation simulations, 1D simulations can be done in reasonable computational time. The implementation of detailed chemistry into a 1D unsteady flow solver provides a further means of validating the reduced mechanisms, and is a good foundation for the implementation of the reduced mechanisms in an unsteady flow solver.

The capability to use detailed reaction mechanisms in an Eulerian unsteady reactive flow solver has been developed. The modular code design involved linking a gas–phase chemical kinetics package CHEMKIN-II [13] with the flow solver, and writing subroutines for evaluation of the equation of state and integration of the reactive step. The stiff reactive step was integrated using an implicit backward differencing ODE solver [14]. At present, this step is quite slow and needs to be improved. A simpler explicit integration method may be used in the future. The design of the flow solver is very modular, with insertion of a new symbolic reaction mechanism allowing immediate study of a different chemical system.

Numerical simulations with this flow solver have been performed within the environment *Amrita* [15]. Adaptive mesh refinement was used to resolve the details of the reaction zone. The gradient of density was used to locate the leading shock wave for refinement purposes, and the gradient in one of the radical species was used for refinement of the reaction zone.

Various validations of the reactive code were performed. To avoid the problem of hydrodynamic instability that occurs in 1D detonation simulations, our initial validations utilized an endothermic reaction to ensure a stable 1D unsteady solution. The reaction chosen was a simple one–step mechanism for dissociating oxygen, with the rate taken from the Maas and Warnatz [11] mechanism. Fig. 2.23 shows the results of a 1D dissociating shock which has propagated down a duct for a certain length of time. The solid lines represent the exact solution, which is the initial condition (the 1D steady solution) propagated a distance $U_s t$ down the duct from its initial location when the shock was at $x = 0$. The points represent the unsteady numerical solution, and the agreement with the exact solution is excellent. The mesh refinement in the reaction zone and leading shock wave is also evident.

To get something of a more dynamic flow, the next validation of the code utilized a 1D shock tube, with the same simple dissociating gas. In general, for a reactive flow, the solution of a shock tube is not a self-similar centered wave system. However, there is such an analytical solution in the limits of frozen and equilibrium flow. Figs. 2.24 and 2.25 show the results of a shock tube calculation in the frozen and equilibrium limits. In each case, the diaphragm was located at $x = 0$ and the initial conditions were those in Table 2.2. The analytical solutions were determined by solution of the shock wave jump conditions and the expansion fan isentropic conditions, using the thermochemistry of the given reaction mechanism. The solutions were obtained that matched the pressure and particle velocity across the contact surface. For the numerical simulations, the frozen flow case was simulated

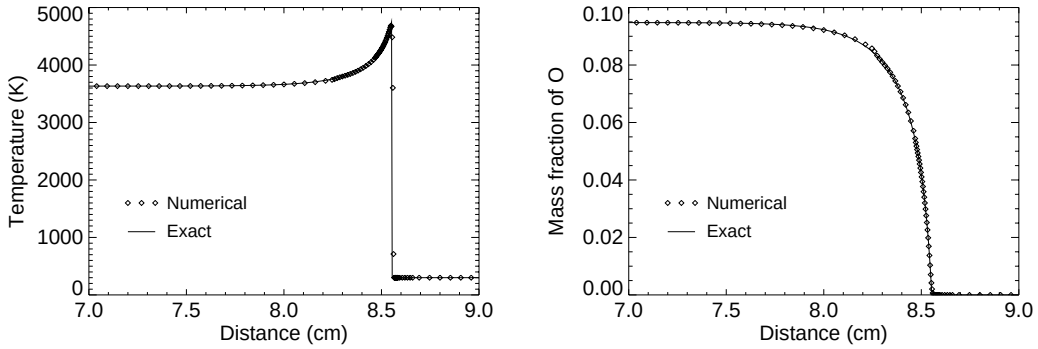

Figure 2.23: 1D shock propagation in dissociating O_2, initially at 1 atm and 300 K. U_s = 3300 m/s, $t = 2.592 \times 10^{-5}$ s.

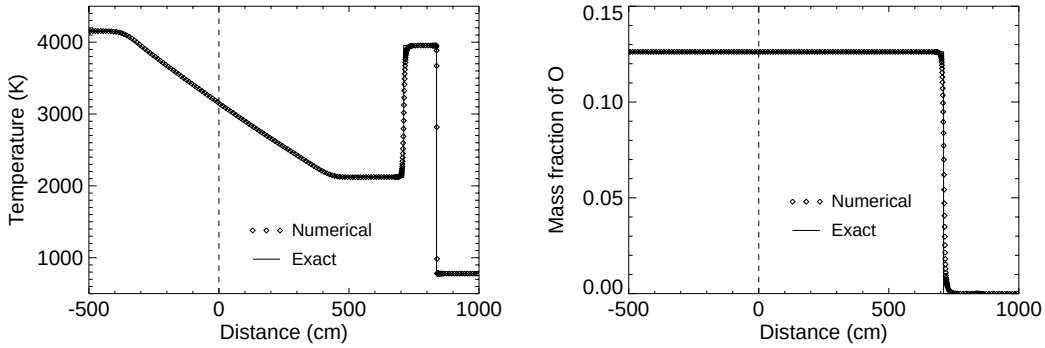

Figure 2.24: Shock tube with dissociating O_2 in frozen limit. Numerical solution computed with reactive step deactivated, exact solution determined analytically. $t = 3 \times 10^{-3}$ s.

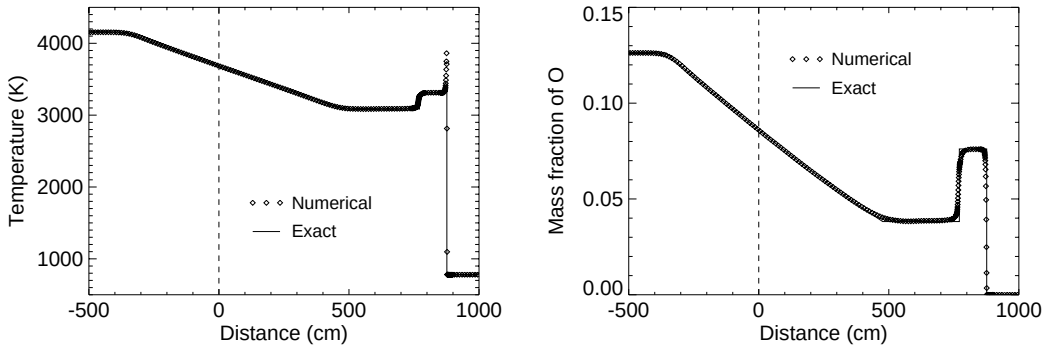

Figure 2.25: Shock tube with dissociating O_2 in equilibrium limit. Numerical solution computed with fast reaction which proceeds almost immediately to equilibrium, exact solution determined analytically. $t = 3 \times 10^{-3}$ s.

Initial states:	P (atm)	ρ (g/cm^3)	composition
Left	60	5	equilibrium O_2–O
Right	0.1	0.05	equilibrium O_2–O

Table 2.2: Initial conditions for shock tube calculations shown in Figs. 2.24 and 2.25.

by simply turning off the reactive step in the flow solver. The equilibrium case was simulated by using non-equilibrium flow with a very fast reaction that proceeded almost immediately to equilibrium. In both cases, the agreement between the numerical and exact solutions are seen to be excellent. The only evidence of the actual non-equilibrium nature of the simulations in Fig. 2.25 is the von Neumann spike in temperature behind the leading shock wave, where the flow rapidly drops from a frozen post-shock condition to an equilibrium post-shock condition.

Our final validation involved the computation of an over-driven 1D detonation. By overdriving the detonation velocity D above the Chapman–Jouget (CJ) velocity D_{CJ}, the detonation can become stable, and the unsteady solution will simply be the steady 1D ZND solution propagating down the duct. This allows us to perform another validation of the reactive code, this time with an actual exothermic detonating flow. Fig. 2.26 shows the shock pressure history as well as the temperature and H atom mass fraction profiles at a given time,

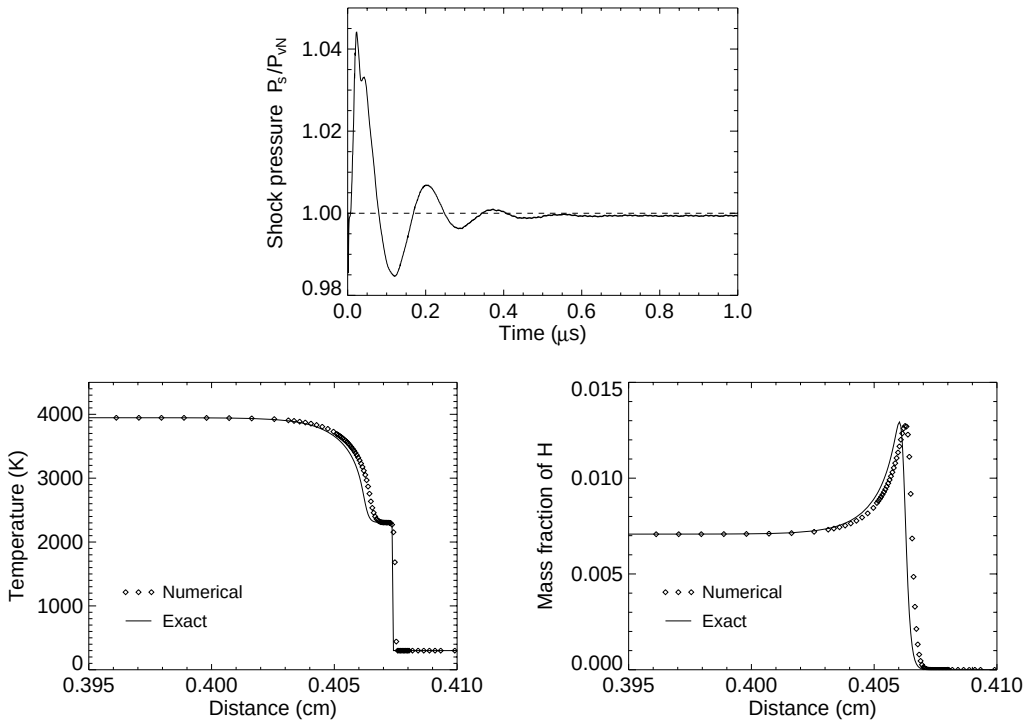

Figure 2.26: 1D detonation in stoichiometric H_2–O_2, initially at 1 atm and 300 K. $(D/D_{CJ})^2 = 1.4$. $t = 1.212 \times 10^{-6}$ s in spatial profiles. Exact solution is steady solution propagated a distance Dt.

for a detonation in stoichiometric H_2–O_2 with over-drive factor $f = (D/D_{CJ})^2 = 1.4$. The

initial oscillations in the shock pressure are due to the startup error as the prescribed sharp shock smears itself across a few computational mesh cells, and flexes as it does so. After some time, the shock pressure settles down to a constant value almost precisely equal to the von Neumann pressure, the post-shock pressure in the ZND steady solution. The apparent phase error in the numerical spatial profiles at the later time is the residual effect of the startup error. By restarting the simulation with the numerically computed smeared shock profile, this startup error could be greatly reduced and the phase error corrected. Other than this error, the numerical and exact solutions agree very well.

2.4.3 Summary of Work Completed in FY98

We have identified and implemented a technique for reaction model reduction in gaseous detonations with realistic chemistry. The technique has been tested on the H_2–O_2 system, as the simplest gaseous detonating system. The reduced reaction models have been implemented into the ZND code for 1D steady flow solutions, and 1D steady calculations have been used to validate the reduced models against detailed reaction mechanisms. The reduced models were found to be satisfactory in this validation.

We have implemented detailed chemistry into an Eulerian unsteady reactive flow solver, using the chemical kinetics package CHEMKIN-II [13]. Using the computational environment *Amrita* [15], and *Amrita* 's mesh refinement capability, we have performed numerical simulations of 1D dissociating shock wave propagation, 1D dissociating gas shock tubes in the frozen and equilibrium limits, and 1D stable detonation propagation. Each of these test cases has been validated against analytical solutions and excellent agreement was found. This leads us to conclude that the unsteady reactive flow solver with detailed chemistry has been successfully implemented.

2.5 High Explosives Engineering Numerical Models

The purpose of this work is to propose numerical engineering models for high explosives (HE) materials. We first introduce the reactive Euler equations in the particular context of HE substances. In particular, we employ the Mie-Grüneisen equation of state (EoS), modified to account for tension. An exact Riemann solver is developed and used as a verification tool for approximate solvers. Roe's approximate solver is used for solving the discrete equations. We also make use of the *Amrita* computational facility in our numerical experiments. Inert and detonating shock tube experiments are performed first. Finally, we present results of the corner turning problem for which fixed and pressure dependent chemical reaction rates are investigated. The physics of HE materials includes, but is not limited to, fluid dynamics and chemistry. Our goal is to numerically simulate the propagation of a detonation wave through reactants which are broken down into products through a series of chemical reactions. These physical phenomena are described by PDEs. The discrete equations are then solved with Roe's approximate linearized solver.

2.5.1 Equations of motion

The fluid dynamics are described by the usual Euler equations (viscous effects are considered negligible). Chemistry is described through a one-step reaction model. The fluid includes reactants and products. The one-step model is an approximation of all chemical reactions occurring during the breakdown of the reactants into products. Of course, "real-life" chemical reactions are multi-step and much more complicated as seen in [17] for example.

The overall fluid density is ρ and the mass fraction of either products or reactants is λ which varies between 0 and 1. In what follows we assume $\lambda = 0$ to be unreacted substance and $\lambda = 1$ reacted. The following relation exists between reactants and products:

$$\rho = \rho_P + \rho_R \quad \text{where} \quad \rho_{\mathrm{P}} = \rho\lambda.$$

The conservation equation for the mass fraction λ is governed by a source term modeling the reaction rate R. The multidimensional reactive Euler equations are thus given by

$$\left\{\begin{array}{rcl} \dfrac{\partial \rho}{\partial t} + \nabla \cdot (\rho \mathbf{u}) = & 0 \\ \dfrac{\partial}{\partial t}(\rho \mathbf{u}) + \nabla \cdot \left(\rho \mathbf{u}^2 + \mathbf{I}P\right) = & 0 \\ \dfrac{\partial}{\partial t}\rho\left(e + \dfrac{\mathbf{u}^2}{2}\right) + \nabla \cdot \left[\rho \mathbf{u}\left(e + \dfrac{P}{\rho} + \dfrac{\mathbf{u}^2}{2}\right)\right] = & 0 \\ \dfrac{\partial}{\partial t}(\rho\lambda) + \nabla \cdot (\rho \mathbf{u}\lambda) = & \rho\, R(P,\lambda) \end{array}\right. \tag{2.19}$$

where

$$R(P,\lambda) = \rho K \left(\frac{P}{P_{VN}}\right)^n (1-\lambda)^{1/2}, \; n\text{integer}. \tag{2.20}$$

It is now necessary to relate pressure P, specific volume $v = 1/\rho$ and internal energy e through an equation of state in order to close the system of equations. The EoS may take various forms like the "γ-law" expression for gases. However, solids usually follow the Mie-Grüneisen EoS. It is based upon the linear relationship:

$$U_s = c_0 + s\, u_p \tag{2.21}$$

where U_s and u_p respectively are the shock and particle velocities. As explained in [25], c_0 is the bulk sound speed for the material at rest and s is related to the isentropic pressure derivative of the isentropic bulk modulus, $K_s' = \partial K_s/\partial P|_s$, through $s = (K_s' + 1)/4$. c_0 and s are generally obtained from experiments. The Mie-Grüneisen EoS general formulation is:

$$P(e,v) = \frac{\mathcal{G}}{v} e + f(v), \tag{2.22}$$

where $\mathcal{G}$ is the Grüneisen parameter. At present, $\mathcal{G}$ is chosen to be a constant but actually is a function of volume and temperature, see [32]. Further models will include varying $\mathcal{G}$, (cf. Section 2.3.

The expression for f in (2.23.a) is given by the shock jump conditions, and is thus clearly valid only for compressed states:

$$f(v) \;= \mathcal{G}\,\frac{\lambda Q}{v} + \begin{cases} \dfrac{\rho_0 c_0^2 \varphi}{(1-s\varphi)^2}\left[1 - \dfrac{\mathcal{G}}{2v}(v_0 - v)\right] & \text{if} \quad v \le v_0 \quad \text{(a)} \\ c_0^2\left(\dfrac{1}{v} - \dfrac{1}{v_0}\right) & \text{if} \quad v > v_0 \quad \text{(b)} \end{cases} \tag{2.23}$$

where Q is the heat release, $\varphi = 1 - v/v_0$, and the 0-subscript represents the material at rest, the reference state. It is important to note that if a rarefaction wave occurs in the material at rest, density drops below the reference density ρ_0 and the EoS is no longer valid. Indeed, the original expression for f shows a minimum for densities between 0 and ρ_0. Consequently, the first derivative of f changes sign within that range. The expression for the sound speed is given by

$$c^2 = -v^2\left(\left(\frac{\partial P}{\partial v}\right)_e - P\left(\frac{\partial P}{\partial e}\right)_v\right) = \mathcal{G}e - f'v^2 + \mathcal{G}Pv. \tag{2.24}$$

For low energy and low pressure (as in a rarefaction), round-off and approximation errors may result in negative c^2. Therefore, following the approach of Miller and Puckett [25], we modify the EoS with a pseudo elastic-solid EoS to accommodate for negative pressure (tension) and preserve positive squared sound speed, see (2.23.b).

Additionally, for smooth flows, the isentropic pressure P_s is given by

$$P_s(v) = -\frac{\mathcal{G}}{v^{\mathcal{G}+1}}\int_{v_i}^{v} f v^{\mathcal{G}} dv + \mathcal{G}\frac{e_i v_i^{\mathcal{G}}}{v^{\mathcal{G}+1}} + f(v) \tag{2.25}$$

2.5.2 Roe's approximate linearized Riemann solver

We choose to discretize equations (2.19) through a finite volume formulation on a structured grid. The multidimensional finite volume discretization reads

$$\frac{\partial}{\partial t}\int_{\mathcal{C}_i} \mathbf{U}\,\mathrm{d}\mathbf{x} + \int_{\partial\mathcal{C}_i} \mathbf{F}(\mathbf{U})\cdot\mathbf{n}\,\mathrm{dl} = \int_{\mathcal{C}_i} \mathbf{S}\,\mathrm{d}\mathbf{x}. \tag{2.26}$$

In order to solve this system of equations we must approximate the expression of the convective fluxes at each cell interface in the mesh. We select Roe's strictly upwind numerical flux, whose one-dimensional expression is:

$$\begin{aligned} \mathbf{F}(\mathbf{U})\cdot\mathbf{n} \sim \;& \Phi^{\mathrm{Roe}}_{i+1/2} = \Phi^{\mathrm{Roe}}(\mathbf{U}_{i+1}, \mathbf{U}_i) = \\ & \frac{1}{2}\left[\mathbf{F}_i + \mathbf{F}_{i+1} - |A_{i+1/2}|\,(\mathbf{U}_{i+1} - \mathbf{U}_i)\right] = \\ & \frac{1}{2}\left[\mathbf{F}_i + \mathbf{F}_{i+1} - R_{i+1/2}\,|\Lambda_{i+1/2}|\,R^{-1}_{i+1/2}\,(\mathbf{U}_{i+1} - \mathbf{U}_i)\right] = \\ & \frac{1}{2}\left[\mathbf{F}_i + \mathbf{F}_{i+1} - R_{i+1/2}\,|\Lambda_{i+1/2}|\,\alpha_{i+1/2}\right] = \\ & \frac{1}{2}\left[\mathbf{F}_i + \mathbf{F}_{i+1} - R_{i+1/2}\,\mathbf{\Phi}_{i+1/2}\right], \end{aligned} \tag{2.27}$$

where, the dissipation matrix A is the Jacobian to $\mathbf{F}$ ($A = \mathrm{D}_{\mathbf{U}}\mathbf{F}$), R is the matrix of the eigenvectors to A and Λ the diagonal matrix of the eigenvalues λ to A ($u \pm c$ and u). In order to preserve accuracy, Roe has shown [28] that A must be evaluated at the following averages (extended to general convex EoS by Glaister [21]):

$$\begin{aligned} \overline{\rho} = \rho_{i+1/2} = \sqrt{\rho_i\,\rho_{i+1}} \qquad & \overline{\beta} = \beta_{i+1/2} = \frac{\sqrt{\rho_i}\,\beta_i + \sqrt{\rho_{i+1}}\,\beta_{i+1}}{\sqrt{\rho_i} + \sqrt{\rho_{i+1}}} \\ \overline{P} = P_{i+1/2} = \overline{\rho}\left(\overline{H} - \overline{e} - \frac{1}{2}\overline{u}^2\right) \qquad & \overline{c}^2 = c^2_{i+1/2} = \frac{\overline{P}\,\overline{P}_e}{\overline{\rho}^2} + \overline{P}_\rho \end{aligned} \tag{2.28}$$

where $\beta = u,\, e,\, H$. It is well known that Roe's scheme requires an entropy correction (see [22, 29] for example) to avoid unphysical rarefaction shock. We use Harten's entropy correction on all waves.

The expression for a non-MUSCL higher order TVD scheme with so-called minmod limiter is given component-wise by, see [30]:

$$\phi^k_{i+1/2} = |\lambda^k_{i+1/2}|\,\alpha^k_{i+1/2} - \mathrm{L}^{\mathrm{k}}_{\mathrm{i+1/2}}\left[|\lambda^{\mathrm{k}}_{\mathrm{i+1/2}}| - \frac{\Delta \mathrm{t}}{\Delta \mathrm{x}}\left(\lambda^{\mathrm{k}}_{\mathrm{i+1/2}}\right)^2\right]$$

where

$$\mathrm{L}^{\mathrm{k}}_{\mathrm{i+1/2}} = \begin{cases} \mathrm{minmod}\left(\alpha^{\mathrm{k}}_{\mathrm{i+1/2}}, \alpha^{\mathrm{k}}_{\mathrm{i+3/2}}\right) & \text{if } \lambda^{\mathrm{k}}_{\mathrm{i+1/2}} > 0 \\ \mathrm{minmod}\left(\alpha^{\mathrm{k}}_{\mathrm{i+1/2}}, \alpha^{\mathrm{k}}_{\mathrm{i-1/2}}\right) & \text{if } \lambda^{\mathrm{k}}_{\mathrm{i+1/2}} < 0 \end{cases}$$

and

$$\mathrm{minmod}\,(\mathrm{x}, \mathrm{y}) = \begin{cases} x & \text{if} \quad |x| < |y| \quad \text{and} \quad xy > 0 \\ y & \text{if} \quad |x| > |y| \quad \text{and} \quad xy > 0 \\ 0 & \text{if} \qquad\qquad\qquad\quad\;\; xy < 0 \end{cases}$$

In what follows, the minmod limiter may be replaced by Roe's "Superbee" limiter [30], or any other technique that will damp out spurious oscillations.

Time marching is achieved through a usual explicit time stepping technique which results in the following scheme:

$$\mathbf{U}^{n+1}_i = \mathbf{U}^n_i - \omega\left(\mathbf{\Phi}_{i+1/2} - \mathbf{\Phi}_{i-1/2}\right) + \Delta t\,\mathbf{S}^n_i$$

where ω accounts for the CFL stability condition and $\mathbf{S}^n_i$ is the discretized source term.

Finally, following Eckett et al. [18], the conservative mass fraction equation that includes the reaction source term is integrated on the particle path and reduces to a simple ODE within each time step. The exact solution is used in the present code but for more general expressions a Runge-Kutta technique may be employed.

All of the following computations are performed with the *Amrita* computational facility which enjoys, among many other features, an adaptive mesh refinement (AMR) algorithm. AMR is especially necessary for correctly capturing flow features such as contact surfaces or reaction zones for example. *Amrita* is being developed by Quirk [27].

2.6 Shock-tube experiments

Following the traditional technique used in fluid dynamics we first solve the Riemann problem that occurs in a shock tube. A basic shock tube consists of two "fluids" separated by a "membrane" [31]. One is a high pressure fluid, the other a low pressure fluid. When the "membrane" is removed 3 waves are generated: a shock, a contact surface and a rarefaction. This Riemann problem may be solved exactly using Riemann invariants. Thus, we first devised an "exact" Riemann solver. This solver, however, requires a numerical integration technique (see the expression of isentropic pressure earlier (2.25)). A Romberg integration technique is employed for which we choose an error of approximation equal to 2^{-7}, well within machine round-off error. For reasonable integer values of $\mathcal{G}$ however the integral may be computed exactly, *e.g.* $\mathcal{G} = 2$, which allows for verification of the integration technique. The exact shock tube solution further permits verification of the approximate solver and serves as a very important tool for developing flow solvers. Our exact Riemann solver is currently limited to non-reactive flows and cannot account for rarefaction shocks. We can show that a rarefaction shock appears for the Kel-F substance with $c_0 = 2.03\text{km/s}$, $s = 1.64$ and $\mathcal{G} = 2$. In all the numerical experiments that follow we only show results for the solvent-pressed HMX material: $c_0 = 3.07\text{km/s}$, $s = 1.79$, $\rho_0 = 1.891\text{g/cm}^3$ and we choose $\mathcal{G} = 0.7$.

2.6.1 Inert HMX

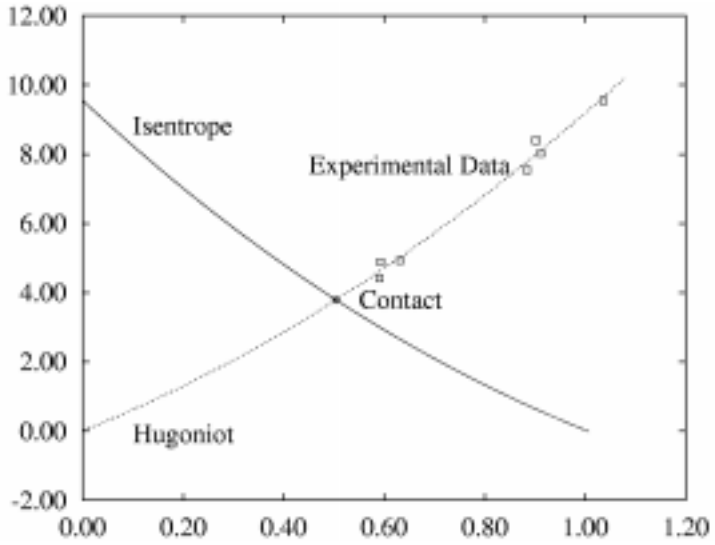

Figure 2.27: Pressure $P(\text{GPa})$ *vs.* velocity $u(\text{km/s})$.

Fig. 2.27 shows the computed isentropic pressure and the pressure along the Hugoniot as functions of the particle velocity. Note that the Hugoniot fits the experimental data given in [24]. In order to function properly, the exact Riemann solver must provide the value for velocity and pressure between the shock and the rarefaction, also known as the $*$-state. This value sits at the intersection of the isentrope and the Hugoniot in the (P, u)-plane. As shown

by the diamond, tagged "contact", the point (P^*, u^*), computed by the exact solver, does fall at the intersection of those curves.

Schlieren images based on the density gradients depict in Fig. 2.28, the initial shock-tube set-up and the solution at $t = 0.02\mu$s, bottom. The three waves described earlier are visible.

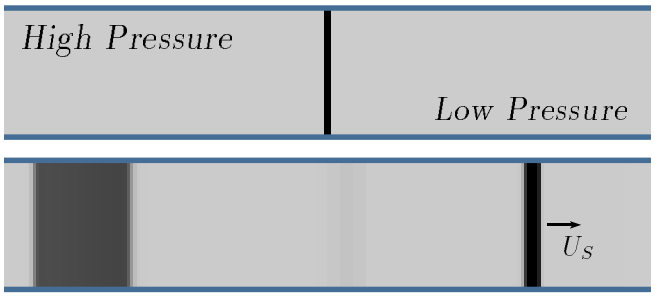

Figure 2.28: Inert shock-tube experiment.

More indepth verification is performed via cross-sections of the density, velocity and pressure as shown Fig. 2.29. The solid line depicts the exact solution and the open diamonds the approximate solution given by Roe's solver. Refinement is based upon density gradients and a contact surface "capturing" criterion as described in [26].

2.6.2 Detonating HMX shock-tube experiments

In order to verify our numerical approach to solving a reactive flow we must first determine the Von Neumann and Chapman-Jouguet pressures. We first choose a fixed reaction rate by setting $n = 0$ and $K = 2\mu\text{s}^{-1}$ in (2.20). We compute the Hugoniot loci for the reactants $\lambda = 0$ and the products $\lambda = 1$ as shown in Fig. 2.30. Thermodynamics theory shows that in order to have a self sustaining propagating wave, the material must be shocked to the Von Neuman pressure P_{VN}. The pressure then drops along the Rayleigh-line in the (P, v)-plane down to the Chapman-Jouguet pressure P_{CJ}. It can be shown that the Rayleigh line is tangent to the products Hugoniot at the CJ point. Furthermore, at the CJ point, the particle velocity in the wave-frame, w, is equal to the squared sound speed, c^2. We refer to Thompson [31] for details. In our case all data is obtained numerically. Therefore, we first compute all the values of P, w, c^2 with the shock-jump conditions, then we construct linear approximations to the P, w and c^2 functions, and finally get the CJ and VN points through a Newton method. The value of the heat-release $Q = 14.70\text{MJ/kg}$ may be adjusted to obtain the desired P_{VN} and P_{CJ}. We refer to [16] for experimental data.

Using Roe's approximate solver we now run detonating shock-tube experiments. In the shock tube, part of the fluid to the left is pressurized to P_{VN} and the remaining fluid is left at rest, zero-pressure. Fig. 2.315a shows the value of pressure *vs.* distance at several time-steps. The pressure first drops from P_{VN} down to P_{CJ} where the reaction initiates. Pressure climbs back up to P_{VN} and a self-sustaining detonation progresses through the tube. Fig. 2.31b shows the value of the pressure at $t = 0\mu$s and at $t = 18.4\mu$s. It appears that the values of P_{VN} and P_{CJ} are slightly underestimated by the approximate solver. This

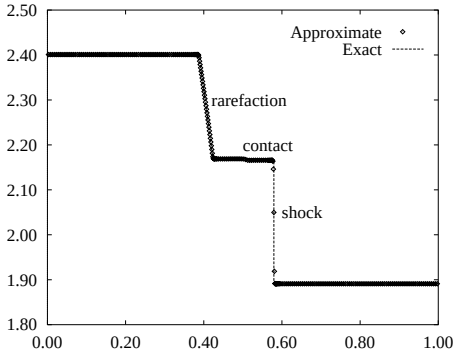

(a) Density $\rho(\mathrm{g/cm^3})$ *vs.* $x(\mathrm{mm})$.

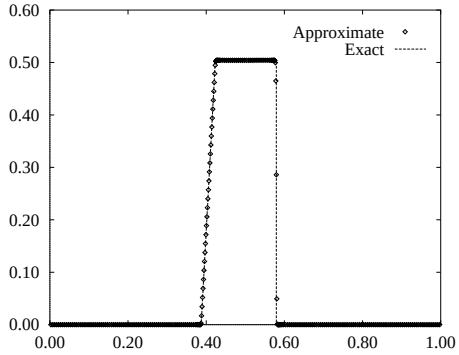

(b) Velocity $u(\mathrm{km/s})$ *vs.* $x(\mathrm{mm})$.

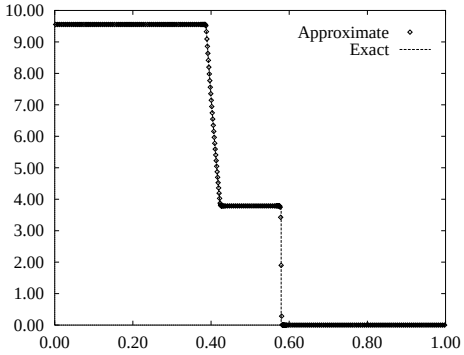

(c) Pressure $P(\mathrm{GPa})$ *vs.* $x(\mathrm{mm})$.

Figure 2.29: Cross-section of the inert shock-tube experiment at $t = 0.02\mu$s.

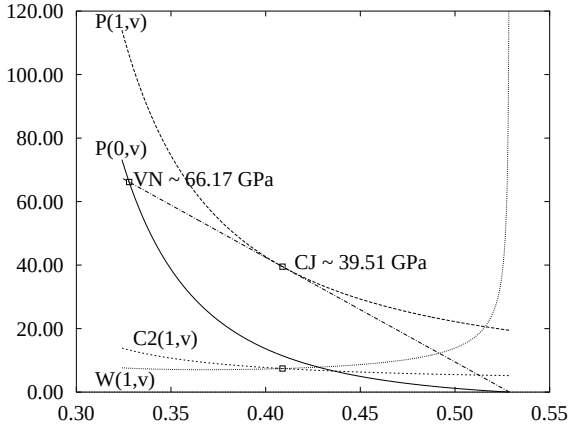

Figure 2.30: CJ and VN points computation.

may be remedied by refining more the reaction zone, and may also be due in part to the rarefaction (Taylor-)wave following the reaction zone.

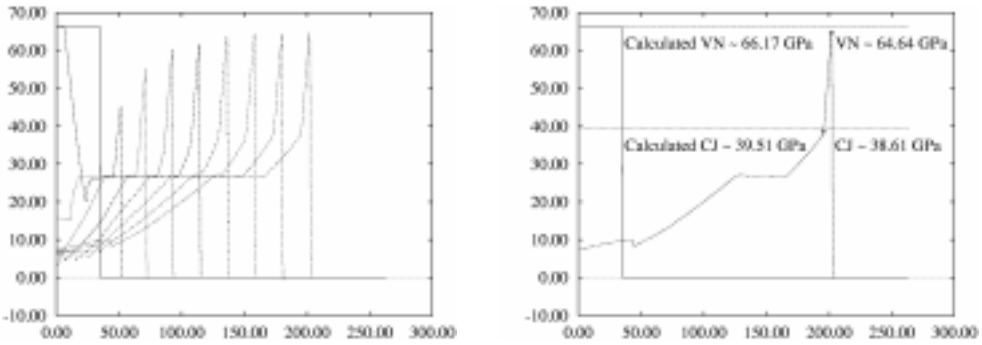

(a) Pressure P(GPa) *vs.* distance x(mm).

(b) Pressure P(GPa) *vs.* distance x mm.

Figure 2.31: Detonating HMX shock-tube experiment.

2.7 Detonating HMX corner turning problem

The set-up for this experiment consists of a shock wave that travels along a channel and diffracts around a corner. This problem is famous in fluid dynamics literature for its difficulty. The shock diffraction generates a very strong rarefaction wave departing from the corner. In gases it results in negative pressures. These negative pressures may be dealt with using Roe's entropy corrected scheme for Mach-numbers no greater than 2.5, in general. Higher Mach-numbers usually require other flow solvers that will not described here (we refer to Quirk for example [27]). However, in the case of solids the problem appears more complex. Generally, the substance at rest has zero-pressure but may support tension (negative pressure). Therefore, it is important that our EoS as described earlier (2.22) accounts for tension. More detailed work will eventually include spallation, cavitation, vacuum as proposed by Miller and Puckett in [25] for example. In this work we limit ourselves to tension and do not account for vacuum.

In order to properly initialize the detonation wave, we first compute the ZND reaction zone [20]. It is achieved by solving an implicit system of ODEs. This system of ODEs is obtained through manipulation of the Euler equations assuming a steady flow ($\partial_t(.) = 0$) and rewriting the equations in a Lagrangian frame. The system is written as

$$\frac{\mathrm{d}}{\mathrm{dt}}\begin{pmatrix} v \\ e \\ w \\ \lambda \end{pmatrix} = \begin{pmatrix} 1 & 0 & 0 & -v\sigma/\eta \\ 0 & 1 & 0 & Pv\sigma/\eta \\ 0 & 0 & 1 & -u\sigma/\eta \\ 0 & 0 & 0 & 1 \end{pmatrix}^{-1} \cdot \begin{pmatrix} 0 \\ 0 \\ 0 \\ R(P,\lambda) \end{pmatrix} \tag{2.29}$$

where $w = u - U_s$, $\sigma = P_\lambda v/c^2$ is the thermicity and $\eta = 1 - w^2/c^2$ is the sonic parameter. Note that at the CJ point $w^2 = c^2$ therefore $\eta = 0$ and the system is not defined, therefore

only an asymptotic solution of the ZND reaction zone is obtained by computing the solution in the limit when $\eta \to 0$.

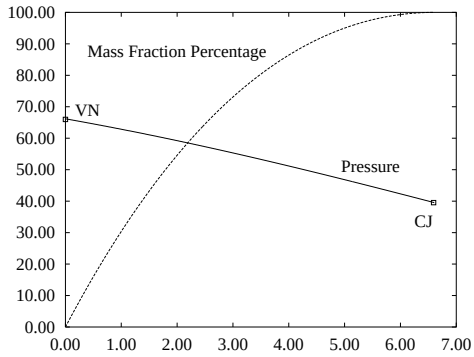

(a) $R(P,\lambda) = 2\,(1-\lambda)^{1/2}$.

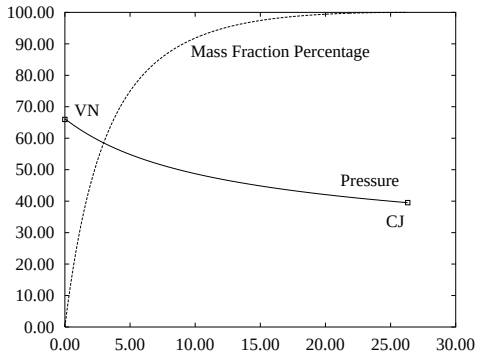

(b) $R(P,\lambda) = 2\left(\frac{P}{P_{VN}}\right)^5 (1-\lambda)^{1/2}$.

Figure 2.32: ZND reaction zone computation.

Fig. 2.32a depicts the pressure solution to system (2.29) for $n = 0$ and Fig. 2.32b for $n = 5$. Also depicted in Fig. 2.32 is the percentage of the mass fraction λ. In both cases, pressure drops from P_{VN} down to P_{CJ}. However, it is obvious that the reaction length increased considerably from $\Delta_R^0 l = 6.60$mm to $\Delta_R^5 l = 26.29$mm. Note that the factor $(P/P_{VN})^5$ in (2.20) acts as a pressure switch for iniating the reaction. Its effect will be described later in the corner turning problem.

2.7.1 Fixed rate and shock collision with higher density substance

In this case we initialize the data with the ZND profile computed earlier with $n = 0$. In order to remove spurious start-up oscillations the code is first run until the front has progressed 5 reaction lengths. Then, the solution is "repainted" by enforcing the solution past the reaction zone to be that calculated $3\Delta_R^0 l$ behind the shock front. This eliminates the oscillation and replaces the "exact" solution with that obtained with the approximate solver. Behind the reaction zone we should have $\lambda = 1$, however the repainted solution is not exact and $\lambda = 1 - \varepsilon$, $\varepsilon << 1$. There is no theory for selecting where to start repainting the solution, only experience. Consequently, the P_{VN} is slightly underestimated and this will have to be accounted for in later experiments. The dimension of the domain is proportional to the reaction zone length within which we enforced 20 computational cells. Fig. 2.33 depicts the detonation wave progressing through the channel at $t = 12.18\mu$s after the start-up error has been removed. The figure on the left depicts the "refinement-flags", *i.e.* where the AMR algorithm performs refinement in the grid. There are 3 levels of refinement each of which is refined twice. The refinement flags shows clearly the interface, to the right, with a higher density inert material ($\rho = 1.5\rho_0$), since refinement is here based on mass-fraction gradient and density gradient. Additionally, this experiment requires an activation pressure "switch". We choose to enforce reaction only if the pressure $P > 0.5P_{CJ}$.

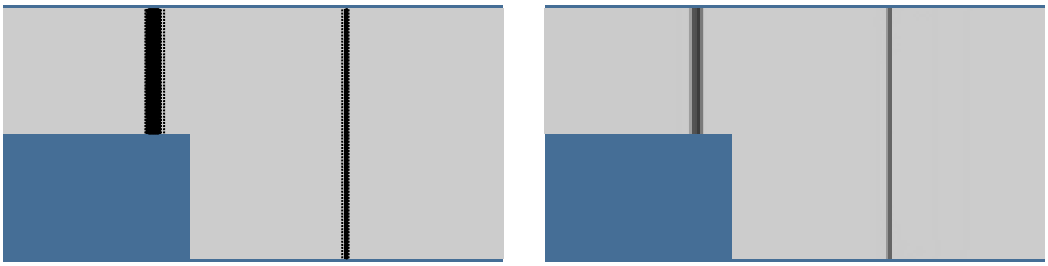

(a) (b)

Figure 2.33: Detonation wave channeling through

Fig. 2.34 depicts the detonation wave diffracting around corner at various time-steps and eventually interacting with the higher density substance. The incident shock wave is transmitted in part through the substance and the boundary of the domain (transmissive BC) while generating another wave that bounces back and interacts with the vortex formed at the corner. The diffracted wave hits the bottom of the domain and bounces back up to interact with the vortex (reflective BC). It is interesting to note that the AMR algorithm loses track of the flow features especially where the flow is grid aligned. This may be improved by changing the tolerance of the refinement criteria for example. Additionally and more likely, our refinement criteria are based only on the x-derivative of the density and mass-fraction, although refinement is performed in both directions. It is clear that, when the flow becomes grid aligned in the x-direction, the x-derivatives of both quantities are negligible, hence the loss of resolution. Performing refinement according to both derivatives of both quantities considerably augment the number of refined cells, hence the calculation time. A subtle balance exists here between feature resolution and computational time.

Interesting flow-features close-ups are depicted in Figs 2.35, 2.36 and 2.37. Boxes in the figures to the left show where the close-ups are performed.

2.7.2 Pressure dependent rate and "dead-zone" phenomenon

A more realistic problem is obtained with the pressure-dependent reaction rate:

$$R(P,\lambda) = 2\left(\frac{P}{P_{VN}}\right)^5 (1-\lambda)^{1/2}$$

The initialization and overall set-up of the experiment is similar to the fixed rate experiment. In this case we initialize the data with the ZND profile computed earlier with $n = 5$.

Figs. 2.38, 2.39 and 2.40 show a comparison between the fixed and pressure dependent rates computations. Each plot is taken at the time when the incident wave has covered the same distance, proportional to the size of the domain. Since the domain size is proportional to Δ_R the pressure dependent computation requires a much bigger domain. The fixed rate experiment requires a physical domain approximately $423 \times 211\text{mm}^2$ while the pressure dependent rate experiment requires approximately $1683 \times 841\text{mm}^2$. For each figure, the

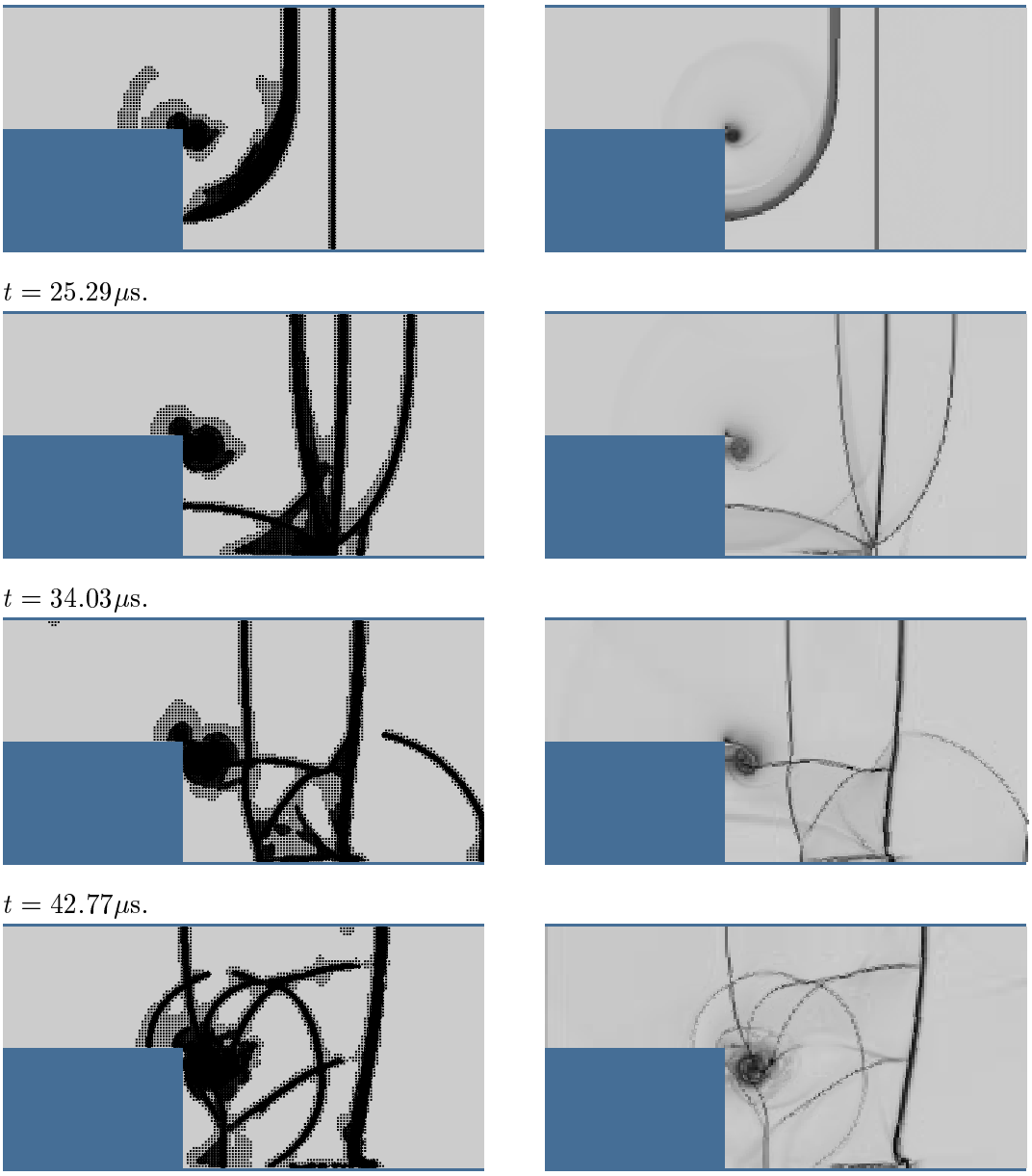

a. Refinement flags. b. Schlieren images.

Figure 2.34: Fixed rate chemical reaction turner-corning problem.

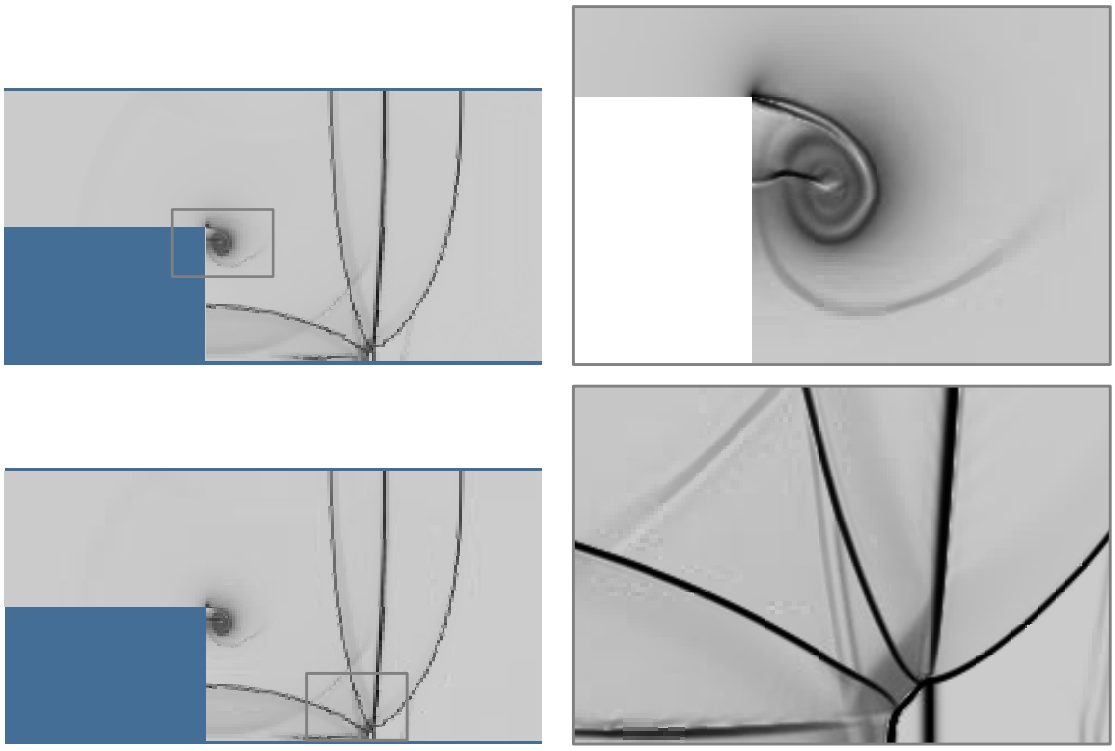

Figure 2.35: $t = 34.03\mu$s.

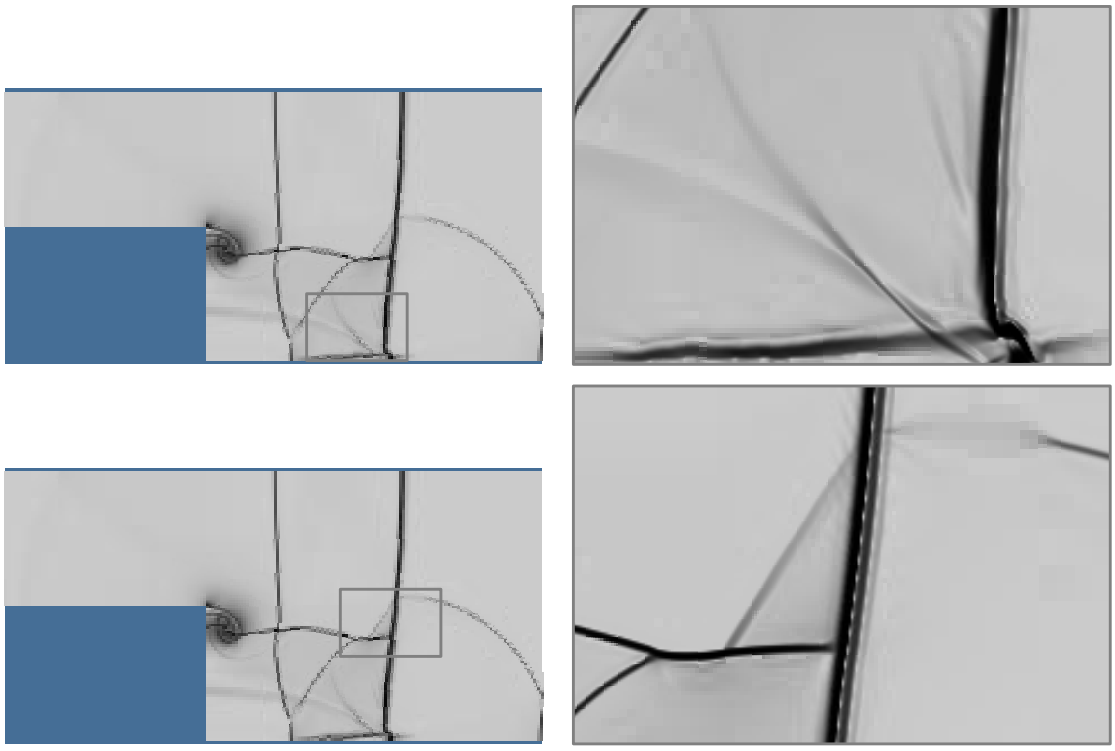

Figure 2.36: $t = 42.77\mu$s.

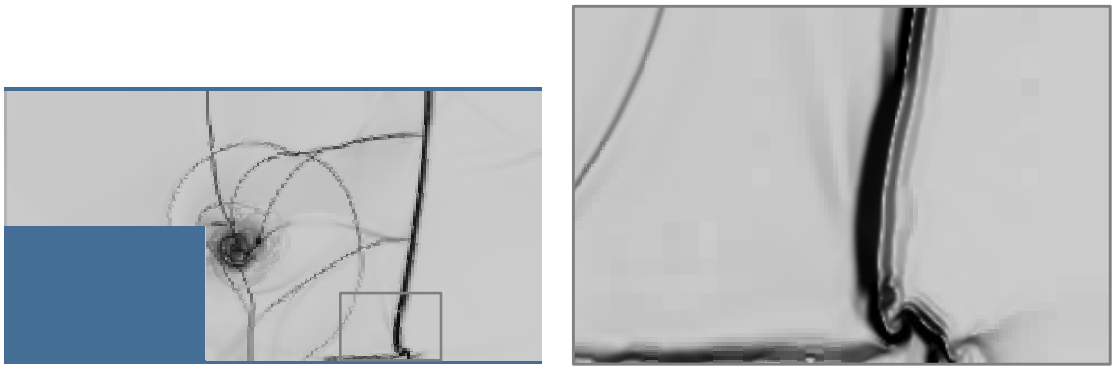

Figure 2.37: $t = 55.89\mu$s.

top plots depict the Schlieren images, while the bottom plots depict the iso-contours of the mass-fraction λ. The left plots are those of the fixed rate reaction experiment and the right plots those of the pressure-dependent rate.

Two important features need be pointed out. First, it is clear that the incident and diffracted waves have essentially same velocity for the fixed rate experiment, while the diffracted wave considerably slows down in the case of the pressure dependent rate. This is due to the fact that if the pressure ratio (P/P_{VN}) becomes small the reaction essentially subsides. The reaction is no longer sustained behind the shock and results in the second feature which is the left-over area so called "dead-zone" where there is essentially no reaction.

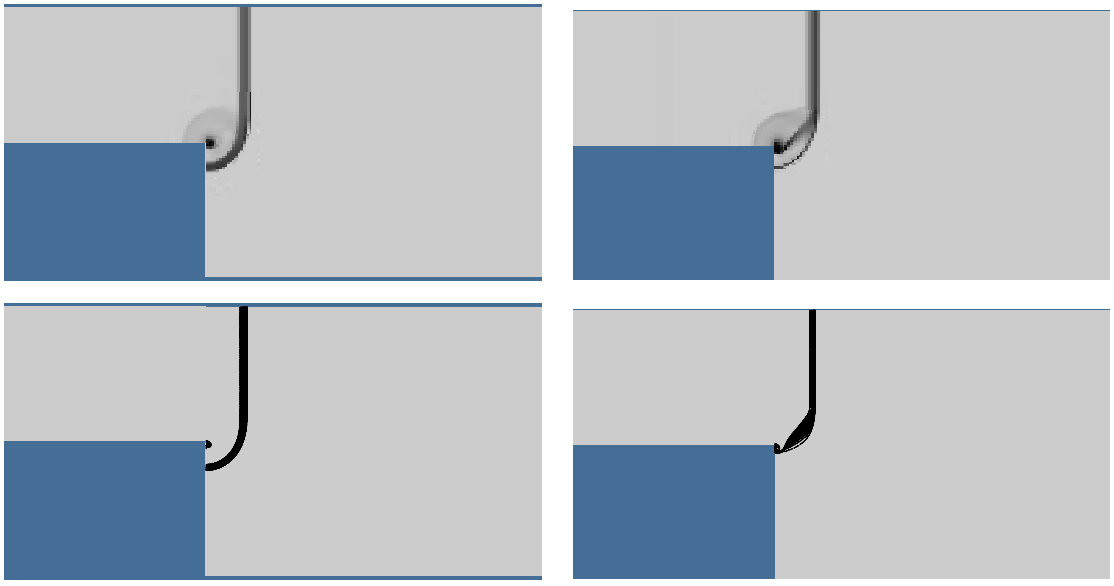

Figure 2.38: $x_I \sim 0.44 x_{max}$.

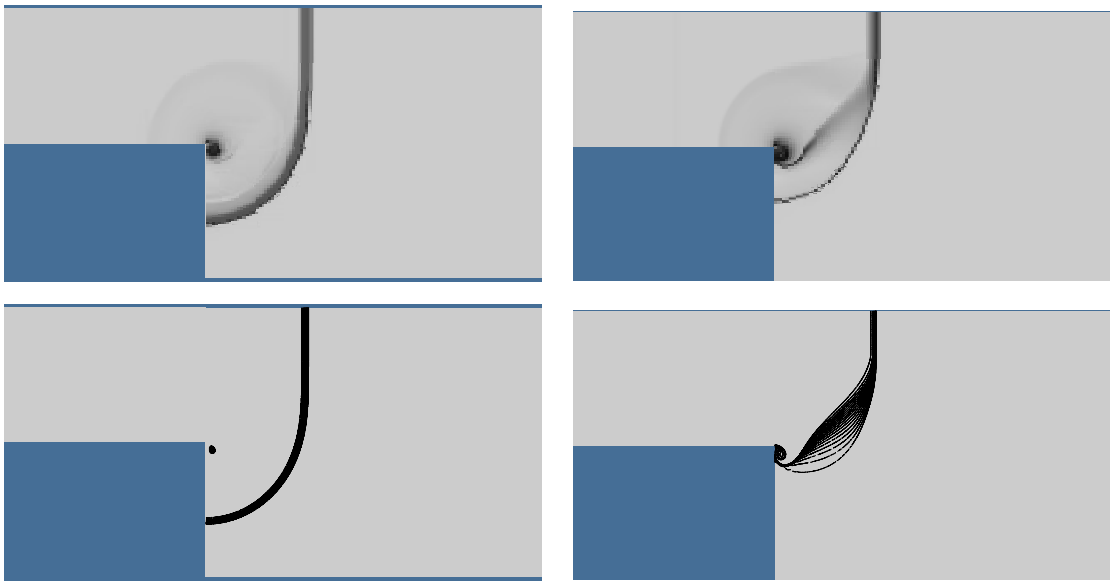

Figure 2.39: $x_I \sim 0.56 x_{max}$.

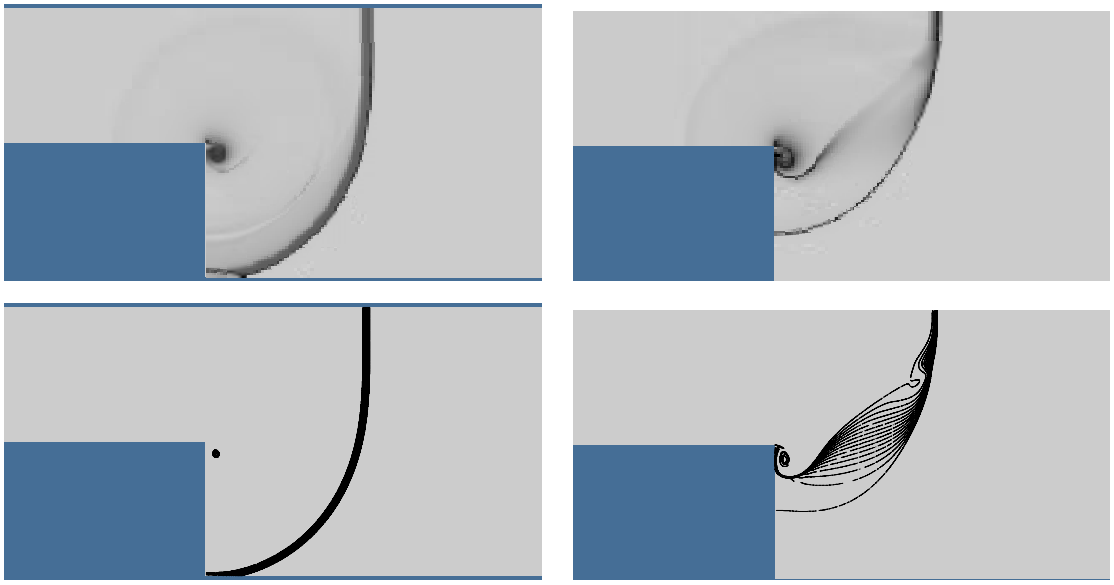

Figure 2.40: $x_I \sim 0.69 x_{max}$.

2.8 Pressure stiffening of rubbery binder:

2.8.1 Introduction

Plastic Bonded Explosives (PBX) are composed of explosive crystals typically 20-200μm in dimension, held together in an elastomeric matrix (typically a 2-5μm thick layer around the explosive crystals). This rubbery matrix comprises only a small fraction of the explosive (3-10% by volume) but, by this very fact (as will be described presently), can have a significant effect on the initiation of detonation in the explosive.

High Explosives function by releasing large amounts of chemical energy when heated to sufficiently high temperatures. The energy release and the expanding gaseous products accelerate the rate of reaction and strengthen the detonation front. In the case of shock wave loading, however, the high temperatures required for the initiation of chemical reaction in these explosives cannot be attained by a homogeneous deformation within the explosive. It is generally understood that in such cases the initiation of detonation occurs in localized, small regions within the explosive (referred to as *hot-spots*) where the local temperatures are high enough to initiate the chemical reactions. Several mechanisms involving local plastic deformation in the explosive have been proposed to explain the origin of hot-spots [33]. These include void collapse, fracture of and shear-banding in the explosive crystals and frictional rubbing between adjacent crystals. In this study our aim is to explore the influence of the rubbery binder in the formation of hot spots. Specifically, we will study the effects of stiffening of the rubbery binder under the imposed pressure on various aspects of hot-spot formation.

2.8.2 Motivation for study

Elastomeric binders used in high explosives typically display rubbery behavior at room temperature and above, and hence possess the low moduli associated with such material. For example, a thermoplastic polyurethane (commercially sold as Estane) that is used as a binder in many high explosives has a rubbery modulus of approximately 2 MPa at 100% elongation and 4 MPa at 300% elongation [34]. Under shock wave loading, the thin binder layer in an explosive is subjected to large pressure and shear loads. Since the binder occurs as very thin layers sandwiched between hard explosive crystals, it experiences large shear strain rates. Current mechanical models [35] of explosives use the rubbery moduli to model the response of the binder. These low moduli values would then permit the binder – and hence the explosive – to sustain only small shear stress levels and correspondingly low inelastic dissipation values. However, it is known that elastomers undergo tremendous stiffening under imposed pressure (see Fig. 1). Fillers and Tschoegl [36] have conducted extensive studies on the influence of pressure on the shear relaxation moduli of several elastomers and have reported moduli increases of up to 3 orders of magnitude under pressures as low as 0.5 GPa. For example, Hypalon 40 exhibits a shear modulus of approximately 1 MPa at 25 C under atmospheric pressure. Under a pressure of 0.46 GPa however, the shear modulus increases to 630 MPa (Fig. 2.41). Under shock loading conditions, the pressures are typically of the order of a few gigapascals before the initiation of detonation. Under these condition, the stiffening of the rubbery binder would lead to higher shear stress levels and correspondingly

higher levels of inelastic dissipation in the binder. This inelastic deformation and heating of the binder can cause local hot-spots to ignite in the adjacent explosive crystals. Furthermore, the increased levels of shear stress sustained by the binder would cause increased shear stresses in the explosive crystals and could cause failure of the crystals and thus form other sources of hot-spots. Increasing temperatures, however, will cause the binder to soften and lower stress levels. It is the objective of this study to examine these competing effects.

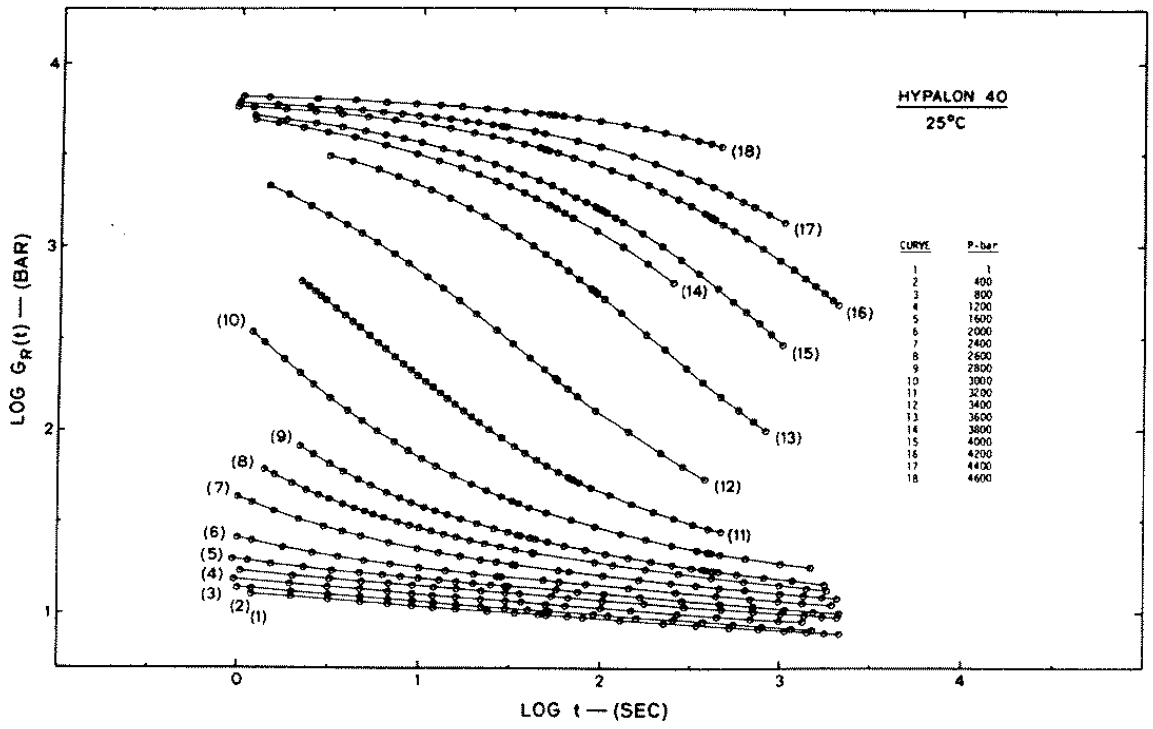

Figure 2.41: Pressure stiffening of an elastomer (from Fillers and Tschoegl)

2.8.3 Accomplishments during FY98

During FY98, we have initiated investigation into this area by conducting some case studies of wave propagation in viscoelastic materials and examining the effect of pressure-induced stiffening. Primarily, we have studied the case of wave propagation in a rod of a viscoelastic material (Case 1) and the case of plane wave propagation in a viscoelastic material (Case 2). Commonly, in viscoelastic materials, the shear modulus modulus of the rubbery state differs from the shear modulus of the glassy state by $2-3$ *orders* of magnitude whereas the corresponding bulk moduli differ by only by a *factor* of $2-3$. Thus, the primary relaxation effects occurs in the shear modulus; this is modified by the stiffening effects of the imposed pressure. While Case 1 (rod propagation) involves a small pressure component and a relatively large deviatoric component in the stress state, Case 2 (plane wave propagation) involves large pressures and a smaller deviatoric component due to the lateral constraint. Hence, these two cases, in a sense, represent two extreme cases of the effect we seek to study

— in Case 1, the effect of shear stiffening could be substantial but the pressures are small; and in Case 2, the shear stresses are small but the pressure — and hence the stiffening — is large. Sample results are presented in a subsequent section.

Formulation of constitutive equations

The constitutive relation for linear viscoelasticity can be written as follows:

$$\sigma_{ij} = 2\int_{-\infty}^{t} \mu_0(t-\xi)\frac{\partial \epsilon_{ij}}{\partial \xi}d\xi + \delta_{ij}\int_{-\infty}^{t} K_0(t-\xi)\frac{\partial \epsilon_{kk}}{\partial \xi}d\xi \tag{2.30}$$

where $\mu_0(t)$ and $K_0(t)$ are the time-dependent shear and bulk relaxation moduli at some reference temperature and pressure (T_0, P_0) [37].

If the temperature changes during the course of the deformation, the material undergoes thermal softening (or hardening) in addition to the time-dependent relaxation. The effect of temperature is usually included in the formulation by utilizing the concept of *intrinsic material time* defined as

$$t' = \int_0^t \frac{dt}{a_T} \tag{2.31}$$

where

$$a_T = a_T(T) = a_T[T(t)] \tag{2.32}$$

is a so-called *shift function* defined with respect to the reference temperature T_0. The viscoelastic formulation is now written as

$$\sigma_{ij} = 2\int_{-\infty}^{t} \mu_0(t'-\xi')\frac{\partial \epsilon_{ij}}{\partial \xi}d\xi + \delta_{ij}\int_{-\infty}^{t} K_0(t'-\xi')\frac{\partial \epsilon_{kk}}{\partial \xi}d\xi \tag{2.33}$$

For the case of a constant temperature T, Eqn. 2.31 reduces to the well-known time-temperature shifting for thermo-rheologically simple materials (lateral shifting of the modulus curves along a logarithmic time axis) and, indeed, the shift factors $a_T(T)$ are obtained from several such constant temperature experiments.

The effect of pressure is similar to that of temperature in that tests conducted at a constant pressure P causes the moduli curves to shift along a logarithmic time axis. Thus, a combined *pressure-temperature shift function*

$$a_{T,P} = a_{T,P}[T(t), P(t)] \tag{2.34}$$

can be defined to replace a_T in Eqn. 2.31. Pressure tends to retard the rate of relaxation whereas temperature tends to accelerate the rate of relaxation. Fig. 2.42 shows the master curves for Hypalon 40 reduced to $(T_0 = 25C, P_0 = 1\text{bar})$ resulting from the shifting of isothermal and isobaric curves 2.41. The inset shows the corresponding shift function $a_{T,P}$.

2.8.4 Summary of computational results

Numerical calculations were carried out with the help of the finite element software ABAQUS. In order to isolate the effect of pressure, temperature effects were not considered. The master

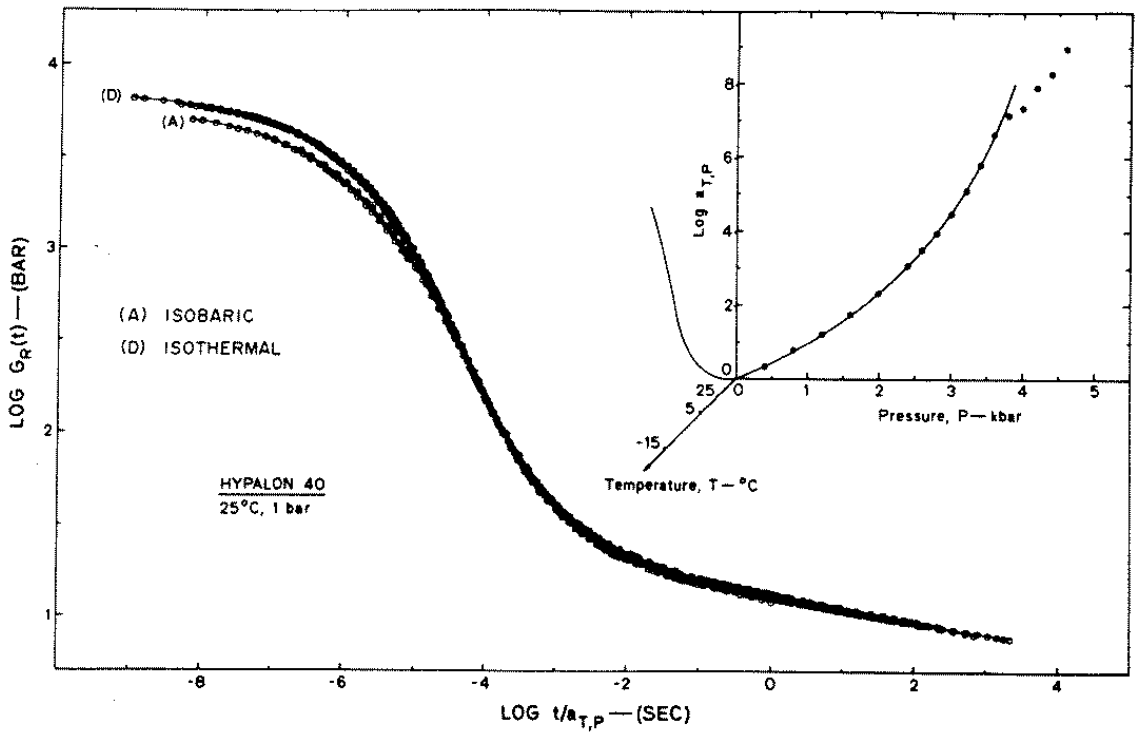

Figure 2.42: Master relaxation curve and shift function

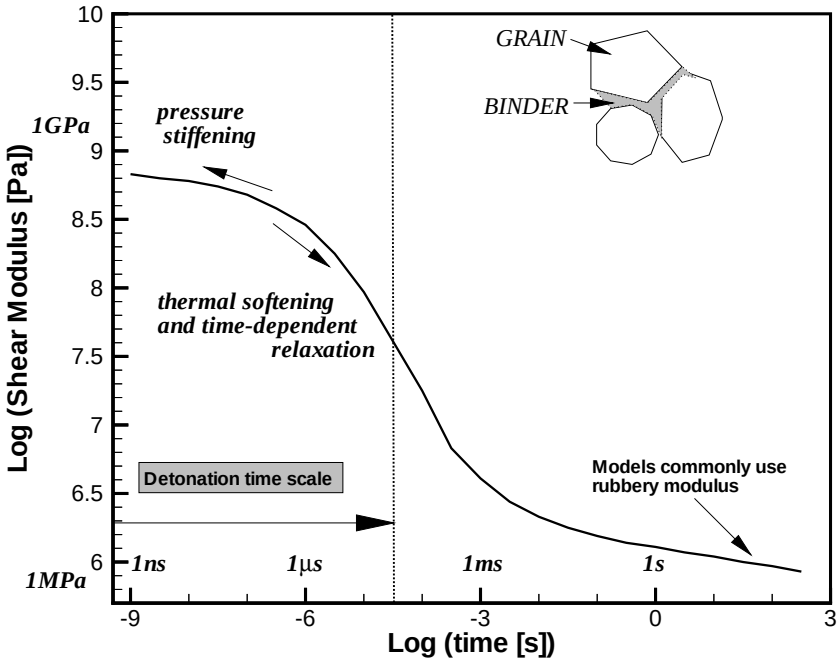

Figure 2.43: Relaxation curve and detonation time scale

relaxation curve data in Fig. 2.42 numerically converted to a Prony series of 13 terms for use in the analysis. The resulting curve is shown in Fig. 2.43 which also shows, schematically, the opposing effects of increasing pressure and temperature on the relaxation modulus. Also included in the figure is the detonation time scale which includes events on the picosecond range to tens of microseconds.

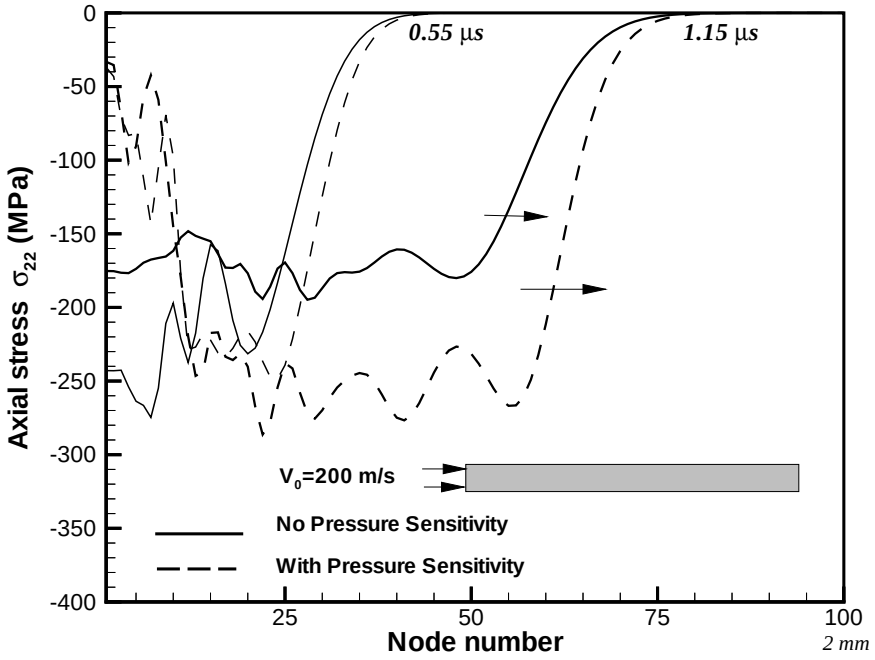

Figure 2.44: Wave propagation in a rod – pressure Effects

Figs. 2.44 and 2.45 show representative results from the computations. As mentioned earlier, two cases were studied. Case 1 (Fig. 2.44) involved wave propagation in a rod and Fig. 2.44 shows the profile of axial stress in the specimen at two different times. Case 2 involved plane wave propagation and Fig. 2.45 shows the wave profile in the specimen at the same two times. In both cases, a velocity of 200 m/s was imposed on the left end of the specimen. Only approximately 1 μs of propagation is shown in the figures (corresponding to a propagation distance of approximately 2 mm) in order to show the effect of pressure even at these early times. In both cases, pressure tends to increase the strength of the wave. In Fig. 2.44 (rod propagation), the time-dependent relaxation is apparent from the reducing strength of the wave for the case with no pressure sensitivity (solid lines). In fact at longer times the stress levels continue to fall rapidly. However, including pressure effects increases the stress levels as the elastomer is stiffened into its glassy state. Plane wave propagation, however, shows only slight increase in stress levels due to pressure stiffening. As observed in an earlier section, this is due to the fact that the deviatioric component of the stress state is small in this case and hence no significant relaxation is observed.

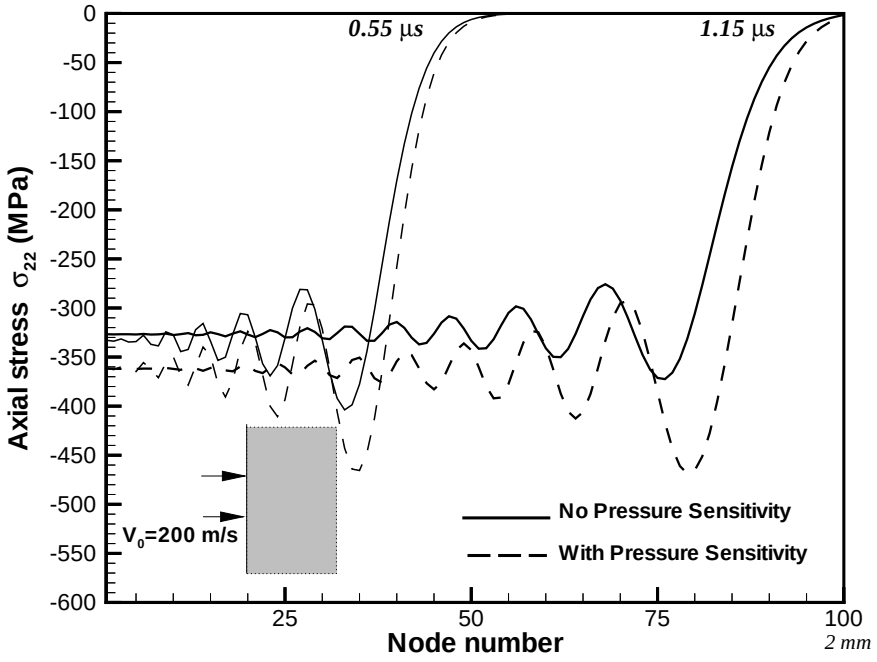

Figure 2.45: Plane wave propagation – pressure effects

2.9 High Explosives Personnel

- *Aeronautics*
  - J. E. Shepherd (PI)
  - E. Morano
  - C. Eckett
  - W. G. Knauss
  - S. Sundaram
  - P. Hung
  - A. Arienti
  - A. Lew
  - R. Fedkiw
- *Chemistry and Materials*
  - S. Dasgupta
  - L. Sun
  - G. Caldwell (visiting)

– R. Muller
– T. Cagin

Chapter 3

Solid Dynamics

3.1 Description of accomplishments for FY 98

The first-year milestones for solid dynamics were:

1. Development of 3-D finite element mesh refinement.
2. Development of 1-D continuum/atomistic models.
3. Dynamics of polymorphic phase transitions.

These milestones have been completed, and in many cases surpassed, except for the modeling of polymorphic phase transitions, which is in progress. A detailed description of accomplishments for FY 98 follows.

3.1.1 Overall goals and objectives

The central objective of the solid dynamics activity within the center is the development of physics-based theories of material behavior under extreme conditions of rate of deformation, pressure and temperature; and the development of advanced computational methods enabling the three-dimensional end-to-end simulation of the dynamic behavior and failure of solids under shock loading.

3.1.1.1 Material modeling

The central paradigm which guides our development of theories of material behavior is the bridging of spatial and temporal lengthscales. In this conception of materials, detailed models of the mechanisms which dominate material behavior at each scale are formulated, and their predictions are used to inform modelling at larger scales. This bridging of scales may be accomplished off-line, through the computation of effective properties; or by multiscale simulations in which several lengthscales–and their interactions–are taken into consideration simultaneously.

We specifically indentify the following lengthscale hierarchy:

1. *Atomistic scale, $l < 10$ nm.* At this scale, the objects of interest are the core structures of individual defects and their interaction with the crystalline lattice. Examples of properties which can be ascertained at this scale are elastic moduli, dislocation core energies, Peierls stresses, vacancy formation energies, surface energies, diffusivities and viscosities.

2. *Nanomechanical scale, 10 nm $< l <$ 100 nm.* This scale is dominated by the interactions between a small number of defects such as dislocations and vacancies. Phenomena of interest occurring on this scale are the formation of dislocation junctions, vacancy generation by jog dragging, and dislocation emission from crack tips.

3. *Submicron scale, 100 nm $< l <$ 1 μm.* Here one considers short-range interactions between large numbers of defects such as determine the hardening and other characteristic of the crystal. Examples are the motion of glissile dislocations through forest dislocations and the condensation of vacancies into voids.

4. *Subgrain scale, 1 $\mu m < l <$ 10 μm.* The behavior at this scale is characterized by the cooperative effect of large numbers of defects leading to the formation of low-energy microstructures. Examples of phenomena occuring on this scale are the formation of dislocation subgrain structures, and processes of void growth and coalescence leading to ductile fracture.

5. *Polycrystalline scale, 10 $\mu m < l <$ 100 μm.* On this scale, the polycrystalline structure of the materials of interest reveals itself. The principal objective is the approximation of the effective behavior of the polycrystal by such techniques as Taylor averaging.

6. *Macroscopic scale, 100 $\mu m < l$.* At the top of the lengthscale ladder the focus turns to macroscopic failure modes such as fragmentation, spall, necking, jetting, and others.

A truly predictive solid dynamics simulation facility must account for all these scales and their interactions. We have research activities underway on all relevant scales. The main accomplishments resulting from these activities are recounted in subsequent subsections.

Materials of primary interest are bcc metals such as Fe and Ta, and structural ceramics such as Al_2O_3. Our objective is to account explicitly for all scales from subgrain to macroscopic in simulations, and to carry out simulations at the atomistic, nanomechanical and submicron scales off-line with a view to computing effective properties.

3.1.1.2 Algorithm development

Some of the main building blocks of the Virtual Testing Facility (VTF) under development are:

1. Automatic generation of unstructured tetrahedral meshes for domains of arbitrary geometry and topology.

2. Error estimation under strongly nonlinear dynamic conditions.

3. Adaptive meshing as a means of minimizing errors, eliminating deformation-induced element distorsion, and resolving fine features in the solution such as shear bands.

4. Energy-momenta preserving variational integrators for the integrating in time the equations of motion and the constitutive equations.

5. Cohesive theories of fracture enabling the direct simulation of complex fracture and fragmentation patterns.

6. Nonsmooth contact/friction algorithms capable of resolving complex collision sequences such as arise in fragmentation.

7. Coupled thermo-mechanical analysis.

8. Multicomponent lagrangian-lagrangian and eulerian-lagrangian algorithms for integrating fluid and solid simulation capability.

Other key concerns are the parallel implementation of all algorithms to ensure scalability and load balance on asci platforms; and the thorough validation and verification of the simulation capability.

3.1.2 Mixed atomistic continuum simulations

R. Phillips and V. Shenoy (Brown University) have used a mixed atomistic-continuum formulation to simulate three-dimensional Lomer-Cottrell junctions in aluminum, both in the absence and in the presence of an applied stress [56]. A calculated junction geometry is shown in Fig. 3.1. The simulations show that this type of junction is destroyed by an unzipping mechanism in which the dislocations that form the junction gradually re-dissociate. The calculated critical stress needed for breaking the junction is comparable to that which is predicted by line tension models. The simulations also demonstrate a strong influence of the intial dislocation line directions on the breaking mechanism. The calculated dislocation binding energies are used as parameters in the forest-hardening model of single-crystal behavior at the submicron scale. Robert Phillips and Vivek Shenoy have extended the mixed atomistic-continuum formulation to account for temperature by a Monte Carlo method.

J. Knap and M. Ortiz have developed a 1D prototype of a stochastic atomistic-continuum theory which accounts for macroscopic thermal effects. The theory envisions an underlying atomistic description, e. g., a monatomic chain in the 1D prototype, and proceeds to coarsen the description by introducing macroscopic kinematic constraints. These constraints may be unstructured and afford various degrees of resolution, from a full atomistic description near lattice defects, to effective thermodynamic behavior in regions where the state fields vary slowly on the scale of the lattice. In addition to the previously developed static theory, the macroscopic description now includes an energy field, which effectively provides a characterization of thermal effects. Based on this approach, we have been able to derive key macroscopic properties of the chain, such as thermal expansion and heat conductivity, on the sole basis of an atomistic potential.

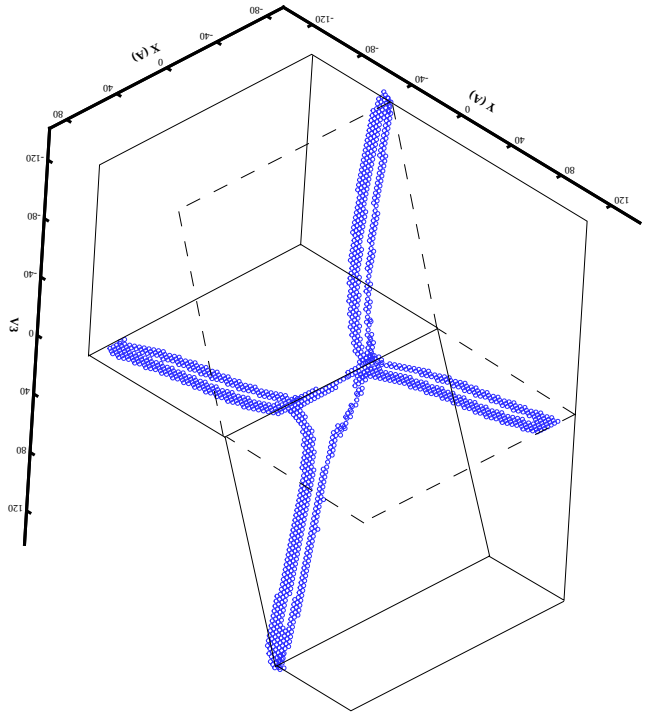

Figure 3.1: Lomer-Cottrell junctions in aluminum calculated using a mixed atomistic-continuum approach [56].

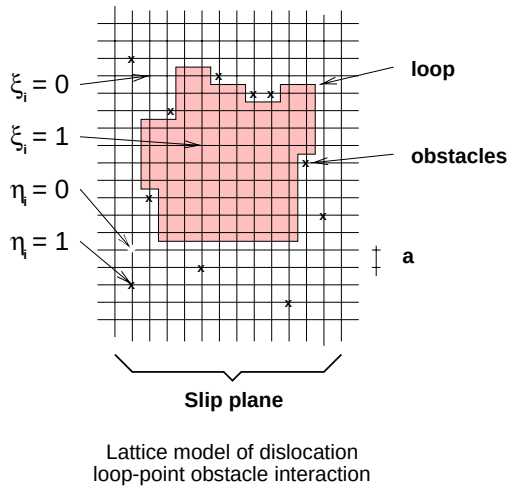

Figure 3.2: Schematic of dislocation/obstacle system,[43, 48].

3.1.3 Single-crystal plasticity model

M. Ortiz and L. Stainier [43, 48] have developed a statistical mechanical theory of forest hardening in which yielding arises naturally as a phase transition. The model envisions an ensemble of dislocation loops moving on a slip plane. The dislocations are presumed well-screened so that their energy is proportional to their length. The motion of the loops is impeded by forest dislocations piercing the slip plane, which we treat as point obstacles. Fig. 3.2. Specifically, the glissile and forest dislocations react to form junctions such as shown in Fig. 3.1. The occurrence of slip at the sites occupied by these obstacles requires the junctions to be dissolved, which entails an expenditure of energy equal to the binding energy of the junction.

In order to simplify the analysis we discretize the slip plane by a square lattice, Fig. 3.2. The energy of the dislocation/obstacle system is, then:

$$E = \sum_{\langle i,j \rangle} \frac{, b}{2}(\xi_i - \xi_j)^2 - \tau b^3 \sum_{i=1}^{N} \xi_i + \sum_{s=1}^{S} \left\{ E^{(s)} \sum_{i=1}^{N} \xi_i \eta_i^{(s)} \right\} \tag{3.1}$$

where all sums extend to the lattice sites, ξ_i is the number of dislocation loops which have cross site i, and the variable $\eta_i^{(s)}$ is one if site i is occupied by a forest dislocation residing in slip system s, and zero otherwise. The first term in E is the dislocation line energy, the second term represents the interaction between the glissile dislocations and the applied shear stress τ, and the third term brings in the binding energies $E^{(s)}$ of the junctions formed by the glissile and forest dislocations. The remaining parameters of the model are the Burgers vector b, which is commensurate with the crystalline lattice parameter, and the dislocation line tension , .

The effective behavior of the dislocation/obstacle system, leading to a complete characterization of the stress-strain response of the crystal, may be obtained by an application of the standard tools of statistical mechanics to the energy (3.1). We have shown that the behavior of a single dislocation loop as it sweeps the slip plane under the action of a resolved

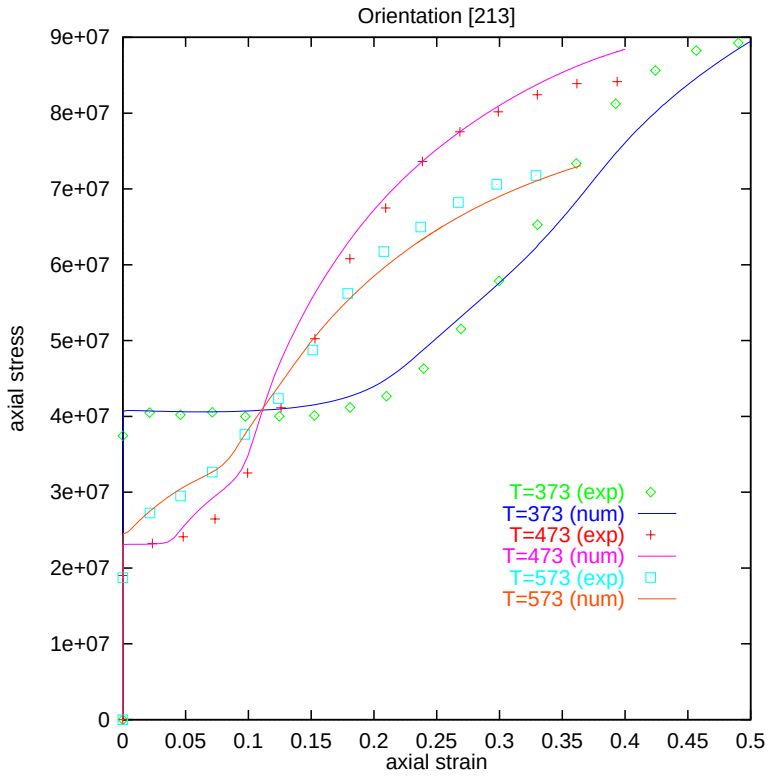

Figure 3.3: Uniaxial test on Ta single crystals. Comparison of predicted [48] and experimental curves (Mitchell and Spitzig, 1965).

shear stress is identical to that of a lattice gas and, equivalently, to the two-dimensional spin-1/2 Ising model. In particular, there exists a critical temperature T_c below which the system exhibits a yield point: the slip strain increases abruptly when the applied resolved shear stress attains a critical value. Above the critical temperature the yield point disappears and the slip strain depends continuously on the applied stress. The critical exponents, which describe the behavior of the system near the critical temperature, coincide with those of the two-dimensional spin-1/2 Ising model.

A comparison of predicted uniaxial-tension stress-strain curves for Ta and the experimental data of Mitchell and Spitzig (1965) is shown in Fig. 3.3. As may be seen from the figure, the predicted stress-strain curves accurately capture the observed stages I and II of hardening and the effect of temperature, including the overall softening of the crystal and the shortening of the stage I at high temperatures.

The dislocation line energy per unit length, or line tension, , required in the hardening model may be obtained directly from calculations of dislocation core energies such as planned for FY99. As mentioned above, some of the requisite dislocation-junction binding energies $E^{(s)}$ have also been computed for aluminum furing FY98 using the mixed atomistic-continum approach mentioned above. The remaining parameters of the hardening model are, chiefly, the elastic moduli of the crystal and their dependence on pressure and temperature. Thereforem all parameters in the nardening model are amenable to calculation by atomistic methods. The calculation of these parameters is presently underway and will continue in

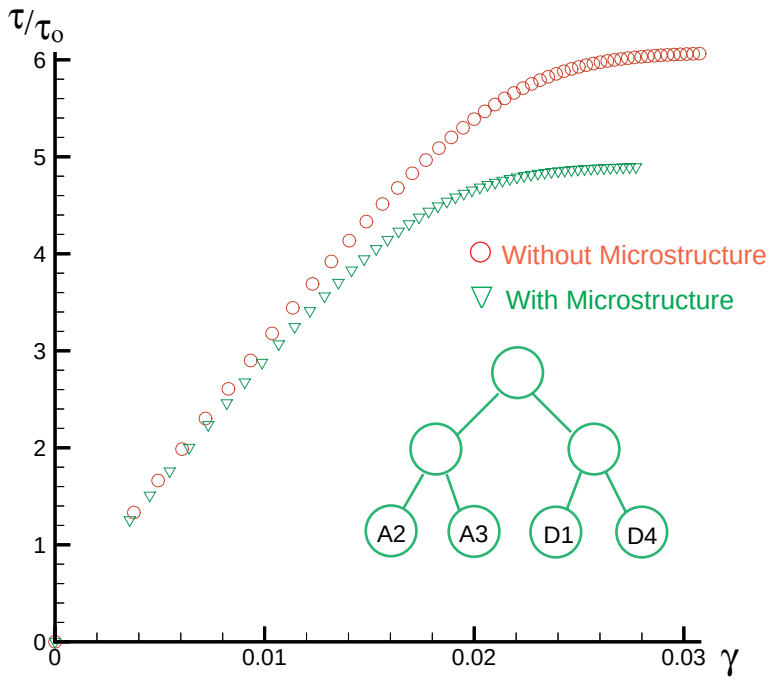

Figure 3.4: Effect of dislocation structure development on the stress-strain curve of an aluminum-copper alloy deformed in simple shear [46].

FY99.

3.1.4 Dislocation structures

Crystals undergoing large plastic deformations are commonly observed to develop characteristic dislocation structures. Often these structures consist of roughly parallel arrays of dislocation walls, and may therefore be regarded as instances of 'lamination' [45]. The formulation of effective theories of single crystal plasticity which explicitly and directly account for the effect of dislocation structure development is a long-standing–and largely unfulfilled–goal of physical metallurgy.

We have developed an efficient algorithm for generating complex laminate microstructures while simultaneously relaxing the incremental energy density of single crystals [45, 46]. The point of departure of the construction is a conventional local model of crystal plasticity. Evidently, only uniform microstructures, generally with multiple slip occurring simulataneously everywhere, may be accounted for with such a model. However, because of latent hardening, the incremental work of deformation incurred by an application of the local model will in general greatly exceed that which is incurred when microstrures are allowed for. The construction presented here exploits the power of recursion to generate complex laminates which result in this energy relaxation. Roughly speaking, the resulting microstructures consist of regions in which a small number of slip systems are activated, thereby mitigating the

effect of latent hardening.

This effect is clearly apparent in Fig. 3.4, which shows an example of application of the construction to the calculation of the stress-strain curve of an aluminum-copper alloy deformed in simple shear [46]. The microstructure consists of 'laminates within laminates', and has the tree structure shown in the inset of the figure. As may be seen from the figure, failure to account for microstructures may result in a gross overestimation of the plastic work incurred during the deformation of a crystal.

3.1.5 Three-dimensional meshing algorithms

A key activity of the solid dynamics group is concerned with the development of robust and versatile tetrahedral meshers applicable to volumes of arbitrary geometry and topology. We have developed data structures which permit the storage of topological information such as required to describe complex solid models [54, 52]. We represent the geometry of all surfaces analytically or by finite-element interpolation. We have also developed an interface with the `ACIS`[1] `.sat` file format which permits the rapid definition of models for subsequent use in simulation. The parser is able to read general topologies and faceted (discrete) geometry representations as provided by `ACIS` files. Fig. 3.5 shows an example of application of this capability to the Virtual Shock Physics specimen. The solid model in this example has been defined using `ACIS`, and the mesh has been subsequently generated using our tetrahedral mesher.

In order the generate a tetrahedral mesh, we begin by constructing a preliminary surface mesh by an advancing front method, with the nodes inserted by a hard-sphere packing algorithm in accordance with a prescribed mesh density. Interior nodes are inserted in a face-centered-cubic (FCC) crystal lattice arrangement coupled to octree spatial subdivision, with the local lattice parameter determined by a prespecified nodal density function. This density function is determined so as to minimize a measure of the error in the solution, as discussed subsequently. Prior to triangulation of the volume, the preliminary surface mesh is preprocessed by a combination of local transformations and subdivision in order to guarantee that the surface triangulation be a subcomplex of the volume Delaunay triangulation. A joint Delaunay triangulation of the interior and boundary nodes which preserves the modified surface mesh is then constructed *via* an advancing front approach. The resulting mesh is finally improved upon by the application of local transformations. The overall time complexity of the mesher is $O(N \log N)$.

The example shown in Fig. 3.6 concerns the meshing of a sphere with a strong gradient in the mesh density distribution. The cross section of the mesh shown in this figure exhibits the six levels of refinement present in the mesh. The different regions of uniform mesh size, or FCC grains, as well as the grain boundaries are also clearly visible. Fig. 3.6 also demonstrates the good performance of the surface mesher, which predominantly results in an optimal coordination number of 6 despite the presence of strong gradients in the mesh density distribution. The overall good quality of the mesh is also evident from the figure.

[1] Copyright © by Spatial Technologies Inc.

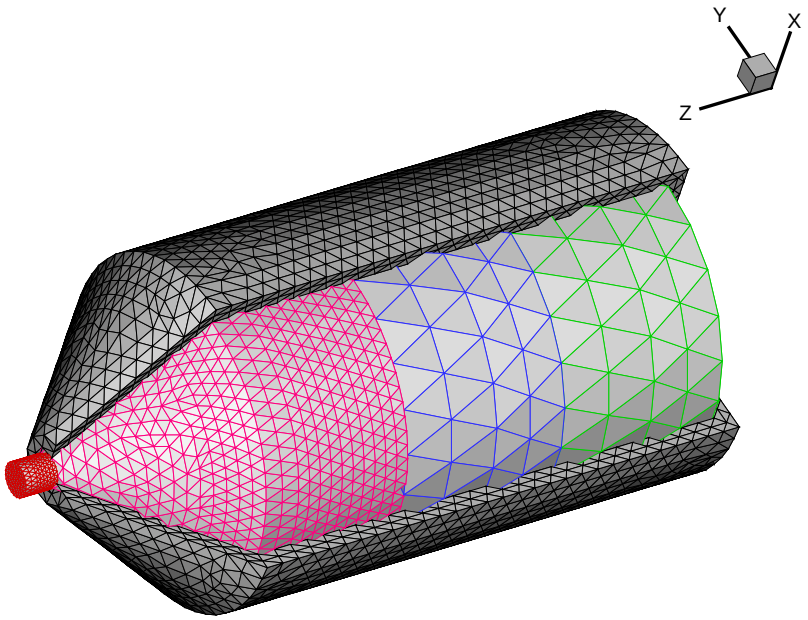

Figure 3.5: Virtual Shock Physics specimen defined using the `ACIS` CAD package and subsequently meshed by our tetrahedral mesher.

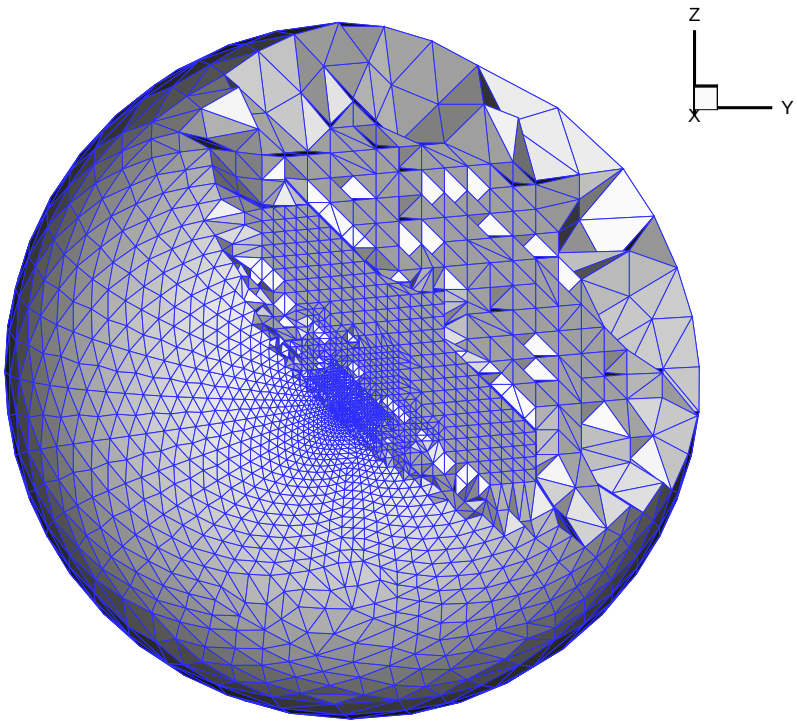

Figure 3.6: Meshing of a sphere with a sharp gradient in prescribed element density (180704 elements).

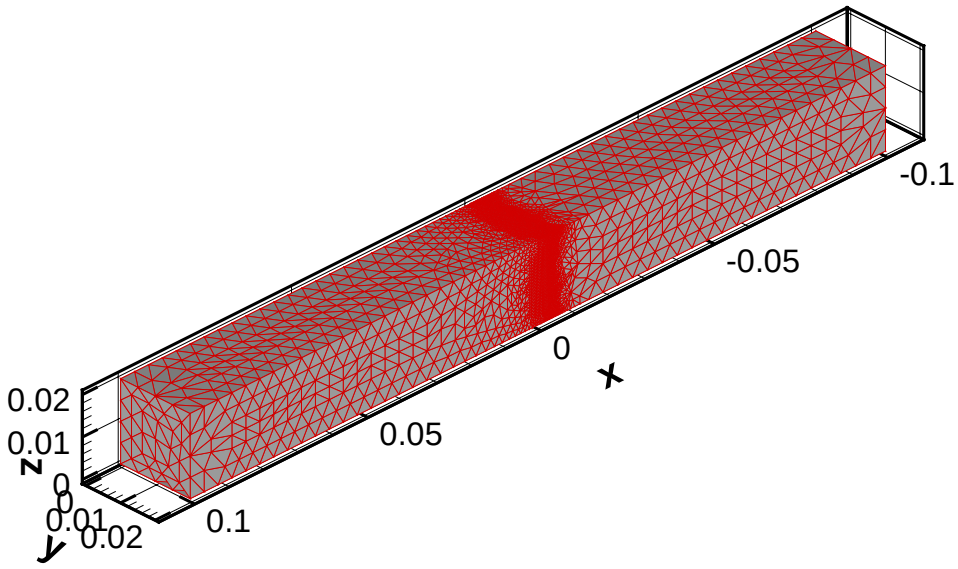

Figure 3.7: Mesh adaption in a shock tube problem [53].

3.1.6 Mesh adaption

One of the distinguishing characteristics of the VTF under development will be the effective use of adaptive meshing in order to:

1. Resolve fine features of the solution on multiple lengthscales.
2. Minimize the error in the solution for a fixed computational budget.
3. Eliminate deformation-induced mesh distorsion in Lagrangian calculations.

As a rational basis for driving the mesh adaption, we [53] have developed error estimators applicable to the strongly nonlinear dynamic problems of interest. Our approach to error estimation, which lies at the core of our mesh adaption strategy, rests on a variational formulation of the incremental boundary value problem of elastic-plastic dynamics as a minimum principle [53, 47]. The optimal mesh-size distribution then follows from *a posteriori* error indicators which are purely local, i. e., can be computed element-by-element. Our three-dimensional mesher is then capable of reconstructing the mesh in accordance with the optimal mesh-size distribution.

Fig. 3.7 illustrates the use of our mesh adaption algorithm in a simulation of a compression wave in a shock tube configuration [53]. This verification test was suggested to one of us (M. Ortiz) by C. McMillan during a visit to the Lawrence Livermore National Laboratory. The ability of the mesh-adaption algorithm to resolve the shock is particularly noteworthy.

The particular problem shown in [53] admits a closed-form analytical solution, which in turn permits the calculation of the actual error in the solution. We have verified that this error does indeed converge at the optimal rate as the number of elements in the mesh is increased [53]. We have also verified that the error bounds are indeed tight, i. e., they are close to the actual error in the solution [53].

3.1.6.1 Fracture and Fragmentation

Another unique feature of the VTF under development concerns the use of cohesive elements [49, 40, 44, 52, 51, 50, 55] to model complex fracture patterns, possibly including fragmentation, such as arise during penetration of brittle targets; and ductile fracture phenomena such as jet breakup. Cohesive elements effectively enable the simulation of intricate systems of cracks as they nucleate, propagate, branch and link up to form fragments. Cohesive elements enable the incorporation into the simulation of *bona fide* fracture parameters such as the spall strength–the peak cohesive traction–and the fracture energy–the area under the cohesive law–of the material. Another appealing attribute of cohesive elements is the fact that they can be used in conjunction with general classes of bulk elements and constitutive behaviors, without restrictions on the size of the plastic zone or the geometry of the solid. In addition, the size of the plastic zone and extent of crack growth are not presupposed *a priori*, but obtained as an outcome of the calculation.

We have developed a class of cohesive elements which account for finite kinematics and irreversible behavior [44]. The cohesive elements have been extensively validated, and the fidelity of the approach thoroughly established. We have taken the expanding ring test of Grady and Benson [41] as a convenient yet challenging validation problem for assessing the fidelity of cohesive models in situations involving ductile fracture. Indeed, in these tests–and in the numerical simulations–fracture is preceded by extensive plastic necking of the ring. Numerical simulations of 1100-0 aluminum samples are highly predictive of a number of observed features, including: the number of dominant and arrested necks; the fragmentation patterns; the dependence of the number of fragments and the fracture strain on the expansion speed; and the distribution of fragment sizes at fixed expansion speed, Fig. 3.8.

We have also validated our cohesive elements in situations involving brittle fracture, such as occurs in ceramics and concrete under dynamic impact [57]. A simulation of the dynamic brazilian cylinder test, as performed by Tedesco *et al.* [58] in a Hopkinson bar on concrete specimens, is shown in Fig. 3.9. The simulation predicts key features of the fracture pattern such as the primary lens-shaped cracks parallel to the load plane, and the secondary profuse cracking near the supports. The primary cracks are predicted to be nucleated at the center of the circular bases of the cylinder and to subsequently propagate towards the interior, in accordance with experimental observations [58]. The primary and secondary cracks are responsible for two peaks in the load history, also in keeping with experiment. The simulations also give accurate transmitted loads over a range of strain rates, Fig. 3.10 which attests to the fidelity of the model where rate effects are concerned. These results validate cohesive elements as they bear on mixed-mode fracture and fragmentation processes over a range of strain rates.

(a) (b)

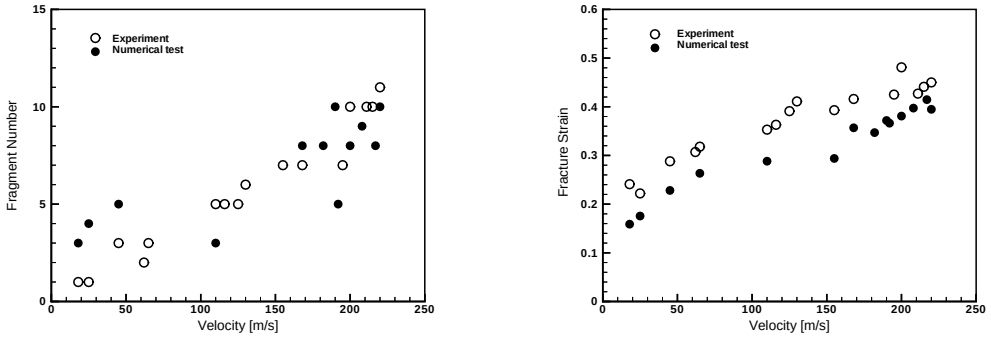

(c) (d)

Figure 3.8: Simulation of the expanding ring test of Grady and Benson [41] on 1100-0 aluminum samples. a) Predicted fragmentation pattern at 18 m/s expansion velocity; b) fragmentation pattern at 220 m/s expansion velocity; c) number of fragments and fracture strain *vs.* expansion velocity; d) fracture strain *vs.* expansion velocity.

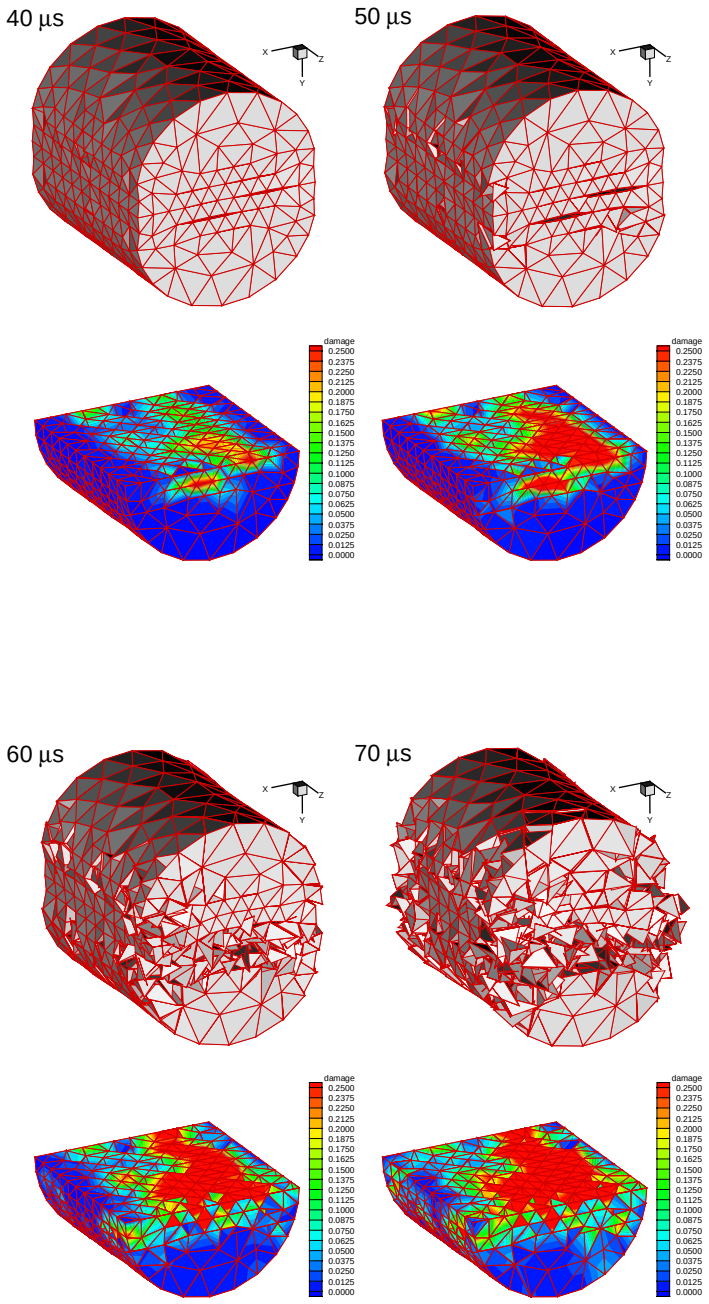

Figure 3.9: Simulation of the dynamic brazilian cylinder test performed by Tedesco *et al.* [58] in a Hopkinson bar on concrete specimens.

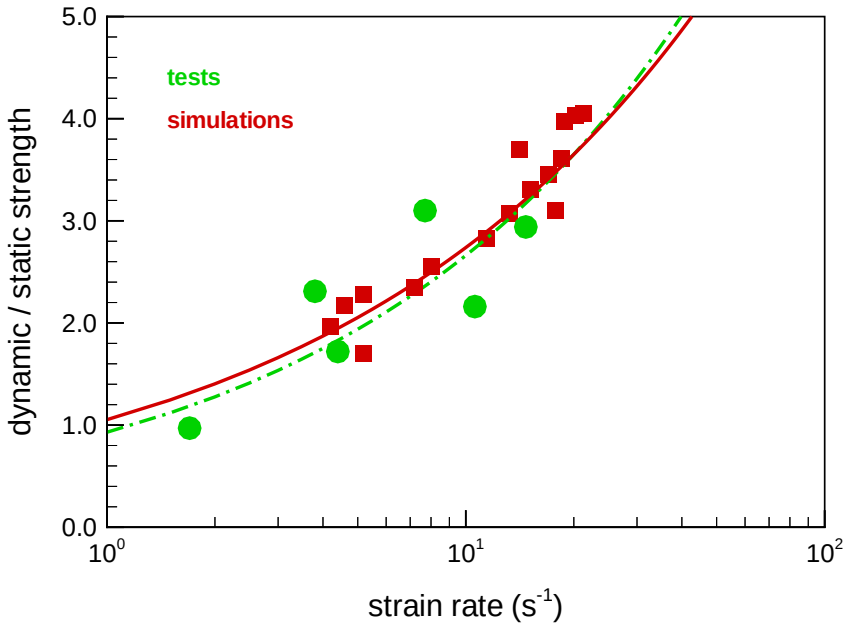

Figure 3.10: Simulation of the dynamic brazilian cylinder test performed by Tedesco *et al.* [58] in a Hopkinson bar on concrete specimens. Comparison between experimental and predicted dynamic strength of concrete *vs.* strain rate.

3.1.6.2 Nonsmooth contact mechanics

Dynamic fragmentation processes, such may be expected to occur in the VTF during testing of brittle materials, often result in the formation of large numbers of fragments which undergo complex collision sequences before they eventually scatter. During the initial stages of fragmentation, the corners of many angular fragments come together at a point, which precludes the definition of a proper gap function as a means of detecting–and constraining–the interpenetration of the fragments. In addition, because of the nonsmooth character of the fragments, normals cannot be uniquely defined in the contact region. Because fragments are tightly packed initially, contact situations arise which involve potential collisions between a large number of bodies.

We have developed robust contact algorithms capable of resolving complex, multi-body, possibly nonsmooth contact situations [42]. The aim here is to be able to simulate the flow of the fragmented, possibly comminuted, material *explicitly*, without in any way smearing or eliminating fragments. Our algorithm accords all bodies an equal role without differentiating between master and slave bodies. This is particularly important in situations such that several angular bodies meet near a point, since for these configurations it is generally not possible to classify the bodies as master or slave. The use of a diagonal mass matrix results in the decoupling of the global contact problem into independent *local* contact problems, each typically involving but a few degrees of freedom. These local problems can efficiently be set up using quadtree/octree searches. The local character of the contact algorithm in the context of explicit dynamics considerably speeds-up the calculations. Furthermore, the independence between the local problems lends itself to an efficient parallel implementation.

A verification test which illustrates the ability of our contact algorithm to deal with nonsmooth situations in three dimensions is shown in Fig. 3.11. The tests concerns the collision of two cubes which come together at a vertex. The cubes undergo finite elastic deformations during impact and interact closely for some time before eventually separating. It bears emphasis that the contact configurations in these two examples are nonsmooth and that normals are undefined in both cases.

3.2 Solid mechanics personnel

- Group Leader:
  - Michael Ortiz
- Faculty:
  - Thomas J. Ahrens
  - Oscar P. Bruno
  - Robert Phillips (Brown University)
- Research staff:

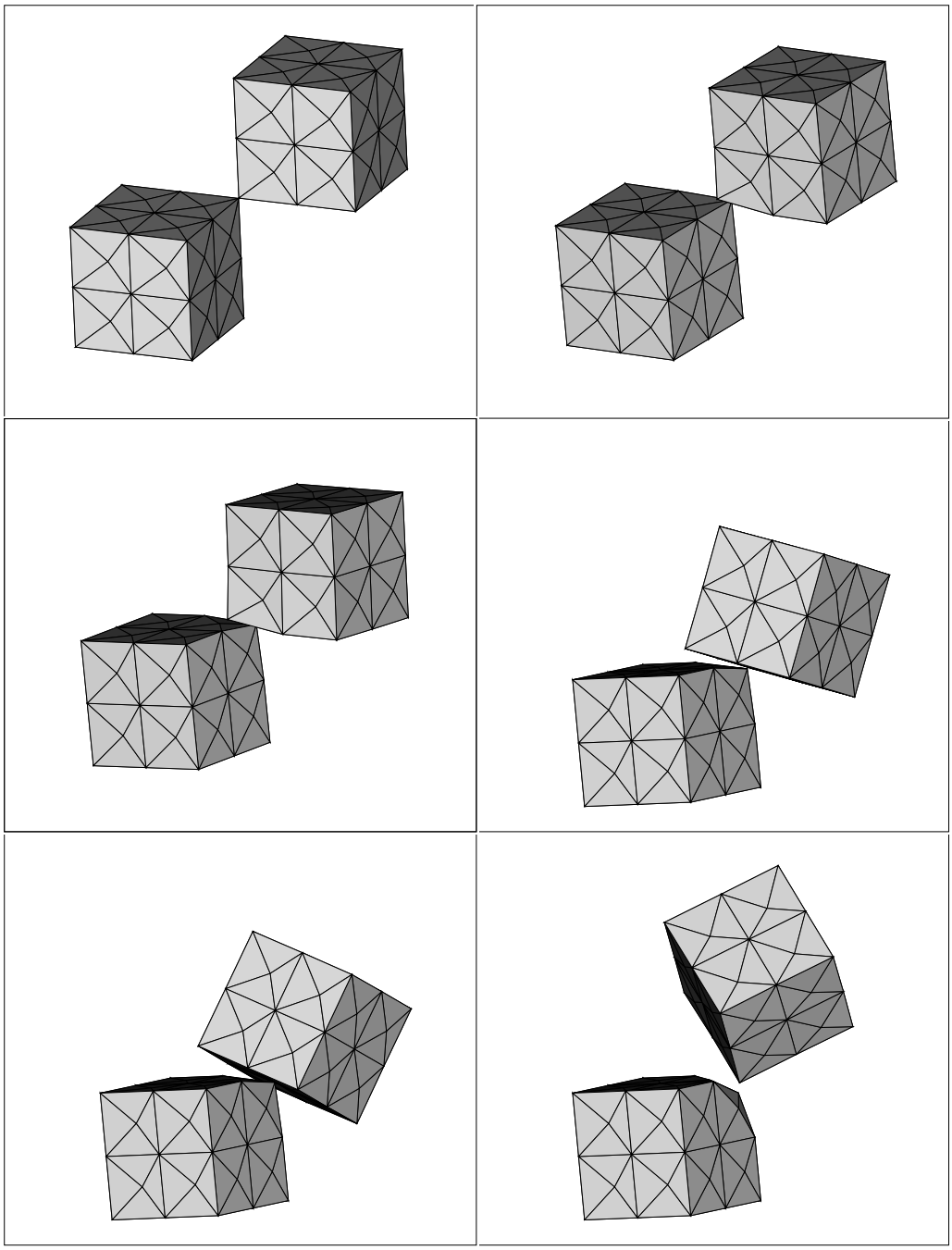

Figure 3.11: Nonsmooth contact algorithm applied to two cubes colliding at two vertices.

  - Petr Krysl (until July 31, 1998)
  - Raul Radovitzky (since August 1, 1998)
  - Daswami

- Post-doctoral students:

  - Couro Kane (50%, until July 31, 1998)
  - Jarek Knap
  - Vivek Shenoy (Brown University)
  - Laurent Stainier
  - Dimitri Vaynblat

- Graduate students:

  - Joe Akins (25%, starting October 1, 1998)
  - Marisol Koslowsky
  - Adrian Lew

Chapter 4

First Principles Materials Properties for Simulating the Dynamic Response of Materials

4.1 Goals for materials properties research

The Caltech facility for simulating the dynamic response of materials aims:

- to develop the methods, software, and parameters for full physics, full chemistry simulations in three-dimensions and
- to put these methods and software into a facility in which engineers and designers can simulate their experiments computationally with validated accuracy and precision.

Because many critical parameters are extremely difficult to obtain from experiment, it is essential that we develop first principles methods sufficiently accurate that the results can be trusted in the absence of experiments. Yet the software, hardware, and methodology must be sufficiently efficient to obtain the answers quickly enough for the designer to rapidly explore alternative designs.

Consequently, the Materials Properties (MP) effort has four thrusts:

1. Provide today the most *accurate parameters* describing the materials properties required for the three key applications in the facility
   - denotation of high explosives (HE)
   - solids subjected to large dynamical loadings (SD)
   - fluids undergoing turbulence and mixing due to shock (CT)
2. *Validate* the accuracy by comparison to experiment under conditions relevant for HE, SD, and CT applications and by comparing to higher level theory on prototypical systems

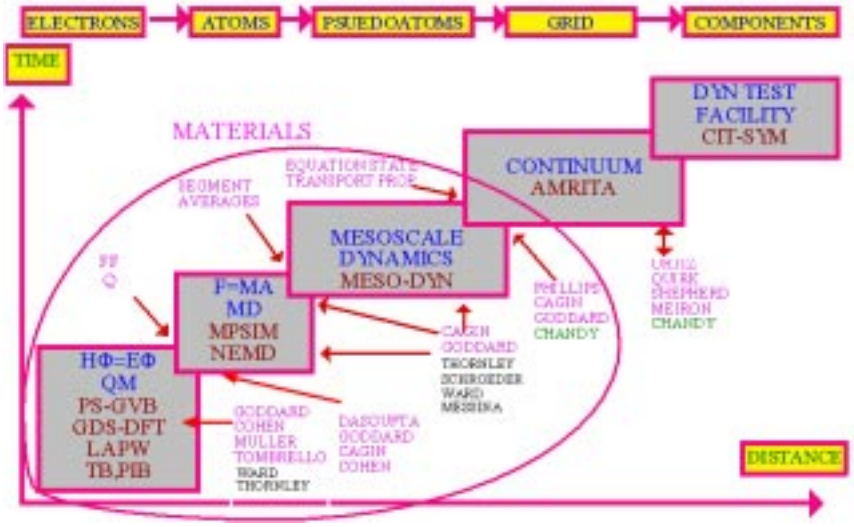

Figure 4.1: Simulation hierarchy from QM to MD to mesoscale to macroscopic.

3. Develop the *new technology* required to predict these properties solely from first principles

4. Implement this technology for optimal performance on massively parallel computing architectures and evolving computer science tools.

To bridge the enormous gap in length and time scales from the most fundamental level [quantum mechanics, QM)], through the atomic level [molecular dynamics (MD)], through the meso scale, to the continuum and macroscopic scales we use a hierarchical strategy as indicated in Figure 4.1. This allows us to focus on the appropriate entities at each level (electrons, atoms, segments, grid points) and to find ways for averaging the parameters from the more fundamental level as input to the next coarser level.

These four thrusts are being carried out simultaneously. For the first year the resources available for MP have been focused more on the first thrust so that the development of HE, SD, CT applications can proceed with the best current parameters. During the second year, we will increase the emphasis on the second and fourth thrusts to establish criteria for accuracy and to allow accurate predictions on larger more complex systems using the state-of-the-art ASCI hardware facilities. In addition, we will initiate an additional emphasis on the third thrust (new methods).

4.2 Materials properties milestones

Our first year milestones included

- quantum mechanical determination of mechanical properties of metals
- development of force fields (FF) for predicting structures and properties of metals (particularly Fe) as a function of temperature and pressure

- extracting from QM force fields for HE materials (particularly TATB)

During the first year, we accomplished these goals. Also, in response to the needs of the various applications, we added further milestones, including

- Developing FF for ceramics as a function of temperature and pressure (for SiO_2, Al_2O_3, MgO)
- QM calculations on Ta metal as a function of temperature and pressure
- Extension of FF methods to describe phase changes in ceramics, metals, and covalent (carbon) systems
- Extension of HE materials of interest to include HMX.

Thus, we have developed accurate FF for ceramics and oxides valid for high pressure and high temperature regimes. We also initiated projects pertaining to second and third year milestones such as development of QM based FF for ceramics and metals, development of MD software for hypervelocity impact and shock wave propagation.

4.2.1 Material properties research for HE applications

In the first year, MP research to support high explosives applications aimed at characterizing the

- equation-of-state for HMX and TATB
- properties of the kel-F binder
- reaction dynamics and molecular processes in shocked HMX and TATB, vibrational analysis of rapid post shock events and shock compression simulations through MD.

4.2.2 Material properties research for SD applications

In the first year, MP activities to support solid dynamics applications focused on

- equation-of-state of metals (Ta, Fe) and ceramics (SiO_2, Al_2O_3, and MgO)
- phase transitions in metals, carbon (graphite, diamond), and ceramics
- determination of the constitutive parameters (such as the elastic constants) at elevated pressure and temperatures for metals, alloys, and ceramics
- thermodynamic properties, and behavior of metals and ceramics under large compressive and tensile loads and large strain rates.

4.2.3 Material properties research for CT applications

In the first year, MP projects pertaining to compressive turbulence and fluid dynamics applications focused mainly on determining the properties of dense fluids, including equation-of-state and transport properties (viscosity, diffusion, and thermal conductivity) at elevated pressure and temperature.

4.2.4 Material properties research and development for software integration (SI) and computer science (CS)

During the first year, the MP activities to support the software integration effort, focused on

- porting the QM software (Jaguar, QM/MSC) developed at Caltech (Goddard lab) to ASCI machines and initial attempts at parallelization
- porting the MD software (MPSim) developed at Caltech (Goddard lab) to ASCI machines and refinement of the parallelization.

We initiated two MP-computer science collaborations. With Ward and Dongarra of U. Tennessee, we are using math libraries to parallelize the QM code. With Thornley (Caltech) we implemented S-threads (developed by Chandy and Thornley) into MPSim to use on the Intel Quad Pentium Pro system.

4.3 New methods and software for MP

4.3.1 Quantum mechanics (QM)

For QM the focus in methods during the first year has been on:

- High accuracy for large systems
- Fast results for large systems
- Periodic systems
- Solvation effects through Poisson Boltzmann (PB) and Generalized Born (GB) solvers.

4.3.1.1 Finite Systems

An important aspect of the Materials Properties efforts during year one has been to make the QM programs scale efficiently on parallel supercomputers. This efficiency is necessary because of the many materials properties that must be computed during the course of the ASCI-ASAP program and because of the large size of the computations necessary to accurately compute these properties. This section will discuss progress made along those lines.

The Materials Properties group uses QM software to model both finite and periodic materials. For finite molecules the workhorse is the Jaguar program suite, developed over the

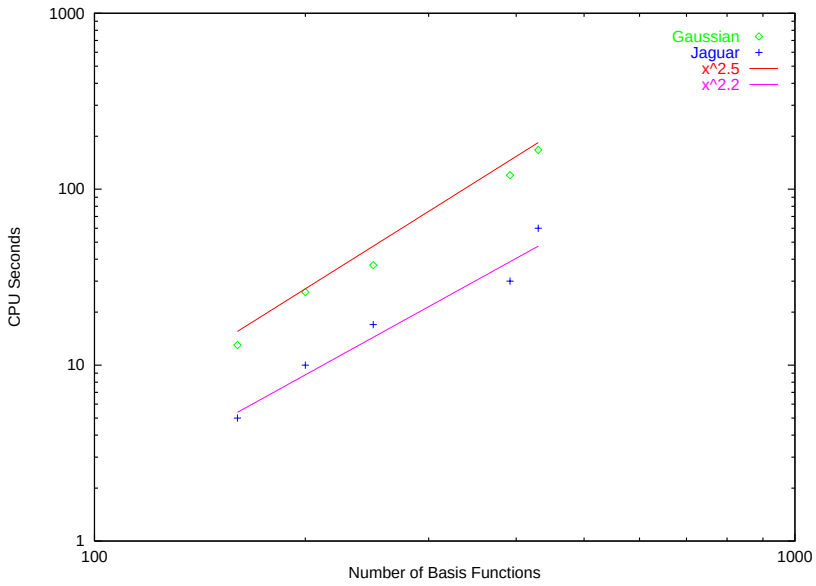

Figure 4.2: Jaguar scaling of the Jaguar QM program (MP2 calculations) with molecular size compared to a typical *ab initio* quantum chemistry program (Gaussian). The data are displayed as a log-log plot.

last 10 years in a collaboration between Caltech, Columbia University, and Schrödinger, Inc. Jaguar differs from other quantum chemistry program suites in that significant work has gone into using numerical techniques that scale efficiently for large systems while retaining sufficient accuracy. This involves multigrid and dealiasing strategies that dramatically improve the scaling for large systems. As a result Jaguar is over 10 times faster than standard programs (e.g. Gaussian and Sparten) for small systems ($\sim$300 basis functions) and scales much better with size, as demonstrated in Figure 4.2. Jaguar is super-fast for both *ab initio* quantum chemistry computations (HF, MP2) and density functional theory (DFT) computations. Special features of Jaguar are fast accurate calculations of solvation effects (using Poisson-Boltzmann and generalized Born methods) and of NLO properties.

We (in collaboration with Columbia and Schrödinger) have initiated the parallelizing of Jaguar. The initial work (on the IBM SP2 and SGI Origin architectures) used a combination of MPI and IBM proprietary message passing libraries. Current parallel performance is shown in Figure 4.3.

Over the next year we will continue the parallelizing of Jaguar by

- replacing the diagonalization step with a divide-and-conquer approach (see below),
- introducing multithreaded approaches to speed performance on shared memory architectures, and
- porting the MPI version of Jaguar to the Blue Mountain and ASCI Red platforms.

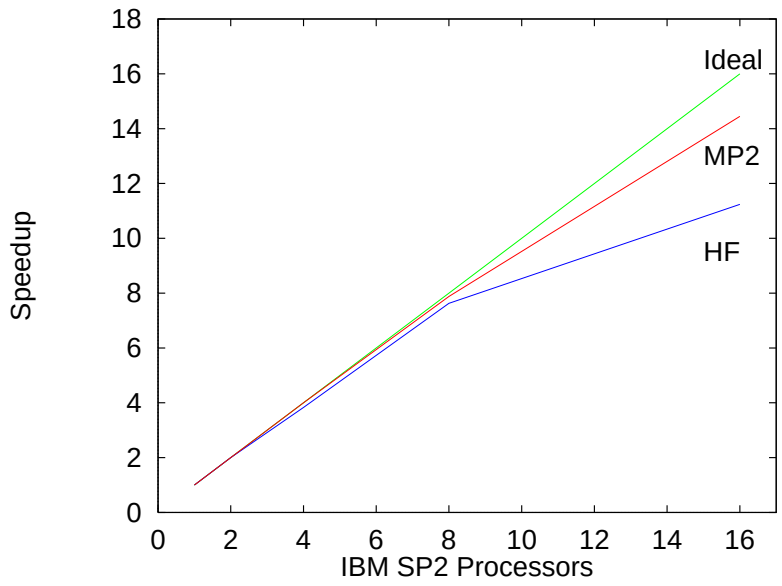

Figure 4.3: Parallelization efficiency of Jaguar (on an IBM SP2 platform).

4.3.1.2 Periodic systems

For quantum mechanical computations on periodic systems (bulk crystals and surfaces), Goddard and coworkers [77] had developed the Gaussian dual space DFT code (GDS/DFT) which uses Gaussian basis functions for accuracy in chemical reactions and for which construction of the Kohn-Sham Hamiltonian scales linearly with size. However, GDS/DFT was limited to single processor systems. Sandia National Laboratories had developed a similar DFT program using Gaussian basis functions but which had been optimized for large parallel applications, as demonstrated in Figure 4.4.

The MP team at Caltech has agreed to incorporate their methodologies (from GDS-/DFT and elsewhere) into Quest for use in the ASCI project. Licensing agreements between Caltech and Sandia have been established which allow the MP team to use Quest, and over the next year we will actively develop Quest in collaboration with Sandia.

In addition, Cohen is developing a Multibasis approach that, like Quest, will be suited to large, parallelized computations, but that will use plane wave basis functions as the primary basis set.

4.3.1.3 Advanced algorithms for large finite systems

As part of the ASCI-ASAP project, we are also developing new algorithms suitable for still larger quantum mechanical computations.

There are two "expensive" parts of a quantum chemical computation:

- formation of the Hamiltonian or Fock matrix, which scales as $\mathcal{O}(N^4)$, but which can be reduced to $\mathcal{O}(N^2)$–$\mathcal{O}(N)$ with appropriate cutoff methods and numerical techniques, and

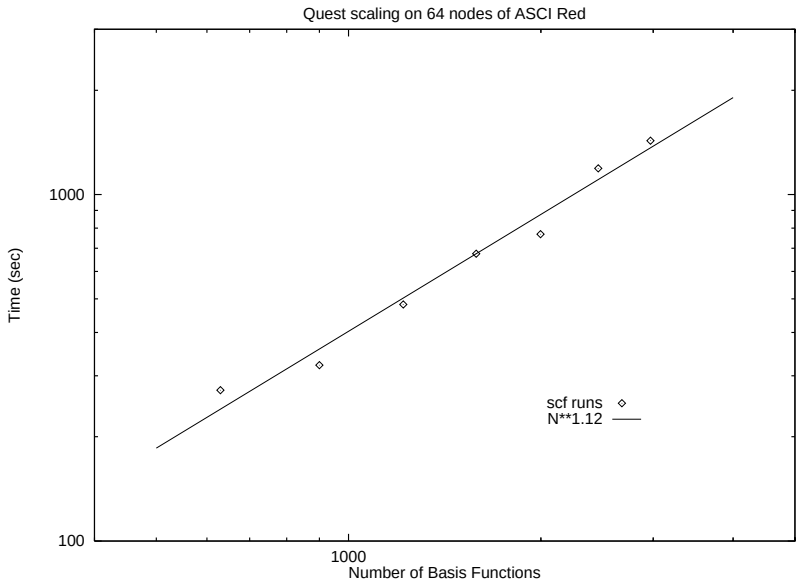

Figure 4.4: Scaling efficiency of the Sandia Quest QM program for periodic systems. The line shows the $N^{1.2}$ scaling achieved by Quest.

- diagonalization of the Hamiltonian, which scales as $\mathcal{O}(N^3)$ but which is much more difficult to reduce to $\mathcal{O}(N^2)$ or $\mathcal{O}(N)$.

For *ab initio* computations using atom-centered basis functions, the formation of the Hamiltonian is sufficiently expensive, that the $\mathcal{O}(N^2)$ Hamiltonian formation step is significantly more expensive than the full diagonalization even through the latter scales as $\mathcal{O}(N^3)$. However, with the ASCI computers it is practical to consider systems sufficiently large that the diagonalization step dominates. Indeed for the more approximate QM methods used on the largest systems and for plane-wave basis sets, the diagonalization step is already dominant. Hence, we initiated a project to use linear algebra techniques to accelerate the diagonalization process, in particular, using banded matrix solvers.

4.3.1.3a Results for Banded Matrix Solvers As a model system, we considered 3 to 6 $C_{15}H_{32}$ alkane chains. These systems range in size from 141 to 282 atoms, and 281 to 562 basis functions. For the largest system, the Fock matrix is banded as shown in Figure 4.5. The LAPACK symmetric diagonalization routine DSYEV takes 93% of the total computation time for a semi-empirical computation on this system.

Table 4.1 shows preliminary results for using three diagonalizers: the LAPACK symmetric diagonalizer DSYEV, a banded matrix diagonalizer (using two different values of the bandwidth, 10 and 60), and a block diagonalizer that takes advantage of the fact that the matrix for this case is block diagonal (not true of Fock matrices in general). Here we see that band diagonalization reduces the scaling significantly.

Although banded matrix diagonalizers decrease the scaling of the diagonalization step from $\mathcal{O}(N^3)$ to $\mathcal{O}(mN^2 + m^2N)$, where m is the band width, we see that these techniques

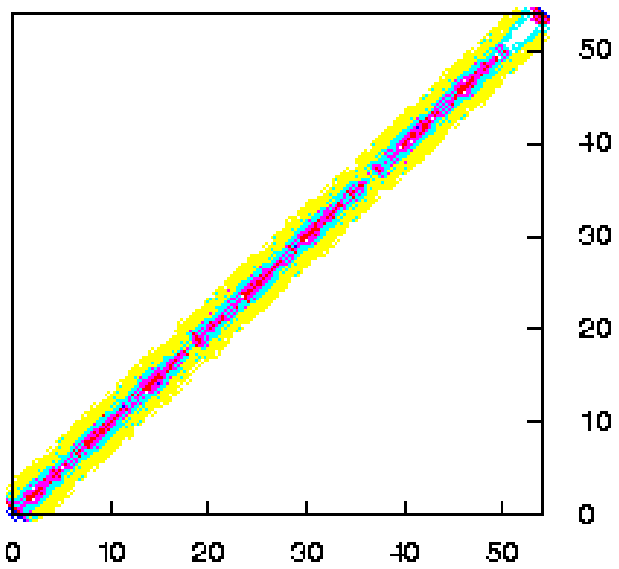

Figure 4.5: The elements of the Fock matrix, showing the banded structure typical of semi-empirical techniques for a system with 562 basis functions. *ab initio* and DFT techniques also lead to similar bands. Here red indicates the largest element, blue the next largest, and yellow smaller but significant, the width is about 50.

Method	3 Alkane Chains	6 Alkane Chains	Scaling
Symmetric Diagonalization	8.73	93.63	3.42
Band Diagonalization ($m = 60$)	70.89	364.38	2.36
Band Diagonalization ($m = 10$)	14.76	69.63	2.24
Block Diagonalization	2.16	8.43	1.96

Table 4.1: Computational times for diagonalization of the Fock matrix of a semi-empirical quantum chemistry calculation.

do not have an advantage until $m < \sqrt{(N)}$.

4.3.1.3b Future Directions—Divide and Conquer The block matrix diagonalizer showed the best performance, but this technique is not generally applicable to quantum chemical systems. In the upcoming year we plan to develop new approaches that will cast the Fock matrix into a form that is as block diagonal as possible. These techniques, known as divide-and-conquer methods, tend to depend on the specific application. We will experiment with schemes to allow the techniques to be as efficient as possible for general cases.

4.3.2 Force fields

Over the last decade, Goddard and coworkers have developed a series of force fields for organics, proteins, polymers, and semiconductors. These force fields (Dreiding [72], UFF, [78] MCXX, [79] biased Hessian [80]) have led to good descriptions of structural, mechanical, and vibrational properties of these systems. The challenge now is to obtain FF that can describe the processes of bond breaking and forming involved in phase transitions and melting, plasticity and fracture, etc. Such processes are critical to describing the dynamic response of materials. Thus, the MP developments in FF have focussed on treating such bond order dependent processes. The main activities, the first year, were:

- Developing accurate valence FF for polymers and high explosives based on high level QM calculations. This is described in 4.4.1
- Developing Morse-Stretch variable charge (MS-Q) FF for phase transitions in ceramics and applying it to oxides of Si, Al, Mg, Ca, B, Zr, and Na.
- Developing the Q-SC many-body FF for phase transitions in fcc and bcc transition metals.
- Developing the reactive bond-order-dependent FF for phase transitions in covalent systems (graphite, diamond, hydrocarbons) generalized to include long-range interactions systematically.
- Developing the qMS-Q FF for ceramics using only first principles QM data.

4.3.2.1 Morse stretch variable charge (MS-Q) FF for ceramics

Because electrostatics play an essential role in determining the structure and properties of ceramics, we consider that the first priority of the FF is to produce plausible charges. Since the charges may depend on the distances, angles, and ligancy, we consider that *the charge must be allowed to readjust to the instantaneous configuration of the atoms.* To do this we use the charge equilibration (QEq) procedure developed by Rappé and Goddard [71] and used in many applications on organic and inorganic systems. Rather than keeping the charges fixed during the dynamics, as in all previous calculations, we now allow the charges to adjust to the instantaneous geometric configuration of the atoms.

	R_o (Å)	D_0 (kcal/mol)	γ
O-O	3.7835	0.5363	10.4112
Si-Si	3.4103	0.2956	11.7139
Si-O	1.6148	45.9970	8.8022

Table 4.2: Morse Stretch Force Field Parameters for SiO_2.

In QEq the charges are determined by requiring that the chemical potential χ_A be equal on all atoms where χ_A is a function of the charges on all the atoms of the system

$$\chi_A\left(Q_1,\ldots,Q_N\right) = \chi_A^\circ + \sum_B J_{AB}\left(R_{AB}\right) Q_B \ .$$

Here, the atomic parameters χ_A° and J_{AA}^o correspond physically to the electronegativity and hardness of the atom and are obtained from the valence-averaged atomic ionization potential (IP) and electron affinity (EA) as $\chi_A^\circ = (IP_A - EA_A)/2$ and $J_{AA}^\circ = (IP_A + EA_A)$. $J_{AB}(R)$ is the shielded Coulomb potential assuming that the charge Q_A on atom A is spherical with radius R_A based on the radius of the atom in the standard state ($R_{Si} = 1.176$ Å and $R_O = 0.669$ Å). The shape of the charge distribution is based on an ns Slater orbital, $\Phi_{n\zeta}^{slat} = N_n r^{n-1} e^{-\zeta r}$, where the orbital exponent ζ_{AB} is given by $\zeta_{AB}^{-1} = (R_A/n_A + R_B/n_B)$. The asymptotic limits of $J_{AB}(R_{AB})$ are

$$J_{AB}(R) = \begin{cases} 1/R & \text{as } R \to \infty \\ J^o & \text{as } R \to 0 \end{cases} \quad .$$

Thus, J_{AB} has the form of a simple Coulomb potential for large R, but is properly shielded for short distances. The QEq parameters used for Si and O are given in Table 4.3. The average charges calculated for various forms of SiO_2 are shown in Table 4.4.

The non-electrostatic interactions (short-range Pauli repulsion, covalency, dispersion, etc.) are included via a simple two-body Morse-Stretch (MS) term,

$$U_{ij}^{MS}\left(R_{ij}\right) = D_0\left[e^{\gamma\left(1-\frac{R_{ij}}{R_0}\right)} - 2e^{\frac{\gamma}{2}\left(1-\frac{R_{ij}}{R_0}\right)}\right] \quad .$$

The MS parameters for Si-O, O-O, and Si-Si, were optimized to describe the properties (density, cohesive energy, elastic moduli, etc.) of $\alpha-$quartz and stishovite as representative four- and six-coordinate polymorphs. We refer to this as the MS-Q FF (MS plus charge). Table 4.2 gives the optimum parameters for D_0 (bond strength), R_0 (bond length), and γ (dimensionless force constant).

Using QEq charges and the Morse-stretch potentials, we studied the melt, glass, and all known polymorphs of silica. Some results for shock compression of α-quartz and silicon glass (to form stishovite) are described in Section 4.4.2.5. The structure of silica glass formed from heating and quenching crystalline SiO_2 are described in Section 4.4.2.6

	χ (eV)	J (eV)	R (Å)
O	8.741	13.364	0.669
Si	4.168	6.974	1.176

Table 4.3: QEq parameters for O and Si

	Number of Molecules	Si	O
α-quartz	3	1.318	−0.659
β-quartz	3	1.293	−0.647
Stishovite	2	1.397	−0.699
β-tridymite	4	1.217	−0.609
α-cristobalite	4	1.281	−0.640
β-cristobalite	8	1.216	−0.608
Keatite	12	1.290	−0.645
Coesite	16	1.339	−0.670
Glass[a]	216	1.318	−0.659
Glass[b]	216	1.313	−0.656
Glass[c]	200	1.328	−0.664

Table 4.4: Average QEq charges for the experimental structures of eight silica polymorphs and glass structures. [a]Starting from β-cristobalite structure (cooling rate 100 K/4ps), [b]Starting from β-cristobalite structure (cooling rate 100 K/8ps), [c]Starting from random structure (cooling rate 100 K/4ps).

4.3.2.2 The Q-SC many-body force fields for metals

We developed the quantum Sutton-Chen (Q-SC) force fields (FF) for FCC transition metals [63] using a Sutton-Chen [64, 65] type many body representation of the metal-metal interactions. Our approach includes the zero-point energy contribution using quasi-harmonic theory. Q-SC leads to accurate properties of FCC transition metals and their alloys under various conditions [66, 67, 68]. Using a similar approach we have now developed the Q-SC FF for BCC transition metals. The many-body FF has the form

$$U_{total} = \sum_i U_i = \sum_i D \left[\sum_{j \neq i} \frac{1}{2} V(r_{ij}) - c\sqrt{\rho_i} \right] \tag{4.1}$$

where $V(r_{ij})$ describes the short-range repulsion due to the Pauli principle as

$$V(r_{ij}) = \exp(-\alpha r_{ij}) \tag{4.2}$$

and ρ_i represents the many-body metallic cohesion which depends on the density function ϕ

$$\rho_i = \sum_{j \neq i} \phi(r_{ij}) \tag{4.3}$$

Here $\phi(r_{ij})$ has the form

$$\phi(r_{ij}) = \begin{cases} \phi_1(r_{ij}) = \exp(-\beta_1 r_{ij}) - \gamma_1 \exp(\beta_2 r_{ij})) & \text{, if } r_{ij} \leq r_1 \\ \phi_2(r_{ij}) = \gamma_2 \exp(-\beta_3 r_{ij})) & \text{, if } r_2 > r_{ij} > r_1 \end{cases} \tag{4.4}$$

where $\phi_1(r_1) = \phi_2(r_1)$ and $\phi_1'(r_1) = \phi_2'(r_1)$ to ensure a smooth connection.

This style of function is similar to the Rosatto et al [69] (RGL) potential, which is based upon the second-moment approximation of tight-binding QM calculations. Our density function ϕ has two terms to prevent the instability of BCC with respect to FCC structure (well known for the RGL potential form).

In the Q-SC FF, the free parameters D, c, α, β_1, β_2, γ are optimized for the pure element (using the modified Levenberg-Marquardt least-squares method) to minimize the difference between theoretical and experimental values of the following properties at zero temperature: bond distance, cohesive energy E_{coh}, elastic constants c_{11}, c_{12}, c_{44}, and unrelaxed vacancy formation energy $E_{VF,unrelaxed}$. Then for alloys we use simple combination rules so that no new parameters are required. Table 4.5 lists the optimized parameters for all metals.

We are using Q-SC parameters to study the lattice dynamics of Ta and Fe (Section 4.4.2.3) and have used it to study plasticity in Ni and NiCu crystal (Section 4.4.2.4) and viscosity of liquid metals (Section 4.4.3).

4.3.2.3 Extended bond order dependent - FF

We developed a general approach for describing chemical processes (bond breaking and bond formation) in materials using FF that properly describe multiple bonds at small distances while describing non-bond (Coulomb and van der Waals) interactions at long distances.

	D ev	c	α Å^{-1}	β_1 Å^{-1}	β_2 Å^{-1}	γ_1
V	3.3098E+02	4.1090E−03	8.37395	0.56263	7.33955	4.7192E−07
Cr	3.7953E+01	6.0126E−03	5.86606	−3.14000	3.52688	4.9373E−01
Fe	3.2903E+04	6.5937E−05	14.37847	1.80938	37.97944	3.8388E−31
Nb	3.4236E+02	1.3743E−02	7.59355	1.85859	11.95463	1.5132E−11
Mo	1.5876E+03	8.2951E−04	9.86355	0.13816	9.78785	1.7358E−08
Ta	2.5190E+03	1.3326E−03	10.18061	1.29765	6.68906	4.4898E−07
W	1.6568E+03	1.1904E−03	9.49126	0.28599	8.17038	2.3762E−07

Table 4.5: The Q-SC many-body FF for BCC transition metals. Note that γ_2 and β_3 are determined by the match condition at R_1. Here $r_1 = 1.70a$ and $r_2 = 2.02a$.

This approach is referred to as the generalized extended empirical bond-order dependent (GEEBOD) FF.

The Brenner bond-order dependent FF sums over all pairs of atoms, with the total potential energy of a system given by

$$V^B = \sum_i \sum_{j>i} \left[V_R\left(r_{ij}\right) - \bar{B}_{ij} V_A\left(r_{ij}\right) \right],$$

where V_R and V_A are the repulsive and attractive part of the pairwise binding potential, respectively. They are taken to have the form of a general Morse potential

$$V_R\left(r_{ij}\right) = f_{ij}\left(r_{ij}\right) \frac{D^e_{ij} S_{ij}}{S_{ij} - 1} \exp\left[-\sqrt{2S_{ij}} \beta_{ij} \left(r_{ij} - R^e_{ij} \right) \right]$$

$$V_A\left(r_{ij}\right) = f_{ij}\left(r_{ij}\right) \frac{D^e_{ij} S_{ij}}{S_{ij} - 1} \exp\left[-\sqrt{\frac{2}{S_{ij}}} \beta_{ij} \left(r_{ij} - R^e_{ij} \right) \right]$$

where

$f_{ij}(r)$ is a cutoff function that explicitly restricts the interaction to nearest neighbors. The bond-order parameter $\bar{B}_{ij}$ is written as

$$\bar{B}_{ij} = \frac{B_{ij} + B_{ji}}{2} + F_{ij}\left(N^H_i(t), N^C_j(t), N^{conj}_{ij} \right)$$

Thus, $\bar{B}_{ij}$ depends on the environment around atom i and j and implicitly contains many-body information. The values of the fitting parameters D^e_{ij}, S_{ij}, β_{ij}, and R^e_{ij}, etc., are taken as in original Brenner parameter set.

Physically, the chemical bond involves the overlap of partially occupied atomic orbitals on nearby atoms where high overlap leads to strong bonds. Because of the Pauli principle, there are two electrons in a normal chemical bond. The interaction between orbitals of *different bonds* is very repulsive for short distances (Pauli principle) and attractive for larger distances (dispersion). The net effect is that non-bond (NB) interactions dominate at a much larger

distance than do chemical bonding (valence) forces. Based on these considerations, we write the total potential energy of a system as follows

$$V^{tot} = \sum_i \sum_{j>i} \left[V_{ij}^V + P_{ij} V_{ij}^{NB} \right]$$

where V_{ij} and P_{ij} are functions of r_{ij}. The superscript V denotes the valence short-range terms (e.g., Brenner) and NB denotes the long-range NB terms. Here $P_{ij} = P_{ji}$ is a screening function that properly weights the NB contribution in the total energy. In this paper we take the form of the screening function to be

$$P_{ij} = f\left(V_{ij}^V, V_{ij}^V\right) \prod_{k \neq i,j} f\left(V_{ik}^V, V_{kj}^V\right)$$

with

$$f(x,y) = \begin{cases} \exp(-\gamma x^2 y^2) & \text{if } x < 0 \text{ and } y < 0 \\ 1 & \text{otherwise} \end{cases}$$

Here γ is a scaling parameter; since the results presented here are not sensitive to the value of γ, we have used $\gamma = 1$.

The screening function eliminates NB interactions between two atoms i, j when they are directly bonded (i.e., $V_{ij}^V < 0$) or when they are both bonded to a common atom k (i.e., $V_{ik}^V < 0$ and $V_{kj}^V < 0$). In both cases, the exponential function P_{ij} becomes negligible small, so that NB interactions do not play a role. Thus, P_{ij} is a mathematical analog to the NB exclusion rules in traditional valence FF. However, the GEEBOD formulation described above is more general and consistent. Unlike normal valence FF the GEEBOD formulation does not use molecular bond information. GEEBOD has been used to study the diamond to graphite phase transition in Section 4.4.2.8

4.3.2.4 FF development future plan

For the MS-Q FF for ceramics, the Q-SC FF for metals, and the GEEBOD FF for covalent systems described above, the parameters were based on fitting experimental data (density, energy, compression, vibrations). Our future work will focus on using accurate first principles QM calculations to optimize the FF with no use of experimental data. This allows us to consider structures not stable at ordinary temperatures and pressure to ensure that the FF is accurate for all T and P.

Thus, for MgO we used QM (DFT GGA) on the B1(NaCl) and B2(CsCl) phases to obtain the qMS-Q FF and then used this FF to predict the equation-of-state (see Section 4.4.2.7).

Similarly we will use the QM-DFT EOS for fcc, bcc, and hcp phases calculations on Ta and Fe to determine defect energies (eg. vacancy formation, surface energies) and energy differences that will be input in determining Q-SC type FF.

We are also using QM calculations to optimize the QEq parameters for a broad set of elements under different ligancy conditions. Then, the *ab initio* DFT/GGA approach will be used to determine the EOS, energetics of possible (in theory and experimentally observed) polymorphs as input for determining non-electrostatic interactions.

4.3.2.5 Progress in molecular dynamics

In MD simulations the FF is used to predict the forces of the N interacting atoms which through solving the coupled sets of the Newton's equations describe the trajectories ($\mathbf{R}_i$, $\mathbf{V}_i$; $i = 1, N$) of the atoms. This ensemble of structures and velocities can then be used to obtain macroscopic properties through the use of statistical mechanics and thermodynamics. For heterogeneous materials such MD simulations may require that thousands to millions of atoms to be considered explicitly. Accurate evaluation of the long-range interactions (electrostatic and dispersion), which decrease slowly with distance, is the most time-consuming aspect for MD simulations of such large systems. This cost is order N^2 for N particles. Thus, a system of 10 million atoms requires the evaluation of 10^{14} terms *each time step*. The standard approach to simplifying such calculations for finite systems has been to ignore the interaction beyond some non-bond cutoff. However, for one million particles this requires maintaining an enormous non-bond list and also leads to errors orders of magnitude too large. For periodic systems such cutoffs leads to unacceptable errors, requiring Ewald approaches which *require* Fourier transforms. This leads to a scaling of $N^{1.5}$, totally impractical for systems with million atoms. Because nanoscale simulations require simulations of millions of atoms, we developed methods and optimized parallel computer programs (MPSim) efficient for high capacity MD. Special features include:

- Cell Multipole Method (CMM) which dramatically reduces the cost of long-range Coulomb and van der Waals interactions while retaining high accuracy. The cost scales linearly with size, allowing atomic-level simulations for million atom systems.

- Reduced Cell Multipole Method (RCCM) which handles the special difficulties with long-range Coulomb interactions for crystals by combining a reduced unit cell plus CMM for interaction of the unit cell with its adjacent cells. The cost scales linearly with size while retaining high accuracy, allowing simulation of crystals having a million atoms per unit cell (the major use is for models of amorphous and semi-crystalline materials).

- Newton Euler Inverse Mass Operator method (NEIMO) for internal coordinate dynamics (e.g., treats torsions only). This allows the solution of the dynamical equations for internal coordinates without inverting the mass tensor (moment of inertia tensor). The cost of NEIMO is linear in the number of degrees of freedom and small compared to other costs for million atom systems. More recently we also developed a new constrained force algorithm (CFA) for massively parallel MD simulation of polymers.

- Advanced MD algorithms to simulate systems under constant temperature and constant pressure conditions.

- Non-Equilibrium MD: We have implemented synthetic equations of motions to simulate various non-equilibrium conditions to predict transport properties such as viscosity, thermal conductivity of materials. Using these methods, we have studied the shear viscosity of metal alloys (see Section 4.4.2.4) and the effect of molecular topology of liquid alkanes on their measured viscosity indices.

- Steady state MD methods are used to simulate non-equilibrium processes such as friction and wear in diamond, metals, and metal oxides. Here, the external work is dissipated through material and coupled to a thermal bath using Langevin equation.

4.3.2.6 MPSim with PB solvation

For many systems the structures and properties are strongly affected by solvent. However, the presence of explicit solvent molecules dramatically increases the cost of the calculations. Thus, it is desirable to represent the effect of the solvent without the necessity of including it explicitly. Recently dramatic progress has been made in using a continuum solvent [Poisson-Boltzmann forces (PBF)] approach to calculate both energies and forces due to the reaction field in the solvent induced by the solute. Here the solvent is reduced to charges and forces on mesh points around the solute(s) and a realistic solvent accessible surface is used to describe the surface of the solute. Indeed accuracies of 0.02 eV in solvation energies have been demonstrated from QM calculations (using Jaguar). We have now implemented this technology into MPSim. This PBF methodology will be tested and optimized over the next year.

4.3.2.7 Lightweight threads for parallel MD

The parallelization in the MPSim program was originally developed on the KSR and reoptimized for SGI Origin 2000 and HP Exemplar. Over the past year John Thornley (CS) has collaborated with the MP group to implement S-threads (lightweight threads) on the Intel Quadpro into MPSim. This leads to a speed-up of 3.6 for 4 processors (see Figure 4.6) for a large scale problem (512,000 atoms rhino virus).

Over the next year we will extend this approach to the QM programs (Jaguar) and will include the S-threads in the PB-F and NEIMO parts of MPSim.

4.4 Applications of MP to simulations of HE, SD, and CT

Materials Properties simulations have been carried out for a number of systems relevant to the HE (see Section 4.4.1), SD (see Section4.4.2), and CT (see Section 4.4.3) applications.

Our accomplishments in the applications area include:

- MD simulation of TATB and HMX high explosives
- simulation of post shock energy redistribution
- QM simulation of metals at high pressures
- MD simulations of phase transition in metals and ceramics
- MD simulations of the viscosity of metal alloys
- development and implementation of new algorithms for MD of hypervelocity impact and atomic level shock processes.

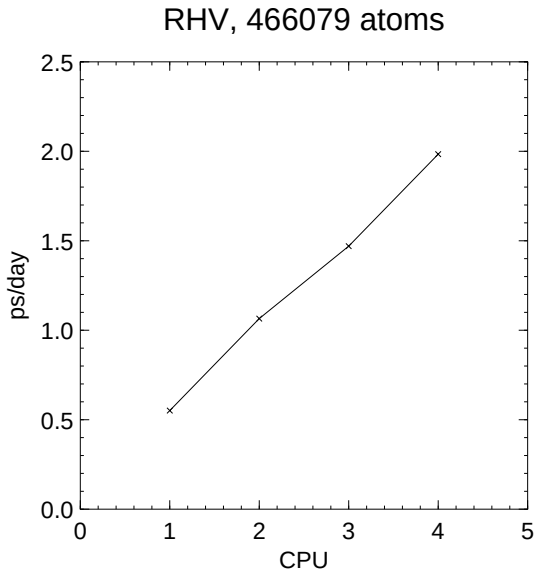

Figure 4.6: Performance of MPSim with Sthreads on the Intel Quadpro computer. This is for the rhino virus capsid (512,000 atoms).

4.4.1 Applications to High Explosives

The first year effort focussed on two key HE materials: HMX and TATB. These calculations used a generic FF (Dreiding [72]) to study

- Density of States,
- Pressure Loading and
- Phase transitions.

Also we started developing a vibrationally accurate FF for DMN, HMX, and RDX using

- DFT (B3LYP) QM calculations on isolated monomers,
- QUEST QM calculations on condensed phase systems

The QM results will be used to obtain a vibrationally accurate FF parameters to study

- Intra- and inter-molecular vibrational energy transfer, phonon - phonon couplings and
- hydrogen-bond effects.

4.4.1.1 Atomic level studies of HMX

HMX exists in four different crystallographic forms

- β, which is stable at normal conditions,

- higher temperature forms α and δ, and
- γ which contains co-crystallized water.

These are shown in Figure 2.1.

The HMX molecule has two stable conformations the chair form (β) and the boat form (α, δ, and γ). We carried out calculations (DFT B3LYP/6-31G**) to show that the gas phase energy for the chair form is lower than the boat form by 0.1 eV (2.2 kcal/mol). The gas phase geometry from QM reproduces the experimental crystallographic geometry with remarkable fidelity (Figure 4.7), within errors expected due to neighboring interactions with other HMX molecules.

The Dreiding FF (Mayo, et al [72]) is a simple generic FF which uses general bonding rules to specify parameters rather than adjusting the parameters to fit experiment. Thus, Dreiding can handle all possible chemical systems based on main group columns of the periodic table. The non-bonded interactions are of the softer exponential-6 form (compared to the steeper Lennard-Jones 12-6 form often used in molecular modeling of biological systems) and describe well the crystal packing for small molecules at low temperature. This FF leads to optimized crystal structures for HMX in very good agreement with experiment, Figure 4.8.

As shown in Figure 4.9, the lattice parameters from Dreiding compare favorably with the experimental data (Ollinger [73]). The cold compression curves predicted for the four different crystal morphologies show differential compressibility, Figure 4.10. The EOS form β-HMX was obtained using both NPT MD (isothermal, isobaric) and NVE MD (adiabatic, fixed volume) as shown in Figures 4.11 and 4.12. The NPT MD shows very slow convergence for the free variable (V), whereas the NVE ensemble shows a much more rapid convergence of the free variable (P). Thus, our EOS work focused on the NVE ensemble. The present results considered just unit cells for short times (20ps or 50ps, respectively) due to the lack of local computing resources. For the next year, the plan is to use the larger ASCI machines at the National Labs for calculations on large supercells for long dynamics times.

We focused first on the grid spacing required for calculation of various thermodynamic properties derived from these EOS (e.g. Gruneissen γ, volume compressibility, thermal expansion coefficient, thermal coefficient of pressure). The pressure range needed is 0-50 GPa (the von Neumann spike). Our computed temperature profile for the HMX reaction zone (Joe Shepherd, personal communication) reaches 1500K, which is a little more than half the currently extrapolated value. This is the temperature range on which we focused. With the NPT ensemble, the cell shape and size are allowed to change. Above 600K, we see evidence of melting (significant distortion of the cell shape), but application of external pressure returns the cell to normal shape and size.

The Dreiding FF does remarkably in describing the frequencies in the 0-200 cm^{-1} region, Figure 4.13. The density of states in the 0-200 cm^{-1} region correlates well with the differential sensitivity of the various high energy density materials, Figure 4.14. This suggests that sensitivity of HE materials involves coupling the shock waves into the low frequency lattice modes, which then need couple to higher frequency intra-molecular vibrations to localize the vibrational energy into bond rupturing modes. The elastic constants and bulk moduli calculated with Dreiding FF also compare well with the recent experimental data from Joe

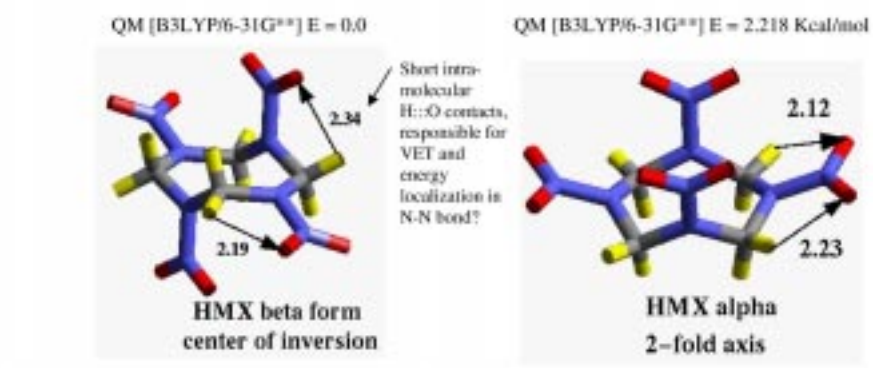

	Experimental Crystal	Gas Phase DFT/6-31G**
N-N	1.354/1.373	1.382/1.401
N-C	1.437-1.472	1.442-1.478
N-O	1.285-1.293	1.224-1.231
N-NO2(inv)	8.0/28.3	7.5/18.6
N-C-N-C	18.1/43.3/101.7/117.1	19.4/43.1/99.3/113.5

	Experimental Crystal	Gas Phase DFT/6-31G**
N-N	1.353/1.366	1.406/1.417
N-C	1.444-1.471	1.458/1.458
N-O	1.214-1.237	1.223/1.224
N-NO2(inv)	3.4/12.2	5.0/20.6
N-C-N-C	64.7/68.2/108.7/105.0	72.2/72.3/93.4/93.6

Figure 4.7: Comparison of energetics and geometry of chair and boat forms of HMX from DFT calculations and experimental X-ray structure.

Zaug of Lawrence Livermore [presented at the $11th$ Detonation Symposium in Snowmass, CO (1998)], Figure 4.15.

Most engineering calculations have considered the specific heat c_v as constant. Since specific heat has a strong dependence on temperature, we have used the vibrational frequencies from our FF (and *ab initio* calculations on single molecule) to calculate the temperature dependence of the specific heat, Figure 4.16. The rotational and translational energy levels are fully populated except at the lowest temperatures. For the molecular crystal, we find that 125 points in the Brillouin zone is sufficient for convergence of the specific heat.

To develop a vibrationally accurate FF for HMX, we started with developing a valence FF for the smaller dimethyl-nitramine $(CH_3)_2$-NNO_2 molecule. We have used DFT (B3LYP/6-31G**) QM to calculate the molecular geometry (Figure 4.17) and vibrational frequencies (Figure 4.19) and used the experimental frequencies to constrain the FF parameters to reproduce the experimental data. The final optimized FF reproduces the molecular crystal parameters quite well, Figure 4.18.

4.4.1.2 Atomic level simulations on TATB

TATB, 1,3,5-triamino-2,4,6-trinitrobenzene (see Figure 2.7), is an insensitive high explosive.

The equation-of-state of TATB was calculated using NPT (constant pressure and constant temperature) molecular dynamics with three different FF:

- Dreiding with LJ non-bond,
- standard Dreiding with Exp6 non-bond, and
- a special planar FF Dreiding.

	HMX-β		HMX-α	
	Experiment	Dreiding Exp-6	Experiment	Dreiding Exp-6
N-N	1.364(l)/1.373(s)	1.329(s)/1.332(l)	1.353(s)/1.366(l)	1.31
N-C	1.437/1.448/1.455/1.472	1.441/1.443	1.444/1.448/1.451/1.471	1.441/1.444
N-O	1.205/1.209/1.221/1.233	1.204/1.206	1.214/1.223/1.236/1.237	1.2
O-N-O	125.5/126.7	115.2/116.1	124.6/124.9	115.6
O-N-N	115.9/116.2/117.4/117.9	122.9/123.8	116.4/117.2/118.6/118.8	122.2
N-N-C	115.1/117.4/118.2	121.5/122.4	115.9/119.2/119.3/119.6	119.3/119.6/119.6/121.1
C-N-C	122.4(l)/123.8(s)	115.1(s)/116.4(l)	119.6/123.7	120.1/121.9
CH::O-N-O	2.192/2.337	2.343/2.432	2.117/2.229	2.245/2.272

	HMX-β			HMX-α		
Cell Params	Expt.	Dreiding Exp-6	% Error	Expt	Dreiding Exp-6	% Error
a (A)	6.54	6.603	-0.96	15.14	14.448	4.57
b (A)	11.05	11.094	-0.40	23.89	24.383	-2.06
c (A)	8.70	8.94	-2.76	5.91	5.809	1.76
α	90.0	90.00		90.0	90.0	
β	124.3	125.55	-1.01	90.0	90.0	
γ	90.0	90.00		90.0	90.0	
Volume (A**3)	519.4	532.799	-2.58	2138.7	2046.46	4.31
σ (gm/cc)	1.894	1.846	2.53	1.839	1.922	-4.51

Figure 4.8: Comparison of optimized Dreiding crystal parameters with experimental values.

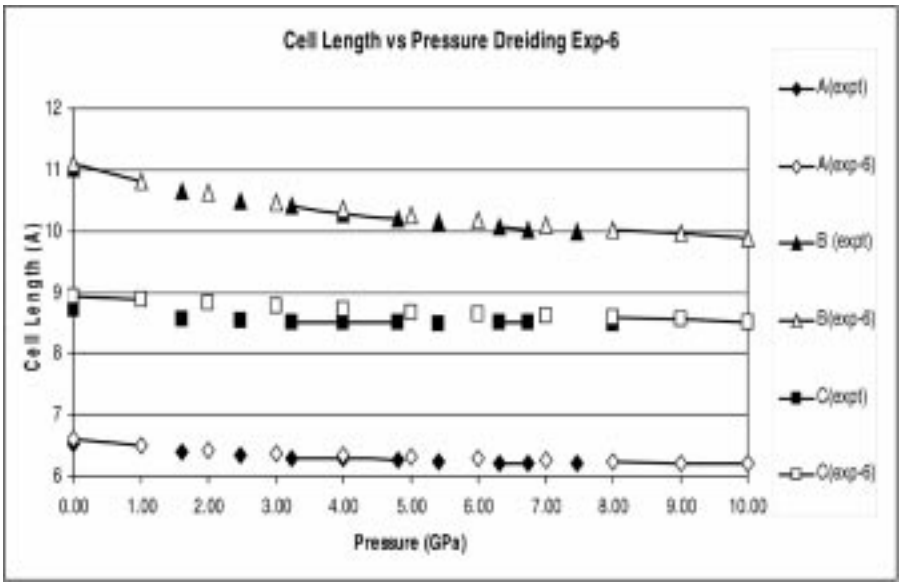

Figure 4.9: Comparison of calculated cold compression curve with experimental data from Ollinger [73]

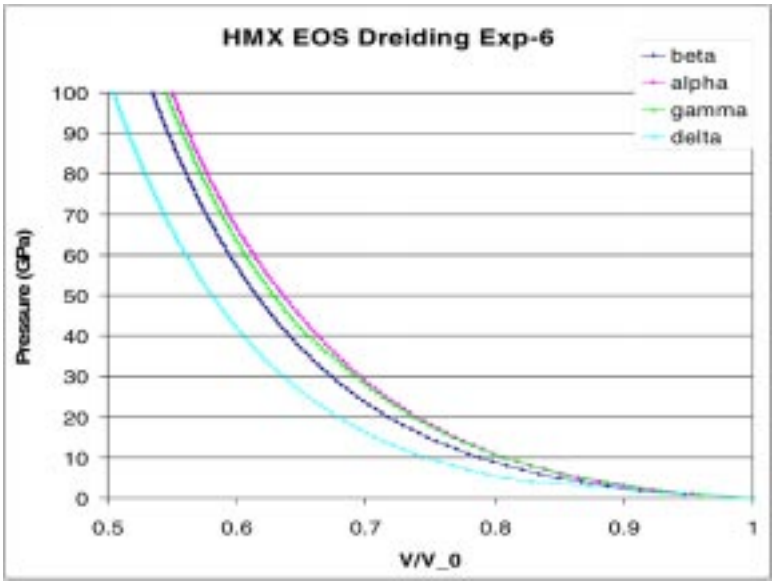

Figure 4.10: Compressibility of the 4 different crystal forms of HMX. These calculations are normalized to V_0, the value at $T = 300$K and $P = 0$.

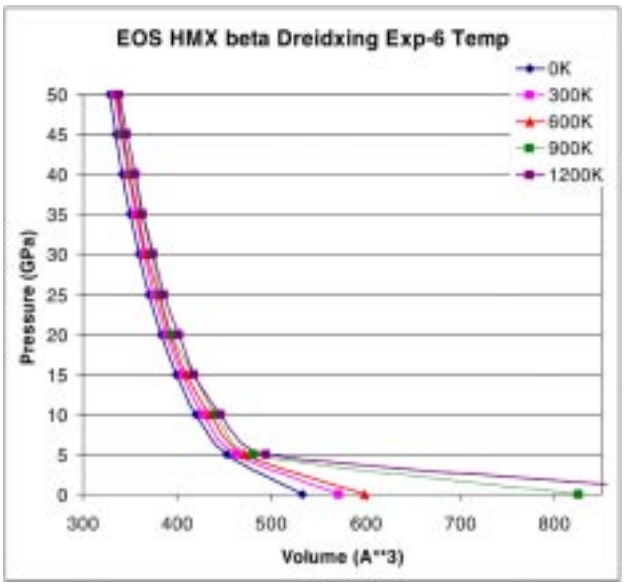

Figure 4.11: EOS of HMX (4 phases) from NPT MD.

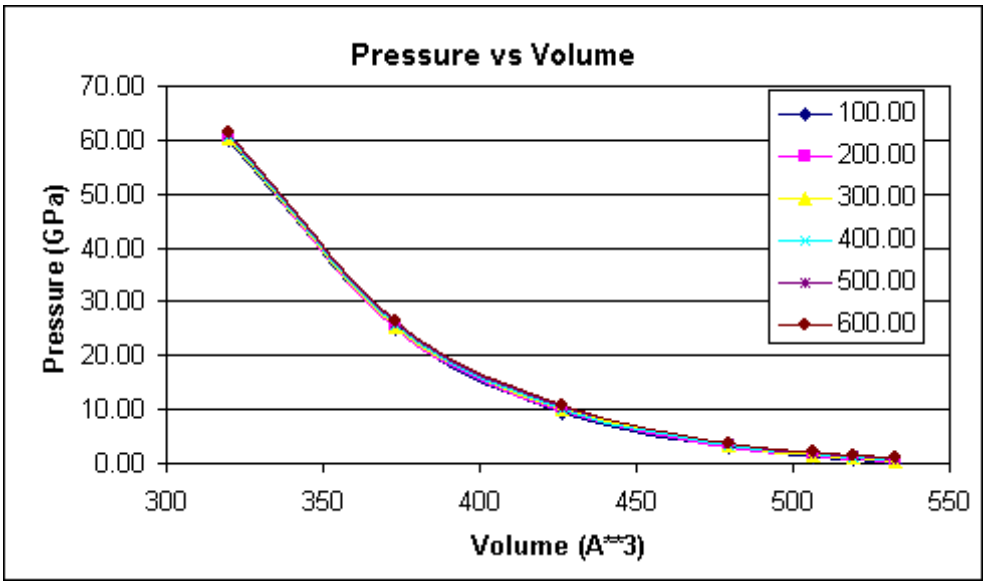

Figure 4.12: EOS of HMX (4 phases) from NVE MD.

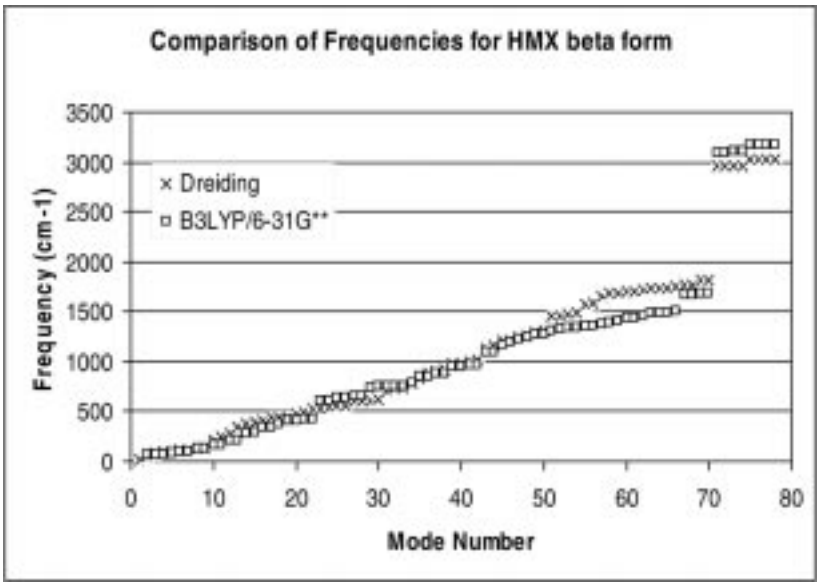

Figure 4.13: Vibrational frequencies for a single HMX molecule from the Dreiding FF and from QM (B3LYP/DFT).

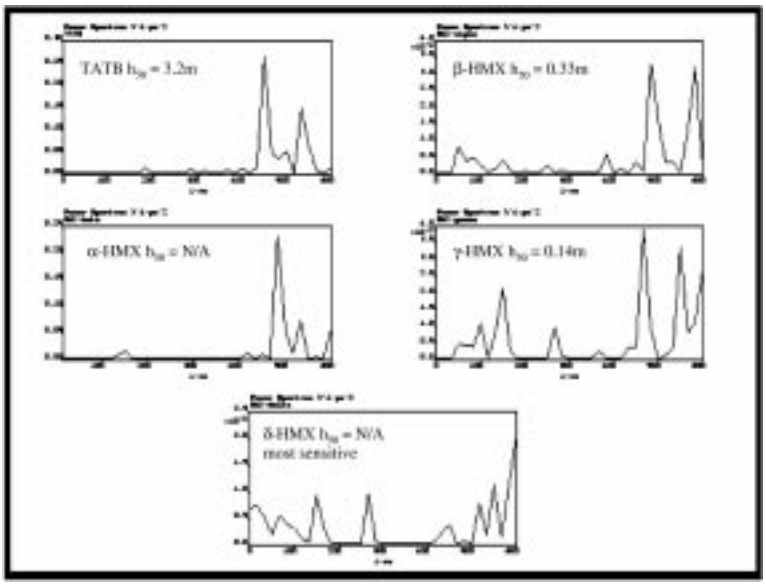

Figure 4.14: Vibrational density of states (using Dreding FF) for 4 phases of HMX and TATB. Also shown is the impact sensitivity. An increased number of modes in the 200 cm^{-1} region correlates with increased sensitivity.

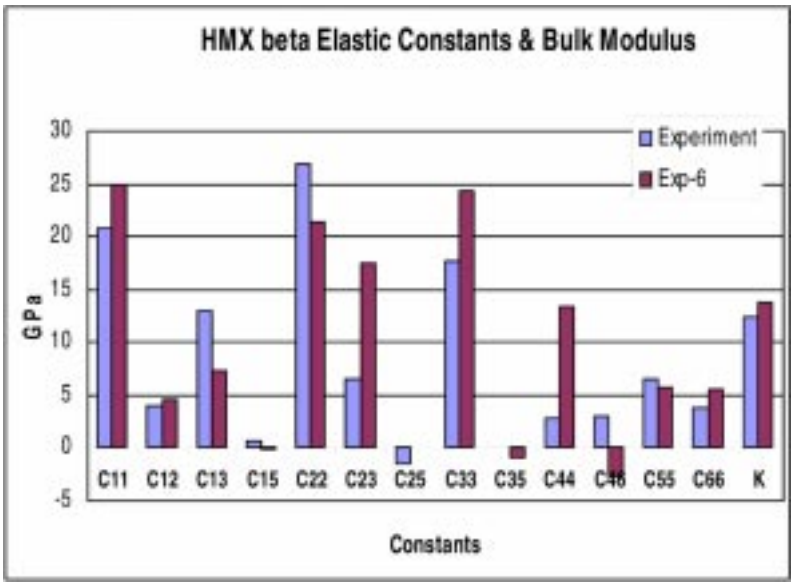

Figure 4.15: Elastic constants, bulk modulus, versus k for β-HMX. From Dreiding FF and from experiment.

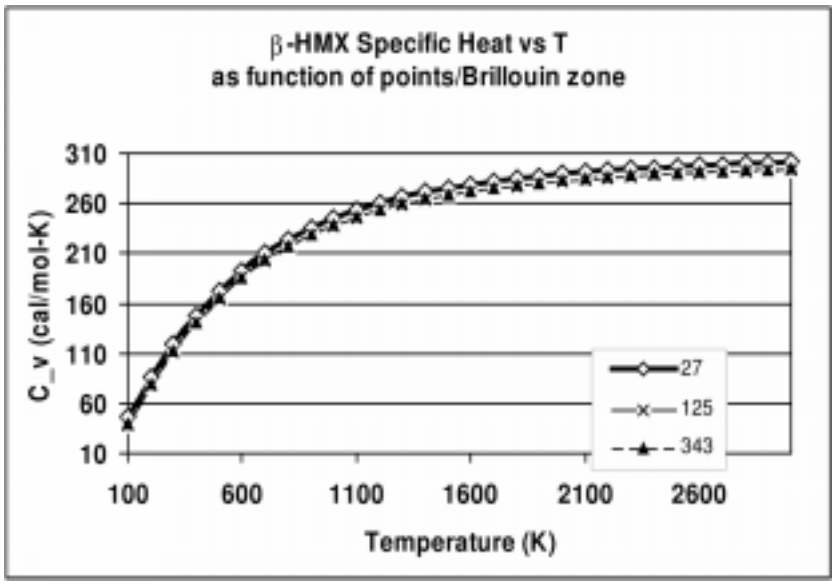

Figure 4.16: Predicting specific heat of the β-HMX molecular crystal as a function of temperature.

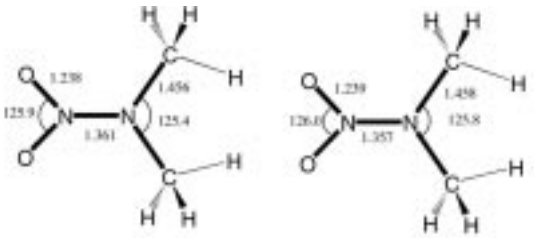

Parameter	QM (B3LYP/6-31G**)	Gas Phase Expt. (ED)	Crystal (X-ray)
N-N	1.385	1.382	1.331
N-O	1.232	1.223	1.237/1.242
N-C	1.459	1.46	1.455/1.449
ONO	125.9	130.4	124.0
ONN	117	114.8	117.8/118.2
CNC	120.3	116.2	124.6
CNN	115.6	127.6	117.6/117.7
NCH(ip)	107.4		
NC2 inversion	28.6	0.0	0.0
NO2 inversion	1.7	0.0	0.0
ONNC dihedral	16.9,164.9	0.0/180.0	0.0/180.0
H:::O	2.386		2.586

Figure 4.17: Geometry of dimethyl-nitramine (DMN) dimer from QM (B3LYP DFT) data and X-ray compared with experiments on a single molecule in the gas phase (electron diffraction) and crystal (X-ray).

We find that the standard Dreiding gives the best fit with experiment.

The Dreiding FF is a generic FF (parameters not adjusted for any particular system). It uses harmonic bond stretch and Exponential-6 van der Waals interactions. The harmonic bond stretch is good at describing vibrations but is *not* appropriate for describing the bond

Parameter	Crystal	This work	% error	Dreiding	%error
a	6.088	6.003	**1.40**	6.296	**-3.42**
b	6.266	6.690	**-6.77**	6.919	**-10.42**
c	5.995	6.079	**-1.40**	5.987	**0.13**
α	90.0	90.0	**0.00**	90.0	**0.00**
β	114.28	116.7	**-2.12**	117.17	**-2.53**
γ	90.0	90.0	**0.00**	90.0	**0.00**
N-N	1.331	1.368	**-2.78**	1.320	**0.83**
N-O	1.237/1.242	1.230/1.232		1.201/1.202	
N-C	1.455/1.449	1.451/1.457		1.445/1.449	
ONO	124.0	125.0		114.3	
ONN	117.8/118.2	117.9		122.4/123.3	
CNC	124.6	127.0		119.8	
CNN	117.6/117.7	116.2/116.9		119.7/120.5	
NC2 inversion	0.0	0.0		0.0	
NO2 inversion	0.0	0.0		0.0	
ONNC dihedral	0.0/180.0	0/180.0		0.0/180.0	
H::O	2.586	2.572		2.709	
H:::H	2.226	2.390		2.277	

Figure 4.18: Crystallographic parameters for DMN crystal from the MCXX force field and from experiment.

Sym	Mode	Experiment	B3LYP/6-31G**	Scale factor	Dreiding	This work	Error
A_1	ν_s(CH3)	3033	3171	0.956	3031	3017	16
	ν_s(CH3)	2948	3061	0.963	3061	2949	-1
	δ_s'(CH3)	**1462**	**1532**	**0.954**	**1649**	**1463**	**-1**
	δ_s(CH3)	**(1441)**	**1504**	**0.958**	**1606**	**1536**	**-95**
	ν_s(NO2)	**1304**	**1353**	**0.964**	**1717**	**1327**	**-23**
	ν(NN)	**1248**	**1271**	**0.982**	**1616**	**1251**	**-3**
	r(CH3)	1023	1039	0.985	1249	997	26
	ν_s(CNC)	838	853	0.983	764	780	58
	δ(NO2)	626	630	0.994	539	615	11
	δ(CNC)	427	408	1.047	427	462	-35
B_2	ν_s(CH3)	3033	3159	0.960	3024	3011	22
	ν_s(CH3)	2948	3064	0.963	2913	2947	1
	ν_s(NO2)	**1528**	**1634**	**0.935**	**1747**	**1600**	**-72**
	δ_s'(CH3)	**(1454)**	**1518**	**0.958**	**1620**	**1444**	**10**
	δ_s(CH3)	1411	1448	0.974	1687	1465	-54
	ν_s(CNC)	1292	1356	0.953	1267	1227	65
	r(CH3)	1110	1061	1.046	1061	1035	75
	r(NO2)	619	630	0.983	485	521	98
	δ(NN)	350	325	1.077	330	376	-26
A_2	ν_s(CH3)	2993	3120	0.959	3027	3012	-19
	δ_s(CH3)	(1456)	1478	0.985	1659	1421	35
	r_|_(CH3)	(1144)	1151	0.994	1042	1021	123
	τ(NO2)	162	169	0.984	156	66	96
	τ(CH3)	107	114	0.939	131	129	-22
B_1	ν_s(CH3)	2993	3122	0.959	3039	3013	-20
	δ_s(CH3)	1455	1487	0.979	1665	1439	21
	r_|_(CH3)	1059	1147	0.915	1133	1061	-61
	ω(NO2)	782	771	0.988	724	758	4
	γ(NN)	225	-117		397	327	-102
	π(CH3)	(115)	162	0.710	117	99	16
				Res. error	153.78	54.1	

Figure 4.19: Comparison of Vibrational frequencies for DMN from experiment, from QM (B3LYP PS), and from the new MCXX force field.

dissociation needed to describe an explosion. Thus, we have modified the Dreiding FF to use Morse potential instead of a harmonic potential to describe the N-N bond dissociation.

The calculation using Dreiding MS gives a density of 1.8852 g/cc at standard temperature and pressure, which is within 2.69% with the experiment. The calculated cell parameters are: A=8.986 (0.27%), B=8.976 (0.58%), C=6.883 Å (1.04%). The planar FF also uses a

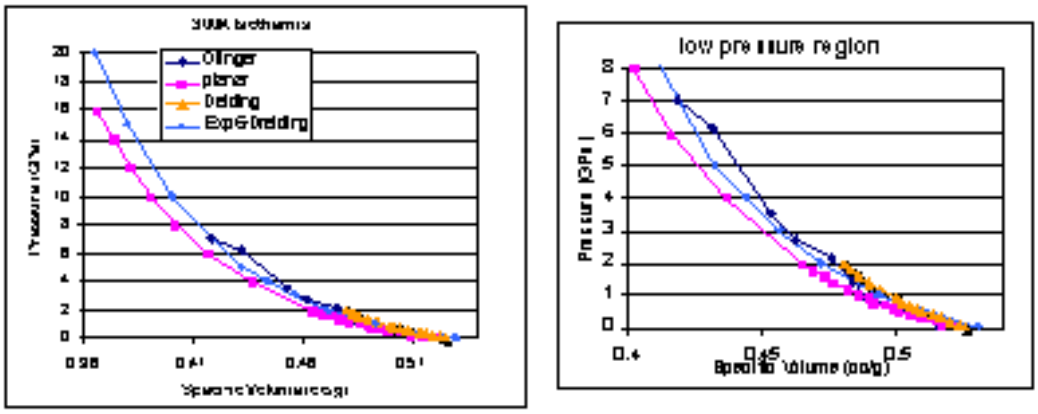

Figure 4.20: Isotherms from MD simulation at 300K for TATB. Shown are the results from the experiment and for three different force fields. The one labelled exp6-Dreiding is the standard FF used in other calculations.

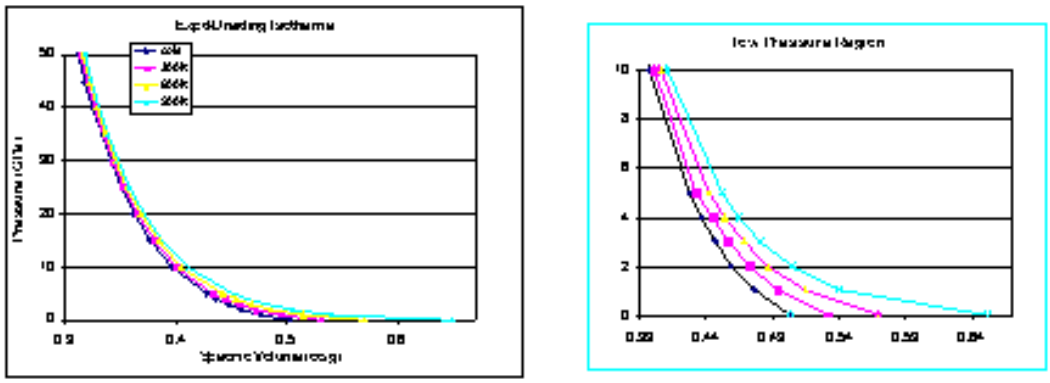

Figure 4.21: Isotherms (including cold compression) for TATB at various T using Exp6-Dreiding FF.

Morse potential for bond stretch and Exponential-6 van der Waals interactions, but it has different parameter settings for Exponential-6 van der Waals interactions. The planar FF does not fit the experiment as well as Dreiding MS. The calculated cold compression and isothermal EOS at various temperatures are shown in Figures 4.20 and 4.21 (Compared with the Ollinger experimental 300K isotherm).

In order to better understand the angle torsion barrier and hydrogen bonding energy, and to improve and validate our FF, we also initiated *ab initio* QM calculations.

Specific heats at constant pressure for gas phase TATB (calculated from the vibrational frequencies) are reported in Figure 4.22 for various temperatures.

In order to determine how well the FF describes the hydrogen bond in condensed TATB, we calculated the dimer binding energy of two TATB molecules as a function of the separation distance (Figure 4.23). This indicates a net dimerization energy of 2.2 kcal/mol.

The torsion energy about the amino dihedral angle was also calculated, Figure 4.24.

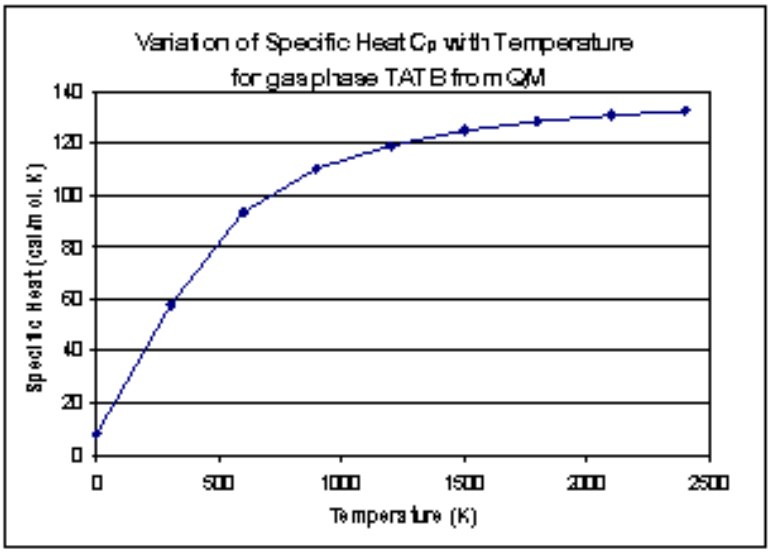

Figure 4.22: Variation of specific heat C_p with temperature for gas phase TATB (using the Exp6 Dreiding FF).

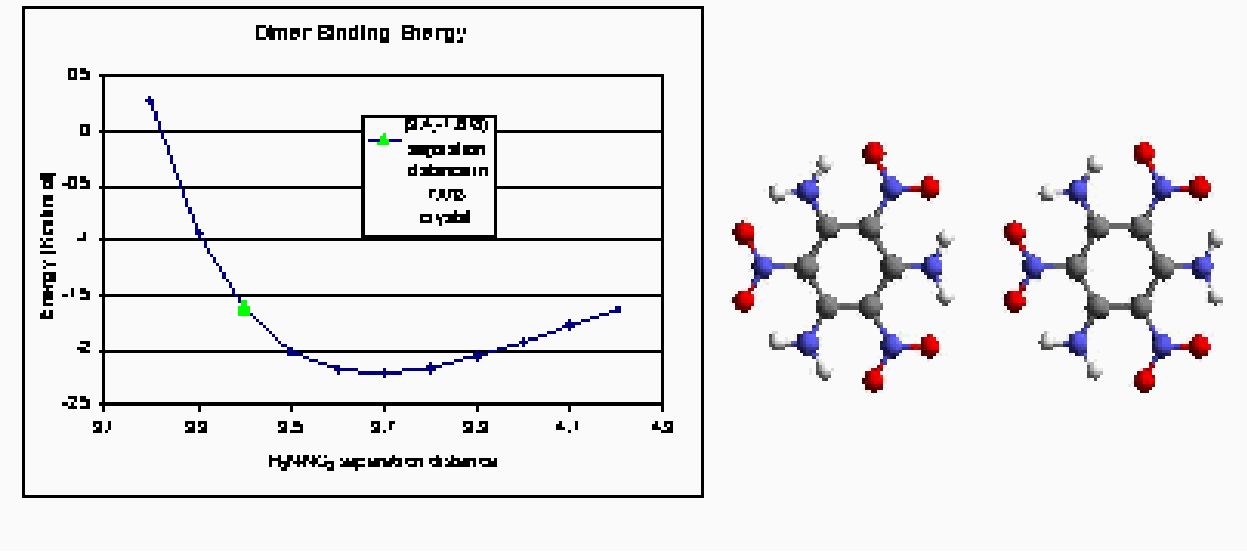

Figure 4.23: Dimer binding Energy of two TATB molecules as a function of the H_2N-NO_2 separation distance.

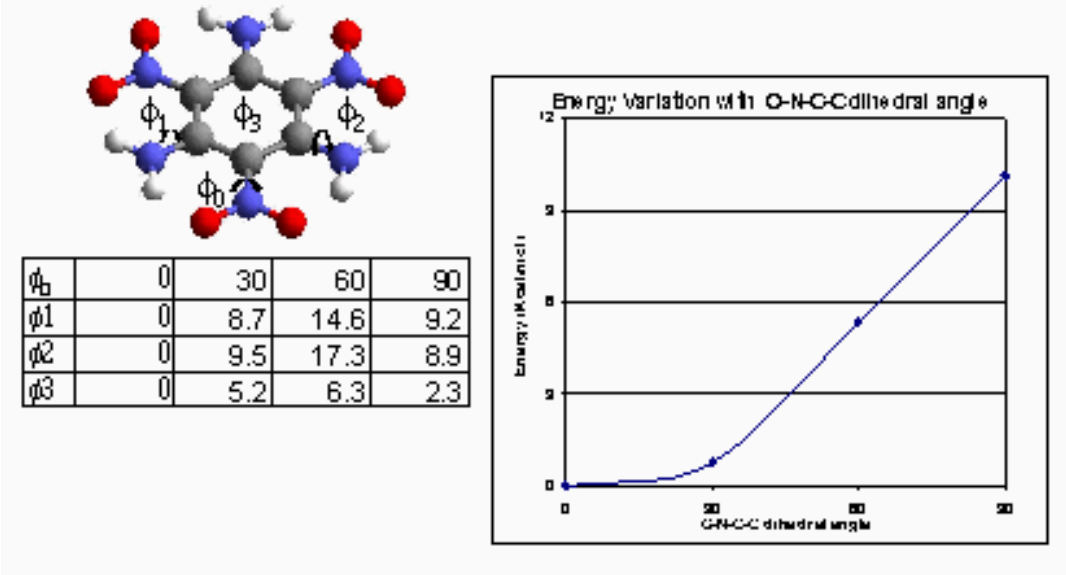

ϕ_0	0	30	60	90
$\phi 1$	0	8.7	14.6	9.2
$\phi 2$	0	9.5	17.3	8.9
$\phi 3$	0	5.2	6.3	2.3

Figure 4.24: Dependency of energy on the O-N-C-C dihedral angle from QM (B3LYP DFT).

4.4.1.3 Future plans in high explosives applications

In the second year, we will use QM to improve the force field. We will also calculate Shock Hugoniots from the isotherms. We will also study the temperature and pressure dependence of Gruneisen parameter of TATB. We will also carry out large scale calculations to study phase transitions and the initial steps of an explosion.

4.4.2 Applications in solid dynamics

4.4.2.1 QM calculations of EOS for Ta metal

We are using QM calculations with periodic boundary conditions to compute the equation-of-state and the elastic constants for Ta. Our first goal in this work was to determine what level of density functional theory is required to reproduce the experimental EOS for Ta.

4.4.2.1a The Local Density Approximation (LDA) Our initial calculations used the simplest level of density functional theory (DFT), the local density approximation (LDA). At this level of theory, the electronic energy is described as a function only of the local electron density at each point in the molecule or crystal. Figure 4.25 compares two sets of experimental results to two sets of DFT results, one using the program Quest and the other using the Cohen Multibasis code. As is clear from the figure, DFT LDA underestimates the volume at each pressure by $\sim$7%.

4.4.2.1b The Generalized Gradient Approximation (GGA) Much better agreement is obtained using the generalized gradient approximation (GGA). At the GGA level of theory, the electronic energy is described as a function both of the local electron density and of the gradient of the electron density at each point in space, thereby including some

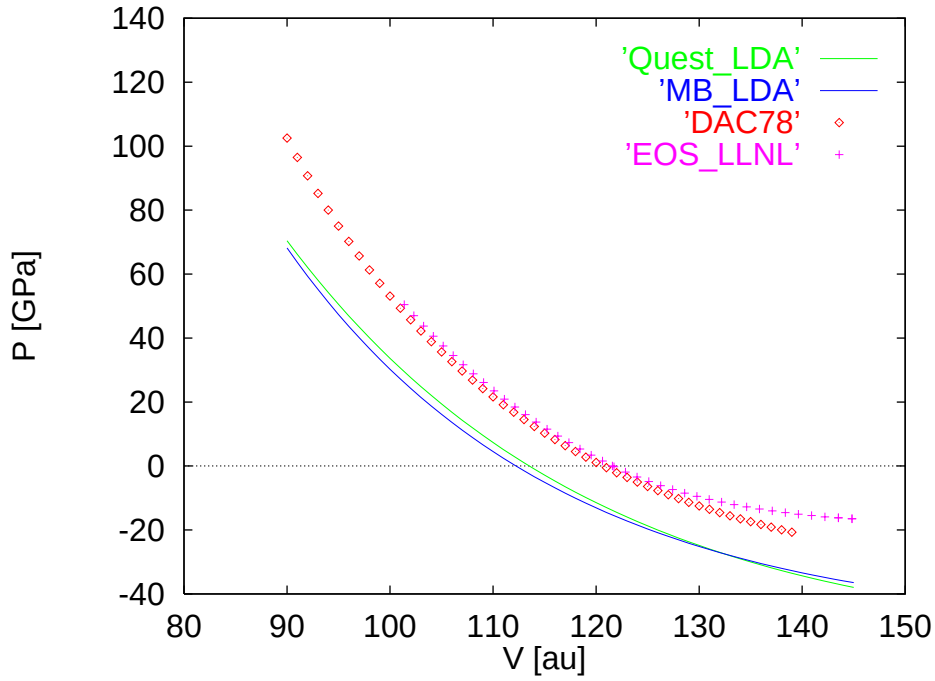

Figure 4.25: The equations-of-state (cold compression) for Ta. Experimental results (crosses and diamonds) are compared with two QM calculations (lines) at the DFT-LDA (local density approximation) level. Conclusion, DFT at the LDA does not agree well with experiment.

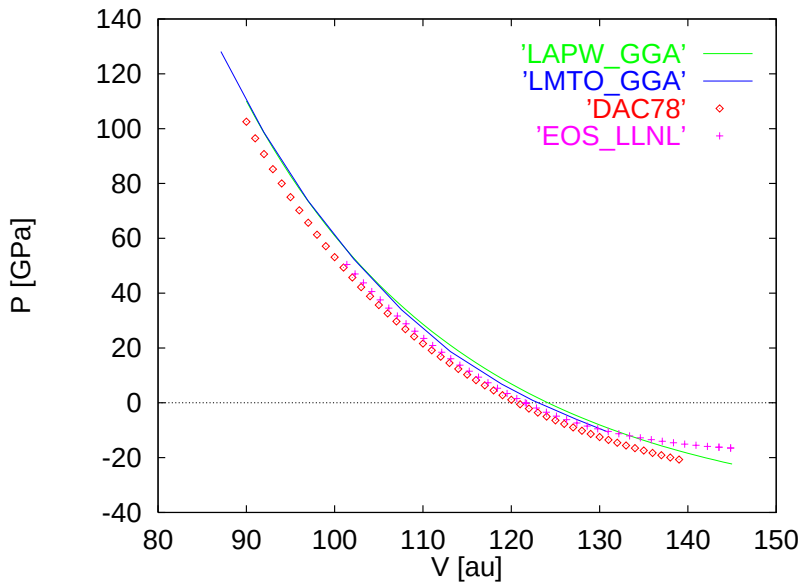

Figure 4.26: The equations-of-state (cold compression) of Ta. The experimental data (crosses and diamonds) are compared with two QM calculations (lines) at the DFT-GGA (generalized gradient approximation) level. Conclusion, DFT-GGA is in reasonable agreement with experiment.

"nonlocal" corrections. Figure 4.26 shows that much better accuracy is attained at the DFT GGA level.

4.4.2.1c Effect of Spin-Orbit Coupling Next we considered the effect of including the spin-orbit coupling part of the Dirac equation on the QM calculation. This is much more expensive but is practical for the small unit cell of Ta.

Figure 4.27 summarizes the results for LDA and GGA levels of theory without spin orbit coupling. (LDA underestimates the volume at a given pressure while GGA slightly overestimates it).

Figure 4.28 shows that including the spin orbit coupling shifts both EOS curves to lower level volume (by $\sim$2%). Thus, with spin-orbit coupling the GGA approximation is nearly identical with the experimental results.

4.4.2.1d Elastic Constants of BCC Tantalum We also calculated the elastic constants of Tantalum using DFT GGA. The results in Figure 4.29 agree well with the calculated experimental results at zero pressure.

4.4.2.2 QM calculation of the EOS for HCP metals

Figure 4.32 shows that the EOS calculated for the HCP structure of Fe (but assuming no magnetic effects) is in poor agreement with experiment. In contrast the calculated EOS for Co and Re (Figures 4.30 and 4.31) agree well with experiment. Since magnetic effects would

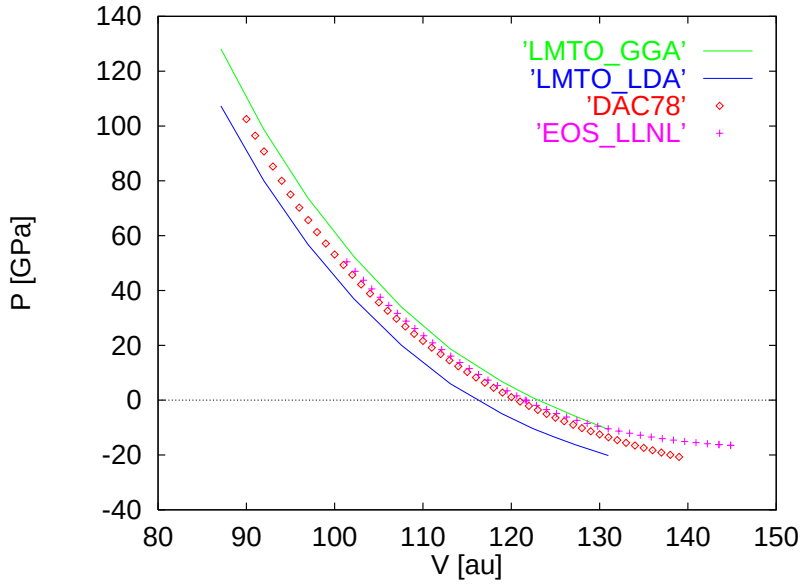

Figure 4.27: Equation-of-state for Ta. DFT at the LDA and GGA levels were carried out without spin-orbit coupling corrections (lines). Experimental results (crosses and dots) are compared to two different QM calculations (lines) the DFT-LDA level. Conclusion, DFT-LDA does not agree well with experiment.

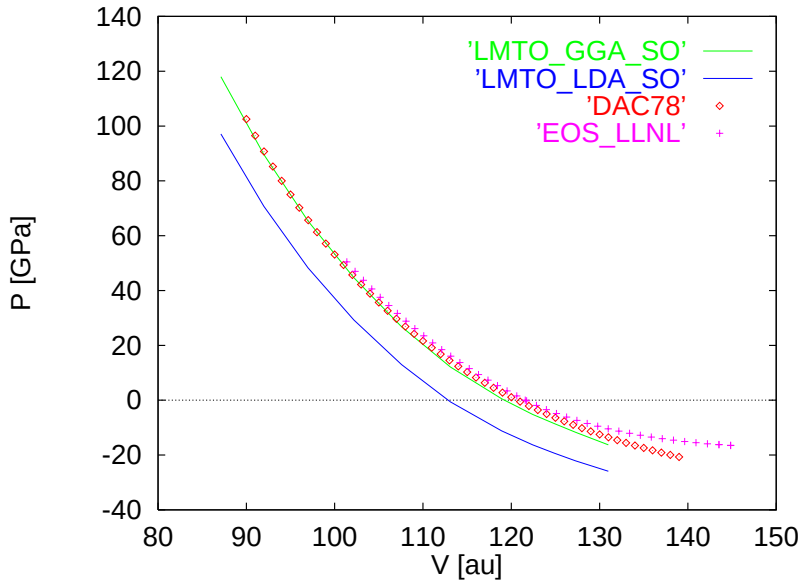

Figure 4.28: The equations-of-state for Ta. DFT at the LDA and GGA level was carried out with spin-orbit coupling corrections (lines). Conclusion, DFT-GGA is in good agreement with experiment.

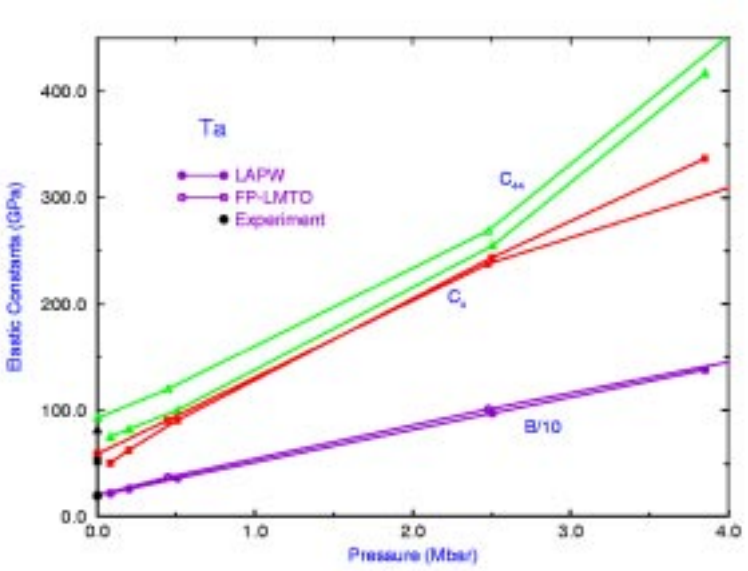

Figure 4.29: Elastic constants for Tantalum calculated using two levels of DFT-GGA theory. Experimental results at $P = 0$ are also shown.

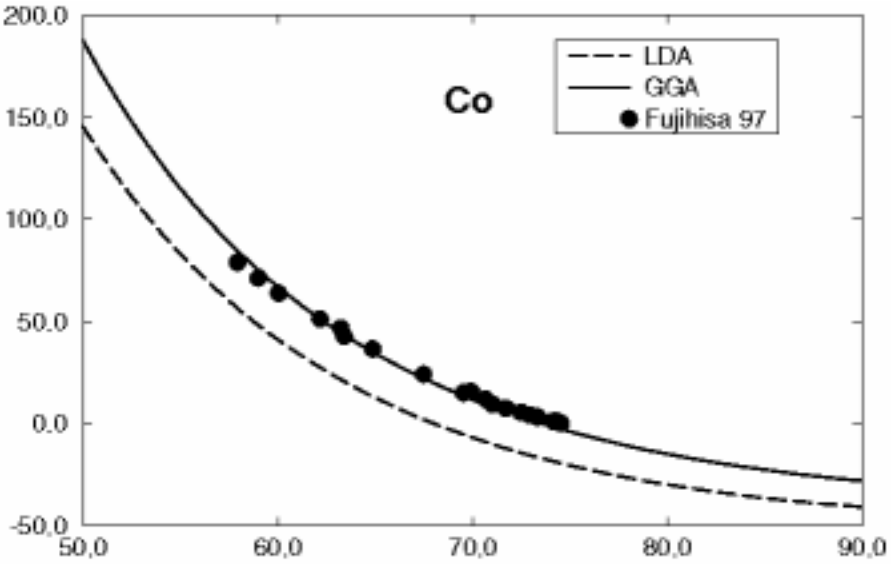

Figure 4.30: Equation-of-state for Co (lines), compared to experiment (dots). Conclusion DFT-GGA is in good agreement with experiment.

not be expected to be significant for Re or Co, but might be expected to play an important role in Fe and since only Fe leads to a disagreement with experiment, we conclude that magnetic effects causes the discrepancy for Fe.

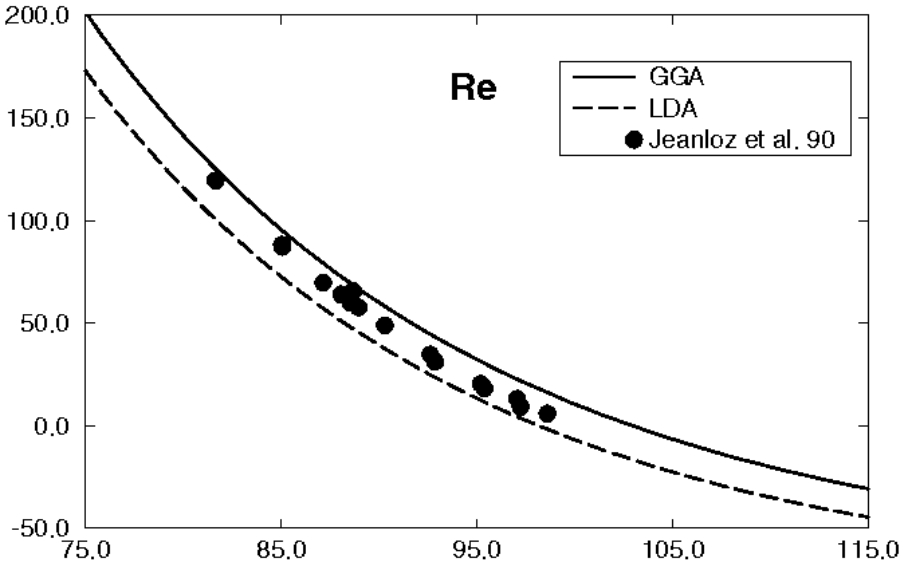

Figure 4.31: Equation-of-state for Re (lines), compared to experiment (dots). Conclusion, agreement between theory and experiment is fair.

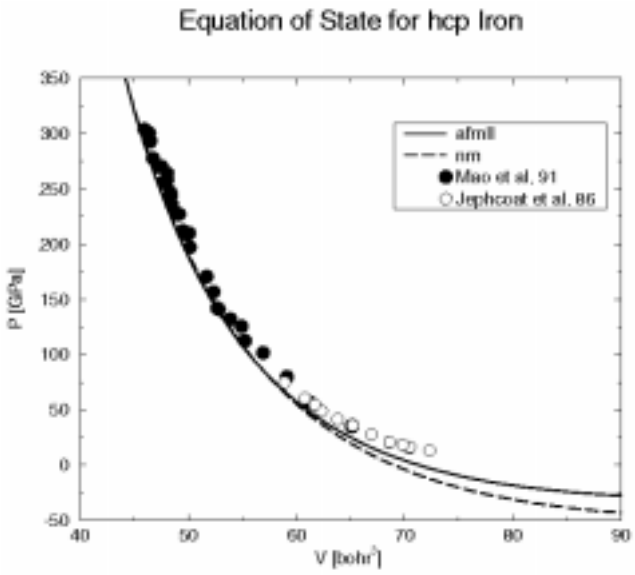

Figure 4.32: Equation-of-state for Fe from QM (lines) and experiment (dots). These calculations do not include magnetic effects. Conclusion, the poor agreement at pressure below 100 GPa indicating that magnetic effects are important.

		a_0	a_{RT}	E_{coh}	B	C_{11}	C_{12}	C_{44}
Fe	exper	2.860	2.865	4.28	173.10	243.10	138.10	121.90
	MSC	2.860	2.857	4.28	173.07	242.79	138.21	122.04
	JO		2.866	4.29	166.78	229.52	135.41	116.69
	GJM		2.866	4.28	167.00	251.00	125.00	120.90
Ta	exper	3.293	3.298	8.10	194.21	266.32	158.16	87.36
	MSC	3.293	3.295	8.10	181.15	264.67	139.39	112.72
	JO		3.303	8.09	187.67	257.57	152.72	82.31

Table 4.6: Comparison of calculated (MSC, JO, GJM) and experimental properties for Ta and Fe. Units: lattice parameter Å; cohesive energy eV; elastic constants GPa. Calculations: MSC, present work; JO, Johnson-Oh potential; GJM, Gao-Johnston-Murrell potential.

		$\nu_{N,L}$	$\nu_{N,T2}$	$\nu_{N,T1}$	ν_H
Fe	exper	9.26	6.45	4.53	8.56
	MSC	8.96	6.03	2.77	8.60
	JO	12.70	9.80	3.10	13.80
	GJM	9.30	6.50	4.50	8.60
Ta	exper	4.35	4.35	2.63	5.03
	MSC	5.43	3.38	1.76	4.84
	JO	4.90	3.05	2.45	3.95

Table 4.7: Calculated and experimental phonon frequencies for Ta and Fe (THz).

4.4.2.3 The properties of bcc metals (Fe and Ta) using the Q-SC FF

Using the Q-SC FF (see Section 4.3.2.2) we calculated various properties of Iron and Tantalum. These properties include the cohesive energy, equation-of-state, moduli and elastic constants, phonon frequencies, vacancy formation energy, and surface energies for various low index surfaces. A summary of these results are given in Tables 4.4.2.3, 4.7, and 4.8. These results will be used as input to the solids dynamics calculations of Ortiz.

4.4.2.4 Strain Induced Amorphization

Molecular dynamics simulations using the Q-SC many-body FF (see Section refmp14), were used to study the deformation of metal alloy nanowires (20Å thick but infinite length) as a function of the strain rate. Such MD simulations allow us to follow the effects of strain at various strain rates independently from those arising from heat dissipation and concomitant temperature increase. These calculations embed the nanowire material in a constant temperature bath (at 300K), eliminating thermal softening effects and allowing us to isolate strain and strain rate effects for temperature effects.

To illustrate the effect of strain rate on the details of deformation, Figure 4.33 displays snapshots of MD simulations on an fcc Ni:Cu nanowire (at 300K) deformed to 100% strain

		$E_{vf}(u)$	$E_{vf}(r)$	$\gamma_{100}(u)$	$\gamma_{110}(u)$	$\gamma_{111}(u)$	$\gamma_{100}(r)$	$\gamma_{110}(r)$	$\gamma_{111}(r)$
Fe	exper		1.69-1.89				2417	2417	2417
	MSC	1.89	1.77	2633	2582	2751	2595	2568	2737
	JO	1.92	1.81				1685	1535	
	MEAM	1.95		2289	1566	1720			
Ta	exper		2.20-3.40				2902	2902	2902
	MSC	3.19	2.74	3661	3696	3811	3538	3646	3798
	JO	2.95	2.76				1990	1880	
	MEAM	3.30		3292	2173	2305			

Table 4.8: Calculated and experimental vacancy and surface properties. (u): unrelaxed, (r): relaxed. Units: vacancy formation energy eV, Surface energies mJ/m^2. MEAM - Modified Embedded Atom Method. .

at various strain rates from 0.5%/psec to 5%/psec in the z-direction. For $\dot{\epsilon} = 0.5\%$/ps cooperative shear events occur within the crystal producing coherent shear bands. These shear bands are coherent "twins." Multiple coherent shearing events result in work hardening and eventually necking before failure. Material in the final neck appears to melt before tensile failure. For strain rates of $\dot{\epsilon}$ =1%/ps and 2%/ps, qualitatively similar behavior is seen. For $\dot{\epsilon}$ =5%/ps, the behavior is fundamentally different. No coherent shear bands or twins are formed within the specimen as the system is strained. Instead, one sees a homogeneous transformation of the specimen into a highly disordered state even at strains of 0.15. This new phase is amorphous. Thus, this homogeneously disordered material undergoes homogeneous uniform flow with no evidence of work hardening or necking.

Figure 4.34 shows how the strain rates affects the stress-strain curves (pure Ni at T = 300K). For all strain rates, the stress increases linearly with strain (ϵ_{33}) up to a stress of approximately 5.5 GPa and 7.5% strain. This elastic yield stress and yield strain far exceeds that of bulk Ni (because our system starts as a perfect crystal, no dislocations). Past the elastic limit (7.5% strain), for lower strain rates ($\dot{\epsilon} = 0.05$ %/ps or 0.5 %/ps), the stress drops rapidly by 50% (to 2.8 GPa). With further strain, the stress again rises, then drops in a repeating cycle. The sample remains crystalline during these step-wise transitions and accommodates the strain by formation of cooperatively sheared regions (twins) with reoriented fcc crystal.

For a tensile strain rate of 5%/ps , we observed a continuous transformation to an amorphous phase, during which the atomic short-range order changes dramatically from a crystal to a glass (lacking the octahedral interstitial sites of fcc). The amorphization transition is associated with the vanishing of the tetragonal shear elastic constants.

Beyond 7.5% strain the system changes from fcc to a glass with accompanying homogeneous plastic flow. Thus, we see a gradual rounding of the stress-strain curve with the apparent absence of the "twinning related" stress drops observed at slower strain rates. The maximum stress occurs at ca. 15% strain where $\sigma_{33} = 9.5$GPa is reached (Ni at 300K). With further plastic deformation, the stress decreases leading to a limiting value of $\sigma_{33} = 3$ GPa. Combining this asymptotic tensile stress with the applied strain rate of 5%/ps, we find an

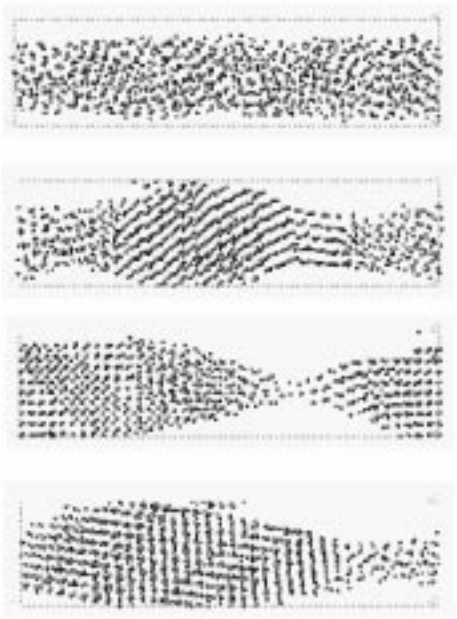

Figure 4.33: Deformation behavior of a CuN nano-rod (20Å thick) at uniform strain rates of 0.5%/ps, 1.0%/ps, 2%/ps, and 5%/ps from left to right. In all cases the temperature is kept at 300K. Shown is the structure after 100% strain.

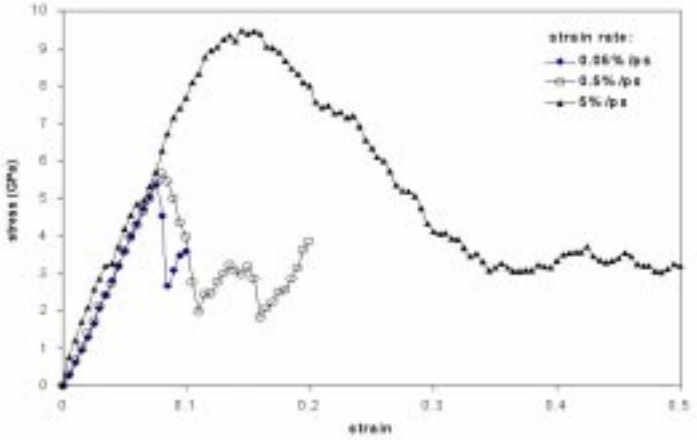

Figure 4.34: Strain versus stress behavior for a Ni crystal at various uniform strain rates (all at 300K).

apparent viscosity of 60 cP, an order of magnitude larger than the typical viscosity for liquid metals at equilibrium.

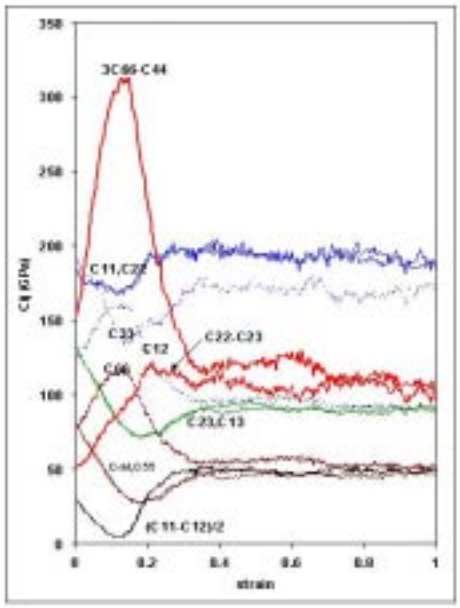

Figure 4.35: Effect of deformation on the elastic constants for the Ni crystal.

Figure 4.35 gives the relevant elastic constants calculated for Ni as a function of strain for $\dot{\epsilon} = 5\%/\text{ps}$. The uniaxial tension in the z-direction breaks the symmetry so that the 3 independent elastic constants of the cubic system are split into to 6 independent elastic constants for the tetragonal system $C_{11} = C_{22}$, $C_{33}, C_{12}, C_{13} = C_{23}, C_{44} = C_{55}$, and C_{66}. For the homogeneous amorphous glass under steady state uniaxial deformation, we observe 4 independent elastic constants: $C_{11} = C_{22}, C_{33}, C_{12} = C_{13} = C_{23}, C_{44} = C_{55} = C_{66}$. We note that $C_{44} = (C_{11} - C_{12})/2$, as for an isotropic solid, and also $3C_{66} - C_{44} = C_{22} - C_{23}$. These relations provide additional confirmation that the system has undergone a crystal to amorphous transformation. Upon release of the externally applied tension on the amorphous sample, we recover isotropic symmetry with 2 independent constants.

4.4.2.5 Pressure induced phase transformations in silica

Quartz and coesite (both four-coordinate Si) have been observed to transform to stishovite at ∼15 GPa in shock experiments. To simulate this process we employed NPT MD methods using the MS-Q FF (see Section 4.3.2.1). These simulations used supercells with 576 to 640 atoms to describe α-quartz, coesite, stishovite, and silica glass.

To investigate the pressure induced phase transformation, we increased the pressure on the system by 1 GPa every ps. (We find similar behavior for loading rates of 0.25 GPa/ps and 0.5 GPa/ps.) Figure 4.36 shows a sharp transition (at 15 to 20 GPa) from α-quartz to

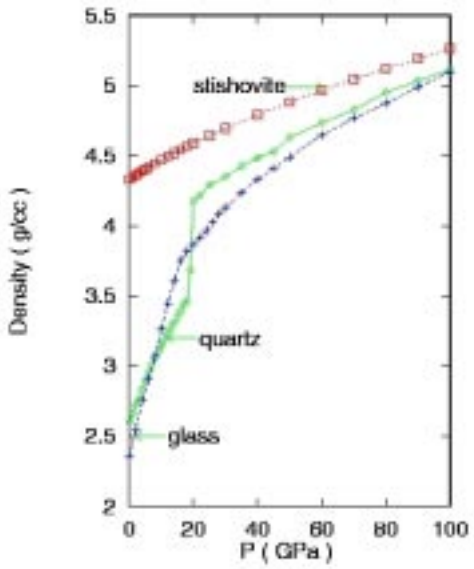

Figure 4.36: Cold compression curves for silica polymorphs

stishovite (containing numerous defects) but the transition from glass to stishovite is quite gradual (17 to 100 GPa).

Starting with α-quartz and using a 1 GPa/ps compression rate, we also did simulations at 500K to 1500K. (Probably the temperatures in shock wave experiments range from 1000 to 1500K.) In Figure 4.37, we see that the phase transition changes from 19.5 GPa (300K), to 16.5 GPa (500K), to 15.5 GPa (1000K) and 14.5 GPa for 1500K. Experiments indicate a transition starting at about 14 GPa for 500K, in reasonable agreement with our result of 16.5 GPa at 500K.

To understand the origin of the difference in the transformation for α-quartz and from the glass, we analyzed the average O-Si-O angle as a function of pressure. Figure 4.38 shows the average bond angles at the Si (over each 1 ps of dynamics) starting with α-quartz. We find a dramatic change between 15 GPa and 20 GPa, where the average bond angle changes from nearly all tetrahedral (109.5°) at 15 GPa to mostly octahedral (90°) at 20 GPa. This indicates an abrupt reconstructive (nondiffusive) structural phase transformation for the crystal.

In contrast for silica glass Figure 4.39 shows that the 5 to 6-coordinate local structures emerge slowly as the pressure increased from 20 to 120 GPa. Here the O-Si-O angle distribution changes appreciably between 20 and 30 GPa and continues to change significantly at higher pressures. This indicates a displacement phase transformation for the glass. Here the rearrangement requires diffusion. Even at 100 GPa, the percentage of six-coordinate atoms for silica glass is less than for the structures obtained from quartz. These results are consistent with the interpretation by Stolper and Ahrens [74] of the experiments [75].

We find that the α-quartz to stishovite transformation is not reversible at our time scales. Thus, relaxing the load from 100 GPa back to zero (at -1 GPa/ps) results in a structure with a density of 3.7 g/cm^3 at zero pressure. This is consistent with experimental observations of

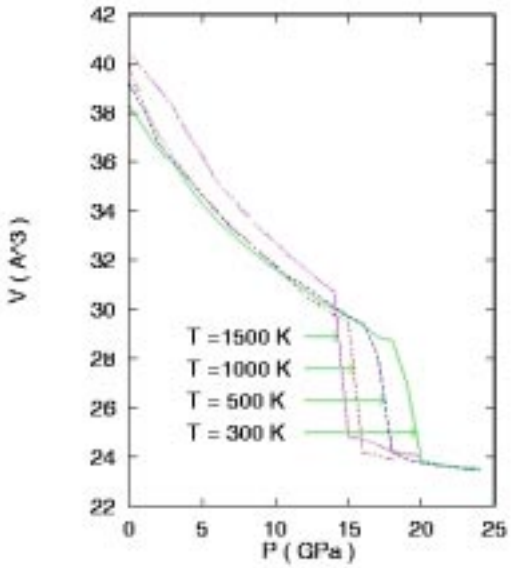

Figure 4.37: Temperature dependence of phase transition in silica

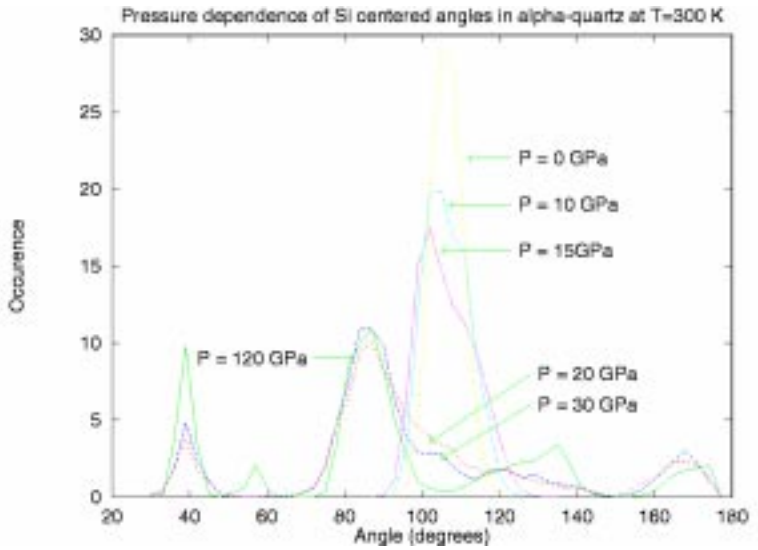

Figure 4.38: Pressure dependence of angle distribution in α-quartz

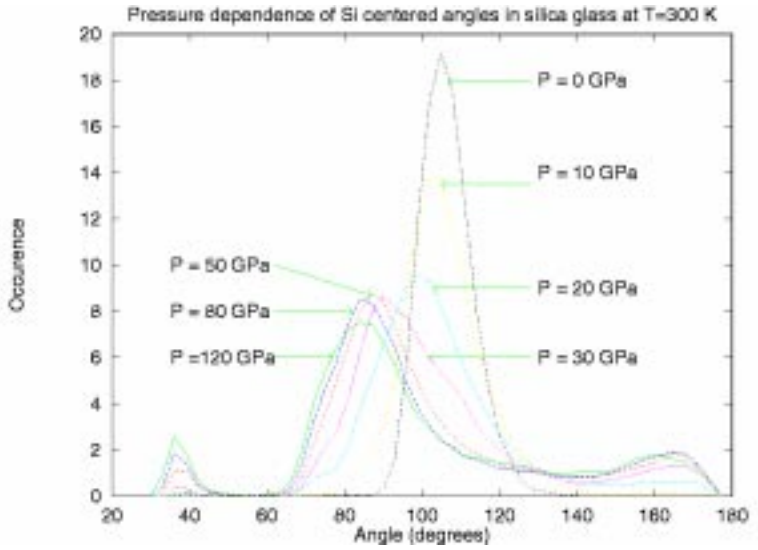

Figure 4.39: Pressure dependence of angle distribution in silica glass

shock wave release isentropes.

4.4.2.6 Structure of vitreous silica from MD with MS-Q FF

To simulate the structural properties of silica glass used the MS-Q FF (see Section 4.3.2.1). To obtain an amorphous structure we prepared the sample in two ways:

- We started with the crystalline form of β-cristobalite (27 unit cells, leading to a supercell with 648 atoms) and annealed the structure at 4000 K with 40 ps of NVT dynamics. We then cooled the system slowly (4 ps per 100 K) using constant volume, constant temperature (NVT) dynamics until 1000 K. At 1000 K, we switched to NPT dynamics and continued cooling at the same rate. Finally, we performed 30 ps NPT dynamics at 300 K, leading to a final density of 2.32 g/cc. In a second simulation we cooled the systems more slowly (8 ps per 100 K) and found the final density, 2.33 g/cc. This indicates that slower cooling is unlikely to change the density. However, cooling at 2 ps/100 K leads to a final density of 2.35 g/cm, indicating that this is too fast. Thus, the 4 ps per 100 K cooling scheme seems adequate for predicting properties of silica glass. The final density 2.32-2.33 g/cc from NPT simulations is 6% higher than experimental silica glass density is 2.20 g/cc.

- A second simulation started with randomly generated structure in a box of 200 Si and 400 O atoms (at a density of 2.20 g/cm^3). Using a similar quenching scheme (4 ps per 100 K), this leads to a final density of 2.33 g/cm^3.

The most quantitative information about the structure of silica glass is from neutron diffraction. The fundamental quantity to be compared between experimental and theoretical results is the total correlation function for neutron scattering, $T(r) = 4\pi r \langle \rho(r) \rangle$, where $\rho(r)$

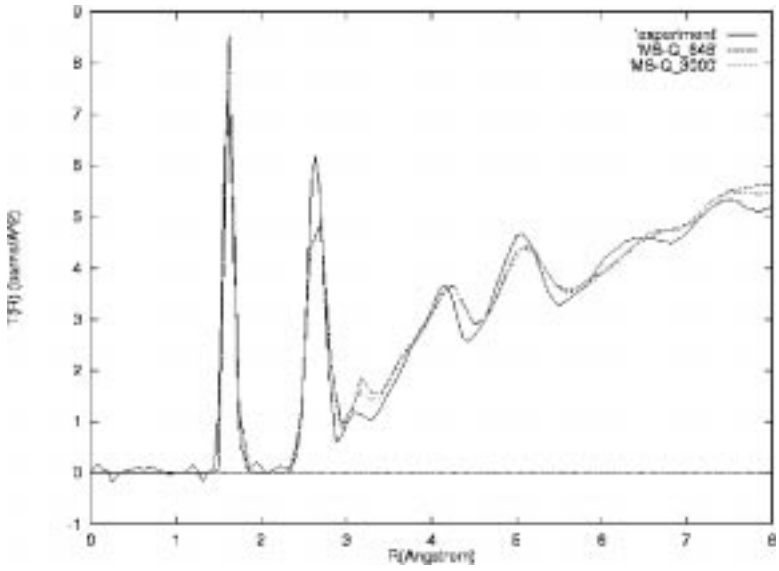

Figure 4.40: Theoretical and experimental total correlation function in silica glass

is the density function. $T(r)$ can be written in terms of neutron scattering lengths, b_X, and the radial distribution function, $G_{ij}(r)$,

$$T(r) = 4\pi r \rho_0 N_{u.c.} \left\{ \sum_{i,j} f_i f_j b_i b_j G_{ij}(r) \right\}$$

where $N_{u.c.}$ is the number of atoms per unit of composition, f_X is the fraction of X-type atoms, ρ_0 is the average density. Using $G_{ij}(r)$, ρ_0 obtained from the 30 ps long NPT MD simulations of three glass structures at 300 K and $b_O = 5.805\ fm$, $b_{Si} = 4.1491\ fm$, we calculated $T(r)$. Figure 4.40 shows that the calculated total correlation functions are in good agreement with an neutron scattering experiment [76] for the first two peaks (up to 3Å), reasonably good for the next 3 peaks (up to 5.5 Å). The simulations do not show the small peaks observed at 6.3 and 7.5 Å. Thus, the simulations account for the Si-O and O-O spacings, indicating that 3-body terms are *not* required to describe the open Si-O-Si bond angles. The discrepancy for $\geq$ 6Å might be due to the periodic supercells or the fast time scale for annealing.

4.4.2.7 The phase diagram of MgO from quantum based FF

To determine the EOS of the B1 (NaCl) and B2 (CsCl) structures of MgO and to investigate the transition pressure for the B1 to B2 transition we used the qMS-Q FF determined from DFT-GGA QM calculations. The QM was carried out for both structures at various pressures and the MS-Q FF was fitted to the QM. The FF was then used to carry out calculations as a function of temperature and pressure. Figure 4.41 shows that the qMS-Q FF fits the QM quite well for volumes down to 1/2 the equilibrium value (pressures to 500 GPa).

The two-body inter-atomic potential in qMS-Q has the same form as the MS-Q FF used for SiO_2. This FF is denoted as qMS-Q to indicate that parameters comes from QM (no

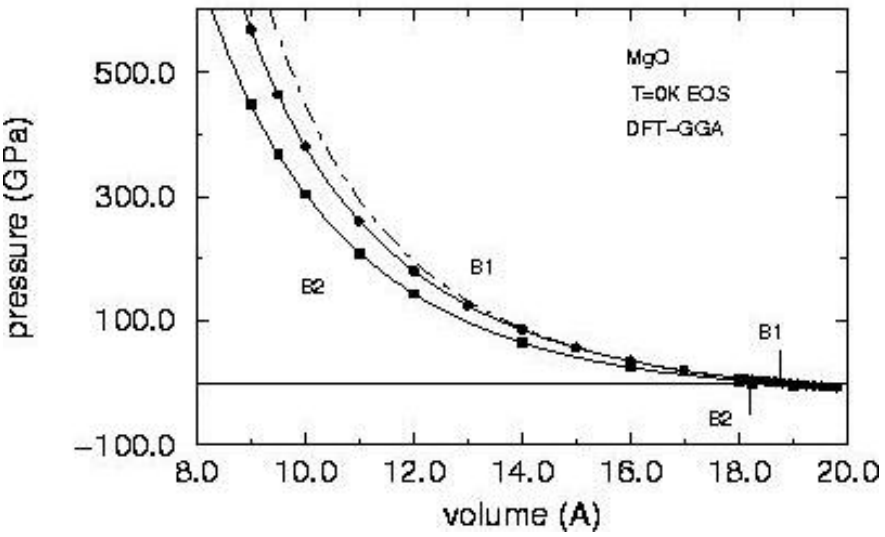

Figure 4.41: equation-of-state of MgO from QM (DFT-GGA) and the MSQ FF

	$D(Kcal/mol)$	γ	$R_0(A)$
Mg-Mg	0.6009	9.6898	3.8621
Mg-O	14.56	7.0834	2.1248
O-O	0.5363	10.4112	3.7835

Table 4.9: Force Field Parameters for MgO

empirical data). The parameters for Mg-Mg and Mg-O interactions were chosen so as to reproduce the bulk modulus and its first and second derivatives (K_T, $K_T^{'}$ and $K_T^{''}$) from the DFT-GGA calculations. We used the O-O parameters from the SiO_2 FF.

The FF parameters resulting from the optimization procedure are listed in Table 4.9.

Using the qMS-Q FF we studied the transition pathway and barriers between the B1 and B2 phases. We calculate the transition pressure to be 410 GPa with an activation barrier (of 6.7 kcal/mol).

To study the phase coexistence we performed NPT MD simulations of the B1, B2, and ligand phases of MgO. For the B1 phase each periodic cell contained 216 atoms while for the B2 case the number was 128. For each (T, P) point we evolved the system for 15ps using the last 10ps to determine properties. In this way we obtained the change in enthalpy and volume between the two solid phases as a function of T for different pressures. This data together with the Clausius-Clapeyron equation was used to obtain the phase boundary between B1 and B2 as indicated in Figure 4.42.

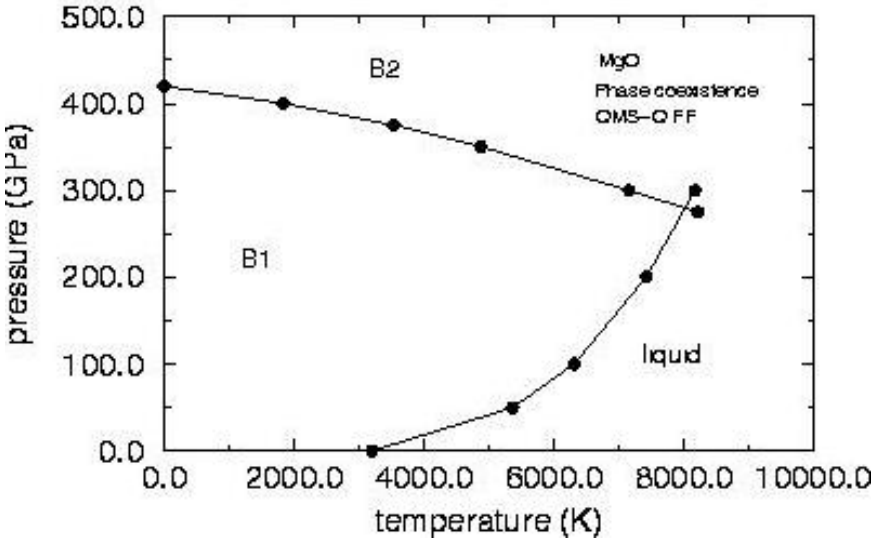

Figure 4.42: Phase boundaries for B1, B2 and liquid MgO from the qMS-Q FF

4.4.2.8 The phase transition from diamond to graphite

At high pressure, diamond is more stable than graphite. However, the graphite crystal is thermodynamically favored at low pressure. It is well known that heating diamond under pressure can transform it to graphite in a typical first order phase transformation. But the time scale of this transformation, the nature of the transformation at the atomic level, and the effective external pressure on the transformation kinetics have not been well studied.

In order to study such transformations in which many bonds must break and form, we developed the GEEBOD FF (Section 4.3.2.3) to model the interactions between carbon atoms. This allows us to use MD methods to study the kinetics of this phase transformation. The GEEBOD FF allows chemical bonds to break and form during dynamical processes, while taking NB interactions into account, (crucial to modeling of graphite).

The simulation details are the following. A quasi two-dimensional periodic boundary system was used in the simulation. 576 atoms were placed in the simulation box. In order to maintain various pressures, 208 argon atoms are also put on top of diamond crystal. NPT dynamics were performed under different external pressures. The temperature was maintained at 3000K. We have not attempted to determine the transformation temperature. Thus, we studied the kinetics of the phase transition under various pressure for a single temperature. The simulation results show that the transition time scale ranges from 30ps to 50ps, Figure 4.43. Under very high pressure (40 GPa), the simulations find no transformation. This confirms that diamond is stable at high external pressure. The time required for this transition to occur increases with increasing pressure. The simulation illustrates that this phase transition starts at the surface and propagates into the diamond crystal. Thus, graphitization happens layer by layer. The diamond (111) surface is the natural surface to form graphitic layer, leading to fast formation of graphite layer to form Figure 4.44. This

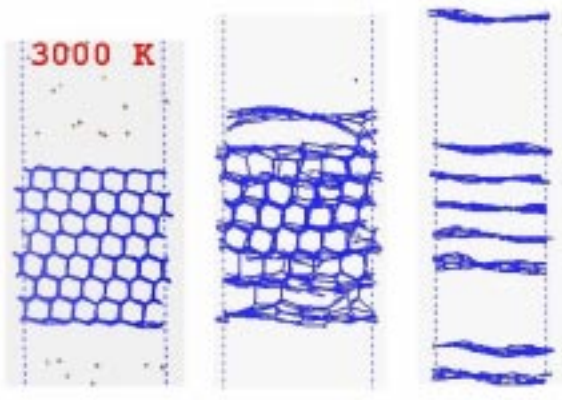

Figure 4.43: Diamond to graphite phase transition at 3000 K. Snapshot at 0 ps, 15 ps and 35 ps

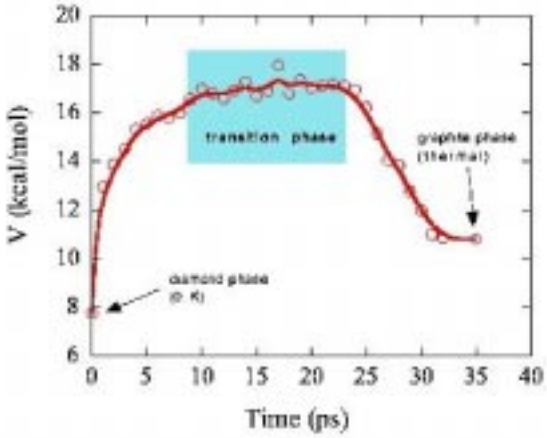

Figure 4.44: Diamond to graphite phase transition at 3000 K. Variation of potential energy

is due to the lower energetic barrier to form a graphite layer. On the other hand, the (100) surface has a higher energy barrier to transform into a graphite layer, making this process much slower.

4.4.2.9 Solid dynamics plans for second year

We plan three main efforts for the next year

1. **Use FF to predict first principles force fields**
    - do QM (DFT-GGA) calculations on BCC, HCP, FCC forms of each metal as a function of volume with and without point defects (vacancies, interstitials)
    - Fit Q-SC FF to the full set of QM results (this determines the functional form in addition to the parameters)

2. **Use the Q-SC FF to calculate energetics of defects in metals as function of P and T**
    - point defects (vacancies, interstitials)
    - surface energies (various low index surfaces)
    - grain boundaries (between various low index surfaces)
    - Peierls stresses and dislocation core energies
3. **Use Q-SC FF to predict high pressure, high temperature properties of BCC metals**
    - calculate EOS of Ta at elevated temperatures and pressures
    - calculate elastic constants of Ta and Fe at elevated temperatures and pressures
    - use large tensile, compressive and shear loads to calculate properties of Fe and Ta beyond the elastic limit
    - use rate dependent (shear, compressive, tensile) loads to calculate properties of Fe and Ta
4. **Hypervelocity impact simulations on Fe and Ta**

4.4.3 Applications to fluid dynamics

Using Non-equilibrium molecular dynamics (NEMD) methods, we calculated the shear viscosity of Cu-Au alloys subjected to a planar Couette shear flow. We used the Q-SC many-body FF [72, 73, 74] described in Section 4.3.2.2, in which parameters were optimized for pure Cu and Au. The parameters for the alloys are obtained using combination rules. These parameters lead to accurate values for surface energies, vacancies energies, and stacking faults.

We considered temperatures of 1500K, 1750K, and 2000K and alloys $Au_x - Cu_{1-x}$ with $x = 0$, 0.25, 0.5, 0.75, and 1.0. The NEMD simulation used periodic boundary conditions with (500 atoms per cubic unit cell). The unit cell length was based on extrapolating the experimental density at the corresponding temperature [77]. For alloys we assumed that the density is given by the linear combination rule

$$\rho_T\left(Au_xCu_{1-x}\right) = \rho_T\left(Au\right)\cdot x + \rho_T\left(Cu\right)\cdot\left(1-x\right)$$

We considered applied shear rates of $\dot{\gamma} = 2$, 1, 0.5, and 0.25 (1/ps). For each shear rate and temperature, we first equilibrated (with NEMD) for N_{EQ} steps followed by $N_{meas} = 9N_{EQ}$ steps which were used to calculate properties. As the shear rate decreases we observed larger fluctuations and slower convergence. Thus, we increased the number of steps. The total number of steps ranged from 20,000 ($\dot{\gamma} = 2$) to 100,000 ($\dot{\gamma} = 0.25$). The calculated viscosity scaled as $\dot{\gamma}$ as shown in Figure 4.45. This relation was used to extrapolate the $\dot{\gamma} = 0$ for comparison to experiment. The results are summarized in Tables 4.10, and 4.11. The calculations are within 1 to 3 % for Cu but high by 12 to 30 % for Au. These exploration calculations will be extended next year by using much slower rates and by considering NPT MD rather than NVT MD.

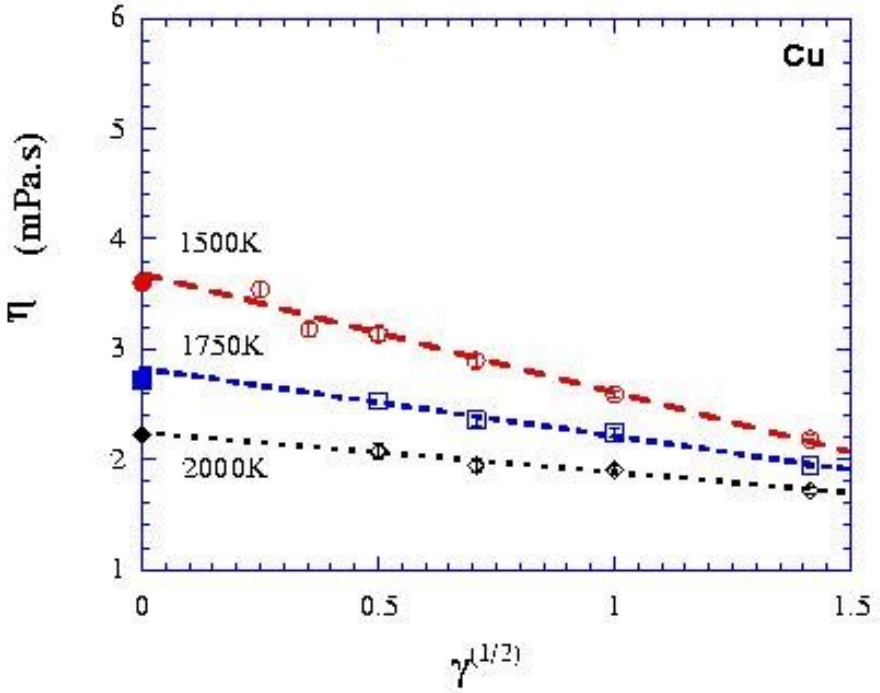

Figure 4.45: Viscosity as a function of shear rate.

T (K)	Cu Sim.	Cu Exper.	Cu_3Au_1 Sim.	Cu_1Au_1 Sim.	Cu_1Au_3 Sim.	Au Sim.	Au Exper.
1500	3.68	3.6	2.64	2.88	3.97	5.86	4.5
1750	2.82	2.72	2.29	2.47	3.21	4.56	3.7
2000	2.24	2.22	1.87	2.04	2.70	3.67	3.2

Table 4.10: Viscosity at zero shear rate, η_0 (mPas).

	Cu	Cu_3Au_1	Cu_1Au_1	Cu_1Au_3	Au
ΔG (kcal/mol)	24.15	16.56	16.05	18.78	23.69
A (mPas)	0.5298	0.7071	0.7711	0.8782	0.949

Table 4.11: Temperature dependence of viscosity calculated for Cu_xAu_{1-x} alloys.

4.4.3.1 Future plans for fluid dynamics

In order to supply reliable first principles input to CT and fluid dynamics effort we will focus on calculating various transport properties at elevated pressures and temperatures for dense fluids.

4.5 Personnel

An integral part of the MP effort is the collaboration with Carnegie Institute of Washington (Cohen). In addition there have been an active collaboration with the University of Tennessee (Ward, Dongarra).

The personnel for the materials properties effort are as follows:

- senior researchers
- William A. Goddard, III (MP team leader)
- Thomas Tombrello
- Ronald E. Cohen, (CIW)
- Tahir Çağın
- Siddharth Dasgupta
- Richard P. Muller

Postdoctoral Fellows (including these supported by other sources)

- Oğuz Gülseren (CIW, ASCI)
- Daniel Mainz (non-ASCI)
- Jianwei Che (non-ASCI)
- Ersan Demiralp (non-ASCI)
- Alejandro Strachan (visitor non-ASCI)
- Hideyuki Ikeda, (visitor, non-ASCI)
- Greg Caldwell (visitor non-ASCI)
- Donald Fraser (visitor non-ASCI)

Graduate Students

- Lu Sun (Materials Science)
- Yue Qi (Materials Science)

- Hao Li (Materials Science)
- Guofeng Wang (Materials Science)
- Ryan Martin (Materials Science)
- Georgios Zamanakos (Physics)

In addditon to the above personnel, professional support staff (Darryl Willick and James Kendall) are partially supported by the project supply the system management, hardware and software support.

Chapter 5

Compressible Turbulence

5.1 Introduction

The goal of the compressible turbulence effort is to simulate high explosively driven turbulence in the virtual facility. In this simulation a strong shock wave is driven into a layered target of test materials. In the initial stages of the research described in this report these materials will be gases, but later work will focus on strong shocks in solids using more realistic equations of state. Ultimately all three dimensional effects will be taken into account including the interaction of the outer solid casing of the facility with the flow.

The interaction of the strong shock with the layered target produces strong fluid mixing. There are essentially three phases that can be identified. The first is the shock-contact interaction which corresponds to the interaction of the strong shock with the contact discontinuities of the target. This gives rise to the generation of vorticity in the fluid. The second involves the reflection of the shock from the end wall of the facility. This reflected shock then interacts again with the fluid undergoing mixing and intensifies the mixing process. This is known as shock-vortex interaction. This gives rise to compressible turbulent mixing which is the final stage. The goal of the compressible turbulence effort is to construct models for the relevant phenomena so that subgrid scale effects can be properly modeled.

Our work in FY 98 was organized according to the various phases of the shock driven mixing process and progress has been made in all of these areas. We describe this progress in more detail in the sections below.

Below we describe the milestones for FY 98 along with a brief description of progress to date.

1. Simulations of high Mach number Richtmyer-Meshkov instability

2. Development of models for 2-D and 3-D shock contact interactions

3. Development of LES models for compressible turbulence

In addition the following activities were begun ahead of schedule in preparation for achieving the second year milestones:

1. Initial investigations of three-dimensional Richtmyer-Meshkov instability

2. Initial investigation of shock-vortex interaction in two dimensions

3. Treatment of multiscale phenomena for turbulence simulation

Finally a new research direction has been initiated in the area of incompressible Rayleigh-Taylor turbulence in collaboration with LLNL. Although our main focus is compressible turbulence, incompressible effects can be important as discussed in the sections below. This observation suggests that turbulence modeling of incompressible but stratified fluids is an important aspect of the modeling process for the full compressible flow and we have therefore strengthened our activities in this area.

5.2 High Mach number Richtmyer-Meshkov Instability

We have completed a large set of simulations in two dimensions of strong shock R-M instability in ideal gases using the *Amrita* CFD environment. These calculations have allowed us to provide a characterization of compressibility effects and to obtain an improved understanding of the dynamics of bubbles in the ensuing mixing layer. We have collaborated in this effort with Dr. Dov Shvarts of Ben Gurion University.

The initial conditions of the R-M instability are parameterized by the Mach number of the incoming shock, M, the ratio of specific heats of the target gases,γ, the amplitude of the perturbation and the density ratio of the target gas layers. At low amplitudes the Richtmyer formula [81] provides an approximation for the growth rate of the instability. From classical one dimensional gas dynamics it is possible to compute the gross interface velocity once the shock has passed through the contact discontinuity as well as the shock velocity. A criterion for the importance of compressible effects can be obtained by considering the sum of the Richtmyer formula growth rate with the interface velocity. If this exceeds or is comparable to the transmitted shock velocity, then this is a clear indication that compressibility effects are important since it is physically impossible for the interface to possess a velocity in excess of the transmitted shock velocity. If this combined velocity is significantly smaller that the shock velocity then the flow in the mixing region essentially becomes incompressible. In this case a potential model has been put forth by Alon, Shvartz and others [82] for the behavior of the bubbles. For those cases where compressibility effects are important further research is required to develop a satisfactory model for the interface dynamics.

An example of this phenomenon is shown in Figure 5.1. Shown in the figure is a numerically generated Schlieren image of the interaction of a Mach 8 shock impinging on an interface. Compressibility effects are strong in this case as evidenced by the diffraction of the shock, the appearance of Mach stems behind the shock, and a complex flow structure behind the shock which drives the subsequent vortex dynamics and mixing of the interface.

Comparison of these calculations with shock tube experiments by Ben Dor [83] and others reveals that the potential flow model works extremely well for the case where the dynamics of the interface are incompressible.

Figure 5.1: A numerical Schlieren image of the interaction of a Mach 8 shock with a perturbed interface. Compressibility effects are strong in this case as evidenced by the formation of Mach stems in the subsequent evolution of the transmitted shock wave

5.3 Shock-contact interaction

Using the work of Samtaney and Zabusky [84] we have extended their approximate circulation theory to calculate the total baroclinic circulation generation due to shock-contact interaction on multi-mode interfaces. The idea is to use classical similarity solutions which can be derived for the interactions of an oblique shock with a contact discontinuity as local solutions for more complex interfaces. The local solutions provide a measure of the circulation deposited on the interface. This technique has proven successful for small amplitude interactions at low to moderate Mach numbers. We have extended it to provide estimates for circulation for multi-mode perturbations generated by strong shocks. An example of this approach is shown in Figure 5.2. An integration over local sections of the interface using the similarity solutions of an oblique shock interacting with an interface provides the dominant contribution to the circulation and forms the basis for the estimates used here.

In order to evaluate this theory we have examined interfaces parametrized as follows:

$$x(y) = \sum_n A_n \cos nky$$

A typical example has modal amplitudes given by $A_1 = 0.35, A_3 = 0.175, A_5 = 0.0875$ and $k = 2\pi/3.2$ The shock Mach number used here is $M = 10$. We have used the theory to estimate the circulation as well as the integrated vorticity across the interface. We have then used high resolution simulation to verify the theory. The results of this comparison are shown in Table 5.1 for a variety of test gases. Note that agreement with the theory is quite good with the worst discrepancy occurring for the case of Helium and Argon. Further

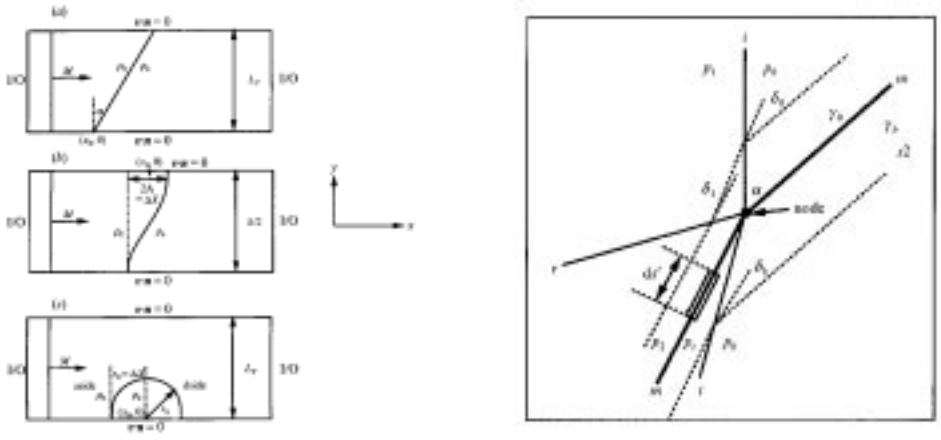

(a) (b)

Figure 5.2: (a) Examples of the application of the Samtaney-Zabusky circulation estimate to shock contact interaction. (b) A diagram of the local similarity solution used to obtain the basic circulation estimates.

Interface	Density Ratio	Atwood Number	Γ (Numerical)	Γ (Theory)	$\lvert\Delta\Gamma\rvert/\Gamma$ (x 100)
Kr-Xe	1.57	0.22	2.232	2.241	0.39
Xe-Kr	0.64	-0.22	2.325	2.459	5.44
Ar-Xe	3.28	0.51	5.020	5.109	1.73
Xe-Ar	0.30	-0.51	6.354	7.314	13.1
Ar-He	10.0	0.82	8.605	9.607	10.6
He-Ar	0.1	-0.82	12.120	16.545	26.7

Table 5.1: Comparison of circulation magnitude computed using the Samtaney-Zabusky theory against that computed using high resolution simulation

investigation is underway to deduce the cause of the larger discrepancies and to assess the possibility of further improvements in the theory.

We have also computed the integrated vorticity given by

$$\sigma(y) = \int \omega(x, y)\, dx$$

from numerical simulations and compared this with the predictions of the theory for Xe-Kr and Kr-Xe interfaces. The results are shown in Figures 5.3 and 5.4 where we plot the integrated vorticity in comparison with results obtained from high resolution numerical simulation. The results indicate that the theory can produce satisfactory agreement for the initial circulation generated by the shock vortex interaction even at high Mach numbers and in the presence of multi-scale perturbations.

Finally we have examined the divergence of the flow at various locations as a function of time. Our simulations indicate that once the shock passes through the density layer, the divergence of the flow, a measure of the importance of compressibility decays rapidly until a

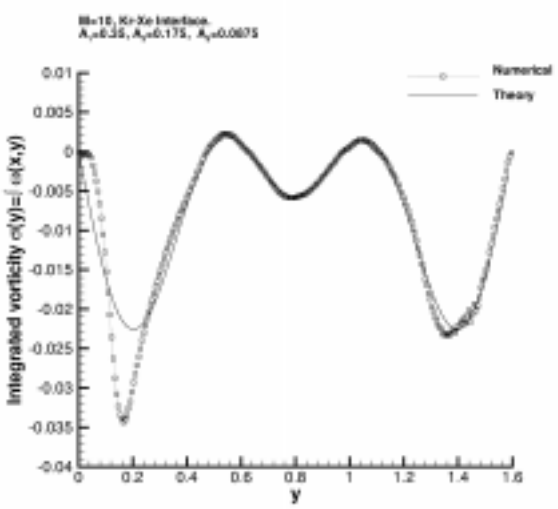

Figure 5.3: Comparison of integrated vorticity as computed using high resolution numerical simulation with the results of the Samtaney-Zabusky theory for a shock propagating from a layer of Kr into a layer of Xe.

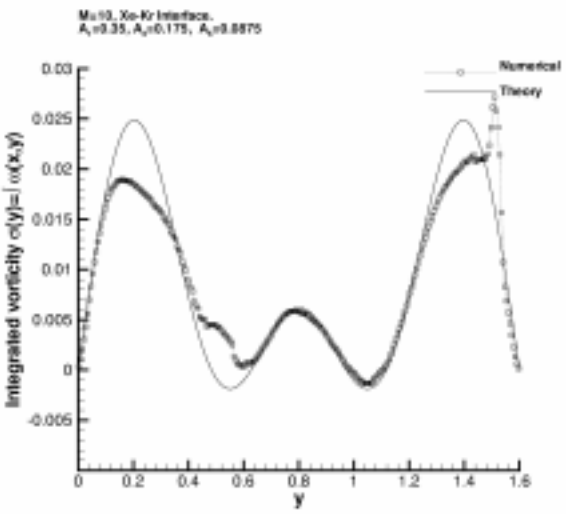

Figure 5.4: Comparison of integrated vorticity as computed using high resolution numerical simulation with the results of the Samtaney-Zabusky theory for a shock propagating from a layer of Xe into a layer of Kr.

reflected shock passes through the vortical region. This is an indication that compressibility effects may be important only for those short intervals during which shocks compress the density gradients. This is shown in Figure 5.5. Thus it is appropriate to consider the examination of density stratified incompressible turbulence in considerations of compressible mixing. Work addressing these issues is described in Section 5.7

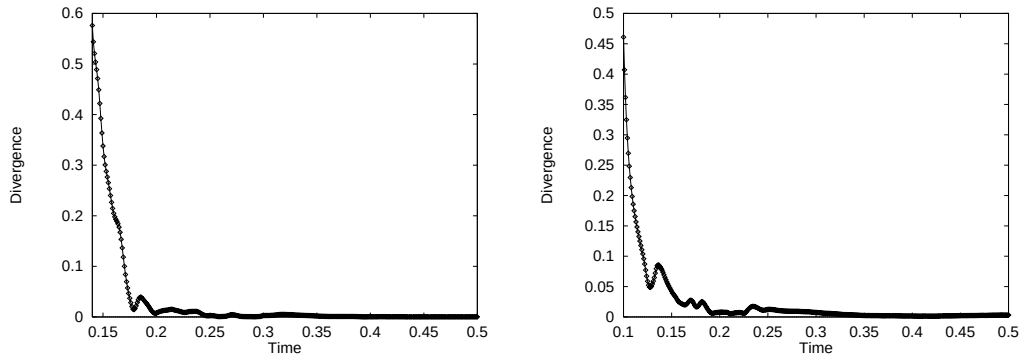

(a) (b)

Figure 5.5: Evolution of the flow divergence $\nabla \cdot \mathbf{u}$ in shock contact interaction. In (a) the evolution is shown for a density ratio of 1.5 and in (b) for a density ratio of 9. Note that in both cases the flow assumes an incompressible character once the shock has traversed the interface.

Platform	Processor	Resolution	np	Time (ms)	Speed-up	Time(μs)
Onyx2	R10000	$64 \times 32 \times 32$	1	5450	1	83
Intel Paragon	i860 XP	$128 \times 32 \times 32$	16	6002	1	732
Intel Paragon	i860 XP	$128 \times 32 \times 32$	64	1984	3.02	968
Intel Paragon	i860 XP	$128 \times 32 \times 32$	128	998	6.01	975
Intel Paragon	i860 XP	$128 \times 32 \times 32$	256	700	8.57	1367
Intel Paragon	i860 XP	$256 \times 64 \times 64$	256	4620	6.6	1127
Cray T3E	Dec Alpha	$128 \times 32 \times 32$	32	300	1	73
Cray T3E	Dec Alpha	$256 \times 64 \times 64$	32	2699	1.12	82
Cray T3E	Dec Alpha	$256 \times 64 \times 64$	64	1201	2.0	73
Cray T3E	Dec Alpha	$1024 \times 128 \times 128$	256	3629	10.58	55
SGI O2K	R10000	$128 \times 32 \times 32$	8	1659	1	101

Table 5.2: Code performance and timings for simulations of the 3-D Richtmyer-Meshkov instability

5.4 Simulations of 3-D Richtmyer-Meshkov Instability

Work is underway to generate high resolution simulations of full three dimensional Richtmyer-Meshkov instabilities. We have constructed a massively parallel simulation capability that utilizes high order Godunov and kinetic theory based solvers on a regular three dimensional mesh. The code utilizes MPI for message passing and is completely portable to all the ASCI environments as well as the Pittsburgh Supercomputing CenterT3E (where all calculations have been performed to date). The code exhibits excellent scalability as shown in Table 5.2. The following should be noted in examining the performance numbers given in the table:

- Speed up is the time taken per iteration scaled by the problem size and the number of processors used.

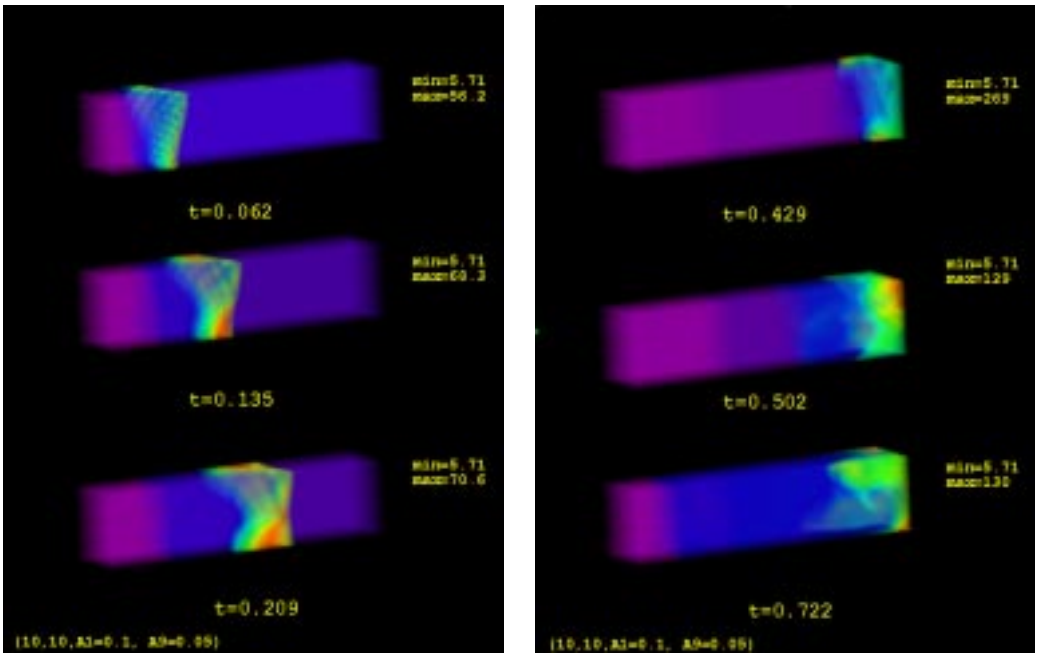

(a) (b)

Figure 5.6: Volume renderings of the interaction of a strong Mach 10 shock with a perturbed interface. The density ratio is 10. (a) Rendering just after the shock has propagated through the interface. (b) Rendering just after reshock of the interface.

- The Cray T3E is comprised of a mix of 300 MHz and 450 MHz processors.
- Code instrumentation indicates a performance of 40 MFLOPS per T3E processor. Therefore, the code performs at 10 GFLOPS on 256 processors.
- Intel Paragon timings are averaged for several runs. The numbers change depending upon the 3D processor mesh configuration chosen.
- The last column is time per processor per local grid cell for one time step.

In the calculations performed to date a strong shock ($M = 10$) impinges on a perturbed interface. The shock then rebounds off the wall and re-compresses the interface. It is in this reshock stage that the strongest growth is seen. Results for the interaction of a strong shock with a multi-mode interface are shown in Figures 5.6a and b. The shock propagates from the lighter gas to the denser. The density ratio is 10. The Figures show a volume rendering of the density field. In Figure 5.6b the shock is seen to reflect off the end wall. A phase inversion occurs at the interface and the interaction of the rebounding shock with the interface essentially makes the interface stationary although the mixing layer continues to evolve.

In Figures 5.7-5.8 we display more detailed diagnostics for an interaction of a strong Mach 10 shock with a randomly perturbed light-to-heavy interface with density ratio 3. The mixing

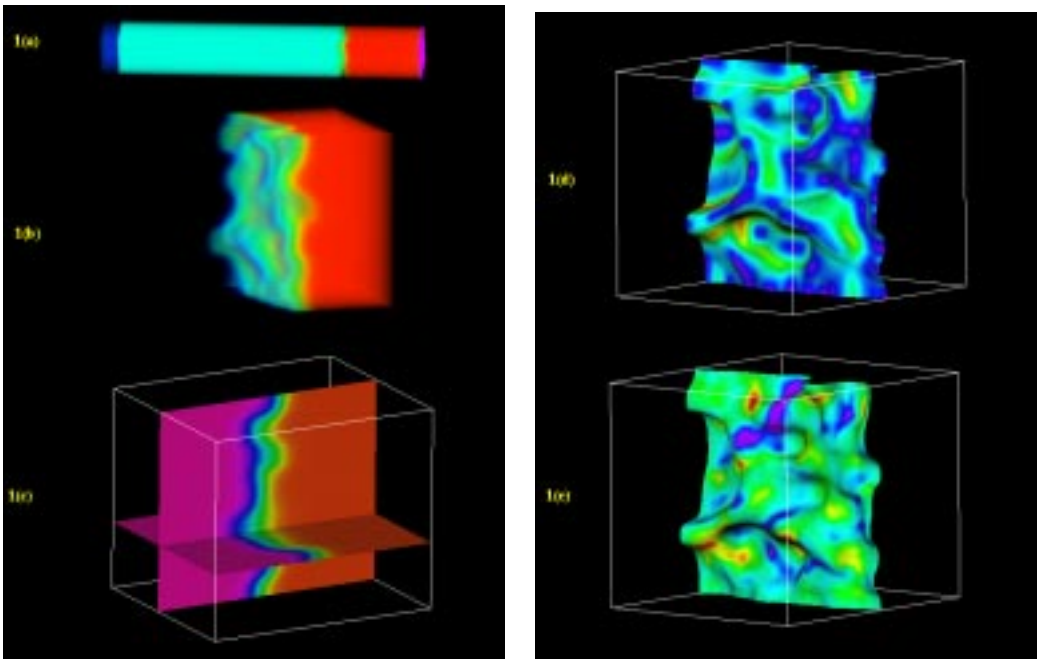

Figure 5.7: Snapshots of density and vorticity at $t = 1.46$ (prior to reshock) for simulation of a strong shock ($M = 10$) Richtmyer-Meshkov instability; see text for details.

layer increases in thickness very slowly before the reshock. This is followed by the reshock event and a sharp increase in the width of the layer. This increase is also accompanied by a large increase in both the stream-wise vorticity and the vorticity magnitude. Figure 5.7 shows a visualization of the layer prior to the reshock event. Parts (a-c) of the figure are renderings of the density field. Parts (d-e) show the interface colored by the stream-wise and maximum vorticity respectively. Figure 5.8 displays a similar set of diagnostics but at a time after the reshock. Note that significantly more mixing has taken place as indicated by the density and vorticity renderings. Of special interest is the formation of plumes. In future work we will be making use of the Responsive Work Bench to further visualize and analyze the plume structures which signify mixing. In particular, it is of interest to understand whether the geometry of the mixing is similar to that described in our work on incompressible Rayleigh-Taylor mixing in section 5.7.

Finally in Figure 5.9 we compare the growth rates for 2-D vs. 3-D instability. It is interesting to note that the growth rates in the early stages of the flow (just after shock-contact interaction) are not dramatically different from the corresponding two-dimensional results. However, a large difference is seen after the reshock event, indicating the importance of three-dimensional vortex dynamics in driving the mixing.

5.5 Shock-vortex interaction

An important phase of the development of shock initiated compressible turbulence occurs when the shock passes through the region of vorticity generated by its initial passage through

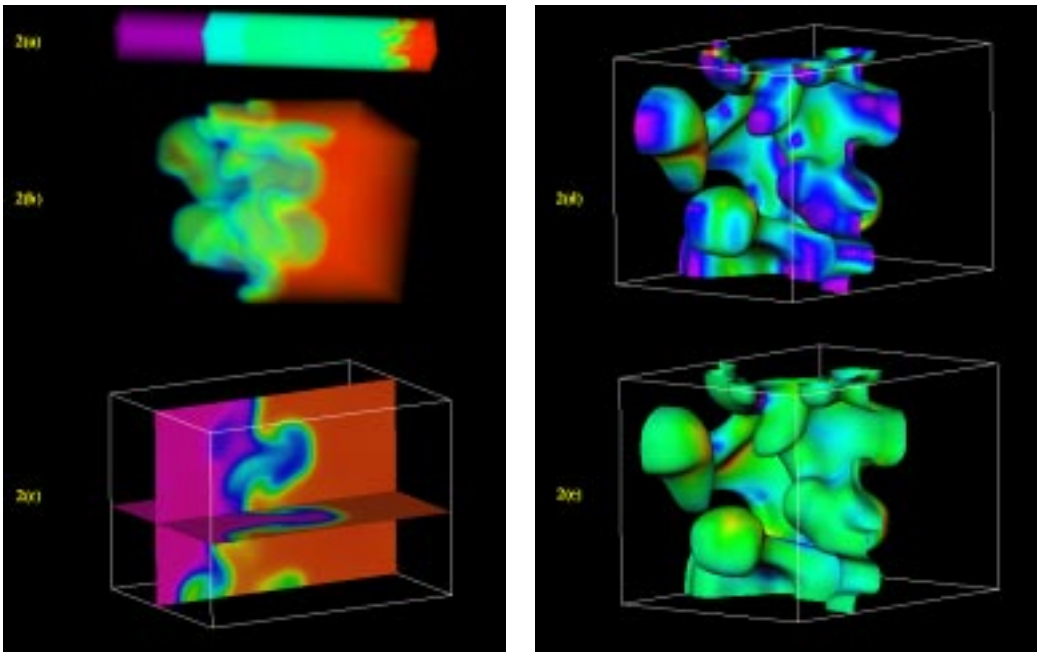

Figure 5.8: Snapshots density and vorticity at $t = 2.92$ (post reshock) for simulation of a strong shock ($M = 10$) Richtmyer-Meshkov instability; see text for details.

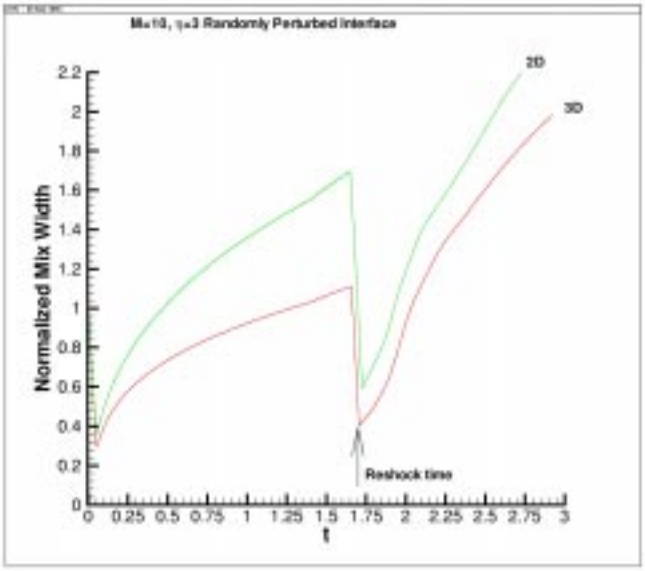

Figure 5.9: Comparison of 2-D vs. 3-D growth rates for strong shock Richtmyer-Meshkov instability

the density gradient. This is the so-called reshock phase and entails a strong shock vortex interaction.

An initial investigation of the shock-vortex interaction has been accomplished using the *Amrita* environment. Two integration schemes have been applied: a second order Godunov

based scheme and a kinetic theory based scheme known as the Equilibrium Flux Method (EFM)[85]. The latter scheme is a true UN-split solver in any spatial dimension and is very robust in the presence of strong shocks.

The initial condition used in this study is a Mach 2 shock which impinges on a vortex layer which is constructed using a compressible variant of the Stuart vortex. The Stuart vortex is a steady periodic solution of the Euler equations. It is a solution of the 2-D Euler equations and is given by

$$\psi(x,y) = \ln\left(K\cosh y + \sqrt{K^2-1}\cos x\right) \tag{5.1}$$

where $\psi(x,y)$ is a stream function. The compressible variant satisfies the two dimensional steady compressible Euler equations written below for the stream function ψ and the density of the flow ρ:

$$\nabla^2\psi - \frac{1}{\rho}(\nabla\psi\cdot\nabla\rho) = -\rho^2 V(\psi), \tag{5.2}$$

$$\frac{1}{2\rho^2}(\nabla\psi)^2 + \frac{A\gamma\rho^{\gamma-1}}{\gamma-1} = H_0 - \int_\infty^\psi V(\psi')d\psi'. \tag{5.3}$$

Here V is the vorticity distribution inside the vortex and A and H_0 are constants.

The compressible variant of the Stuart vortex has been computed numerically by Pullin, Moore, and Meiron [86]. An advantage in using this type of initial condition in our studies is that it provides an unambiguous value of the initial vorticity until the shock interacts with the vorticity layer. Other initial conditions would entail some evolution which would change the local vorticity distribution. The compressible Stuart vortex produces a free stream far field flow which is of the shear layer type in that it asymptotes to equal and opposite values of velocity at large distances. This velocity can be used as a measure of the shear layer strength. In our studies we have been able to generate Stuart vortices with free stream Mach numbers of $M = 0.6$. Thus there can be substantial compressible effects in the core of the Stuart vortex.

In studies performed to date the ratio of normal velocity difference across the shock is comparable to the shear velocity across the vortex. The shock therefore interacts strongly with the vortex layer. This is demonstrated in Figures 5.10 where a Schlieren image of the density is presented. Figure 5.11 depicts the computed vorticity. The figures show clearly the diffraction of the shock and the complicated shock patterns which result. In the future we will be conducting a more through investigation of the parameter space for the shock vortex interaction and investigating the theoretical modeling of the amplification of the vorticity by the shock interaction. We will also extend our investigation to the realm of three-dimensional shock vortex interactions.

Our goal here is to perform a very highly refined series of investigations that can be used to help diagnose our Large Eddy Simulation work (LES). These detailed simulations of the shock-vortex interaction will provides us with important diagnostic information on the shock-vortex interaction. It is anticipated that direct comparison can then be made using the proposed LES model for compressible turbulence. The detailed simulations will be invaluable in diagnosing how well our proposed LES model based on the dynamics of compressible vortices performs in predicting the enhancement of the sub-grid vorticity by shock waves (see Section 5.6 below).

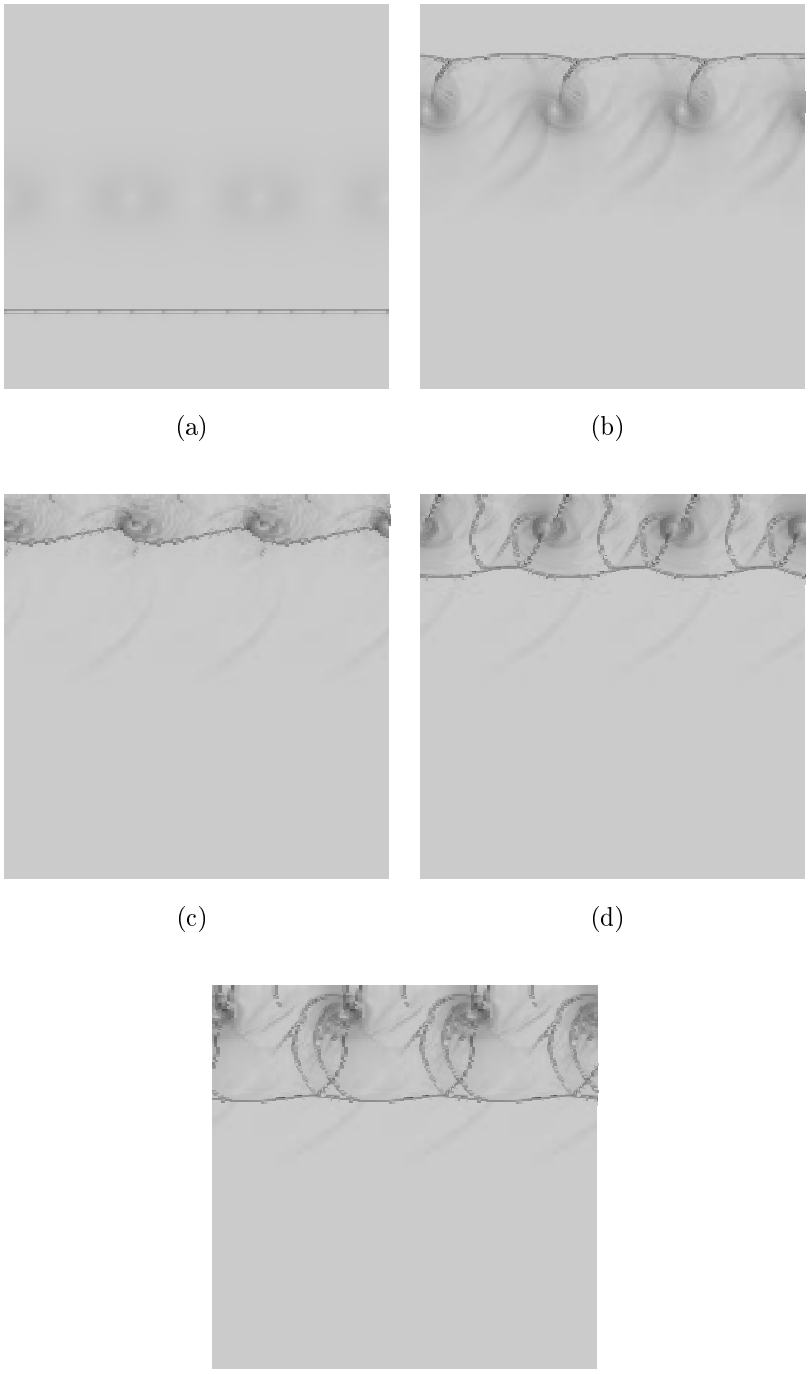

(a) (b)

(c) (d)

(e)

Figure 5.10: Schlieren images of density for shock vortex interaction

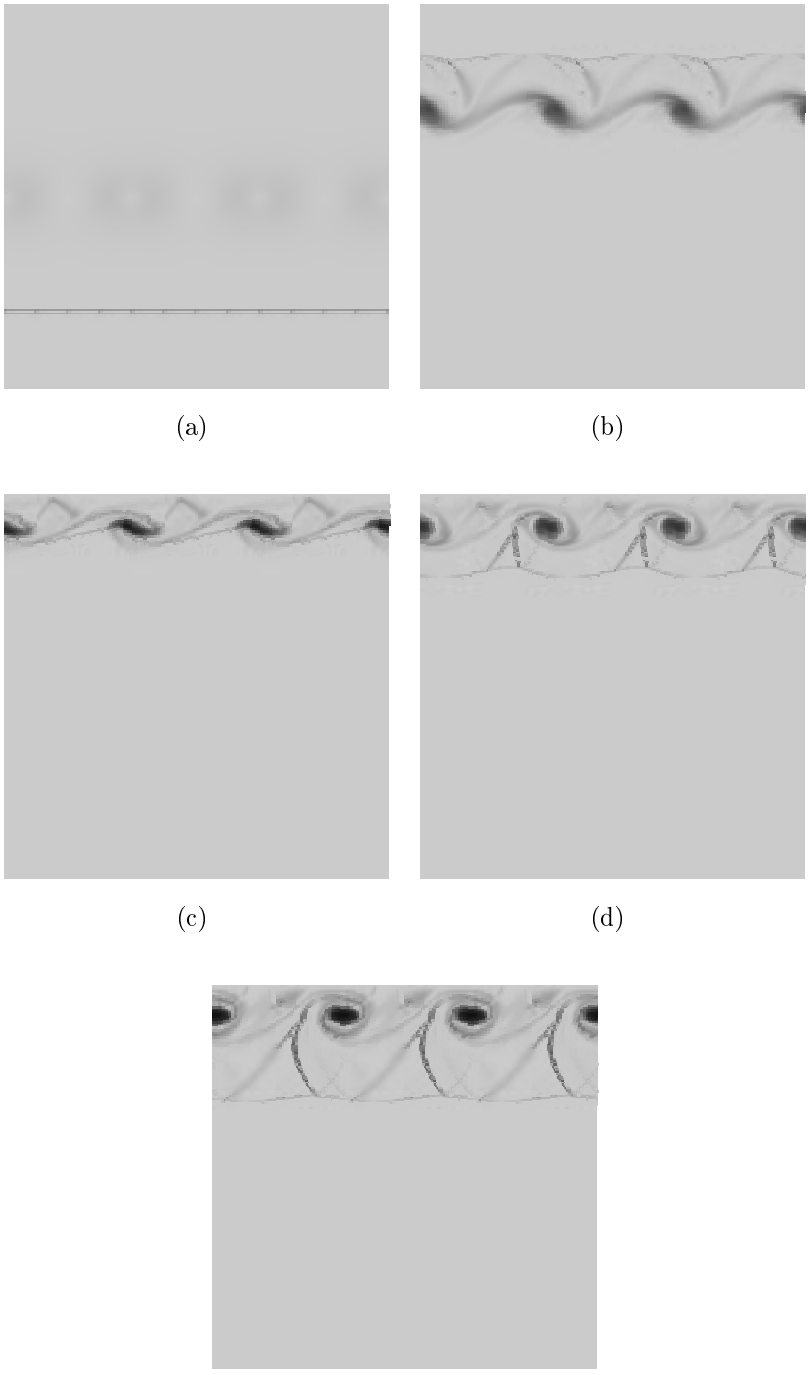

(a) (b)

(c) (d)

(e)

Figure 5.11: Greyscale images of vorticity field for shock vortex interaction

5.6 Large-eddy simulation of turbulent flows

Work has been initiated on the development of a version of the stretched-vortex subgrid-stress (SGS) model for large-eddy simulation (LES) of compressible flows. The idea is to extend the SGS model of Pullin and Saffman [87]. This is a structural model based on the key assumption that the subgrid structure consists of straight, stretched vortices, aligned within cells of the resolved field in a way that depends on the local resolved rate-of-strain tensor. The resulting subgrid stresses are proportional to the subgrid kinetic energy K and the subgrid component of the total local dissipation ϵ is equal to the product of K and the component of the resolved rate-of-strain tensor aligned with subgrid vortices.

We briefly describe below the main ideas behind this approach. We begin by examining the incompressible Navier-Stokes equations in filtered form given by

$$\frac{\partial \widetilde{u}_i}{\partial x_i} = 0, \tag{5.4}$$

$$\frac{\partial \widetilde{u}_i}{\partial t} + \frac{\partial}{\partial x_j}\left(\widetilde{u}_i \widetilde{u}_j\right) = -\frac{\partial \widetilde{P}}{\partial x_i} - \frac{\partial \tau_{ij}}{\partial x_j} + \nu \frac{\partial^2 \widetilde{U}_i}{\partial x_j \partial x_j} \tag{5.5}$$

where

$$\widetilde{u}_i(\mathbf{x}, t) = \int G(\mathbf{x} - \mathbf{x}') u_i(\mathbf{x}', t) \mathbf{x}'. \tag{5.6}$$

and

$$\tau_{ij} = \widetilde{u_i u_j} - \widetilde{u}_i \widetilde{u}_j \tag{5.7}$$

The subgrid motion is represented by a vortex within each cell. With this model the subgrid stresses are

$$T_{ij} = K\ (\delta_{ij} - e_i\, e_j)\,, \tag{5.8}$$

$$K = \int_{k_c}^{\infty} E(k)\, dk. \tag{5.9}$$

A Kolmogorov model for the subgrid energy spectrum is used to provide $E(k)$:

$$E(k) = \mathcal{K}_0\, \epsilon^{2/3}\, k^{-5/3}, \quad k\,\eta \le J, \quad \eta = \left(\frac{\nu^3}{\epsilon}\right)^{\frac{1}{4}} \tag{5.10}$$

$$E(k) = 0, \qquad k\,\eta > J. \tag{5.11}$$

where $\mathcal{K}_0$ is the Kolmogorov prefactor and η is the Kolmogorov scale. In this scaling $J = 1$. The representative vortices in each cell (or at grid points) are assumed to be aligned with the principal eigenvector of the resolved rate-of-strain tensor $\widetilde{S_{ij}}$.

In the physical space version of this model the information about the energy spectrum is obtained by examining a structure function in physical space. From this local information it is possible to estimate both the subgrid stress and dissipation. No double filtering is needed in order to estimate model parameters and direct estimates of the subgrid contribution to turbulent transport are provided.

A version of the model for incompressible flow which operates in Fourier space has been tested for both decaying turbulence and for turbulent channel flow. These tests are useful

owing to the large direct-numerical-simulation (DNS) data base that exists for incompressible flow. Figure 5.12 shows the profiles of the mean stream-wise velocity and the root mean square (RMS) quantities for a turbulent channel flow. The flow is bounded by two parallel rigid walls at $z = 0$, $z = L$. The Reynolds number Re_τ, based on the wall friction velocity and the channel half width L is 180. This computation used a Galerkin spectral-element numerical method. The results are superior to those produced with the Smagorinsky model and give good agreement with DNS calculations at the same Re_τ.

Further progress has been made in two directions. First, we believe that the Fourier space version of the stretched-vortex model will be unsuitable for compressible-flow codes owing to the presence of shocks. To address this problem, a physical-space version (as described above) has been developed based on estimation of model parameters using the second-order velocity structure function, rather than the energy spectrum of the resolved flow. This approach has been tested in decaying incompressible turbulence using several different numerical methods including the *PRISM* [88] spectral-element method of Henderson and an implicit or "compact" finite difference method [89], with satisfactory results. The channel flow calculation is being repeated with this new model version incorporated into the *PRISM* code. Second, the appropriate LES equations have been developed in conservation form for compressible flow with a view to formulating the model for this case. The presence of compressibility necessitates the need for additional modeling terms, these being the subgrid kinetic energy, the subgrid heat flux, a subgrid triple velocity correlation and the subgrid viscous work.

We briefly describe these issues below. The compressible Navier-Stokes equations are

$$\frac{\partial \rho}{\partial t} + \frac{\partial \rho u_i}{\partial x_i} = 0, \tag{5.12}$$

$$\frac{\partial \rho u_i}{\partial t} + \frac{\partial (\rho u_i u_j + p/\gamma M^2 \delta_{ij})}{\partial x_j} = Re^{-1} \left(\frac{\partial \sigma_{ij}}{\partial x_j} \right), \tag{5.13}$$

$$\frac{\partial E}{\partial t} + \frac{\partial [(E + p/\gamma M^2) u_i]}{\partial x_i} = \frac{1}{PrRe(\gamma - 1)M^2} \frac{\partial}{\partial x_i} \left(k \frac{\partial T}{\partial x_i} \right) + \frac{1}{Re} \frac{\partial \sigma_{ij} u_j}{\partial x_i}, \tag{5.14}$$

where

$$\sigma_{ij} = \mu \left(\frac{\partial u_i}{\partial x_j} + \frac{\partial u_j}{\partial x_i} \right) - \frac{2}{3} \mu \frac{\partial u_k}{\partial x_k} \delta_{ij}, \qquad \mu = T^{0.76}, \tag{5.15}$$

$$E = \frac{p}{(\gamma - 1)\gamma M^2} + \frac{1}{2} \rho (u_j u_j), \tag{5.16}$$

$$p = \rho T, \tag{5.17}$$

and k is the dimensionless thermal conductivity. Here the equations have been scaled relative to a characteristic length scale L, velocity scale U, density ρ_0, sound speed c_0, energy ρU^2, and pressure $p_0 = \rho_0 c_0^2/\gamma$. The reference viscosity and conductivity are μ_0 and k_0, respectively and the Reynolds number and Mach number are given by $Re = \rho_0 UL/\mu_0$, $M = U/c_0$.

Using Favre filtering where $\widetilde{q} = \bar{\rho} q / \bar{q}$ the continuity equations become

$$\frac{\partial \bar{\rho}}{\partial t} + \frac{\partial \bar{\rho} \widetilde{u}_i}{\partial x_i} = 0. \tag{5.18}$$

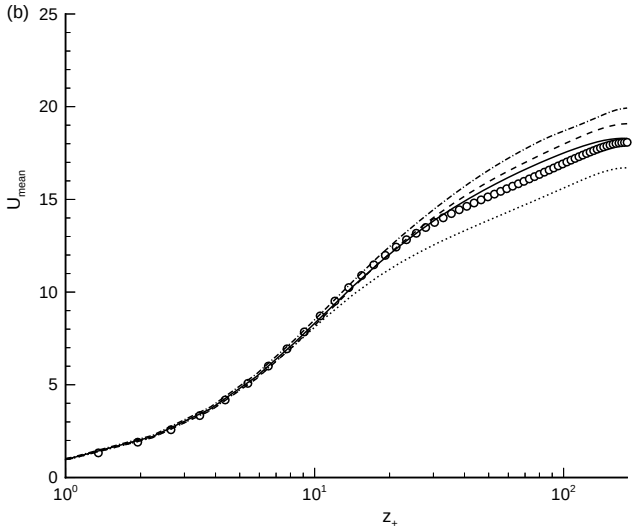

(a)

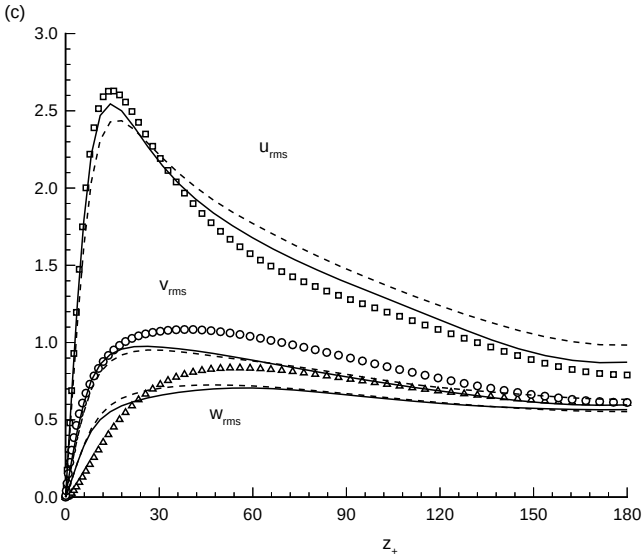

(b)

Figure 5.12: Channel flow at $Re_\tau = 180$. (a) Mean stream-wise velocity. Symbols, DNS [90]. Solid line, dashed line - two different vortex orientation models, dot-dashed line - Smagorinsky model with Van Driest wall damping, dotted line - under-resolved DNS. (b) RMS turbulence quantities.

The momentum equations become

$$\frac{\partial \bar{\rho}\widetilde{u}_i}{\partial t} + \frac{\partial(\bar{\rho}\widetilde{u}_i\widetilde{u}_j + \bar{p}/\gamma M^2\delta_{ij})}{\partial x_j} = Re^{-1}\left(\frac{\partial \widetilde{\sigma}_{ij}}{\partial x_j}\right) - \frac{\partial T_{ij}}{\partial x_j}, \tag{5.19}$$

where

$$T_{ij} = \bar{\rho}(\widetilde{u_i u_j} - \widetilde{u}_i\widetilde{u}_j) \equiv \bar{\rho}\,\tau_{ij}.$$

and the energy equation becomes

$$\begin{aligned}
\frac{\partial \bar{E}}{\partial t} + \frac{\partial(\bar{E} + \bar{p}/\gamma M^2)\widetilde{u}_i}{\partial x_i} &= \frac{1}{PrRe(\gamma-1)M^2}\frac{\partial}{\partial x_i}\left(k\frac{\partial \widetilde{T}}{\partial x_i}\right) && (5.20)\\
&\quad + Re^{-1}\frac{\partial(\widetilde{\sigma}_{ij}\widetilde{u}_j)}{\partial x_i} && (5.21)\\
&\quad - \frac{1}{(\gamma-1)M^2}\frac{\partial(\bar{\rho}q_i)}{\partial x_i} && (5.22)\\
&\quad - \frac{1}{2}\frac{\partial[\bar{\rho}(\widetilde{u_j u_j}u_i - \widetilde{u_j u_j}\widetilde{u}_i)]}{\partial x_i} && (5.23)\\
&\quad + Re^{-1}\frac{\partial(\widetilde{\sigma_{ij}u_j} - \widetilde{\sigma}_{ij}\widetilde{u}_j)}{\partial x_i}, && (5.24)
\end{aligned}$$

where

$$\begin{aligned}
\bar{E} &= \frac{\bar{p}}{(\gamma-1)\gamma M^2} + \frac{1}{2}\bar{\rho}(\widetilde{u}_j\widetilde{u}_j) + \frac{1}{2}\bar{\rho}(\widetilde{u_j u_j} - \widetilde{u}_j\widetilde{u}_j), && (5.25)\\
q_i &= \widetilde{Tu_i} - \widetilde{T}\widetilde{u}_i, && (5.26)\\
\overline{p} &= \overline{\rho}\,\widetilde{T}. && (5.27)
\end{aligned}$$

The subgrid scale stresses are again in this extension of the incompressible model given by

$$\tau_{ij} = K\,(\delta_{ij} - e_i\,e_j)\,, \qquad K = \int_{k_c}^{\infty} E(k)\,dk.$$

The SGS triple correlation and the SGS viscous work term are expected to be negligible, while the subgrid kinetic energy is already available within the stretched-vortex SGS model. A model for the subgrid heat flux has been formulated wherein the heat flux is modeled as the subgrid convection of a passive scalar by a nearly axisymmetric subgrid vortex.

In order to test this scheme a 3D compressible flow code has been written (Ravi Samtaney, NASA Ames) based on a variable-order compact Padé finite-difference scheme. Periodic boundary conditions in 3D are assumed, although this can be relaxed. This code has been tested by computing the decay of compressible box turbulence at a Mach number $M_{rms} = 0.1$, Figure 5.13 shows a view of the iso-surfaces of the vorticity at the RMS value, twice the RMS value and three times the RMS value. An interesting feature of this visualization is the apparent transition from sheets to tubes as one samples higher levels of the vorticity. We are currently verifying this code via comparisons with Wray's calculations of decaying incompressible turbulence. An issue to be addressed in the future is the performance of such turbulence models in the presence of shock waves. A related issue is the use of low order Godunov type methods in compressible turbulence calculations.

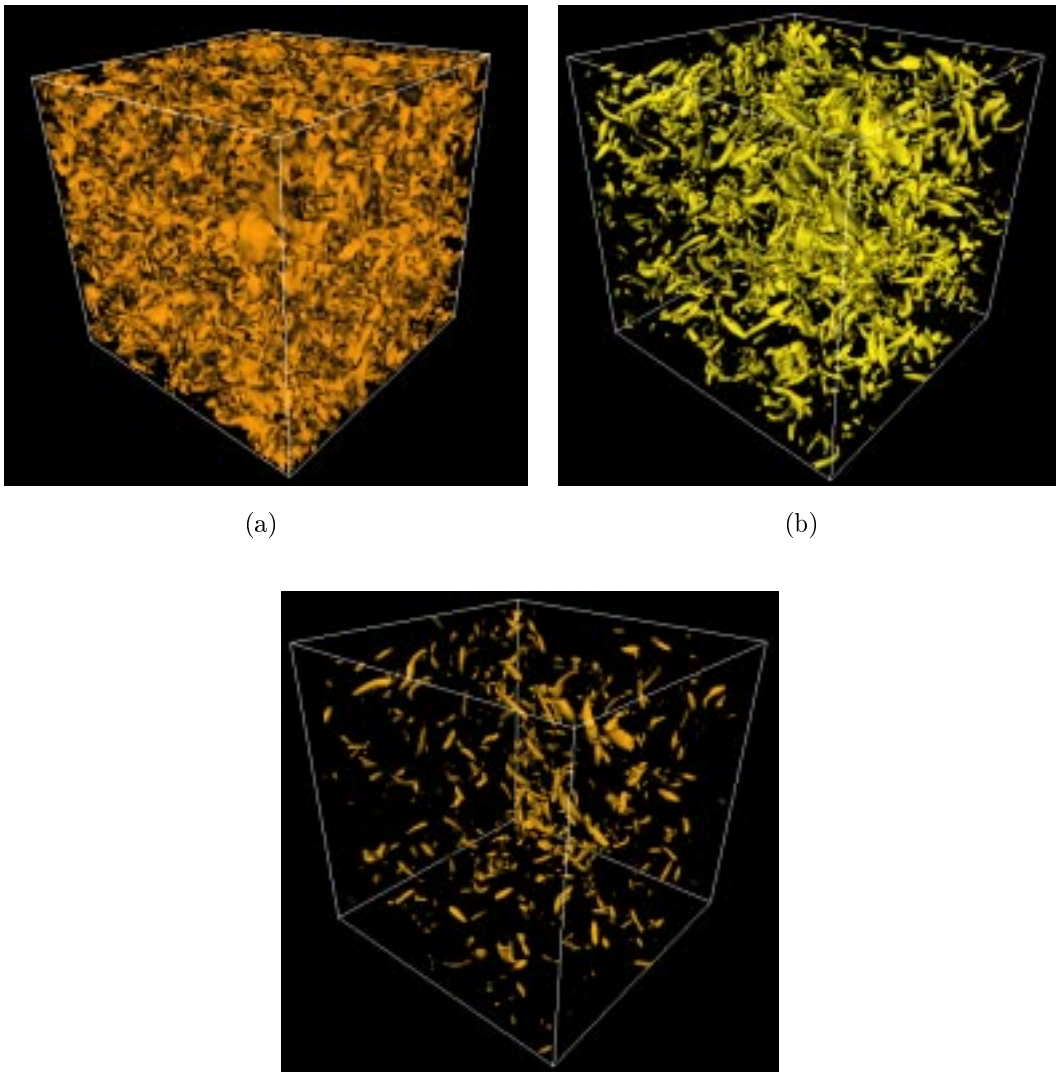

(a) (b)

(c)

Figure 5.13: Vorticity isosurfaces for 192^3 computation of decaying compressible turbulence, $M_{rms} = 0.15$ using a 10'th-order compact Padé scheme. (a) $\omega = \omega_{rms}$, (b) $\omega = 2\omega_{rms}$, (c) $\omega = 3\omega_{rms}$.

5.7 Incompressible Rayleigh-Taylor Turbulence

Work has been initiated on the study of mixing in incompressible Rayleigh-Taylor and Richtmyer-Meshkov turbulence. While this was not a part of the original proposed research plan, our work on compressible Richtmyer-Meshkov instability has shown that under shock interaction the divergence of the flow is large but then rapidly decays once the shocks have propagated away from the stratified region. Thus parts of the flow actually consist of largely incompressible regions of stratified flow. We have therefore initiated a series of investigations aimed at understanding incompressible density-stratified turbulent flow.

A particular focus of this work is the study of mixing in multi-phase flows. This is not modeled correctly by classical turbulence theories which are based on spectral approaches in describing turbulent flow rather than geometric approaches. Such spectral approaches do not lend themselves well to the formulation of mixing models. In addition a proper model of fluid mixing is essential in the simulation of high Reynolds number flows. Mixing in fact influences the dynamics strongly in variable density flows and occurs at the smallest spatial length scales which cannot be resolved by direct numerical simulation. Insights gathered from detailed studies of mixing in incompressible stratified flows can be used to formulate more accurate turbulent models.

In collaboration with Andy Cook at LLNL [91] we have analyzed the structures generated by the Rayleigh Taylor instability of two miscible fluids. Cook's simulation is a high resolution study performed on the LLNL ASCI Blue machine. These calculations use a resolution of $512 \times 256 \times 256$. Density fields at a variety of times were stored on the Caltech HPSS system. Post-processing of this data was performed to examine the density isosurfaces and other diagnostics of the flow field. An example of the plume like structures which dominate the flow are seen in Figure 5.14

The post-processing of this data and its subsequent visualization produced many new insights. In particular our diagnostics indicate a similarity of the geometrical structures with those measured experimentally in other high Reynolds number flows such as turbulent jets. In Figure 5.15 we provide some examples of the kind of diagnostics produced in our investigation. Shown in this figure is the density field at the mid-height plane. At the right of each sub-figure are the levels sets corresponding to the density level $\rho = 2$. At late times it can be seen that the nature of the fluid structures in the mid-plane has changed due to local instabilities thought at present to be of the Kelvin-Helmholtz type. Isoscalar surface measurements of the type visualized and analyzed in this work are found to be more complex then self-similar fractals. In particular they exhibit a scale-dependent coverage dimension for 2-D slices of scalar level sets that increases with scale, from unity at small scales to 2 at large scales.

In order to ensure that the geometrical measurements made on this flow are not reflecting numerical artifacts we have also initiated the construction of an alternative simulation methodology for stratified incompressible flows of this type. We are employing a very high order spectral simulation based on the spectral element method due to R. Henderson. The spectral code (*PRISM*) (discussed in the previous section) has the ability to refine the flow in various regions using nonconforming spectral elements which are in turn used to provide adaptive refinement according to user selected criteria. A parallel implementation of this capability is underway and we are also in the process of integrating *PRISM* in to our virtual test facility through the use of the scripting interface. An example of the capabilities of *PRISM* is shown in Figure 5.16. Here we simulate the buoyant rise of a drop of fluid surrounded by a fluid of higher density. In future work we will use *PRISM* to perform highly resolved simulations a fully three dimensional Rayleigh Taylor unstable fluid. These results will be then used to elucidate further aspects of the structural dynamics of unsteady stratified turbulence and to provide further input for the development of turbulence models which properly incorporate mixing.

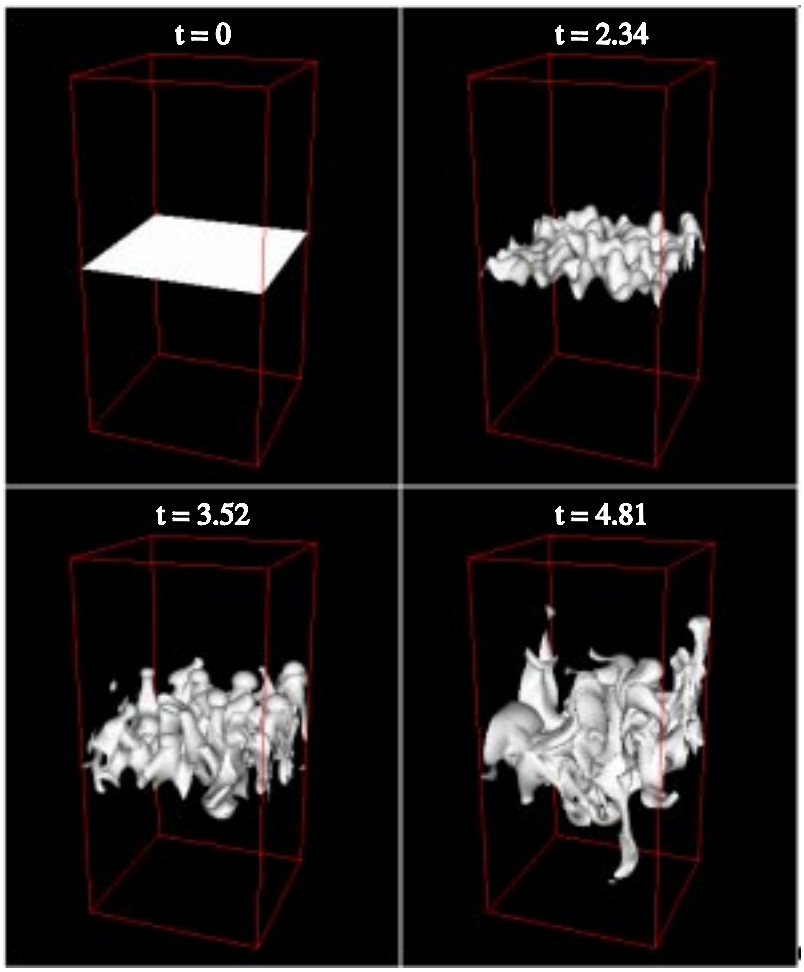

Figure 5.14: Isosurfaces of density at various times for the Rayleigh-Taylor instability of two miscible fluids. $\rho = 3$ fluid initially on top, $\rho = 1$ fluid on the bottom. Plot of $\rho = 2$ isosirface at indicated times.

5.8 Multi-scale phenomena in turbulence simulations

We have undertaken an investigation of a generic approach to subgrid modeling. The objective is to develop a general framework for the analysis of subgrid modeling for a variety of flows, both compressible and incompressible [92]. Our initial efforts are centered around the development of a suitable regularization scheme for both scalar transport and incompressible flow. Later efforts will be directed towards extensions of these ideas to flows with shock waves.

Our initial focus centers on the subgrid modeling (for LES) of both the scalar advection equation as well as the advection of mass, momentum and energy as expressed in the Navier-Stokes equations. In other previous efforts, the subgrid terms are usually modeled via a Smagorinsky type model for the subgrid stress. Our analysis of the scalar transport equation points to a quadratic dependence on the strain and rotation tensors for the subgrid stresses. We have applies a new filtering approach to the scalar advection equation which provides exact subgrid transport for a smooth velocity field. The approach is perfectly generic and

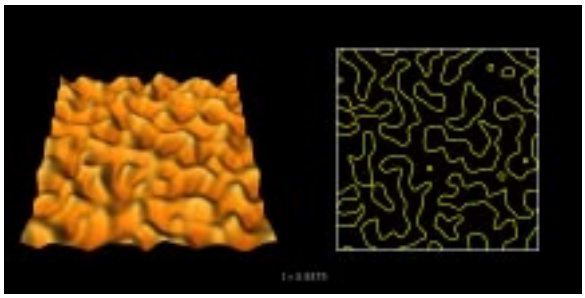

(a)

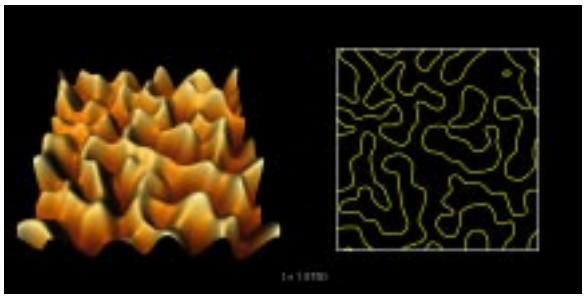

(b)

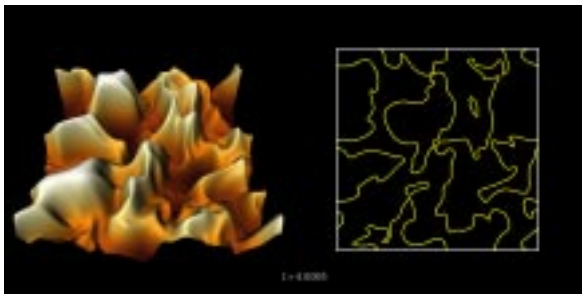

(c)

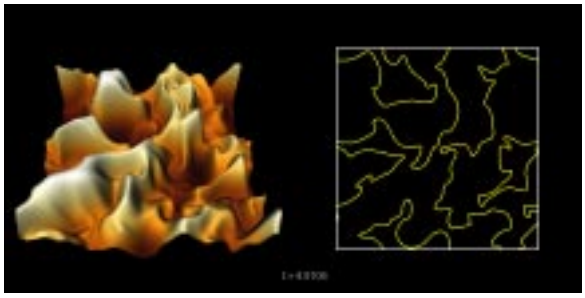

(d)

Figure 5.15: Density field at mid-height plane for Rayleigh-Taylor instability of two miscible fluids. At the right of each figure are the level sets of the density corresponding to $\rho = 2$

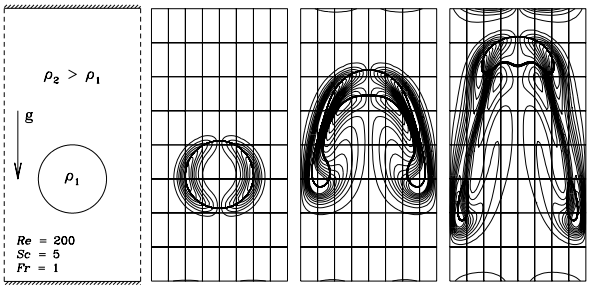

Figure 5.16: Isosurfaces of density at various times of a rising buoyant 2-dimensional droplet. Simulation performed using spectral element methods

applied to all forms of multi-scale behavior.

One important aspect of this approach, however, is that the resulting equations for the filtered quantities are ill-conditioned and some stabilization procedure is required in order to obtain meaningful results. The regularization scheme we have adopted is the application of a particle method. We have applied this idea to the filtered scalar transport equation. This approach provides for a rational regularization of the ill-conditioned terms. We have tested the approach on chaotic transport by 2-D flow. Work is in progress on a three-dimensional extension of these ideas.

We have also initiated work on the extension of these ideas to flows containing shocks and/or contact discontinuities. At present this work is limited to nonlinear hyperbolic systems.

5.9 Personnel

- Faculty
  - Dan Meiron
  - Tony Leonard
  - Paul Dimotakis
  - Dale Pullin
  - Brad Sturtevant
  - Greg Miller (Chicago)

- Research Staff
  - Ravi Samtaney
  - Ron Henderson
  - Branko Kosovic
  - James Patton
- Graduate Students
  - Gerard O'Reilly
  - Tobias Voelkl
  - Piet Moeleker
  - Jerry Shan
- Undergraduate Students
  - Gabe Powers

Chapter 6

Computational and Computer Science

6.1 Introduction

The computational and computer science program was obtained by starting with the overall goals of the Virtual Test Facility for Simulation of Dynamic Response of Materials and working backward to determine strategic research advances necessary to achieve these goals. Six areas critical to the success of the facility were identified:

- Problem-solving environments for distributed collaborative computing,
- Composition and integration of diverse, complex computational modules,
- Methods for exploiting current and future ASCI system architectures,
- Scalability and load balancing of fundamental algorithms,
- Geometric modeling and advanced visualization for model validation,
- Scalable parallel input and output.

Integrating diverse, complex computational modules while ensuring scalability and portability across ASCI computing environments is a recurring theme in the development of the facility. Each of the above research areas, starting with the distributed problem-solving environment as a foundation, contributes to the integration tasks and supports the construction of the facility.

The first year milestones for Computational and Computer Science listed in the revised proposal were:

- Initiate construction of 2-D prototype of virtual facility using *Amrita* as an integrating framework with existing solid dynamics and detonation capabilities. Computational and Computer Science researchers will increase participation in this activity as staff is recruited.
- Implementation of parallel fluid and solid dynamics codes. Scalable linear algebra algorithms will initially be introduced into selected materials codes

- ScaLAPACK ported to ASCI platforms. ScaLAPACK will also be installed on CACR systems. Other scalable parallel linear algebra algorithms will be evaluated and installed as appropriate
- Subdivision representations will be introduced into the geometric modeling for solids
- PABLO used to characterize end-to-end parallel I/O for ASCI applications. PABLO will be installed on the ASCI Blue systems and the CACR HP Exemplar. Selected ASCI applications will be instrumented, measured and analyzed. Selected Caltech project computational modules will be instrumented, measured and analyzed
- RIO, SILO, and other APIs will be evaluated
- A parallel application-to-archive testbed will be established using the HP Exemplar and HPSS
- Initial experiments with threads libraries using Caltech project computational modules. Computational modules from materials properties will be the first candidates.

The following text reports completion of the above milestones with two exceptions.

- It was deemed premature to initiate instrumenting, measuring and analyzing the application components of the Virtual Test Facility. Instrumentation of selected application components will be initiated during the coming year. Measurement and analysis of these components, plus components instrumented earlier under an NSF Grand Challenge, will be initiated.
- A parallel application-to-archive testbed was not established due to delays in recruiting postdoctoral staff and acquiring an upgrade of the CACR IBM SP to support HPSS. A postdoctoral scholar was recruited during the last quarter. An upgrade of the CACR IBM SP is now anticipated in late 1998 or early 1999.

6.2 Problem-solving environments for distributed collaborative computing

The activity in problem-solving environments for distributed collaborative computing is currently being pursued primarily by the Globus group at the Information Sciences Institute of the University of California and by Indiana University. The ISI group has focused on making Globus available at Caltech and evaluating performance on ASCI platforms, while the Indiana group has explored longer term approaches to PSE construction.

The primary activity of the Globus group has been to provide support for the Globus Grid Toolkit on the ASCI platforms that are being used by the ASCI project at Caltech. Of particular concern was support for the HP Exemplar and SGI Origin 2000 at Caltech. During the past year, we have ported Globus to these platforms and have supported deployment and maintenance. In collaboration with the University of Chicago Alliance Center (the Flash

Center), we have contributed to the development of a scalable multi-protocol implementation of the Message Passing Interface (MPI) for the ASCI Blue Pacific environment. One challenge of implementing MPI in this environment is the range of communication methods that are available: from shared memory within a SMP node, to low-latency message passing between nodes within a system, and high-latency networking between systems. Another problem facing MPI implementations is scalability to a large number of nodes. By exploiting the multi-method protocol capabilities of the Globus communication library, both of these issues can be addressed. Building on Globus components, members of the Chicago Flash Center have constructed an MPI implementation and ported it to the LLNL computer. By using a shared memory protocol module developed during the past year by the Globus group at ISI, this implementation is able to surpass the performance of the vendor's MPI on several of the test cases.

Efforts in the past year by Indiana University have concentrated on developing software component architectures for scientific computing and infrastructure tools for secure distributed computing and communications. In the period from September 1997 to March 1998, we created a prototype component architecture for a specific application, the solution of large sparse linear systems of equations. The Linear System Analyzer (LSA) prototype has components which encapsulate sparse matrix manipulations such as scaling, reordering, filtering based on value, providing basic information, and solving. LSA [93, 94, 95, 96] goals included [97]

- create an architecture that provides a GUI-based, visual programming model for connecting high performance codes;
- provide a tool useful for an important area of ASCI research, the development of solution strategies for linear systems;
- provide a tool that can be used for teaching, and for applications scientists to manipulate and work with sparse matrix codes without having to be experts; and
- provide ready access to high performance architectures

The design used Java for a front-end GUI, which orchestrated the various components, let a user graphically connect them together as desired, and kept track of the connections, components, and their states. No actual numerical computing occurred within Java, however. Each component is actually an HPC++ process, which in turn either directly carries out the numerical computations or calls the Fortran or C routines which do the computation. To make it easy for applications scientists to add components to the system, generic wrapper code is provided. This wrapper code consists of generic component functions which all LSA components must provide, such as "read a linear system from my input port", "send a linear system", "execute", "set internal parameters", etc. For particular components the user then only need provide a small amount of code to actually invoke the computational code in the component. HPC++ was used because it allows remote method invocation (RMI), which starts up processes on distributed machines and provides functions for communicating with those processes. In this way components can run on various networked supercomputers without the user having to write any communications code. The actual run-time system used

by HPC++ for communications is Nexus , which provides efficient communication between heterogenous machines. HPC++ was also used because of its importance to other ASCI projects at LANL. A major accomplishment of the LSA project was the ability to seemlessly invoke methods from the Java front-end, which are executed by HPC++, and to have errors and exceptions raised in one language caught and handled by the other.

Although the LSA has been successful, it is limited to one application area. Components in the LSA can only be connected as a tree, because it is necessary to be able to undo some matrix operations such as scaling and reordering in the reverse order of the operations. Over the past eight months, we have been working with the Common Component Architecture group, consisting of representatives from ORNL, LANL, Sandia, LLNL, and ANL to develop standards for a more general component architecture capable of supporting a broad range of DOE high performance systems. The CCA has developed a general model for component ports as the key interface between components. This will allow software components developed within one component framework to be used in other frameworks. This model was presented at the SC98 conference. Based on this, we have created the Component Architecture Toolkit (CAT), which is the first component system to incorporate the current CCA standards. The CAT provides the ability to connect components in an arbitrary way, creating computational graphs that include cycles. It uses the port model, which should allow our components to be seemlessly integrated into other frameworks. The CAT uses the Globus framework to locate and manage hardware resources on which to run components. Most importantly, the CAT introduces a new conceptual model for Globus distributed computing. Both software and hardware components are treated as distributed resources which a user locates on the network using a distributed database system in a single framework. A user locates a software component using an LDAP GUI mechanism. The GUI then consults the Globus Metacomputing Directory Service for machines which can run the software component. Once found, the component is instantiated on the remote machine and can be wired together with other components. Although still a prototype, the CAT system was used at SC98 for a High Performance Computing Challenge demonstration. This project tied together a parallel industrial finite element code, a high-end 3D immersive visualization tool, and various sparse linear solvers in an integrated parallel simulation of a complex engine part from Pratt & Whitney. The project won an award for "Best Industrial Collaboration".

6.3 Composition and integration of diverse, complex computational modules

The Software Integration group, headed by Michael Aivazis (Caltech, CACR) and including representatives from each application area, is a cross-project activity with weekly group meetings supplementing the continuing interaction with specific applications. The challenge facing the Software Integration group during the first year of the project was to assemble the components of the Virtual Testing Facility (VTF) as parts of a common framework. These components of the VTF, which were identified as part of the original proposal, are sophisticated, state of the art simulation engines in their respective research areas that were developed independently of each other and were designed as stand-alone applications. It

was anticipated that each engine would have to undergo an architectural assessment and that some modifications would be necessary. The composition of diverse codes at this scale presents the following conceptually orthogonal challenges:

- The transition from stand-alone application to component of a framework implies that the engine must relinquish control of the simulation cycle and essentially become event-driven. Even though this is not the only possible solution to this problem, it is the architecture that imparts the most flexibility to the overall implementation.
- The coupling of the simulation engines requires significant flux of information at their respective boundaries, which implies a significant level of compatibility of data representations. If such compatibility is not already present, one must construct a layer that facilitates the exchange of the required information.
- Each of the simulation engines is in itself a medium-sized software project (roughly 100 KLOC) that consists of a mix of source code written in a variety of programming languages with different conventions, building and testing practices. Their composition into an overarching application requires careful management of the software development effort and presents issues that are not normally faced by academic research groups.

The remainder of this report consists of a brief overview of the progress made in each of the above areas.

6.3.1 Composition framework

The originally proposed candidate for the VTF coordination/composition framework was James Quirk's *Amrita* . *Amrita* is designed to simplify and, wherever possible, automate many of the repetitive tasks that are part of the full development cycle of scientific computation. It provides uniform access to many of the system level facilities and a scripting environment designed to drive simulation engines. In particular the fluids engine `amr_sol` is very tightly integrated in this environment. Both the environment and the code are being successfully used by the HE group. Its success as an investigative tool and the fact that it can serve as a composition framework made *Amrita* a natural candidate for the VTF. However, its wider acceptance by the collaboration was very slow.

The Executive Committee of the collaboration responded to this situation by commissioning an in-depth assessment of *Amrita* 's suitability as the integrating component of the VTF. This assessment validated most of *Amrita* 's design decisions. According to the assessment, *Amrita* 's most attractive feature was the presence of an interpretive layer, which minimizes the programming overhead required by users, provides an excellent educational tools and makes the system easily accessible to testing and validation harnesses. In addition, the architectural demands placed by *Amrita* on the component engines were found to be sound in principle.

However, the assessment uncovered the following problems:

- The coupling between the framework and the computational engines must be more flexible and less intrusive. It should be possible to develop the framework and the engines in parallel, with only minimal interference of the former with the research efforts of the engine developers. Furthermore, it should be possible to leverage the substantial effort required to integrate these engines outside any given high-level framework.

- *Amrita* provides its own scripting language that the users would have to learn. This special purpose language was perceived as a barrier, partly due to the associated learning curve and partly due to the fact that its scope is limited to the *Amrita* framework and its mastery does not provide added value to the research groups.

- *Amrita* is implemented as a large (roughly 250 KLOC) collection of Perl scripts written by a single author. A project of this size requires very careful management and becomes problematic at this scale when its maintenance is entrusted to a group of developers. Significant parts of this system would have to be rewritten in a language with much more support for disciplined development than is possible in Perl.

In response to these problems, the details of the composition/coordination layer were further refined. A three-tier model has been chosen, with the simulation engines at the bottom and the interpretive layer at the top. The middle layer consists of a set of C++ classes that provide for the decoupling of the top and bottom layers. Abstract base classes provide the basic encapsulation interface, while descendant classes provide access to specific engines. This layer provides maximal flexibility by isolating both the modifications required to support a different top layer and the effort required to integrate another computational engine in a given framework.

For the interpretive layer we chose Python, a well supported, portable, robust and mature interpretive language with extensive support for modern development paradigms that is easily extensible and embeddable. Python is already in use at the national laboratories and is being actively maintained by a large community of developers.

6.3.2 Computational engines

The transition from *Amrita* to the new three-tier model for the integration of the components of the VTF had the unfortunate ramification of leaving the project without a framework implementation and no integrated simulation engines. We felt that the solid mechanics code, `adlib`, would present a greater integration challenge that the previously scripted fluid mechanics code so we focused our efforts in the direction of `adlib`.

The incorporation of `adlib` into the new framework required a careful architectural assessment of the library. The library was already sufficiently modular so that no modifications to its structure were required. We proceeded by performing a thorough memory usage and defect analysis using state of the art development tools such as Purify and Insure++. We then modified the engine's building procedure in order to generate it as a shared library and constructed the Python binding layer. Finally, we took driver code for an existing simulation of a sphere impinging on a metal plate and generated the Python script equivalent. This procedure validated all the required steps for integrating the solid mechanics code into the

VTF. Furthermore, the source code for `adlib` was ported to all the ASCI platforms. We conducted a performance analysis, identified the single-processor bottlenecks and initiated the parallelization of the code.

Two very sophisticated fluid mechanics codes, James Quirk's `amr_sol` and Ron Henderson's *PRISM*, had been successfully integrated in the *Amrita* framework. Work is now underway to recover the functionality of these engines in the new framework. In addition, we are currently studying the suitability of a variety of other fluids codes and we plan to integrate the appropriate codes, thereby extending the set of simulation engine choices.

6.3.3 Management of the software development effort

The problem of managing a software effort of this magnitude is being addressed by providing extensive support for every stage of the development life cycle.

6.3.3.1 Development infrastructure

The consistency and quality of the project source base must be evaluated continuously. To accomplish this, the software integration group is responsible for securing consensus on development policy and constructing the associated infrastructure. We have established a project wide source repository and we are in the process of implementing a full program of configuration and release management. We are implementing uniform software building procedures that our group will maintain, so that the individual research groups can be freed of this burden and be insulated from each other's practices. In an attempt to detect incompatibilities between the various components as early as possible, we are instituting regularly scheduled and automated builds, thereby ensuring that the latest version of the source base can be compiled and linked successfully. We are in the process of constructing the infrastructure required to implement large scale automated testing and validation of the source as part of the regularly scheduled builds. This includes test suites consisting of benchmark simulations with known expected behavior and regression test suites that document bug fixes.

6.3.3.2 Software craftsmanship

In order to further enhance the quality of the project code we are constantly evaluating state of the art development tools. Thus far, we have purchased tools such as Purify from Rational Software and Insure++, TCA, InUse and CodeWizard from ParaSoft. These tools provide an automatic and reliable way to detect software defects that are very hard to pinpoint unaided by automatic tools. Other tools, such as the TotalView debugger are still in the evaluation process. In addition, we have identified the following areas as in need of immediate attention:

- The assembly of programming guidelines, especially for C++ programming, that will allow the developers to leverage industry experience in the construction of large software projects.

- Training of the collaboration members in the various aspects of the development effort, including seminars about C++ and Python.

6.4 Methods for exploiting current and future ASCI system architectures

Sthreads is being developed as a practical and efficient system for high-performance multithreaded programming on shared-memory multiprocessors. As a testbed for programming their systems, A collaboration with the Caltech Materials and Process Simulation Center provides an application testbed, namely, MPSim, a molecular dynamics application. The programming system, Sthreads, has undergone continued development and tuning throughout the year in response to applications experiences. The focus of development has been on commodity symmetric multiprocessors (e.g., quad-processor Intel Pentium Pro systems) running commodity operating systems (e.g., Windows NT). At this stage, it has been found to be valuable to support this one highly-accessible platform well, and concentrate on research and development. At later stages, when the design is more stable, Sthreads will be ported to a variety of other platforms. Over the past year, experiments with MPSim have centered on exploring the paradigm of multithreaded programming with dynamic thread creation and many more threads than processors. This approach allows complex multithreaded algorithms to be expressed more compactly and with less programmer effort, compared to the traditional scientific supercomputing approach of one long-lived thread per processor with occasional synchronization operations (e.g., barriers). Dynamic thread creation allows more natural multithreaded algorithm structures to be expressed, and load balancing is much simpler with more threads than processors. Initial experiments using Sthreads to port MPSim to a quad-processor Pentium Pro running Windows NT demonstrated excellent performance. It has been shown that performance is maintained with many more threads than processors. As a result, MPSim's complex load balancing strategy was replaced with the much simpler approach of randomly assigning atoms to threads. The results of this work have been accepted for publication [98]. The emphasis of ongoing work with MPSim is to consider the performance of multithreaded programs under conditions where the multiprocessor platform is shared with other concurrent tasks. This is important in realistic research and development scenarios, where powerful computing platforms are shared by many concurrent users. It is also important in the development of complex simulation programs, in which the algorithm naturally subdivides into many separate multithreaded components that run and interact concurrently. It is hypothesized that dynamic thread creation and many more threads than processors are vital to obtaining good performance under these conditions. From the results of these experiments, the aim is to develop sophisticated multithreaded materials simulations programs, in which multithreaded simulations at many different scales run concurrently and continue to develop the Sthreads system to provide high level support for developing structured multithreaded applications of this kind.

6.5 Scalability and load balancing of fundamental algorithms

6.5.1 Porting the solid dynamics engine

During the last quarter, the solid dynamics engine, `adlib`, was ported to all ASCI platforms and the HP V and X-Class systems. Basic profiling runs were conducted, to better understand the available analysis tools in addition to revealing performance characteristics of the solid dynamics application. A coherent Makefile is being created to reflect the new array of platforms supported by `adlib`. In addition, scripts on how a user submits a development and production `adlib` run per site and system are documented and available. Using a perscribed problem provide by the solid dynamics group, the Hutchings problem, for sample runs on the HP, the explicit time integration computation was identified as a sequential bottleneck. Parallelizing the computation and combining elemental internal forces was straightforward. The parallelized explicit dynamics loops were implemented in MPI. The resulting code has been tested for correctness on simple problem sizes across 1 to 32 cpus. Profiling has shown there are still many opportunities for increased efficiency in the computation of internal and external force arrays, essential to the code's spatial finite element discretization and central difference time stepping algorithms. The sequential and parallel version of `adlib` will benefit from improvements to data management techniques to accommodate existing and more demanding cpu and data movement requirements. Profiling `adlib` has revealed obvious hurdles in particular sections of code that must be conquered before making a 3-D version of the code. Simple simulations of hard spheres impacting a steel plate with poor mesh refinement easily demonstrate why better resolution meshes are required. Profiling shows finer meshing to be a sequential bottleneck in the current code.

6.5.2 Banded Eigenproblems in Quantum Mechanics

As part of the project, materials scientists are investigating very large problems in quantum mechanics. There are two "expensive" parts of a quantum chemical computation:

- formation of the Hamiltonian (also known as the Fock matrix), which requires $O(N^4)$ floating point operations (flops) where N is the order of the matrix, but which can be reduced to $O(N^2)$ with appropriate cutoff methods (resulting in a banded matrix) and numerical techniques, and

- diagonalization (i.e., computation of all the eigenvalues and eigenvectors) of the Hamiltonian, which requires $O(N^3)$ flops and is much more difficult to reduce further.

As it turns out, for ab initio computations that use atom-centered basis functions, the formation of the Hamiltonian has not yet been reduced to the point that it is less expensive than a full O(N3) diagonalization. However, with current trends it is just a matter of time before the diagonalization step dominates. Moreover, in other types of computations, such as those with semi-empirical Hamiltonians or those using plane wave basis sets, the diagonalization step is already dominant. Hence, the University of Tennessee participants

have worked this year in cooperation with the Materials and Process Simulation Center, on developing new algorithms to accelerate the diagonalization process, in particular, using banded matrix solvers.

A new LAPACK-like algorithm was developed that computes all the eigenvalues via traditional LAPACK algorithms but computes the eigenvectors by performing inverse iteration on the original banded matrix. The algorithm insures orthogonality of the eigenvectors by invoking a Gram-Schmidt process for sufficiently close eigenvalues. This produces an algorithm requiring $O(m^2N^2)$ flops, where m is the bandwidth. Thus, the new algorithm should perform better on problems that have a bandwidth less than $\sqrt{N}$. Test cases of random matrices show this to be the case. Preliminary tests on a set of alkane chains indicate that this relationship will hold on real problems as well. Since larger systems typically have smaller bandwidth when compared with the order of the matrix, the new algorithm is expected to provide savings for those time-consuming problems. For very large problems, the savings are expected to be significant.

A parallel version of the above algorithm, a scaLAPACK-like version, is currently under development. As stated above, the algorithm will provide significant savings when applied to very large problems; thus, a parallel version will be required.

Although the new parallel algorithm is expected to provide considerable savings, other approaches have the possibility of providing much larger savings, maybe even reducing the number of flops to $O(mN^2)$ or lower. These algorithms also have much better parallel structure and may yield vastly superior parallel algorithms. These approaches involve using block submatrices with a divide and conquer scheme or with a tridiagonalization scheme. Investigations into these approaches have just begun.

6.6 Geometric modeling and advanced visualization for model validation

In algorithmic research the following items have been accomplished:

1. **MAPS Multiresolution Adaptive Parameterization of Surfaces** Presented at Siggraph this year, MAPS deals with the issue of establishing compact and smooth parameterizations for arbitrary topology surfaces with user supplied constraints such as feature interpolation. The underlying algorithm is an essential component in any work which seeks to establish a proper manifold structure for arbitrary connectivity meshes as they appear in applications.

2. **Interactive Animation of Structured Deformable Objects** This work deals with building fast and very robust integrators for finite difference models of flexible materials. For interactive application both utmost speed and robustness are required. The former favors explicit integration methods, the latter implicit methods. An explicit scheme has been developed which corresponds to a truncated implicit scheme. It retains the speed advantage of explicit schemes while gaining the robustness of implicit schemes. The method has been deployed successfully on the RWB, where forces supplied by the user may very rapidly and wildly.

Continuing research activities include:

1. new interactive modeling methods for semi-immersive environments for surfaces and 3D sketching environments
2. compression of arbitrary connectivity meshes
3. parameterization of progressive meshes
4. extraction of arbitrary topology iso surfaces from volumes with subdivision connectivity meshes
5. loop subdivision surface wavelets.

These activities, supported primarily by other projects and involving numerous graduate and undergraduate students, are geared towards developing fundamental algorithms and paradigms. However, the research results are expected to be highly relevant for large scale geometry manipulation (e.g., acquisition, editing, storage, transmission, display, simulation) as needed in simulation and visualization.

The project is leveraging ongoing work on the Responsive Work Bench (RWB). An Inventor based infrastructure for the RWB has been built and is being refined. Inventor was selected since it provides the least hurdle to users who want to evaluate the potential of the RWB for their work. All that is needed is to write a data file in Inventor format (a widely supported format and a subset for VRML). User interface elements are being refined as more experience is gathered with application scenarios. In particular, common components are being identified and abstracted into libraries.

Visualization of large data sets has become as much a challenge in computational hardware as it is a challenge in human-computer understanding. We have explored different and better ways of visualizing data sets resulting from simulations of the Rayleigh-Taylor instability. Current efforts include visualization of data attributes in a interactive and dynamic visualization system, on-the-fly parallel isosurface extraction on a remote super computer while displaying results on a local workstation, and interactive display of isosurfaces and isocontours on the Responsive Work Bench.

A dynamic environment has been created using IRIS Explorer in which scientists have available not only the plethora of tools provided within Iris Explorer but also tools adopted from available toolkits such as VTK (the Visualization Toolkit [99]) and specially generated tools. With this environment the researcher is able to bring new data sets in, and with the use of the visual scripting language that IRIS Explorer represents, is able to create and adapt visual schemes to the new data.

Experiments have been initiated to create seamless communication between IRIS Explorer on a workstation with some graphics capabilities but limited resources and IRIS Explorer on a parallel computer system able to analyze and extract features from stored large data sets. This allows the larger machine to pre-load several data sets, handle computational intensive analysis, and give visualization feedback to the researcher within minimal response time,

Visualizing large data sets within a semi-immersive environment, the Responsive Workbench, poses three challenges:

1. how to correctly utilize the paradigm that this Workbench presents in of itself,

2. how to accurately visualize the pertinent data given the constraints of the environment, and

3. how to create tools for interaction between the user and the data.

Data resulting from the Rayleigh-Taylor instability is inherently 4 dimensional (3D data field and time), thus the transition onto an inmersive system is an obvious one. Time, in this case, may be manipulated as a variable to allow the user to either appreciate the phenomena as it occurs transitions, or the user may opt to use it to analyze a specific time frame.

Currently, each time step of this data sets is of size $256 \times 512 \times 216$ Isosurfaces extracted from this data set result in an average of 1,200,000 triangles. Thus, the rendering of such a large dataset in an interactive 3D environment is beyond most hardware's capabilities. To overcome this problem, a set of evenly distributed isosurfaces is pre-calculated and the resulting triangle mesh of each decimated. Thus, the shape and main features of the surface were preserved, while reducing the number of triangles to be rendered by hardware. By the same token, texture memory was exploited to interactively calculate and display data's isocountours, which when displayed dynamically against a semi transparent isosurface lets the scientist perceive fluid interaction taking place inside the data field, with the aid of the isosurface for spatial perception.

6.7 Scalable parallel input and output

The PABLO Group at the University of Illinois has continued to develop I/O instrumentation for MPI-IO and HDF that can correlate I/O requests across I/O library boundaries. This instrumentation has been used to analyze the behavior of important, I/O-intensive applications and libraries, both locally and remotely. The results of these analyses are guiding I/O hardware configuration and performance tuning, as well as development of new I/O libraries that embody knowledge gained from I/O analysis and optimization[100, 101, 102].

Prototype MPI-I/O instrumentation software has been extended, adding new features in response to the results of internal testing, and. ported from SUN Solaris, where it was originally developed, to the SGI Origin2000, HP Exemplar, and IBM SP systems. To maximize its potential utility, the instrumentation was tested on

- the SGI Origin with both MPICH-1.1.1 MPI and the native SGI MPI using the Argonne ROMIO toolkit as the MPI I/O library and

- the HP Exemplar and IBM SP systems using MPICH-1.1.1 together with an instrumented version of ROMIO.

A key feature of the MPI-IO analysis toolkit is its correlation of MPI-IO calls with underlying UNIX I/O patterns. By correlating the number, type, and cost of UNIX I/O routines invoked by each MPI-IO routine, one can quantify MPI-IO overheads and assess implementation efficiency. Moreover, the MPI-I, UNIX, and HDF I/O instrumentation (described

below) allows users to either generate traces for post-mortem analysis or compute I/O summaries during program execution. Real-time analysis results in I/O summaries whose size is independent of program execution time or I/O volume, albeit with some loss of detail – all dynamic information on time varying I/O patterns is lost. However, by supporting both post-mortem and real-time analysis, users can balance I/O instrumentation data volume and perturbation against the need for fine detail. In addition to software porting and testing, a manual has been prepared to illustrate use of the MPI-IO instrumentation library. This manual, "A User's Guide to Pablo MPI I/O Instrumentation," and the MPI-IO instrumentation software are available via the Pablo WWW site.

To complement the MPI-IO instrumentation software, an instrumented version of the NCSA HDF (Hierarchical Data Format) library, version 4, has been packaged and distributed. This I/O instrumentation, which is based on the Pablo performance analysis toolkit, is now being distributed as part of the standard HDF software and is available via the HDF WWW site [103]. HDF version 4 is widely used in the computational science and engineering community. The HDF research group is using what they learned in implementing HDF version 4 to develop a new version of HDF, HDF5, that targets MPI-IO as a low-level I/O library. To help the HDF developers optimize the performance of HDF5 and to provide users with a toolkit for optimizing applications that use HDF5, a version of the I/O instrumentation system that supports the new version of HDF is being developed. An instrumented version of the HDF5 prototype release is now available. As HDF5 continues to evolve and mature, the PABLO group will continue to work with the HDF5 developers, Caltech, and the DP laboratories to measure and tune the HDF5 implementation.

Experience has shown that software layering is a potential source of performance loss. Unless performance-critical information is propagated across interface boundaries, lower level libraries and runtime systems may be unable to deliver the desired performance. Hence, the toolkit supports multilevel analysis of I/O requests (i.e., requests from HDF5, the interactions of those requests with the underlying MPI-IO toolkit, and their ultimate instantiation as UNIX I/O requests).

In addition to creation of I/O analysis software, the I/O performance of two local applications (Cloud and KLIENG) and three ASCI applications (EULER, ARES, and ALE3D) have been instrumented and measured. A detailed report and a paper that describe the results of these experiments are being prepared.

The first of the three ASCI applications, EULER, is a 3-D hydrodynamics code from Los Alamos National Laboratory that simulates high-speed fluid flow and high rate multimaterial deformation problems. The I/O behavior of the instrumented EULER code was measured on 128 processors of the NCSA Origin2000. During a 20-minute execution of a test problem, EULER wrote approximately 17 gigabytes of data, mainly restart and graphics dumps. Analysis of the I/O traces showed that output occurs in bursts and that this behavior leads to substantial contention for I/O devices. As a result of the EULER measurements, an I/O benchmark program was developed to simulate EULER's bursty I/O patterns and used to assess the I/O capabilities of the NCSA Origin2000. A preliminary analysis of the benchmark data suggests that the NCSA EMC network-connected disk arrays are a major bottleneck.

The second code, ARES, from Lawrence Livermore National Laboratory (LLNL) is a

block structured mesh, arbitrary, Lagrangian-Eulerian, hydrodynamics code with multigroup radiation diffusion. ARES uses a parallel strategy of domain decomposition and explicit MPI. The code is written in C and uses the SILO library to access its data structures. Nearly all of the I/O is performed as a result of calls to the SILO library. To measure the I/O behavior of ARES, the SILO library was instrumented. A wide range of experiments were conducted on the LLNL IBM SP/2 using the PIOFS file system with both IBM's MPI and a version of MPI developed at LLNL. Measurements showed that ARES, like EULER, exhibits a pattern of I/O bursts. Given the same number of processors, the performance of ARES was better with the LLNL version of MPI than with the IBM MPI. For example, on 64 processors, 1.7 gigabytes of data were read or written. This was completed in 1722 seconds using IBM MPI and in 1502 seconds using the LLNL MPI. Likewise, the time spent doing I/O fell from 13.9% using the IBM MPI to 5.2% with the LLNL MPI.

The third code, ALE3D, was also developed at LLNL. It is an unstructured mesh, arbitrary, Langrangian-Eulerian, three-dimensional continuum, mechanics code with material strength. It uses a parallel strategy of domain decomposition and explicit MPI. The code is written in both C and F77 and uses the SILO library to access its data structures and to perform the majority of the I/O. As with ARES, the I/O behavior of this code was measured with an instrumented version of SILO. The majority of tests were conducted on 64 processors using both the IBM and LLNL versions of MPI. The behavior of both the PIOFS and GPFS parallel file systems was measured with a variety of sequential and parallel read/write options. Not all of this I/O data has been analyzed. However, a preliminary analysis suggests that (a) the I/O is bursty and (b) the GPFS file system is much faster than PIOFS.

Building on the lessons gained from ongoing I/O studies, the PABLO Group has continued to develop PPFS II (Portable Parallel File System), a user-level I/O library. PPFS II relies on real-time performance measurement, qualitative access pattern classification (e.g., using trained neural networks and hidden Markov models), and a fuzzy logic rule base to adaptively choose and configure I/O policies. They have configured their Linux cluster to support PPFS II experiments and extended PPFS II on the cluster to support adaptive file striping and are conducting local performance experiments as a prelude to large-scale measurements on the Caltech Beowulf cluster and the NCSA cluster.

6.8 Personnel

- Dr. Paul Messina (PI, currently on leave)
- Dr. Jim Pool (acting PI)
- Prof. Randy Bramley (Indiana)
- Prof. Dennis Gannon (Indiana)
- Prof. Bob Ward (Tennessee)
- Prof. Jack Dongarra (Tennessee)
- Prof. Dan Reed (UIUC)

- Prof. Peter Schroder
- Dr. Carl Kesselman (USC-ISI)
- Dr. John Thornley
- Dr. Michael Aivazis
- Dr. Roy Williams
- Dr. John Salmon
- Dr. Rudiger Westermann
- Dr. Mathieu Desbrun
- Dr. Maciej Brodowicz
- Mr. Santiago Lombeyda
- Mr. H. Ishi
- Mr. G. Siklos
- Mr. James Patton
- Ms. Sharon Brunett

Chapter 7

Implementation Plan for FY '99

7.1 Updated Simulation Development Roadmap

The roadmap for the project remains unchanged and is repeated here in the form presented in our revised proposal. The roadmap represents those areas in which simulation capability must be developed in order to complete the proposed construction of our virtual facility.

- Stage 1 - Detonation of high explosives
    1. Electronic structure models of individual explosive molecules and intermediates.
    2. Molecular dynamics models of chemical reactions under dense fluid conditions. Force fields based on structures developed in item 1.
    3. Mechanisms (chemical reaction pathways) and explicit kinetic parameters for specific explosive systems (e.g., HMX, TATB). Simplified reaction mechanisms for CHNO explosives
    4. Approximate reaction rate expressions for simplified reaction mechanisms under dense fluid conditions.
    5. Equations of state appropriate for simplified reaction mechanisms.
    6. Micromechanics-based models of composite explosives that treat pressure dependent binder stiffness, binder-particle and particle-particle interactions.
    7. Numerical simulation environment for 3-D AMR computations of reactive, compressible flow.
    8. High-performance computing implementation to use ASCI-class parallel computing facilities effectively.
    9. Integrating chemistry, solid mechanics and hydrodynamics.
- Stage 2 - Interaction of strong shock waves with solid materials
    1. Predictions of equations of state, thermodynamic properties, and temperature and pressure dependence of elastic moduli.

2. Phase transition models that describe the onset and extent of martensitic, reconstructive, melt, and vaporization phase changes, both for loading and unloading processes.
3. Physically based constitutive relations representative of the behavior of solids under the extreme conditions of pressure, temperature, and strain rate that account, for example, for rate sensitivity, mechanical hardening, as well as micromechanical effects such as dislocation interactions and phase transitions.
4. Fracture and fragmentation models that account explicitly for individual cracks as they nucleate as well as robust and efficient contact algorithms capable of accounting for all the contact and frictional interactions between particles.
5. Advanced solid modeling capability to facilitate adaptive 3-D meshing in simulations involving cracking and fragmentation as well as automatic and adaptive advancing front methods to ensure closure and sliver-free meshes.
6. High-performance computing implementation to use ASCI-class parallel computing facilities effectively.
7. Integration with Eulerian CFD solvers for fluid-solid interactions.

- Stage 3 - Shock-induced compressible turbulence and mixing

1. 3-D high-resolution computation of shock-contact and shock-vortex interactions to compute initiation of mixing for strong shocks.
2. Accurate computation of the subsequent development of mixing.
3. Accurate computation of reshock of the mixing layer by strong reflected shocks.
4. Investigations of compressible turbulence and mixing utilizing realistic equations of state.
5. Development of subgrid scale turbulence models based on interactions of compressible vortices. Reliable turbulence models that can model the mixing phenomena on subgrid scales.
6. Integration of turbulence modeling into high-performance computing implementation

7.1.1 FY99 Milestones

- High Explosives

1. Development of carbon clustering models
2. QM calculations of reaction rate kinetics for HE
3. Molecular dynamics simulations of binder-chemical interactions
4. Begin development of 3D AMR
5. 2-D prototype of integrated virtual facility

- Solid Dynamics
    1. Development of damage and crack modeling
    2. Mixed atomistic-continuum modeling in 2D with defects
    3. 2-D prototype of integrated virtual facility
- Material Properties
    1. Parallel implementation of DFT capability to study solid-solid phase transformations and transition metals
    2. Implement QMC in ab initio QM codes
    3. Develop new density functionals for metals
- Compressible Turbulence
    1. 2D simulations of Richtmyer-Meshkov instability including reshock and shock-vortex interactions
    2. LES based on compressible vortices developed and implemented
    3. Validation of 2D results from existing experimental database
- Computational Science
    1. Nexus and Globus will be ported to the ASCI environments
    2. Responsive Workbench evaluated for advanced visualization
    3. Integration of modules demonstrated via PSE
    4. Enhanced PABLO for ASCI environments
    5. 2-D prototype of virtual facility

7.2 Implementation Plan

The sections below detail the implementation plan for the Caltech Alliance Center in year 2.

7.2.1 High Explosives

7.2.1.1 Material properties

We have concentrated in the past year on the explosives HMX and TATB, and the binder materials Kel-F and Estane. In year 2 we will continue our efforts in characterizing these materials. For HMX the following research activities will be pursued in characterizing material properties:

- EOS (P,V,E,T curves) with Level 0 force field for supercell using NVE dynamics

- Development of vibrationally accurate Level 1 force field
- EOS (P,V,E,T curves) with Level 1 force field for supercell using NVE dynamics
- EOS (P,V,E,T curves) with Level 0 force field for defective supercell
- Molecular dynamics of single molecules with impulse
- Reactive force fields using switching functions
- MD of shock wave propagation
- Reaction networks for HMX based on primary and secondary reactions of RDX

For TATB we will pursue the following research activities on the material properties of this explosive:

- QM calculations on torsional barriers and inter-molecular H-bond potentials
- Development of vibrationally accurate Level 1 force field
- EOS (P,V,E,T curves) with Level 1 force field for supercell using NVE dynamics

The binders, Kel-F and Estane will be analyzed and the following activities are planned:

- EOS (P,V,E,T curves) with Level 0 force field for supercell using NVE dynamics
- QM calculations on torsional barriers and potential derived charges
- Development of more accurate Level 1 force field
- EOS (P,V,E,T curves) with Level 1 force field for supercell using NVE dynamics

Finally we will examine issues relating to binder-grain interactions through the following tasks:

- EOS (P,V,E,T curves) with Level 1 force field for supercell using NVE dynamics for TATB-KelF and HMX-Estane

In the coming year, we will also initiate further work in quantum mechanics to improve our force field. The isothermal compression curves for all explosives will be recomputed with these improved force fields. We will also study the temperature and pressure dependence of the Gruneisen parameter of TATB. If the appropriate computational resources are available, molecular dynamics computations investigating phase transitions and dislocations will be carried out.

7.2.1.2 Reduced reaction networks

In our ongoing research on the implementation and design of reduced reaction networks the next step is to implement the reduced reaction models we have developed thus far into the Eulerian unsteady flow solver and compare the reduced models with the detailed mechanisms via unsteady 1D detonation simulations. This will first be done with stable overdriven detonations, followed by unstable detonations. Two-dimensional simulations can then be performed with the chosen reduced reaction models. After standard cellular detonations are computed, some more complicated geometries will be examined, including the corner turning problem.

All of this development work will continue to be performed with the H_2–O_2system in the early stages. This system is the simplest to consider, and allows computational runs of reasonable time, so that we can perform many test runs on a workstation and experiment with the behavior of the stiff chemistry in unsteady flow simulations. Once suitable confidence is obtained, the plan is to transition to systems that are more relevant to high explosives, namely nitramines (nitromethane, HMX and TATB). These systems represent a great deal more complexity, with detailed reaction mechanisms containing several hundred reactions. However, the modular design of the flow solver allows a seamless switch between different chemical systems. At present, work is still required on the detailed reaction mechanisms for nitramines. Once this information becomes available, we can begin to work on reducing the mechanisms, implementing them in our flow solvers, and performing analogous computational studies to those described in the H_2–O_2system.

7.2.1.3 Thermodynamic analysis

In the coming year, we will implement in a hydrodynamic code of an engineering model for HMX based on the materials properties computed thus far. To this end, additional analysis of MD results is required. We remarked that NPT dynamics shows large deviations in specific volume at low compression when compared to NVE samples for the same conditions. Presently, the NVE approach appears to be the most promising.

Also, extension of this investigation in the region of high temperatures and pressures along the Hugoniot will be pursued. Additional work in this direction may include validation of analogous MD simulations obtained for TATB and Kel-F. Furthermore, we believe that a better understanding of the behavior of a solid under tension is required for the numerical simulation of rarefaction waves. Previous experiences indicate that this is an essential feature in a robust hydrodynamic code.

7.2.1.4 Engineering model for HMX and TATB

In the following, we discuss the tasks required to further develop the engineering model for simulation of detonation in high explosives such as HMX and TATB. We will, in collaboration with the MP and SD teams, investigate the corner turning problem in the case of a two-phase fluid and a deforming boundary (the outer casing) This requires a better understanding of the governing EOS. The solid phase (reactants), is modeled with the Mie-Grüneisen EOS while the gas phase (products) is modeled with the Jones-Wilkins-Lee EOS, for example.

Furthermore, the material in the solid phase experiences strong rarefaction from the reference state at the corner where the detonation wave diffracts. We will therefore continue our efforts in designing appropriate methodologies to treat the solid material in tension.

In FY99 we will also investigate the feasibility of a model for solid-fluid interaction based on the Ghost Fluid Method (GFM) [9]. This scheme allows to properly interface a solid phase, discretized by any available Lagrangian finite element code, with a "fluid" phase, described in a Eulerian framework. Early efforts will include a number of proof-of-concept problems for GFM, particularly the dynamical shock loading of a cylindrical shell, see [10]. In our past experiments, the boundary modeling of the corner and the channel were rigid (reflective BC). In FY99, a model that includes a deforming boundary will be implemented. We will use level-set functions for capturing the fluid-solid interface and the "ghost-fluid" technique for the boundary conditions [19]. Furthermore, this technique can also be used to capture flow features such as contact discontinuities between substances defined by different EOSs.

We summarize the proposed tasks in constructing an engineering model below:

- Two-phase fluid:
  - JWL EOS for products ($\mathcal{G}(v)$,$C_v(T)$)
  - Engineering models for reaction rate (JTF and "ignition and growth")
  - Robust EOS models for material in tension
  - Alternative flow solver (local Lax-Friedrichs)
  - Thermal and mechanical equilibrium model
- Deforming boundaries:
  - Level set functions to capture fluid/solid (inert) interface
  - "Ghostfluid" technique for boundary conditions

7.2.1.5 Pressure stiffening of rubbery binder

Currently, efforts are underway to study a more relevant and interesting case: that of combined pressure and shear loads imposed on a thin layer of binder sandwiched between two explosive grains. This configuration is representative of the state of stress and deformation experienced by the rubbery binder in a sample of high explosive subjected to shock loading. This case also uncouples pressure and shear loading and permits a better examination of the effect of pressure on the shear relaxation, and hence, the shear stresses. The high strain rates that the thin binder experiences also cause high inelastic dissipation rates and the associated heating of the binder. Efforts will be made to incorporate appropriate formulations for this inelastic dissipation in order to study the temperature increases associated with this deformation process and the possibility of developing 'hot-spots'. The opposing effects of pressure and temperature will be studied within this framework. Progress on these issues will direct further work including 2D (or possibly 3D) finite element analysis of representative grain-binder geometry and interactions in a high explosive. In summary, the work projected for completion in FY99 is as follows:

1. Development of constitutive equations for the inelastic deformation of the binder and the associated dissipation.

2. Study of binder stiffening and heating under combined pressure and shear loading.

3. Study competition between pressure stiffening and thermal softening.

7.2.2 Solid Dynamics

We shall continue with the activities of the first year concerned with the development of parallel adaptive meshing and nonsmooth contact capability; cohesive models of brittle and ductile fracture and fragmentation; Taylor averaging in polycrystals; crystal plasticity models of aluminum and tantalum based on dislocation mechanics, statistical physics, low-energy dislocation structures, latent hardening and thermal effects; mixed atomistic-continuum simulations of dislocation junctions leading to the determination of binding energies to be used in single crystal models; extensions of the mixed atomistic-continuum theory to account for thermal effects.

We shall also continue to collaborate with Michael Aivazis in the development of middleware for the integration of the various modules of the virtual testing facility, including material property data, such as equations of state, transport properties, and others to be provided by the material properties group; and Eulerian CFD capability, including equations of state appropriate for high explosives, under development by the HE group.

The following additional activities have been scheduled for next year in order to meet the proposed milestones.

1. *Development of equations of state for polymorphic materials.* We shall continue this activity into FY99. Efforts presently underway include the use of inclusion models to develop equations of state for Fe, including hysteresis; and the formulation of kinetic relations for the propagation of phase boundaries.

2. *Development of damage and crack modeling.* We plan to broaden the scope of our activities by undertaking the modeling of damage accumulation in metals, leading to spall. The modeling will account for processes of void nucleation due to vacancy aggregation, void growth and void coalescence, resulting in the development of spall planes. The damage models will be coupled to crystalline slip mechanisms, and, in consequence, to shear band formation. We also plan to continue the development of cohesive models of fracture and fragmentation in three dimensions.

3. *Mixed atomistic-continuum modeling in 2D with defects.* During FY98 we have developed a 1D prototype of a mixed atomistic-continuum theory which accounts for thermal effects. During FY99 we shall undertake the implementation of the theory in more than one dimension, and the application of the resulting capability to the study of the dynamic behavior of dislocations and its dependence on temperature and pressure, including dislocation mobility, dislocation junction binding energies, line tension and other effects. The results of these simulations will be incorporated into statistical mechanical models of hardening in crystals, also under development.

4. *2D and 3D prototype of the integrated VTF.* We are close to being able to run complete simulations of the proposed virtual facility in two and three dimensions. The main focus of activities during next year will be the parallel implementation of the computational facility in ASCI computers, with particular emphasis on issues of scalability. The following subtasks have been identified:

   (a) *Time-integration algorithm.* We shall develop MPI versions of the explicit dynamics and thermal analysis algorithms.

   (b) *Meshing.* Meshing will be parallelized by recourse to domain decomposition. Our data structures are well-suited for this purpose: the subdomains simply become part of the solid model and the mesher knows to mesh each subdomain independently, which affords the desired concurrency.

   (c) *Contact.* Two main aspects of the contact algorithm will be addressed from the standpoint of parallel implementation: mechanics and searches for potential contacts.

      i. *Contact Mechanics.* Because of our use of explicit dynamics, it follows that the contact problem can be decomposed into small and independent local problems [42]. These local problems can be solved in parallel with little or no communication between processors.

      ii. *Contact Searches.* A time-consuming part of the contact algorithm is concerned with the determination of potential contacts [38]. Specialized data structures, which are already part of our products, such as point-region oct-trees [39] help to reduce the time complexity of the search operations. Due to their importance in several of our algorithms, we shall develop a parallel implementation of oct-tree searches.

7.2.3 Materials Properties

7.2.3.1 Methodology and software

7.2.3.1a Parallelization of Jaguar code Over the next year we will continue the parallelizing of Jaguar by

- replacing the diagonalization step with a divide-and-conquer approach (see below),
- introducing multithreaded approaches to speed performance on shared memory architectures, and
- porting the MPI version of Jaguar to the Blue Mountain and ASCI Red platforms.

7.2.3.1b Banded matrix solvers The block matrix diagonalizer showed the best performance, but this technique is not generally applicable to quantum chemical systems. In the upcoming year we plan to develop new approaches that will cast the Fock matrix into a form that is as block diagonal as possible. These techniques, known as divide-and-conquer methods, tend to depend on the specific application. We will experiment with schemes to allow the techniques to be as efficient as possible for general cases.

7.2.3.2 FF development

For the MS-Q FF for ceramics, the Q-SC FF for metals, and the GEEBOD FF for covalent systems described above, the parameters were based on fitting experimental data (density, energy, compression, vibrations). Our future work will focus on using accurate first principles QM calculations to optimize the FF with no use of experimental data. This allows us to consider structures not stable at ordinary temperatures and pressure to ensure that the FF is accurate for all T and P. Thus, for MgO we used QM (DFT GGA) on the B1(NaCl) and B2(CsCl) phases to obtain the qMS-Q FF and then used this FF to predict the equation-of-state (see Section 4.4.2.7).

Similarly we will use the QM-DFT EOS for fcc, bcc, and hcp phases calculations on Ta and Fe to determine defect energies (eg. vacancy formation, surface energies) and energy differences that will be input in determining Q-SC type FF.

We are also using QM calculations to optimize the QEq parameters for a broad set of elements under different ligancy conditions. Then, the *ab initio* DFT/GGA approach will be used to determine the EOS, energetics of possible (in theory and experimentally observed) polymorphs as input for determining non-electrostatic interactions.

7.2.3.3 Applications to high explosives

In the second year, we will use QM to improve the force fields for TATB and HMX. We will calculate Shock Hugoniots from the isotherms. We will study the temperature and pressure dependence of Gruneisen parameter of TATB. We will also carry out large scale calculations to study phase transitions and the initial steps of an explosion.

7.2.3.4 Applications to solid dynamics

We plan three main efforts for the next year

1. Use FF to predict first principles force fields
    - do QM (DFT-GGA) calculations on BCC, HCP, FCC forms of each metal as a function of volume with and without point defects (vacancies, interstitials)
    - Fit Q-SC FF to the full set of QM results (this determines the functional form in addition to the parameters)
2. Use the Q-SC FF to calculate energetics of defects in metals as function of P and T
    - point defects (vacancies, interstitials)
    - surface energies (various low index surfaces)
    - grain boundaries (between various low index surfaces)
    - Peierls stresses and dislocation core energies
3. Use Q-SC FF to predict high pressure, high temperature properties of BCC metals
    - calculate EOS of Ta at elevated temperatures and pressures

- calculate elastic constants of Ta and Fe at elevated temperatures and pressures
- use large tensile, compressive and shear loads to calculate properties of Fe and Ta beyond the elastic limit
- use rate dependent (shear, compressive, tensile) loads to calculate properties of Fe and Ta

4. Hypervelocity impact simulations on Fe and Ta

7.2.3.5 Applications to compressible turbulence

In order to supply reliable first principles input to the CT and fluid dynamics effort we will focus on calculating various transport properties at elevated pressures and temperatures for dense fluids.

7.2.4 Compressible Turbulence

In FY99 work is planned in the following directions.

7.2.4.1 Shock-contact and shock-vortex interaction

We will continue our study of shock-sontact interaction focusing on the 3-D modeling of the interaction using the Samtaney-Zabusky model. Our studies will examine the validity of the Samtaney-Zabusky model at high Mach number for a wider range of data. We will continue our full three dimensional simulations using our regular mesh code. We will however transition to a full 3-D AMR capability for more accurate simulation as this becomes available. The 3-D solver is currently under development in collaboration with the University of Chicago Alliance Center (Greg Miller) and makes use of the DAGH adaptive mesh refinement class library (developed by Manish Parashar). It also has the capability to perform multi-phase calculations and this will become valuable as we consider multi-material versions of the instability. We will also examine issues of scalability arising in both the regular mesh codes as well as the AMR-based solvers.

In the area of shock vortex interaction we will expand upon our initial study of shock-vortex interaction and examine the available parameter space more thoroughly. In particular these calculations will be used to develop a database of accurate numerical calculations that will then be used to diagnose the stretched vortex subgrid LES model (discussed below). An important question in these calculations is how the subgrid model deals with strong shock interaction. The expanded set of calculations to be performed will be used to make detailed comparisons with the LES model.

Finally we will use the Responsive Workbench facility to examine the geometric structure of the plumes generated via the shock vortex interaction. An important question arises in terms of the geometrical similarity of these plume structures to those calculated in other forms of compressible turbulent mixing.

7.2.4.2 LES modeling

We will perform further LES tests for incompressible flow, e.g. rotating channel and other test cases using the Henderson *PRISM* code. This should thoroughly test the stretched-vortex SGS model in several fluid-dynamics settings. We will also perform $256^3/512^3$ DNS of decaying compressible turbulence using the Samtaney compact Padé code with order $2-10$, at a root-mean square turbulent Mach number $M_t = 0.6 - 0.8$. This will serve as a test case for the SGS/LES model. In this range of M_t, shocklets are to be expected. Finally we will perform $32^3/64^3$ LES of decaying turbulence with the compact Padé scheme with order $2-10$. We will also perform $32^3/64^3$ LES of decaying turbulence with a second-order Godunov finite-volume scheme. The aim is to test the dependence of model/LES performance on numerical method and order. This is essential in order to build a robust modeling capability.

An important issue to be investigated is the role of resolved-scale/sub-grid shocklets in the subgrid dynamics. We expect the tests described above to clarify the scope of this problem and indicate the possible need for an SGS shocklet model. Successful completion of the above program should achieve the second year milestones while contributing to the turbulence modeling and compressible mixing sections of the overall project roadmap (Stage 3). It should also produce a modeling capability suitable for detailed calculation of the 3D turbulent Richtmyer-Meshkov instability. It is intended that the SGS modeling effort will produce "plug-ins" that can be incorporated into any hydrodynamic code produced by other groups in the project, for example either the Cook or Henderson 3D Rayleigh-Taylor codes. In the third and subsequent years of the project, other fundamental modeling issues will be addressed. These will include modeling of SGS temperature and pressure fluctuations and SGS modeling for non perfect-gases, for example substances well approximated by the Mie-Gruneisen or other equations of state.

7.2.4.3 Incompressible Rayleigh-Taylor Turbulence

We will continue the development of the *PRISM* methodology for simulating binary mixing based on spectral element methods with adaptive local refinement. The advantage of this approach will be a larger range of parameters (Re and Sc) available to DNS, along with the ability to treat more general boundary conditions. At the same time we will develop a code using the same type of spatial discretization for more general multicomponent transport. This framework will serve as the testbed for our compressible-flow turbulence models. Finally, we will continue our interaction with the CS group to develop visualization tools for the large 3D data sets that will be generated by these simulations. These visualization tools will be applied to both data on regular grids (existing R-T database generated by A. Cook at LLNL) and the block-structured grids associated with the new methods being developed at Caltech. Tasks to be performed in the coming year:

1. 3D R-T simulations at low Mach number (including M=0)
2. Implementation of multicomponent transport
3. Use of *PRISM* as a testbed for turbulence models

4. Enhancement of our capabilities for visualization and analysis of 3D time-dependent data sets

7.2.5 Software Integration and the VTF

One of the important goals of the Caltech ASCI Alliance is to demonstrate the integrated simulation of Eulerian fluid dynamics with deforming boundary coupled to Lagrangian solid dynamics. This forms the backbone of the virtual test facility (VTF) that will be used to perform end-to-end simulations. We have outlined a sequence of activities that will result in a two-dimensional version of the VTF at the end of FY99. These steps are:

1. Define test problem
2. Identify simulation components and algorithms
3. Write/test proof-of-principle software
4. Demonstrate loose coupling computation of test problem with simplified geometry (tube) and physics (Mie-Gruneisen HE model, elastic solid)

7.2.5.1 Test problem

The test problem that we have identified is the propagation of a detonation inside of a cylindrical metal tube. This problem can be modeled at several different levels depending on the type of physical model used for the metal and detonating material. The simplest version of this problem (Fig. 7.1a) is to consider a shock wave or detonation propagating in a gas inside of an elastic solid. To the solid, the detonation or shock appears as a traveling load, exciting waves in the solid. There are several regimes of wave propagation in the solid depending on the speed of the detonation relative to the various wave speeds possible in the solid. These are, in order of lowest to highest speed:

1. flexural waves
2. shear waves
3. dilational waves in a bar
4. pure dilation.

Whenever the gas wave (shock or detonation) speed is equal to one of the solid wave speeds, a resonant response is created in the solid. For small deformations in the solid which produce negligible waves in the gas, this problem has been extensively studied [59, 10] Analytic solutions and experimental measurements are available for the case of near-resonant excitation of flexural waves in the solid. It is our intention to use these results for validation and verification of the 2D prototype of the VTF.

A more complex situation that is of great relevance to the high explosives community is the case of a detonating high explosive inside of a plastically-deforming solid. This occurs

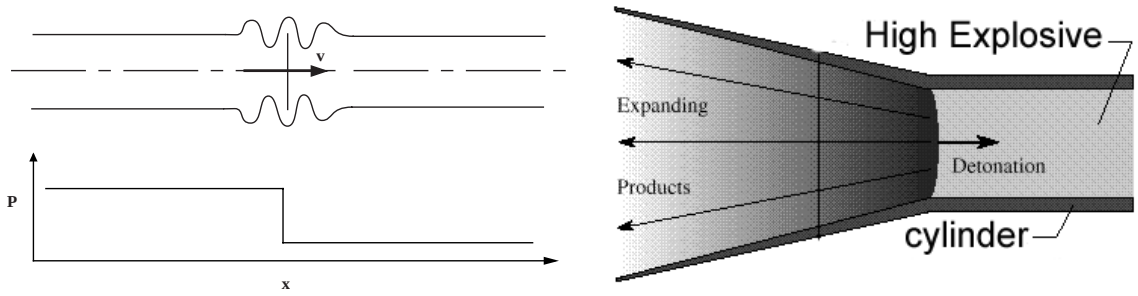

(a) (b)

Figure 7.1: a) Schematic of excitation of flexural waves by shock wave moving inside a thin-walled cylinder. b) Schematic of cylinder test used to characterize high explosive performance. After [61]

in the so-called "cylinder test", Fig. 7.1b, a commonly used experiment to determine the ability of an explosive to push metal and calibrate empirical equations of state for detonation products (for example, see [61]). There is extensive data available from the DOE laboratories on the motion of the cylinder wall and the curvature of the detonation front that can be used for validating simulations.

7.2.5.2 Components and algorithms

There are three major components to the VTF:

1. An Eulerian solver for modeling HE detonation and compressible turbulence
2. A Lagrangian solver for modeling solid mechanics with plasticity and fracture
3. a boundary coupler method that ties together the Eulerian and Lagrangian solutions at the fluid-solid interface.

The fluid solver module will use a modern compressible flow solution method such as a linearized Riemann solver with appropriate entropy corrections, and limiters to minimize oscillations around shock fronts. The solver will be based on an Eulerian formulation and initially will be used on a uniform mesh; adaptive mesh refinement capability will be added later. The equations of state will be modeled using standard engineering models that have been developed for the solids, high explosive products and ideal gases. Much of this software either can be adapted from legacy code or has already been developed in the first year of this program. The major extension will be to add the algorithm for the coupling of external boundary conditions and boundary motion.

The solid mechanics module will use the Lagrangian, continuous rezone, finite element model formulation currently incorporated into `adlib`. This software has a multiphysics capability including plasticity and fracture. This is existing software that minor additions will be made to in order to export the boundary location and boundary conditions to the boundary coupler. The ability to treat strong shock waves is currently under investigation.

The boundary coupler module will pass information between the fluid and solid solver modules and keep track of the boundaries between the solution domains. Within the fluid domain, a level set approach will be used to track the boundary of the fluid. The boundary is intrinsic to the Lagrangian approach of the solid module and it will be necessary to force the level set surface to fit the Lagrangian boundary. The boundary module will exchange forces, positions and velocities between the fluid and solid modules. A time-step broker module will use information about boundary motion and maximum time-step from both solid and fluid module to determine a maximum time step for the coupled simulation.

7.2.5.3 Proof-of-principle code

The development of the VTF will proceed in stages in order to take advantages of existing software. First, a single program will be written that will incorporate simplified versions of the solid, fluid and boundary coupler modules. This software will be used as a test bed for the proposed ideas and work through the issues involved in implementing the various modules. This code will provide the proof-of-principle for the techniques we have proposed for carrying out the integration of fluid and solid solutions.

In the simplest version, the fluid module is a one-dimensional ideal gas simulation and the solid module is simply lumped masses suspended by springs. Results of a simulation with a single spring-mass element at the end of a shock tube are shown in Fig. 7.2. The model for the fluid will be extended to two-dimensions and ultimately, three dimensions with adaptive mesh refinement.

The solid module for the model 2D problem of a cylindrical shell will be implemented at various levels of approximation. The simplest model will be a single PDE's based on a thin-shell representation. This will be refined to a full 2D linear elastic module, and finally to 2D nonlinear finite-element elastic model. The ultimate model will be the full `adlib` package.

7.2.5.4 Steps to 2D VTF

We will develop the proof-of-principle code as modular elements. Once the principles have been demonstrated with simplified modules in a single program, the fluid, solid and boundary coupler modules will be divorced into separate programs. These programs will then be driven using a script based on the Python programming language. Communication sockets will be used to exchange boundary information, broker the time step choice and coordinate the solution update. A full-up simulation in serial will be carried out for the case of small amplitude elastic waves in the cylindrical shell. The results will be verified against analytic solutions for elastic waves and validated against CIT laboratory experimental data for shock and detonation waves. Once the serial simulation is completed, parallel implementation and scaling studies can begin.

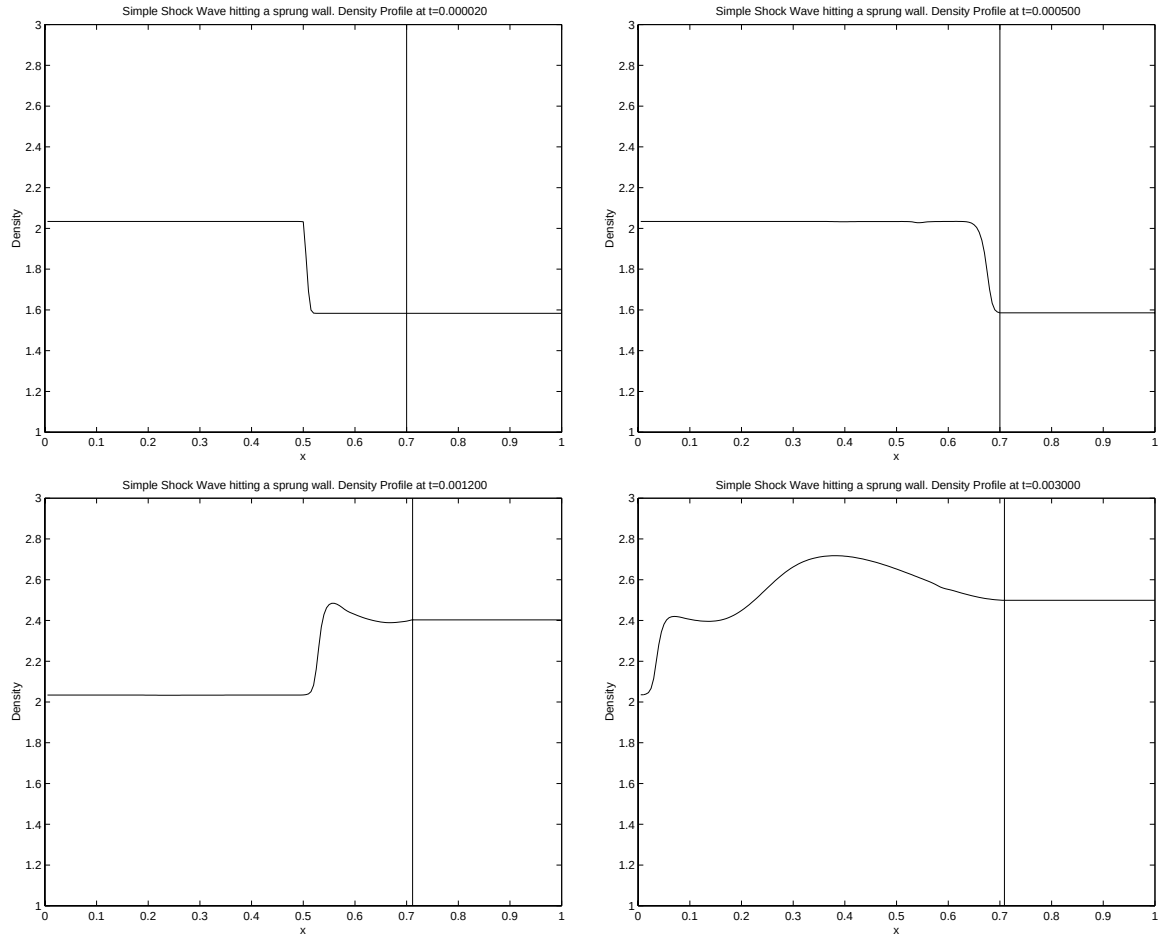

Figure 7.2: Simulation of shock wave reflecting from a spring-mass system. Solution by P. Hung using the Ghostfluid technique [62].

7.3 Budget for FY'99

Category	Discipline	Allocation
Faculty Salaries		
	High Explosives	$117,000
	Solid Dynamics	$150,250
	Material Properties	$52,000
	Compressible Turbulence	$84,250
	Computer Science	$46,673
	Administration	-
subtotal faculty		$450,173
Staff Salaries		
	High Explosives	$30,000
	Solid Dynamics	$29,700
	Material Properties	$156,000
	Compressible Turbulence	$60,000
	Computer Science	$363,711
	Administration	$130,290
subtotal staff		$769,701
Graduate stipends		
	High Explosives	$53,100
	Solid Dynamics	$39,144
	Material Properties	$70,000
	Compressible Turbulence	$25,595
	Computer Science	-
	Administration	-
subtotal grad stipend		$187,839
Total salaries		$1,219,874
Staff Benefits		$258,613
	Total grad stipend	$187,839
	Stipend benefits	$150,271
Consulting		
	High Explosives	-
	Solid Dynamics	-
	Material Properties	$10,000
	Compressible Turbulence	-
	Computer Science	-
	Administration	-
subtotal consulting		$10,000

Category	Discipline	Allocation
Equipment		
	High Explosives	-
	Solid Dynamics	-
	Material Properties	-
	Compressible Turbulence	-
	Computer Science	-
	Administration	-
total equipment		-
Computing support		
	High Explosives	-
	Solid Dynamics	-
	Material Properties	-
	Compressible Turbulence	$10,000
	Computer Science	-
	Administration	-
total computing support		$10,000
Travel		
	High Explosives	$10,000
	Solid Dynamics	$10,000
	Material Properties	$7,914
	Compressible Turbulence	$10,000
	Computer Science	$10,000
	Administration	$10,063
total travel		$57,977
Supplies and expenses		
	High Explosives	$12,926
	Solid Dynamics	$14,432
	Material Properties	$16,184
	Compressible Turbulence	$12,627
	Computer Science	$25,734
	Administration	$14,250
total supplies and expenses		$96,156
Total direct costs		$1,990,732
Indirect costs		$1,030,657
Total subcontracts		$464,610
Subcontract Ind costs		$14,000
Total		$3,500,000

7.4 Cross Center Interaction Plan

The center's strategy for integration is three-fold.

1. We have organized the research activities by integrating members of various disciplines into each research group. As an example the high explosives research group consists of members of the materials properties group who have been tasked with conducting research activities on the materials properties of HE but with constant input from the members of the HE group focused on simulation of detonation. A similar integration has been achieved with regard to the solid dynamics group in that members of the materials properties group are collaborating actively to compute defect energies and other important quantities which will be used in the simulations of the solid dynamics group.

2. The software integration group has been tasked with the construction of a 2-d prototype of the virtual facility. Its activities in year 1 include bringing in all relevant codes under the VTF harness. In year 2 an object oriented integration framework will be initiated which will enable the applications codes to communicate among themselves and with the VTF harness. The objective is that by the end of year 2 we will have integrated our 2-d high explosives capability with the 2-d solid dynamics Lagrangian capability of `adlib`.

3. All models developed for high explosives as well as for solid dynamics will be integrated into the 2-D prototype. Our first integrated calculations will be the cylinder test and corner turning problem. In addition we will begin work on a materials property data base to integrate materials properties developments into the facility.

Collaborations with the DOE labs will be expanded to include a Symposium on Verification and Validation of Computational Solid Mechanics Codes, to be held at Caltech, December 9-11, 1998, with partial support from the Caltech's ASCI Center. The advisory committee to the symposium includes Christian Mailhiot of LLNL and Paul Yarrington of SNL, and the symposium will take place with extensive participation by DOE scientists. Additional workshops on Materials Properties and High Explosives have been scheduled as well and will provide additional input to the center integration process.

7.5 ASCI computing resource plan

7.5.1 Estimated ASCI computing resource usage (including PSC)

Listed in the table below are our estimates for usage of the ASCI computational facilities. These are simply preliminary estimates. We will refine these estimates based on our assessment of project needs in the near future:

Discipline	Sandia	LLNL	LANL	PSC
High Explosives	20,000	5000	15000	20,000
Solid Dynamics	50,000	20,000	10,000	5000
Materials Properties	50,000	20,000	100,000	10000
Compressible Turbulence	50,000	50,000	20,000	20,000
Computational Science	10,000	10,000	10,000	10,000

7.5.2 Additional Resource Requirements:

We request ASCI support for an increase in speed of our ESNET connection to OC-3. We realize that this would require allocation of funds to the ESNET project, not to Caltech. We need increased speed in order to use the large ASCI platforms at the Labs, for wide-area metacomputing experiments, and for telecollaboration with our colleagues at the ASCI Labs. This increase in speed should take place as soon as possible.

7.6 Center Management

7.6.1 Internal reviews and project assessments

Internal project reviews are again planned for the months of January, May and September/October. These are spaced at four month intervals. The last may be a formal site visit depending on DOE/DP review requirements. It is our intention to include all members of our TST at these four month reviews. Our experience with this format has been positive and productive. The internal project reviews are followed by meetings of the steering committee to review progress.

Regular meetings of the PI' and associated key investigators will take place at monthly intervals to assess progress and to ensure proper deployment of center resources. Finally key center administrative staff meet weekly to ensure that administrative needs for the center (i.e. budget reporting, system administration, processing of receipts and travel) are being met

7.6.2 TST Activities

As stated above it is anticipated that the TST will participate in all regular full project reviews which will take place at 4 month intervals. In addition we anticipate meeting with selected TST members as issues of importance to various project disciplines arise.

Bibliography

[1] Cambridge crystallographic data base

[2] Mayo, S.L., Olafson, B.D., Goddard, W. A., "DREIDING - A GENERIC FORCE-FIELD FOR MOLECULAR SIMULATIONS" *J. Phys. Chem.* **94** (26), 8897-8909 (1990).

[3] C.S. Yoo, H. Cynn, W. Michael Howard,N. Holmes. *Equation of state of unreacted high explosives at high pressures.* 11^{th} International Detonation Symposium, Snowmass, Colorado August 31, September 4, 1998.

[4] R.R. Bernecker. *Observations on the Hugoniot for HMX.* 1996

[5] B. Olinger, Roof, B. and Cady, H., *The Linear and Volume Compression of βHMX and RDX to 9 GPa (90 Kilobars)*, Proceeding Symposium (International) on High Dynamic Pressures, Paris France, 1979, p. 3.

[6] S.P. Marsh (editor), *LASL Shock Hugoniot Data*, University of California Press

[7] J.C. Goutelle, O. Heuze, *A new temperature-dependent equation of state for inert, reactive, and composite materials.* 11^{th} International Detonation Symposium, Snowmass, Colorado August 31, September 4, 1998.

[8] R.L. Gustavsen, S.A. Sheffield, LANL, *Unreacted Hugoniots for porous and liquid explosives.* AIP conference proceedings 309, Part 2, Colorado 1993.

[9] R. P. Fedkiw, X.D. Liu. *The Ghost Fluid Methods for Viscous Flows.* UCLA CAM Reports, Oct 1998

[10] W.M. Beltman, J.E. Shepherd. *Structural response of shells to detonation and shock loading.* GALCIT Report FM98-3, April 1998.

[11] Maas, U. and J. Warnatz (1988). Ignition processes in hydrogen–oxygen mixtures. *Combust. Flame 74*, 53–69.

[12] Lam, H. S. (1993). Using CSP to understand complex chemical kinetics. *Combust. Sci. and Tech. 89*, 375–404.

[13] Kee, R. J., F. M. Rupley, and J. A. Miller (1989). Chemkin–II: A Fortran chemical kinetics package for the analysis of gas-phase chemical kinetics. Technical Report SAND89-8009, Sandia National Laboratories.

[14] Shampine, L. F., H. A. Watts (1979). DEPAC – Design of a user oriented package of ODE solvers. Technical Report SAND79-2374, Sandia National Laboratories.

[15] Quirk, J. J. (1997). *An Introduction to Amrita*. http://www.amrita-cfd.com/.

[16] B. Dobratz, *LLNL explosives handbook - Properties of chemical explosives and explosive simulants*, LLNL Report UCRL-52997, (1981).

[17] C. Eckett, *ASCI FY-98 Report*, (1998).

[18] C. Eckett, J. Quirk, and J. Shepherd, *The role of unsteadiness in direct initiation of gaseous detonation*, GALCIT-CALTECH Report FM 97-19, (1997). Submitted to JFM.

[19] R. Fedkiw, T. Aslam, B. Merriman, and S. Osher, *A non-oscillatory Eulerian approach to interfaces in multimaterial flows (the Ghost Fluid Method)*, UCLA Report CAM98-17, (1998).

[20] W. Fickett and W. Davis, *Detonation*, University of California Press, 1979.

[21] P. Glaister, *An Approximate Linearised Riemann Solver for the Euler Equations for Real Gases*, Journal of Computational Physics, 74 (1988), pp. 382–408.

[22] A. Harten, *High resolution schemes for hyperbolic conservation laws*, Journal of Computational Physics, 49 (1983), pp. 357–393.

[23] J. Johnson, P. Tang, and C. Forest, *Shock-wave initiation of heterogeneous reactive solids*, Journal of Applied Physics, 57 (1985), pp. 4323–4334.

[24] S. Marsh, *LASL shock Hugoniot data*, University of California Press, 1980.

[25] G. Miller and E. Puckett, *A high-order Godunov method for multiple condensed phases*, Journal of Computational Physics, 128 (1996), pp. 134–164.

[26] J. Quirk, *A parallel adaptive grid algorithm for computational shock hydrodynamics*, Applied Numerical Mathematics, (1996), pp. 427–453.

[27] ——, *Amrita - a computational facility (for cfd modelling)*, in VKI 29th Lecture Series, 1998.

[28] P. Roe, *Approximate Riemann solvers, parameter vectors and difference schemes*, Journal of Computational Physics, 43 (1981), pp. 357–372.

[29] R. Sanders, E. Morano, and M. Druguet, *Multidimensional dissipation for upwind schemes: Stability and applications to gas dynamics*, Journal of Computational Physics, 145 (1998), pp. 511–537.

[30] J. Tannehill, D. Anderson, and R. Pletcher, *Computational fluid mechanics and heat transfer*, Taylor & Francis, 1997.

[31] P. Thompson, *Compressible fluid dynamics*, McGraw-Hill Book Company, 1972.

[32] V. Zharkov and V. Kalinin, *Equations of state for solids at high pressures and temperatures*, Consultants Bureau, New-York, 1971.

[33] Chaudhri, M. M., 1989, Proceedings of the 9thSymposium (International) on Detonation, pp.857–867.

[34] B F Goodrich Data

[35] Liu, C., unpublished Los Alamos National Laboratory report.

[36] Fillers, R. W. and Tschoegl, N. W., 1977, Transactions of the Society of Rheology 21:1, pp 51–100.

[37] Knauss, W. G. and Emri, I. J., 1981, Computers and Structures, Vol. 13, pp 123–128.

[38] S. W. Attaway, B. A. Hendrickson, S. J. Plimpton, Gardner, C. T. Vaughan, M. W. Heinstein, and J. S. Peery. Parallel Contact Detection Algorithm for Transient Solid Dynamics Simulations Using Pronto3D. *Presented at S̈ymposium on Development, Validation, and Application of Inelastic Methods for Structural Analysis and Design,Ï996 ASME International Mechanical Engineering Congress on Exposition (IMECE96), Atlanta, GA, November 17-22, 1996*, 1996.

[39] H. Samet. *The Design and Analysis of Spatial Data Structures.* Addison-Wesley, New York, 1990.

[40] G. T. Camacho and M. Ortiz. Computational Modelling of Impact Damage in Brittle Materials. 33 (20-22):2899–2938, 1996.

[41] D. E. Grady and D. A. Benson. Fragmentation of Metal Rings by Electromagnetic Loading. *Experimental Mechanics*, 23:393–400, 1983.

[42] C. Kane, E. A. Repetto, M. Ortiz, and J. E. Marsden. Finite element analysis of nonsmooth contact. *Computer Methods in Applied Mechanics and Engineering*, 1998. in press.

[43] M. Ortiz. Plastic yielding as a phase transition. *Journal of Applied Mechanics, ASME*, 1999. in press.

[44] M. Ortiz and A. Pandolfi. A class of cohesive elements for the simulation of three-dimensional crack propagation. 1998.

[45] M. Ortiz and E. A. Repetto. Nonconvex energy minimization and dislocation structures in ductile single crystals. 1998. in press.

[46] M. Ortiz, E. A. Repetto, and L. Stainier. A theory for predicting dislocation structures and their effect on the hardening of single crystals. in preparation, 1999.

[47] M. Ortiz and L. Stainier. The variational formulation of viscoplastic constitutive updates. *Computer Methods in Applied Mechanics and Engineering*, 1998. to appear.

[48] M. Ortiz and L. Stainier. A mean-field statistical theory of forest hardening in ductile single crystals. in preparation, 1999.

[49] M. Ortiz and S. Suresh. Statistical Properties of Residual Stresses and Intergranular Fracture in Ceramic Materials. 60:77–84, 1993.

[50] A. Pandolfi, P. R. Guduru, M. Ortiz, and A. J. Rosakis. Finite element analysis of experiments of dynamic fracture in c300 steel. *International Journal of Solids and Structures*, 1998. to appear.

[51] A. Pandolfi, P. Krysl, and M. Ortiz. Finite element simulation of ring expansion and fragmentation. *International Journal of Fracture*, 1998. to appear.

[52] A. Pandolfi and M. Ortiz. Solid modeling aspects of three-dimensional fragmentation. 1998.

[53] R. Radovitzky and M. Ortiz. Error estimation and adaptive meshing in strongly nonlinear dynamic problems. 1998.

[54] R. Radovitzky and M. Ortiz. Tetrahedral mesh generation based on node insertion in crystal lattice arrangements and advancing-front-Delaunay triangulation. 1998. in press.

[55] E. A. Repetto, R. Radovitzky, and M. Ortiz. Finite element simulation of dynamic fracture and fragmentation of glass rods. to appear in *Computer Methods in Applied Mechanics and Engineering*, 1999.

[56] D. Rodney, V. B. Shenoy, R. Phillips, and M. Ortiz. The three-dimensional structure of dislocation junctions in fcc metals. *In preparation*, 1998.

[57] G. Ruiz, A. Pandolfi, and M. Ortiz. Three-dimensional finite-element simulation of dynamic brazilian tests on concrete cylinders. in preparation, 1998.

[58] J. W. Tedesco, C. A. Ross, and S. T. Kuennen. Experimental and numerical-analysis of high-strain rate splitting tensile tests. *ACI Materials Journal*, 90(2):162–169, 1993.

[59] M. Beltman *S*tructural Response of shells to detonation and shock loading GALCIT Report FM 98-3, April 1, 1998.

[60] M. Beltman, E. Burcsu, J. E. Shepherd, and L. Zuhal, "The Structural Response of cylindrical shells to internal shock loading" Proceedings of the International Symposium on Computational Technologies for Fluid/Thermal/Chemical Systems with Industrial Applications. Joint ASME/JSME meeting, San Diego, July 26-30, 1998.

[61] L. G. Hill, "Detonation product equation-of-state directly from the cylinder test," Paper 2780, 21rst International Symposium on Shock Waves, Great Keppel Island, Australia, July 20-25, 1997.

[62] R. P. Fedkiw, T. Aslam, B. Merriman, S. Osher "A Non-Oscillatory Eulerian Approach to Interfaces in Multimaterial Flows (The Ghost Fluid Method)" submitted to J. Comp. Physics 1998.

[63] Y. Kimura, T. Çağın, Y. Qi, and W. A. Goddard III, Phys. Rev. B, submitted.

[64] A. P. Sutton and J. Chen, Philos. Mag. Lett. **61**, 139 (1990).

[65] H. Rafii-Tabar and A. P. Sutton, Philos. Mag. Lett. **63**, 217 (1991).

[66] Y. Qi, T. Çağın, and W. A. Goddard, III Phys. Rev. B1, in press.

[67] T. Çağın, G. Dereli, M. Uludoğan, M. Tomak, Phys. Rev. B1, in press.

[68] Y. Qi, T. Çağın, and W. A. Goddard, III Phys. Rev. E, submitted.

[69] V. Rosatto, M. Guillopé, and B. Legrand, Philos. Mag. A **59**, 321 (1989); F. Cleri and V. Rosato, Phys. Rev. B **48**, 22 (1993).

[70] D. W. Brenner, Phys. Rev. B **42**, 9458 (1990).

[71] A. K. Rappé and W. A. Goddard III, J. Phys. Chem. **95**, 3358 (1991).

[72] S. L. Mayo, B. D. Olafson, and W. A. Goddard III, J. Phys. Chem. 94, 8897 (1990).

[73] Ollinger, B.; Roof, B.; Cady, H. "The linear and volume compression of beta-HMX and RDX to 9 GPa"; Actes Du Symposium International Sur Le Comportement des Milieux Denses Sous Hautes Pressions Dynamiques, 1978, Centre d'Etudes Nucleaires de Saclay.

[74] E. M. Stolper and T. J. Ahrens, Geophys. Res. Lett. **14**, 1231 (1987).

[75] J. W. Swegle, J. Appl. Phys. **68**, 1563 (1990), and references therein.

[76] A. C. Wright, J. NonCryst. Solids **179**, 84 (1994).

[77] X. J. Chen, J-M. Langlois, and W. A. Goddard III, Phys. Rev. **52**, 2348 (1995). X. Chen, X. Hua, J. Hu, J-M. Langlois and W. A. Goddard III, Phys. Rev. **53**, 1377 (1996).

[78] A. K. Rappé, C. J. Casewit, K. S. Colwell, W. A. Goddard III, and W. M. Skiff, J. Am. Chem. Soc. **114**, 10024 (1992).

[79] N. Karasawa, S. Dasgupta, and W. A. Goddard III, J. Phys. Chem. **95**, 2260 (1991).

[80] S. Dasgupta, T. Yamasaki, and W. A. Goddard III, J. Chem. Phys. **104**, 2898 (1996).

[81] R. D. Richtmyer, Taylor instability in shock acceleration of compressible fluids, *CPAM*, **XIII**, 297-319, 1960.

[82] U. Alon, J. Hecht, D. Mukamel, D. Shvarts, *Phys. Rev. Lett.*, **72**, 2867, (1994).

[83] O. Sadot, L. Erez, U. Alon, D. Oron, L. Levin, Study of Nonlinear Evolution of Single-Mode and 2-Bubble Interaction under Richtmyer-Meshkov Instability, *Phys. Rev. Let.*, **80**, 1654-1657,(1998).

[84] R. Samtaney, N. J. Zabusky, Circulation deposition on shock-accelerated planar and curved density-stratified interfaces: models and scaling laws, *J. Fluid Mech* **269** 45-78, (1994).

[85] J. M. Moschetta, D. I. Pullin, A robust low diffusive kinetic scheme for the Navier-Stokes equations, *J. Comp. Phys.* **133**, 193-204 (1997).

[86] D. W. Moore, D. I. Pullin, and D. I. Meiron, On steady compressible flows with compact vorticity; the compressible Stuart vortex, to appear, J. Fluid. Mech. (1999).

[87] D. I. Pullin, J. D. Buntine, P. G. Saffman, On the spectrum of a stretched spiral vortex, *Phys. Fluids*, **6**, 3010-3027, (1994).

[88] R. D. Henderson, G. E. Karniadakis, Unstructured Spectral Elements for Simulation of Turbulent Flows, *J. Comp. Phys.*, **122**, 191-217, (1995).

[89] S. K. Lele, Compact finite-difference schemes with spectral-like resolution, *J. Comp. Phys.*, **103**, 16-42, (1992).

[90] P. Moin, J. Kim, Numerical investigation of turbulent channel flow, *J. Fluid Mech.* **118**, 341-377, (1982).

[91] P. E. Dimotakis, H. J. Catrakis, A. W. Cook, J. M. Patton, On the geometry of two dimensional slices of irregular level sets in turbulent flows, *Proceedings, 2'nd Monte Verita Colloquium on Fundamental Problematic Issues in Turbulence*, (1998)

[92] A. Leonard, P. Moeleker, Subgrid modeling for the filtered scalar transport equation, *Proceedings, 2'nd Monte Verita Colloquium on Fundamental Problematic Issues in Turbulence*, (1998)

[93] R. Bramley, Component Architectures for Distributed Scientific Problem Solving, *IEEE Computational Science & Engineering*, 5(2), pp.5 0-63 (1998).

[94] R. Bramley, D. Gannon, T. Stuckey, J. Villacis, The Linear System Analyzer, submitted to IEEE book on PSE's, March 1998.

[95] J. Balasubramanian, E. Akman, F. Breg, S. Diwan, and M. Govindaraju. The LSA System, Java98 ACM Conference held in Palo Alto, CA.

[96] Fabian Breg, Shridhar Diwan, Juan Villacis, Jayashree Balasubramanian, Esra Akman, and Dennis Gannon, Java RMI Performance and Object Model Interoperability: Experiments with Java/HPC++, Concurrency and Experience, 1998.

[97] See also http://www.extreme.indiana.edu/pseware/LSA/LSAhome.html

[98] John Thornley, Maria Hui, Hao Li, Tahir Cagin, and William Goddard III, "Molecular Dynamics Simulation on Commodity Shared-Memory Multiprocessor Systems with Lightweight Multithreading" High Performance Computing Symposium of the Advanced Simulation Technolgies Conference 1999

[99] W. Schroeder, K. Martin, B. Lorensen, The Visualization Toolkit, Prentice Hall, 1998,

[100] Daniel A. Reed, Ruth A. Aydt, Luiz DeRose, Celso L. Mendes, Randy L. Ribler, Eric Shaffer, Huseyin Simitci, Jeffrey S. Vetter, Daniel R. Wells, Shannon Whitmore, and Ying Zhang, "Performance Analysis of Parallel Systems: Approaches and Open Problems," Joint Symposium on Parallel Processing (JSPP), pp, 239-256, Nagoya, Japan, June 1998

[101] Daniel A. Reed and Randy L. Ribler, "Performance Analysis and Visualization," Computational Grids: State of the Art and Future Directions in High-Performance Distributed Computing, Ian Foster and Carl Kesselman (eds), Morgan-Kaufman Publishers, August 1998.

[102] Huseyin Simitci and Daniel A. Reed, "A Comparison of Logical and Physical Parallel I/O Patterns," International Journal of Supercomputer Applications and High Performance Computing, special issue (I/O in Parallel Applications), Fall 1998.

[103] http://www.ncsa.uiuc.edu/